MANCHESTER
1824
The University of Manchester

Beam Dynamics and Applications of Dielectric Wakefield Accelerator Structures

A thesis submitted to the University of Manchester for the degree of
Doctor of Philosophy
in the Faculty of Science and Engineering

2023

Toby J. Overton
Department of Physics and Astronomy
School of Natural Sciences

Contents

Word Count: 38190

List of figures

List of tables

List of publications

Journal Publications

T.J. Overton, T.H. Pacey, Y. Saveliev, N. Joshi, S. Mathisen, B.D. Muratori, N. Thompson, M.P. King, & G. Xia (2023). Experimental Study of Transverse Beam Dynamics in Dielectric Wakefield Structures. *Submitted to Nuclear Instruments and Methods in Physics Research: Section A*

T.J. Overton, Y. Saveliev, T.H. Pacey, & G. Xia (2023). On Broadband Longitudinal Profile Measurements using a Dielectric Wakefield Streaker. *Submitted to Journal of Instrumentation*

Y. Saveliev, T.J. Overton, T.H. Pacey, N. Joshi, S. Mathisen, B.D. Muratori, N. Thompson, M.P. King, & G. Xia (2022). Experimental study of transverse effects in planar dielectric wakefield accelerating structures with elliptical beams. *Physical Review Accelerators and Beams, 25(8)*, 081302.

Conference Proceedings

T. J. Overton, T. H. Pacey, Y. M. Saveliev, and G. Xia, "Beam Dynamics and Drive Beam Losses Within a Planar Dielectric Wakefield Accelerator", in *Proc. IPAC'22*, Bangkok, Thailand, Jun. 2022, pp. 641–644. doi:10.18429/JACoW-IPAC2022-MOPOMS010

T. J. Overton, T. H. Pacey, Y. M. Saveliev, and G. Xia, "A Stable Drive Beam for High Gradient Dielectric Wakefield Acceleration", in *Proc. IPAC'21*, Campinas, Brazil, May 2021, pp. 528–531. doi:10.18429/JACoW-IPAC2021-MOPAB151

T.H. Pacey *et al.*, "Recent Experimental Results from the Dielectric Wakefield Acceleration Program at CLARA Facility", presented at *IPAC'23*, Venice, Italy, May. 2023, to be published

T. H. Pacey *et al.*, "Development of a 6D Electron Beam Diagnostics Suite for Novel Acceleration Experiments at FEBE on CLARA", in *Proc. IBIC'22*, Kraków, Poland, Sep. 2022, pp. 1–5. https://jacow.org/ibic2022/papers/mo1c3.pdf

Abstract

Dielectric wakefield accelerators (DWAs) have been experimentally shown to accelerate electron bunches with gradients orders of magnitude larger than using conventional RF-based particle accelerators. DWAs have future and present applications, as a potential future replacement technology for high-energy electron accelerators, and as compact passive devices for beam manipulation and bunch diagnostics. This thesis presents experimental and simulation studies of these applications. Experimental results are presented, carried out by the author and collaborators at the CLARA/VELA facility at Daresbury Laboratory, providing measurements of longitudinal and transverse fields excited by electron beams propagating in planar and circular dielectric lined waveguides (DLWs). The use of transversely shaped beams to suppress instabilities in DWAs were investigated and the transverse fields with this scheme are evaluated.

An efficient simulation framework, DiWaCAT, for modelling the wakefields inside DLWs has been developed and benchmarked against commercial software and experimental results. DiWaCAT was used for simulations of the high-charge and high-momentum beams required for a future accelerator based on DWA. Transverse instabilities were investigated in this regime and methods for suppression presented and analysed.

DLWs as passive diagnostic devices are of increasing interest at accelerator facilities. A dielectric wakefield streaker for longitudinal bunch diagnostic has been explored and the performance evaluated for two beam regimes. The work presented provides a potential operating window for a dielectric wakefield streaker, extending the range of facilities where the passive diagnostic could be used.

Declaration of originality

I hereby confirm that no portion of the work referred to in the thesis has been submitted in support of an application for another degree or qualification of this or any other university or other institute of learning.

Copyright statement

i The author of this thesis (including any appendices and/or schedules to this thesis) owns certain copyright or related rights in it (the "Copyright") and s/he has given The University of Manchester certain rights to use such Copyright, including for administrative purposes.

ii Copies of this thesis, either in full or in extracts and whether in hard or electronic copy, may be made *only* in accordance with the Copyright, Designs and Patents Act 1988 (as amended) and regulations issued under it or, where appropriate, in accordance with licensing agreements which the University has from time to time. This page must form part of any such copies made.

iii The ownership of certain Copyright, patents, designs, trademarks and other intellectual property (the "Intellectual Property") and any reproductions of copyright works in the thesis, for example graphs and tables ("Reproductions"), which may be described in this thesis, may not be owned by the author and may be owned by third parties. Such Intellectual Property and Reproductions cannot and must not be made available for use without the prior written permission of the owner(s) of the relevant Intellectual Property and/or Reproductions.

iv Further information on the conditions under which disclosure, publication and commercialisation of this thesis, the Copyright and any Intellectual Property and/or Reproductions described in it may take place is available in the University IP Policy (see http://documents.manchester.ac.uk/DocuInfo.aspx?DocID=24420), in any relevant Thesis restriction declarations deposited in the University Library, The University Library's regulations (see http://www.library.manchester.ac.uk/about/regulations/) and in The University's policy on Presentation of Theses.

Acknowledgements

I would like to thank everyone who has contributed to my development over the past 8 years at The University of Manchester. My supervisor, Guoxing Xia, for his dedicated support and for allowing me the opportunity to contribute to the Novel Acceleration Group at UoM. His guidance and encouragement have been instrumental in shaping my research journey. I would like to express my sincere thanks to Roger Jones for introducing me to accelerator physics and the work of The Cockcroft Institute as an undergraduate, I do not believe I would have chosen this path if it were not for the passion he showed for the subject.

The supervision I have received from Yuri Saveliev has been invaluable. His meticulous attention to detail, patience, and commitment to scientific excellence have been a true inspiration. I am grateful for the knowledge and skills I have gained under his guidance. I am also deeply grateful to Thomas Pacey for his fundamental contributions to my research. His willingness to engage in discussions, tackle challenges together, and provide insightful perspectives have greatly influenced the direction and progress of my work. Not many PhD students can rely on such a dedicated supervisory team and the work presented in this thesis would not have been possible without them.

I extend my gratitude to all my colleagues who have contributed to my development. Where help has been provided for work relevant to specific chapters, that has been acknowledged on a chapter by chapter basis.

To my parents and entire family, I am grateful for their unwavering support and encouragement. Their belief in me has been a constant source of motivation and strength throughout my academic journey. I want to express my heartfelt appreciation to my partner, Justin, for his continuous support, understanding, and encouragement. Your presence in my life has provided me with the emotional support and stability I needed during the challenges of this journey.

Chapter 1

Introduction

1.1 Particle Accelerators

Particle accelerators exist for the purpose of delivering charged particle beams to a target location, serving the primary objectives of the given machine. In applications utilising charged particles produced by accelerators, the primary processes involve either the collision of the particles delivered by the accelerator, their delivery onto a target to generate other particles (e.g., neutrons or short-lived charged particles), or the production of photons through a radiation process.

Low and medium energy particle accelerators have applications in a wide range of fields. Industrial applications include material processing with electrons and the provision of x-rays for imaging (such as used in cargo scanning). Medical applications of particle accelerators utilise both direct particle beams and radiation sources, for imaging and radiotherapy. Radiotherapy treatments include radiation sources and the delivery of particles (electrons, protons, or other hadrons) onto a target region. Uses of high energy accelerators include particle colliders for high energy physics (HEP) and light sources (synchrotron radiation sources and free electron lasers (FELs)). Such light sources can image the fine detail of structures, with uses in physics, medicine, biological sciences, chemistry, and more [1].

The size of a linear accelerator (linac) is primarily determined by the accelerating gradient of the field used to accelerate the charged particles. In conventional accelerators, this field is generated by driving RF electromagnetic (EM) waves in metallic cavities. These cavities, operating at frequencies from tens of MHz to ≈ 10 GHz can typically achieve accelerating gradients up to 100 MV/m, limited by breakdown effects at cavity surfaces.

Cutting-edge conventional technologies are seen in proposed colliders for HEP applications. Two examples of proposed colliders operating at the highest accelerating gradients possible with RF cavities are the International Linear Collider (ILC), based on superconducting RF-cavities, and The Compact Linear Collider (CLIC), based on

novel normal-conducting RF cavities.

The ILC is designed to use superconducting RF cavities, operating at 2 K, to achieve an an average accelerating gradient of 20-40 MV/m. At this accelerating gradient, including other beam optics and diagnostics, to achieve a centre-of-mass energy of 250-500 GeV the total length of the accelerator is designed to be 31 km (i.e. 15.5 km per electron/positron branch). At the time of writing, the construction of the ILC has not been realised. The primary reason for this is the significant cost associated with building and operating such a large-scale facility. Estimates for the cost of the ILC range from $5.5 billion (excluding labour) [2] to $25 billion [3]. Accelerators designed for non-HEP purposes operate at smaller scales, but they still possess significant size and cost considerations. This limitation restricts the number of facilities that can be constructed, whether it pertains to the number of energy frontier accelerators globally or the availability of medical linacs for treatment within a specific country.

CLIC is a proposed $e^+ - e^-$ collider using normal conducting RF cavities. In order to achieve high accelerating gradients in normal conducting cavities, whilst avoiding heat dissipation in the cavity walls, normal conducting structures must operate with short pulsed power [4]. CLIC is designed to use a two-beam acceleration system; a high current, low energy drive bunch generates short RF pulses, transferred via a series of waveguides to the main RF cavity. These cavities are designed to operate with an RF frequency of 12 GHz and accelerating gradients between 72 and 100 MV/m [5]. To achieve centre-of-mass energies of 380 MeV for the first phase of operation, CLIC would have a total length of 11 km [5].

Both of these machines require large infrastructure for operation. Any future upgrades to these machines with the same accelerating gradient will linearly increase the size of the accelerator. In order to reduce the size of accelerators, it becomes necessary to employ acceleration techniques capable of achieving higher accelerating gradients. The objective of shrinking accelerator sizes is relevant regardless of whether the goal is to produce beams comparable to those produced by large laboratory facilities, achieve table-top scale accelerators, or accelerate beams towards the energy frontier.

1.2 High-Gradient Accelerators

1.2.1 The Need for Smaller and Higher Energy Accelerators

The infrastructure required for accelerators at the energy frontier limits the number of facilities that can host such a machine. Similarly, the size and cost of medium and

low-energy accelerators limits the number of such machines that can be built in a country or region. Therefore, technology to limit the size and/or cost of accelerators increases the accessibility of accelerator-based science and applications.

Producing higher energy beams with conventional RF-based acceleration methods requires increasing the acceleration length since the acceleration gradient is limited by breakdown effects in conventional cavity resonator based structures. To overcome this limitation, novel acceleration methods have been proposed to achieve higher accelerating gradients. Rather than conventional metallic cavities, novel acceleration methods include exciting fields inside plasma or dielectric-lined structures. These fields can be driven by a charged particle beam or a high-powered laser.

International effort and collaborations has been focused on determining the future direction of accelerator research. For example, the update to the European Strategy for Particle Physics addressed the larger questions around HEP research and determined the main focus of the community [6]. Two areas of high-priority research were outlined. The first was the building of an accelerator with existing technology at the current energy frontier (multiple TeV electrons or a hadron collider with centre-of-mass energy at least 100 TeV). The second related to the need for 'novel' accelerator technology, specifically:

> *"technologies under consideration include high-field magnets, high-temperature superconductors, plasma wakefield acceleration and other high-gradient accelerating structures, bright muon beams, energy recovery linacs"*

[6]. A similar process was completed by the US HEP community through the Snowmass exercise [7]. In this review, a larger focus was placed on the physics goals of future experiments. The executive summary highlighted advanced accelerator concepts as a priority for the accelerator community, specifically mentioning plasma and structure-based wakefield acceleration as research topics of interest. A more detailed review of accelerator physics within the Snowmass exercise is given in [8]. Wider reviews, including those conducted at the national level, play a crucial role in setting the agenda and goals for individual institutions; one such example being the 'STFC Strategic Framework for Future Accelerator Science and Technology Development' for UK funded research [9]. Within this framework, the European Strategy is referred to as providing the wider strategic landscape within which the UK accelerator community fits. The need for novel acceleration techniques is listed within the key theme of aligning future research with future infrastructure needs. In this context, plasma and dielectric wakefield accelerators are named as priority technology areas to explore and develop [9].

1.2.2 Requirements for Novel Acceleration Methods

International collaborations, such as the ALEGRO and Snowmass exercises [8][10], have identified challenges the community must address for the realisation of high-gradient acceleration technologies. No novel acceleration method has demonstrated the beam quality and reproducibility required for a future high energy accelerator facility. Consequently, research efforts are directed towards generating high-brightness beams and optimising novel acceleration techniques to fulfill these requirements.

Near-term applications of novel acceleration methods have been explored by the community. An accelerator technology must be demonstrated to produce particle beams that are suitable for specific external user experiments before it can be considered for high-energy facilities [11]. As such, a likely candidate for a demonstrator is an FEL facility, allowing for the demonstration of beam reproducibility and the ability to deliver beam parameters suitable for external user experiments. The most developed of these is EuPRAXIA, which will act as an FEL facility based in plasma wakefield acceleration [12]. An FEL facility has also been proposed based on structure-wakefield acceleration at the Argonne Wakefield Accelerator facility, providing multiple beamlines for applications including medical imaging [13]. An FEL based on these technologies could also be used as an 'energy booster' for an existing facility, providing a higher energy upgrade without the need for significant infrastructure and reduced ongoing power demands.

Applications of novel acceleration techniques for beam manipulation have been developed in recent years. Examples include the removal of longitudinally correlated energy spread (chirp) from a beam [14][15] and the excitation of a longitudinally varying kick to reconstruct the longitudinal bunch profile, commonly referred to as streaking and the device as a streaker [16]. A streaker is an example of a passive device (i.e. no power requirement) that is able to replace a diagnostic requiring an RF power supply (namely a transverse deflecting cavity).

1.3 Structure of Thesis

The work presented in this thesis can be broadly divided into three parts. The first part focuses on dielectric wakefield acceleration (DWA) and the methods used to calculate and simulate the fields in DWAs. Chapter 2 provides an overview of novel acceleration techniques, with a specific focus on DWA. In this Chapter, the active research areas will be identified, providing motivation for the work in this thesis. In Chapter 3, the background of theoretical calculations of electromagnetic (EM) fields within dielectric lined waveguides (DLWs) is discussed. Furthermore, Chapter 4 describes a simula-

tion framework designed to calculate wakefields produced in DWAs. The simulation framework presented in Chapter 4 serves as the foundation for the results presented in subsequent chapters of the thesis.

The second part of the thesis centers around the study of transverse dynamics in DWAs and their practical application in accelerator design. Experimental studies were conducted at the CLARA/VELA facility at Daresbury Laboratory, and the setup of the machine during the experiments is detailed in Chapter 5. Results from experiments are presented in Chapter 6. These experiments were performed with a lower energy electron beam than required with a future DWA, allowing for study of the transverse fields in detail. The chapter describes the 3D fields within an adjustable gap planar DLW and a circular DLW, comparing the two structure geometries. In Chapter 7, the conclusions drawn from the previous chapter are tested through simulations using beam parameters representative of a future DWA designed for high-gradient acceleration. This chapter explores potential schemes for stable long-distance DWA, including the use of transversely shaped (elliptical) bunches and alternating planar DLW orientations. The preservation of beam quality throughout the DWA stage and the evaluation of beam-breakup (BBU) effects causing instabilities in DWAs are also discussed. The simulation study in this part utilises beam parameters achievable with current technology, capable of exciting accelerating gradients of approximately 100 MV/m, as required for future 'practical' applications.

The final part of the thesis, Chapter 8, investigates the feasibility of a passive dielectric streaker for longitudinal bunch diagnostics. The geometry and layout of the streaker are optimised for improved resolution, and a comprehensive simulation study is conducted for two distinct types of beams and facilities. These parameter spaces include an medium-energy electron test facility requiring a variety of beam profiles, as well as facilities that demand the measurement of ultra-short (fs-scale) high-energy bunches, such as free-electron laser (FEL) facilities or accelerators based on other novel techniques such as laser wakefield acceleration (LWFA).

Chapter 2

Concepts and Technologies for Future Accelerators

2.1 Novel Acceleration Concepts

In line with the requirements of future accelerators, a number of 'novel' techniques have been proposed for accelerating charged particle bunches. These techniques include structure-based wakefield accelerators and plasma-based wakefield accelerators. The accelerating fields in both of these wakefield accelerators can be beam-driven or laser-driven. Beam-driven methods require the production of a high-energy particle beam from which energy can be extracted. Therefore, the total size of a beam-driven accelerator also includes a facility to generate the driving bunch.

The following section provides a brief overview of each concept in turn, including significant experimental results towards the realisation of practical uses of each scheme.

2.1.1 Plasma-based Acceleration

Plasma can be described as an electrically neutral 'sea' of charged particles, as shown in Figure 2.1(a). Ions (positively charged) and electrons (negatively charged) independently exhibit collective motion when an external force is applied. Due to a lower mass, the electron collective motion occurs over shorter time frames than ion motion [17].

An external EM field can penetrate through a plasma, providing the frequency of the field is sufficiently high. This field causes a perturbation in electron and ion densities, with the plasma returning to the stable state once the field is removed. Due to the inertia of the particles, the collective motion will oscillate about the equilibrium position until the stable state is restored. Plasma wakefield acceleration utilises perturbations in electron density to generate strong EM fields. The perturbation can be driven by either the Coulomb field of an energetic charged particle bunch or the ponderomotive force driven

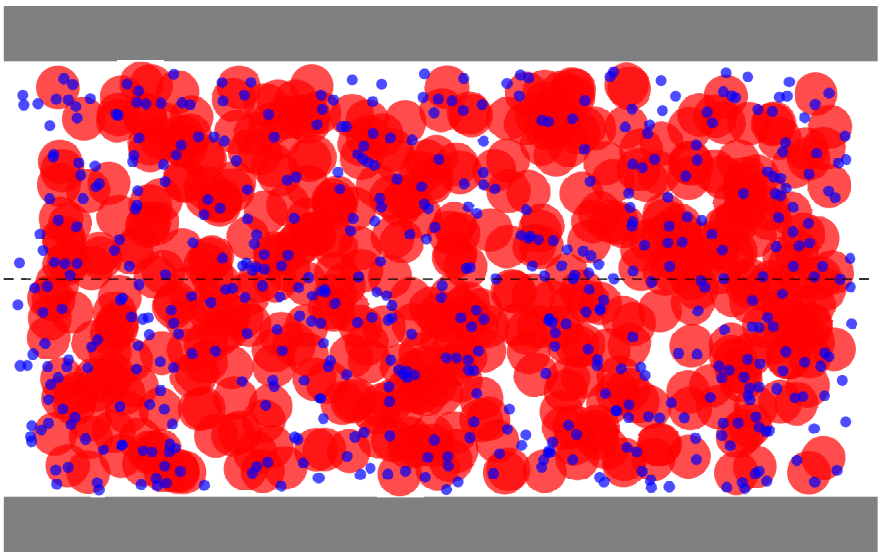

(a) Plasma with no beam/laser interaction.

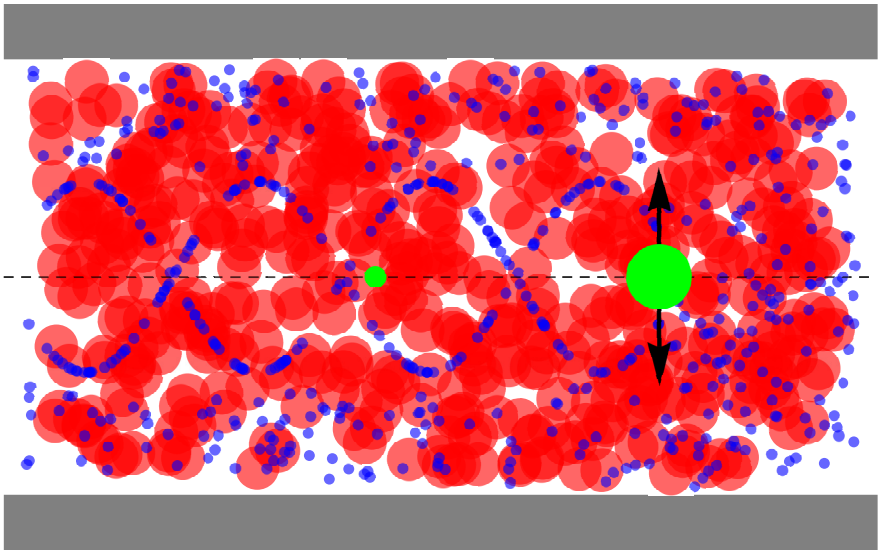

(b) Accelerating regime with drive beam/laser on the right and main/witness bunch on the left.

Figure 2.1. Plasma consisting of positive ions (red) and electrons (blue) with and without beam/laser interaction.

by an intense laser beam. With a strong enough perturbation, a non-linear response is induced in the plasma [18]. As illustrated in Figure 2.1(b), oscillatory motion produces a bubble-like wake in which a main/trailing bunch can be accelerated. This main bunch can be externally injected into the plasma, as if the case with the driving beam/laser, or plasma electron trapped/self-injected into the wakefield. Whilst shown in the bubble behind the drive bunch, this as a visual aid and the drive and main bunch are often in the same bubble.

The maximum accelerating gradient in the blowout-regime, a highly non-linear regime where all electrons are expelled from a region in the plasma, is given by

$$E_z^0 = \frac{m_e c \omega_p}{e} \approx 96\sqrt{n_0[\mathrm{cm}^{-3}]}[\mathrm{V/m}], \tag{2.1}$$

where m_e is the electron mass, e is the charge of an electron, c is the speed of light in vacuum, n_0 is the unperturbed electron density, and ω_p is the plasma frequency defined by

$$\omega_p = \sqrt{\frac{e^2 n_0}{\varepsilon_0 m_e}}, \tag{2.2}$$

where ε_0 is the permitivity of vacuum [19]. A plasma density $n_0 \sim 10^{17}$ cm^{-3}, as suggested for future applications in [10], gives a maximum accelerating field ~ 30 GV/m: orders of magnitude larger than can be achieved in conventional cavity resonator-based accelerators.

High accelerating fields do not cause breakdown of the plasma; in plasma accelerators the field strength is limited by the breakdown of the wave (rather than plasma), at which point electrons from the initial plasma are injected into the bubble, loading the accelerating field and reducing the efficiency of overall acceleration [20]. This feature also means that an electron bunch can be trapped and then accelerated within the plasma itself; self-injected electron bunches are typically only considered for laser-driven plasma wakefield acceleration.

The length of the accelerating phase in plasma wakefield accelerators, and thus the maximum length of the main beam bunch, is typically given by half the plasma wavelength, λ_p, which in the linear regime is given by

$$\lambda_p = \frac{2\pi c}{\omega_p} \approx \frac{3.3 \times 10^4}{\sqrt{n_o[\text{cm}^{-3}]}}[\text{m}] \tag{2.3}$$

[21]. Taking the example of a plasma density $n_0 \sim 10^{17}$ cm^{-3}, the maximum bunch length would be less than 15 fs. Therefore, plasma schemes are attractive for the production of ultra-short bunches. However, it is important to note that in plasma wakefield accelerators, the non-linear and high-frequency nature of the accelerating fields can result in large energy spreads [22]. Work to mitigate large energy spreads includes shaping driving bunches and/or plasma staging to shape the wakefield in such a way to minimise energy spread [23][24][25].

Laser Wakefield Acceleration (LWFA)

Plasma wakefield accelerators were initially proposed as a method for bunch generation and acceleration, utilising an intense laser beam to trap and accelerate an electron bunch [26]. The plasma wave is excited by the laser ponderomotive force, i.e. the radiation pressure exerted by the EM density gradient in the laser pulse. For maximal efficiency, the laser pulse length should be approximately half the plasma wavelength

[26]. Proper matching of the laser pulse length to the plasma wavelength is crucial for maximising the energy gain and overall performance of the plasma wakefield accelerator. Achieving these pulse lengths was a limiting factor in the early years of LWFA research. To compensate, multiple laser pulses were used, timed such that the individual wakes amplify. So called plasma beatwave acceleration was first experimentally demonstrated in 1992 [27], with a 700 MV/m accelerating gradient measured from externally injected electrons. The development of chirped-pulse amplification technology allowed for compact laser pulses with intensity and pulse length required for LWFA [28].

Acceleration with GV/m gradients has been measured over multiple cm of plasma. In 2014, a team at BELLA accelerated a 6 pC electron bunch over 9 cm with an average gradient of 46 GV/m [29]. The total energy gain achievable in single-stage LWFA is limited by depletion in laser quality, laser dephasing, and diffraction. Staging acceleration over multiple plasma sources can mitigate for this effect. Staged LWFA, using two plasma sources was demonstrated at BELLA in 2016; an electron beam with a central energy of 120 MeV energy was generated from a gas-jet target followed by a maximum energy gain of 100 MeV through a discharge capillary [30]. A guided laser beam can also allow for acceleration over longer distances; in 2019 acceleration of 8 GeV over 20 cm was demonstrated [31].

Naturally, positrons cannot be accelerated through self-injection and require external injection. In the case of externally injected bunches, the physics involved is charge asymmetric. At the end of a plasma bubble the field focuses an electron bunch but would instead defocus a positron bunch. Consequently, the position within the bubble for the injection of electron and positron bunches must be individually considered.

In LWFA schemes, the pulse repetition rates are constrained by the repetition rate of the high-energy laser pulses that are necessary to drive fields. To achieve higher repetition rates in the kHz and MHz range, advancements in laser technology are needed [10]. Alternatively, laser beatwave acceleration techniques could be used at these frequencies due to lower laser power requirements.

Beam-Driven Plasma Wakefield Acceleration (PWFA)

There are two schemes proposed for PWFA, electron-driven and proton-driven wakefields. With the electron-driven case, as first proposed in 1985 [32], the Coulomb field of the electrons expel plasma electrons which then return to the equilibrium position, overshooting and producing the oscillating ‘bubble’ when in the non-linear regime. The proton-driven case uses the same principle and first proposed in 2009 [33], however the plasma electrons are attracted to the beam, overshooting the equilibrium position and

producing the characteristic 'bubble'.

PWFA regimes do not suffer from the dephasing effect seen with LWFA over typical accelerating distances due to the relativistic drive beam energy [34][35]. By tuning the plasma and beam parameters, the transverse wakefields produced by the plasma can keep the beam focused over long distances [36]. Thus, PWFA experiments are typically conducted over m-scale lengths rather than the cm-scale typical of LWFA.

Electron-driven PWFA was experimentally demonstrated at the Argonne Advanced Accelerator Test Facility (AATF) in 1988 with a maximum field of 1.6 MV/m measured, matching theoretical expectations [37]. The high gradients promised by PWFA have been demonstrated, with energy doubling of the tail (from 42 to 84 GeV) with ~ 52 GV/m gradient measured [38]. This experiment demonstrated high gradients with the caveats of large energy spread. Recent experiments have demonstrated the effect of beam loading, i.e. shaping the drive bunch can flatten the accelerating wakefield, reducing energy spread (with average variation in wakefield reduced by 40% compared to a Gaussian profile) with the caveat of slightly reduced accelerating gradients [25]. Energy spread has also been shown to be minimised by setting the correlated energy spread (chirp) such as to match the inverse of the energy spread added by the plasma wakefield [24].

Proton-driven PWFA has the potential to use high energy and high charge proton accelerators to accelerate electrons/positrons to the energy frontier. Using beam parameters from the SPS beamline at CERN, simulation studies showed electron bunches accelerated with GV/m gradients [39]. The AWAKE experiment at CERN acts as proof-of-principle for proton-driven PWFA HEP applications, using proton beams delivered from the SPS beamline [40]. Bunches delivered by SPS have typical RMS bunch lengths of 7 cm after compression, longer than the approximate 100 μm length, approximately equal to the plasma wavelength, required to effectively drive the Rb-plasma used for AWAKE. Self-modulation instability (i.e. the self-induced transverse wakefields in the plasma) creates microbunches of the correct length and drive wakefields in the plasma [41]. In future experimental runs, the self-modulation will be seeded by a preceding electron bunch as demonstrated in [42]. This self-modulated bunch will then be utilised to accelerate another electron bunch in a second plasma cell, with the aim of avoiding shot-to-shot variation in proton phase [43]. During Run-1 of the experiment, the proton self-modulation was demonstrated and electrons were accelerated through the 10 m long plasma cell to energies of 2 GeV [41][44]. Future aims of the AWAKE experiment include demonstrating the acceleration of electrons with controllable emittance, i.e. electrons with applicability to HEP [43].

Positron acceleration with PWFA works in the same way as electron acceleration,

with the caveat that focusing fields for electrons instead defocus positron bunches. Positron acceleration was first demonstrated in 2003, with the tail of a positron driving bunch accelerated with a maximum energy gain of 80 MeV (with 56 MeV/m gradient) [45]. In 2015, at FACET, 120-200 pC positron bunches were accelerated to 24.5-26 GeV (accelerating gradient up to 5 GV/m) with 4-6% FWHM energy spread [46]. Proton-driven PWFA with positron bunches has been studied through simulations, with minisation of energy spread and emittance conservation with the use of a hollow plasma channel and preceding electron bunch [47].

2.1.2 Dielectric Structure Based Acceleration Schemes

Beam-Driven Dielectric Wakefield Acceleration (DWA)

Charged particle bunches travelling in a waveguide excite wakefields, defined as longitudinal and transverse EM fields generated by the bunch and reflected within the waveguide back towards where the bunch is propagating [48]. In a metallic waveguide, such as an RF accelerating cavity, these wakefields are caused by cross-sectional variation in the cavity surface. Wakefields are typically an inconvenience and cause beam instability.

Structure-based wakefield devices utilise the wakefields generated by charged particles in a waveguide to produce high-gradient accelerating fields for a secondary main bunch. Typical schemes utilise either circular/cylindrical or planar/slab dielectric lined waveguides (DLWs). A schematic of the Couloumb fields generated by relativistic charged particles is shown in Figure 2.2. A wavefront is formed perpendicular to the source particle by the superposition of the individual spherical EM field potentials. The electric field profile can be derived from the Liénard-Wiechert potentials or with a Lorentz transformation of the Coulomb field [49]. The velocity of a relativistic charged particle, and therefore the group velocity of the wavefront, is greater than the local speed of light in a dielectric material. This condition satisfies the the criteria for the generation of Cherenkov radiation [50]. As shown in Figure 2.3, inside a DLW the wavefront is refracted, and reflected back into the vacuum channel behind the drive bunch. Once the reflected wave returns to the vacuum channel, the field within the vacuum chamber oscillates with accelerating and decelerating phases. The generation of Cherenkov radiation by the charged particle decelerates the drive bunch and leads to short-range 'self-fields' between Cherenkov wavefronts.

The fields scale with drive bunch charge, leading to typical proposed DWA schemes consisting of a high-charge (typically $\sim$nC) drive bunch accelerating a short lower charge main bunch [51]. DLW structures have been shown to sustain fields orders of

magnitude larger than RF structures. Maximum fields of 13 GV/m were measured at the surface of a fused silica DLW (with maximum on-axis field of 5 GV/m) [52]. The presence of such high fields leads to the observation of non-linear effects. However, it has been observed that a linear response can be maintained up to 850 MV/m [53]. The durability of dielectric materials at high repetition rates (>100 Hz) has not been investigated, with potential issues being charging of dielectric from beam losses within structures or damage from high fields over time.

Proof-of-concept experiments have been conducted with and without a witness bunch for acceleration. The first experimental demonstration of DWA was conducted in 1988 at AATF [54], using cylindrical DLWs with radius 6 mm and 6 mm dielectric thickness. In this study the longitudinal fields excited by a 2 nC, 30 ps long driver were mapped for three dielectrics using a variable delay witness bunch. Relatively low accelerating fields (0.25 MV/m) were measured, however it was noted by the authors that the transverse stability was improved compared to comparable PWFA experiments by a number of the same authors [37].

In 2016, using a shorter (200 to 500 fs total length) driving bunch and smaller structure (150 μm inner radius), a witness electron bunch was accelerated at a gradient of 320 MV/m over 0.1 m at FACET [55]. The fields produced in DLWs exhibit charge symmetry, i.e. equal in magnitude and opposite sign when using electron/positron drive bunches, as demonstrated in [56]. Work has also been focused on increasing the efficiency and stability of acceleration in DWA, towards the goal of a practical DWA. Details of progress towards a usable DWA in given in Section 2.2.

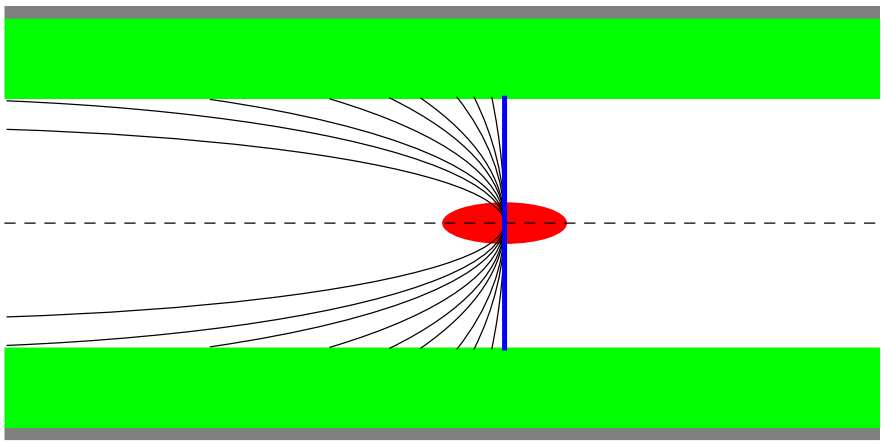

Figure 2.2. Spherical electromagnetic potentials (black) of the Couloumb field from a relativistic point-like particle (red). The individual potential lines interfere constructively perpendicular to the particle, forming a wavefront (blue). The dielectric layer is in green and conducting surface grey.

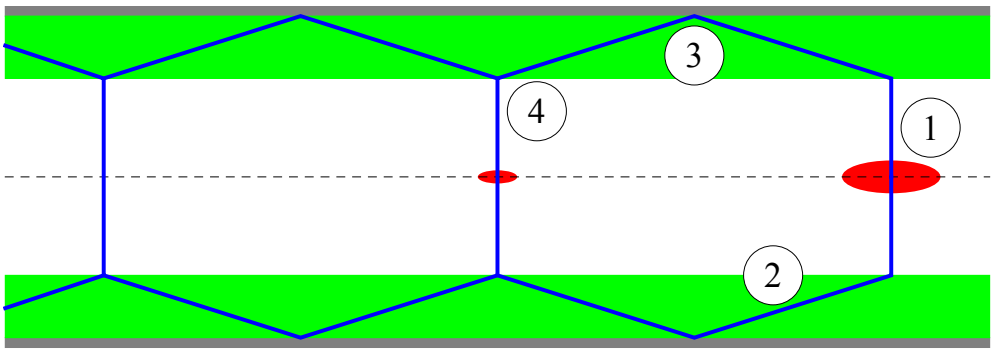

Figure 2.3. Schematic diagram of Cherenkov radiation in a DLW, generated by a charged drive beam (right-hand red disk). 1) The coulomb field generated by the drive beam produces a wavefront as in Figure 2.2. 2) The wavefront is refracted by the dielectric, with angle calculated from the dielectric relative refractive index. 3) This radiation is reflected from the conducting metal back towards the vacuum. 4) Radiation is refracted at the dielectric-vacuum boundary, where a trailing main/witness bunch can be accelerated. Processes 2-4 repeat along the waveguide in an oscillatory manner.

Laser-Driven Dielectric Wakefield Acceleration (DLA)

DLA schemes take advantage of dielectric-lined corrugated structures to excite high accelerating fields. A plane-wave laser pulse propagates perpendicular to the dielectric structure, which slows the phase velocity of the pulse. Within the corrugated dielectric structure, electromagnetic (EM) fields of alternating sign are generated parallel to the beam axis, typically with THz-scale frequencies [57]. Structures typically used for DLA have apertures and spacings between corrugations $\sim 0.1 - 1$ μm; these dimensions need to be of the same order as the laser wavelength.

As with DWA, the dielectrics used for DLA are able to sustain large fields without breakdown effects. Longitudinal fields up to 9 GV/m have been measured with the UCLA Pegasus beamline, with accelerating gradients up to 1.8 GV/m [58]. Non-linear field effects were observed at these gradients, reducing the average accelerating field to 850 MeV/m, equal to the maximum sustainable electron drive field within DLWs reported in [53]. Laser-damage to dielectric materials is a limitation on the materials that can be used for DLA, with materials required to have a high damage threshold [59][60]. Non-relativistic bunches electrons have been accelerated with gradients up to 370 MV/m measured [61]. The small aperture of the structures limits bunch charge transportation, with 3 fC accelerated in [58]. DLA is able to be operated at much larger repetition rates (2.7 MHz in [62]) increasing the integrated bunch charge delivered by DLA. The realisation of a practical DLA accelerator will require electron sources with MHz repetition rates, μm-scale beam sizes, and nm-scale normalised emittance [10]. DLA is equally suitable for electron and positron acceleration.

2.1.3 Alternative Structure-Based Acceleration Techniques

Beam-driven acceleration schemes have been proposed for high-gradient metallic structures. In these schemes, the wavelength of the accelerating field is determined by the parameters of the structure. To effectively interact with the accelerating field, the pulse length of the driving source needs to be sufficiently short. This ensures that the form factor of the bunch contains frequencies equal to the accelerating field.

Metallic Corrugated Structures

Strong wakefields are excited in metallic corrugated waveguides due to the changing cross-section size. The metallic structure is arranged as shown in Figure 2.4. When a short electron bunch propagates within such a corrugated structure, it generates a wakefield with a frequency determined by the structure gap, corrugation spacing, and corrugation depth, typically GHz-THz. The magnitude of EM fields in metallic corrugated structures are limited by the same breakdown effects seen in conventional RF structures. Since the breakdown threshold increases with frequency, higher acceleration gradients can be achieved in metallic corrugated structures [63].

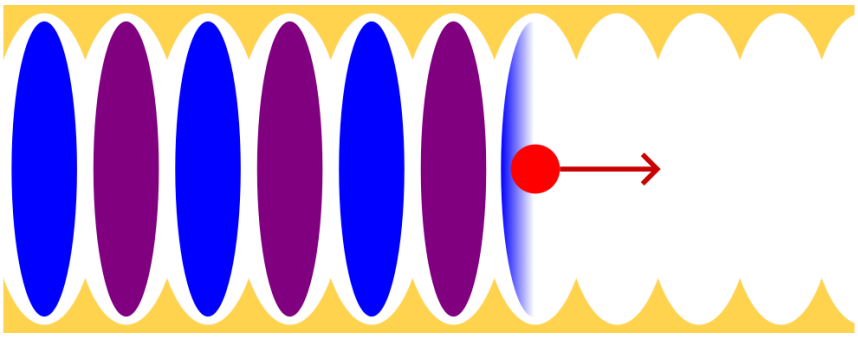

Figure 2.4. Schematic of a metallic corrugated waveguide with EM fields driven by a drive bunch (red). The drive bunch excites an EM field which oscillates in magnitude behind the drive bunch. The transverse cross-section can be planar, with changing structure gap (rectangular corrugations), or cylindrical with changing aperture (circular corrugations).

Typical corrugated structures used in accelerators have apertures $\sim$mm in order to excite frequencies in the THz range. The manufacturing tolerances for these structures are typically $\sim$10 µm [64]. The requirement for high tolerances over a large number of corrugations presents a manufacturing challenge for corrugated structures.

Metallic corrugated structures include closed structures and 'two-half'/open structures. In two-half structures, separate corrugated top and bottom planar plates are placed in the beam path with a gap between them. In closed structures, the entire structure is sealed, forming a closed cavity with a vacuum gap inside. Two-half structures were used in experiments at FACET, measuring peak accelerating fields of 300 MV/m and peak

surface EM fields of 1.5 GV/m with a frequency of 400 GHz [65]. These fields were excited by a single drive bunch, in contrast to experiments with corrugated structures at Argonne Wakefield Accelerator (AWA) facility in [66]. Here, fields of 85 MV/m with a frequency of 91 GHz were excited using a train of three equal charge drive bunches. As with DWA, the wakefield excited is proportional to drive bunch charge and in both of these experiments the drive bunch charge was ≈ 2 nC. Recent experiments at AWA with structures fabricated by Pohang Accelerator Laboratory have shown the ability to manufacture closed cylindrical structures with the required tolerances. When normalised to drive bunch charge, fields of 35.4 MV/m/nC were excited using a train of four drive bunches; with simulations showing the same structure could excite 100 MV/m/nC fields using drive bunches with optimal bunch length [64].

A proposal has been put forward to utilise metallic corrugated waveguides as a collinear wakefield accelerator for a future multi-beam X-ray free electron laser (XFEL) [13]. This concept involves generating a drive bunch using conventional RF technology and then splitting it into multiple beams. Each of these beams is subsequently compressed and used to accelerate multiple main bunches in a collinear arrangement.

Two-Beam Acceleration (TBA)

In the beam-driven schemes discussed previously, the energy from a drive bunch is extracted and delivered to a main/trailing bunch in the same beampipe, i.e. collinear wakefield acceleration. The principle of TBA is to extract power from a drive bunch and utilise it to generate RF fields in an accelerating cavity containing the main bunch. This is shown schematically in Figure 2.5. Wakefields are excited by a series of pulsed drive bunches, as in other structure-based accelerators, within a power extractor and transported to the main accelerating cavity. In this sense, the drive beam power extractor can be compared to a kylstron in a conventional RF system. Metallic disk structures have been demonstrated as power extractors [67]. 400 MW power values have been extracted using such structures, with accelerating gradients of up to 300 MV/m achieved at AWA [68].

Unlike collinear acceleration schemes such as DWA and PWFA, TBA schemes do not require simultaneous transport of two beams with different parameters in the same beam line. Instead, the transport of each beam is optimised separately ensuring that the beam quality of the main bunch and energy extraction from the driving bunch are both optimised. The counterpoint to this is the need to install two separate beam lines next to each other.

TBA using dielectric structures have been proposed [69]. 3 ns long flat-top RF pulses

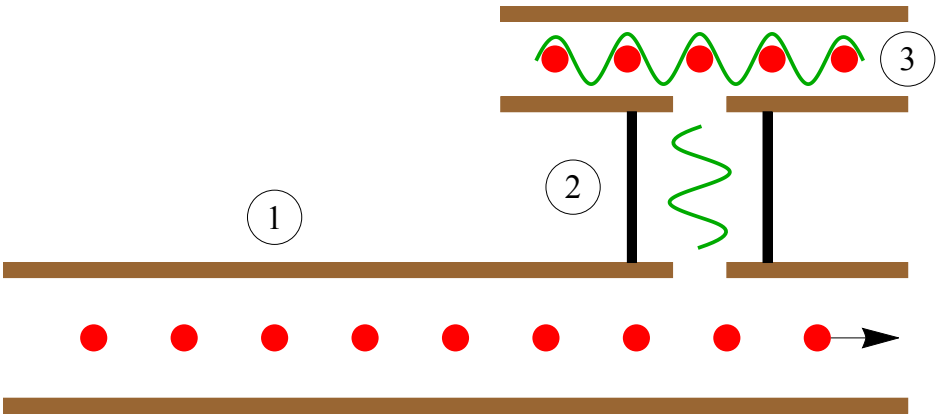

Figure 2.5. Schematic layout of a TBA accelerator system. A series of short drive beams within a power extractor (1.) is used to generate an RF pulse transported in 2 and accelerate a main bunch in 3.

with 200 MW power were extracted from bunch trains without breakdown effects [70]. The power extractor is designed such to extract a single-mode pulse which is used as the accelerating field for the main bunch. Dielectric structures are advantageous when producing shorter wavelengths, and therefore higher accelerating gradients. Dielectric-based TBA has been proposed for the Argonne Flexible Linear Accelerator, with the structure and drive bunch train designed such to sustain ∼300 MV/m accelerating fields with 32 GHz frequency [71].

An example of a TBA scheme using metallic cavities is The Compact Linear Electron Collider, described in Section 1.1. CLIC is planned to operate with accelerating gradients between 72 and 100 MV/m [5]. The technology developed for CLIC makes this the most mature of considered novel accelerating method, however the limit on achievable gradients are still considerably lower than DWA and plasma sources and avoiding breakdown effects is a considerable challenge [72].

2.2 Overview of Dielectric Wakefield Acceleration Research

As with other novel acceleration techniques, the overall goal of DWA research is to achieve efficient, reproducible, and stable acceleration of electron beams at high gradients, with beam quality suitable to user applications.

DWA holds promise as a novel acceleration method which can be completely passive and made using conventional materials. In this sense, DWA can be seen as a middle ground between conventional metallic cavity based accelerators, with accelerating gradients <100 MV/m, and plasma-based accelerators with GV/m gradients possible. If used as an energy booster for an existing facility, DWA requires no external power (unlike plasma or laser-driven acceleration methods). The efficiency of such a dielectric wakefield accelerator booster would be given solely by the efficiency of energy transfer from a

drive bunch to main bunch. The dielectrics used, such as quartz or ceramics, are readily available and significantly cheaper to manufacture than metallic resonator cavities.

The accelerating field excited is directly proportional to the drive beam charge [51]. Large accelerating fields have been measured at facilities capable of delivering beams with large peak currents, requiring bunch charges $\sim$nC. Facilities capable of producing such beams for DWA research include FACET at SLAC (with an overview of results and upcoming experiments in [73]) and the Argonne Wakefield Facility (for example in [74]).

The efficiency of a DWA stage is given by the relative energy gain in the main bunch compared to the energy loss of the drive bunch. The transformer ratio (TR) is the ratio of peak acceleration and deceleration fields, a figure of merit in beam-driven wakefield accelerators. A large TR allows for larger main bunch energy gain with maximal efficiency. For a drive beam with symmetric longitudinal profile, the maximum TR is 2 [51]. A non-symmetric beam profile can be used to increase the transformer ratio beyond this, however this is at the expense of peak accelerating field [75]. This non-symmetric profile can be achieved using a single bunch or a drive bunch train, where the charge of each pulse contributes to the overall desired current profile. Using a drive bunch train with increasing charge, a maximum TR of 3.4 was measured at AWA [76]. Using a single bunch, the total bunch length should be set approximately equal to half the fundamental wavelength of the Cherenkov radiation (i.e. encompassing the space between the vacuum wavefronts in Figure 2.3) with large current at the tail [51][77]. This has been shown experimentally at AWA with a 'triangular' distribution in [74], with a measured transformer ratio of 4.65 ± 1.21. The same principle has been demonstrated in PWFA schemes, with a maximum transformer ratio of $4.6^{+2.2}_{-0.7}$ reported in [78].

Several methods of forming optimally shaped profiles have been investigated. One method, using an emittance exchange beamline, is to collimate the beam in a dispersive section of the beamline. The transverse beam profile in a dispersive section relates to longitudinal position in a non-dispersive section, as in Figure 2.6. This method have been shown in relation to the generation of train of microbunches in [79] and a single longitudinally shaped drive beam in [80]. Using a mask naturally reduces the bunch charge of the drive beam relative to the total charge produced. Generating high charge ($\sim$ nC) drive bunches at high repetition rates will dissipate large amounts of power within the collimator. An alternative method is to use the accelerator optics to generate a desired longitudinal profile. The work presented in [81][82] shows the potential to set a desired longitudinal profile by backtracking the beam optics from the DWA stage to the electron gun. The laser temporal shape used at the electron gun can then be determined using the desired bunch shape. Unlike using a mask, both repetition rate and bunch

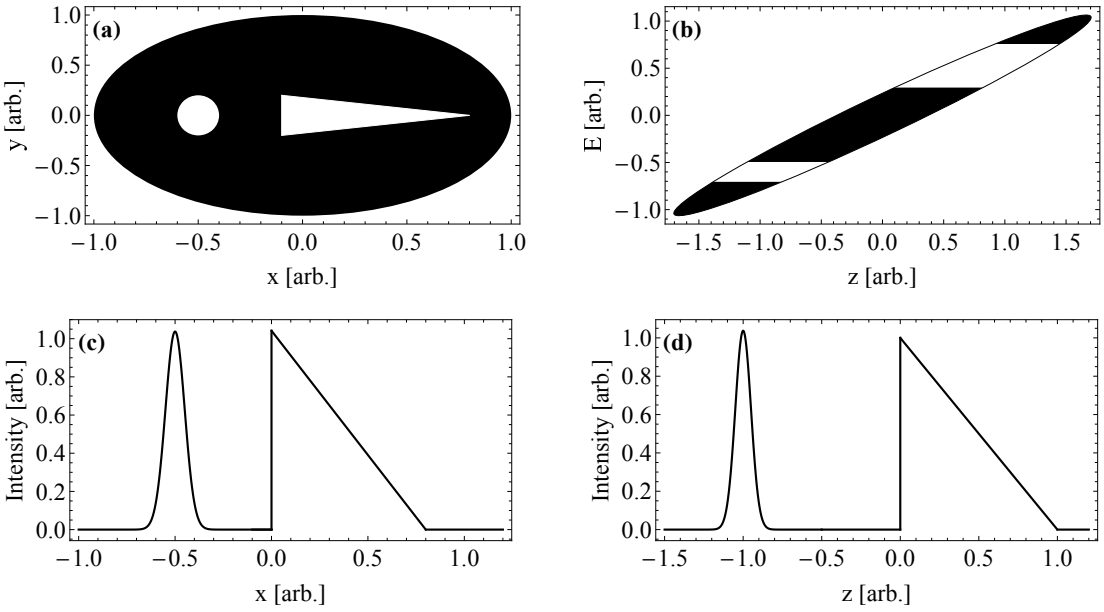

Figure 2.6. Schematic of longitudinal profile generation using a mask/collimator. The mask is positioned in a dispersive section. (a) The transverse cross-section of the mask. (b) Longitudinal phase space of the beam. The beam before collimation is given by the outline and collimated sections filled black. (c) Transverse profile after passing through the mask. (d) Longitudinal profile in a non-dispersive section.

charge can be maximised, with 10 nC at 500 kHz proposed in [81]. Testing of dielectric structures at such high repetition rates has not been completed, however no damage to the dielectric was observed whilst using 3.3 nC bunches at over 28 hours of operation at 10 Hz [55].

Beam stability in DWAs is an area of active research. Beam position jitter, introducing shot-to-shot random offsets within DLWs, or structure misalignment can lead to single-beam breakup instability (BBU) due to strong transverse wakefields. On-axis, transverse wakefields can degrade beam quality over long distances. Surrounding the DWA with permanent quadrupole magnets is proposed to mitigate BBU, so called Balakin, Novokhaski, Smirnov (BNS) damping [83]. Simulations have shown the effectiveness of this scheme in circular DLWs [84]–[87].

The symmetry of transverse wakefields in planar/slab DLWs can be exploited using alternating horizontally and vertically (H+V) orientated DLWs in series [88]. Alternating DLW orientations operate in a similar manner to a standard FODO cell of quadrupole magnets, defocusing and focusing the beam in each transverse plane in alternate DLW orientations. These transverse fields are a feature of the DLW geometry and the symmetry can be exploited in all uses of planar DLWs. Transverse field cancellation with a H+V setup has been investigated in [89] in relation to the THz driven acceleration of a main bunch in a DLW and simulations have shown the preservation of beam quality over long distances using a H+V setup for DWA [90][91]. Experimentally, preliminary results for beam parameters consistent with a DWA drive bunch have been presented in [92].

Simulations are required to effectively investigate and optimise DWA beam dynamics. These simulations are often either computationally expensive, or rely on simplification or large assumptions on the fields in DWAs. Efficient and flexible simulation hardware, that does not require large computing infrastructure, is required to effectively study future DWA schemes. This requirement is recognised by the wider novel acceleration community, and is not limited to DWA, as detailed in [10].

Whilst circular and planar DLWs have been independently researched, comparisons of the two geometries have not been conducted. Beam instabilities are observed in both DLW geometries, but comparisons of the mechanisms and limitations of between the two geometries is required before practical DWAs can be considered.

2.3 Beam Manipulation with Wakefield Devices

Wakefields excited by bunches in dielectric and corrugated structures can be utilised to manipulate bunches, taking advantage of the intrinsic self-synchronisation of fields with the bunch and the dependence of field strength with longitudinal position within the bunch [93]. The fields are generated by the bunches themselves, requiring no external power sources (i.e. passive devices). Two notable schemes are energy dechirpers and passive streakers. Both DLWs and metallic corrugated structures share the same principle of using the wakefields excited by a bunch so are considered together in this section.

2.3.1 Passive Energy Dechirper

An energy chirp, or correlated energy spread, is the relationship between the momentum of a particle and longitudinal position within the bunch. Producing very short bunches ($\sim$1 fs), such as required at FEL facilities, requires large bunch compression. Bunch compression through a magnetic chicane requires a negative chirp (higher energy at the tail). However, whilst this chirp is required for the generation of desired short bunches, energy spread (either uncorrelated or from a chirp) is disadvantageous for FEL performance; energy spread broadens the frequency spectrum of generated radiation and reduces the radiation power. Removing the chirp from the beams longitudinal phase space (LPS) requires a longitudinal EM field inversely matching the chirp (i.e. a lower, or increased negative, field at the tail). The wakefields excited by a bunch in a DLW fit such criteria: the decelerating field produced within the bunch increases from head to tail so long as the bunch length is shorter than the wakefield wavelength.

DLWs have been proposed as dechirpers (minimising the chirp) and as chirp linearisers

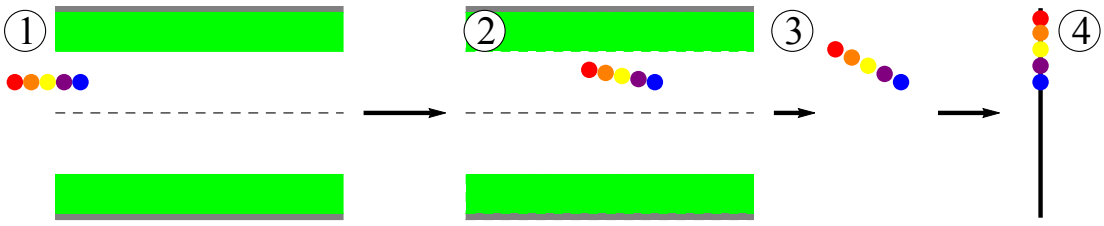

Figure 2.7. Schematic diagram of a dielectric wakefield streaker process for a beam with longitudinal profile represented by different coloured circles. 1) A charged particle beam enters off-centre in the DLW, receiving a dipole-like kick. 2) Within the DLW the beam is kicked with strength as a function of longitudinal position. 3) Between the end of the streaker and downstream screen the angular kick received increases the transverse variation between longitudinal slice. 4) The transverse profile is measured at a downstream screen, from which the longitudinal profile can be reconstructed.

(removing non-linear components from the LPS). The latter was first proposed in 2010 with a DLW [94] and demonstrated experimentally with a corrugated structure in 2014 and 2015 [95][96]. Dechirping was demonstrated with a planar DLW in 2014 [14] and circular corrugated pipe in the same year [97].

Dechirpers using corrugated structures and DLWs have been proposed and installed at existing facilities. Planar structures are preferred due to the ease of varying the structure gap, and therefore wakefield strength. Transverse wakefields in planar structures can be compensated using H+V pairs. Metallic corrugated dechirpers have been proposed and commissioned at FEL facilities: LCLS (installed) [98][99], SwissFEL (planned) [100], and SHINE (installed) [101]. These have demonstrated improvements in FEL performance as a result of dechirping. A dechirper using a pair of planar DLWs is planned at the CLARA facility and described in [102][103][15].

2.3.2 Passive Longitudinal Bunch Diagnostics

The transverse wakefields excited on-centre/on-axis in a DLW or corrugated structure can be described as quadrupole-like, with dipole-like fields excited off-axis. This field provides a longitudinally varying kick to the beam, akin to a conventional RF transverse deflecting cavity (TDC). Downstream from a streaker or TDC the kick applied is translated to a transverse position, as shown schematically in Figure 2.7. The relationship between the transverse and longitudinal position allows for the mapping of a measured streak to a longitudinal profile. It is possible to reconstruct the longitudinal profile by propagating backwards from the measured profile, provided that the field profile is known or can be calculated.

A TDC is traditionally operated such that the centre of the bunch is positioned at or near the zero-cross point of the RF field. Therefore, the head of the bunch is kicked/streaked in the opposite direction as the tail and all regions of the bunch have equal resolution [104]. This is not the case in a passive streaker, with the profile non-linear and strongly

dependent on bunch charge and accurate trajectory into the streaker. The advantages and disadvantages of a passive streaker will be discussed in detail later, in Chapter 8.

Dechirpers and passive streakers can utilise the same structures, making them versatile tools; for example, the LCLS dechirper has been proposed for longitudinal diagnostics [105][106]. The performance of a passive streaker using a circular DLW was been demonstrated in 2016 at SwissFEL [16] and for a circular corrugated pipe in 2018 at PAL-ITF [107]. A corrugated structure streaker has been installed at Swiss-FEL; details of measurements benchmarked against a TDC are given in [108]. These measurements confirm that the resolution of longitudinal profile reconstruction is poor at the head of the bunch where the transverse field produced is minimal. A passive streaker using a pair of orthogonal planar DLWs has been proposed for the CLARA facility [109]. Current research on passive streakers have been focused on individual facilities; a more comprensive study is required to set a range of facilties suitable for such a diagnostic.

Chapter 3

Theory of Wakefields in Dielectric Lined Waveguides

Wakefields produced in particle accelerators can be considered as the Coulomb fields produced by individual charged particles being scattered, slowed or reflected by boundary conditions. Wakefields are generated by a relativistic charged particle bunch travelling through a DLW. Beam-driven wakefield accelerators are two-beam systems: with a drive beam exciting the initial wakefield which is used to accelerate a witness bunch. This chapter focuses on the calculation methods for determining the wakefields in DLWs, excited by the drive beam. Two specific cases are discussed in planar DLWs: the conformal mapping method and the transverse operator method. Additionally, the chapter explores techniques for controlling three-dimensional (3D) fields by shaping the particle distribution within the DLW. This discussion considers the efficiency and stability of drive beams within a collinear accelerating setup.

3.1 General Solution for Fields in Dielectric Lined Waveguides

When charged particle beams propagate through a DLW, they generate two types of fields: self-fields and Cherenkov radiation. Cherenkov radiation is produced when charged particles travel near a dielectric material at a speed greater than the local phase velocity of light within that medium. Self-fields are formed due to the interaction of the charged particle and the dielectric boundary, i.e. caused by the generation of Cherenkov radiation. An additional form of self-fields are space-charge effects due to the relativistic Coulomb fields.

For a relativistic particle, the field in the laboratory frame of reference is 'stretched' in the longitudinal direction. The perpendicular components of the force, $\mathbf{F}_\perp = (F_x, F_y)$, scale such that

$$F_\perp \propto \gamma^{-2}, \tag{3.1}$$

where γ is the Lorentz factor [49]. This factor arises due to the Lorentz transformation of the Coulomb field in the rest frame to the lab frame. Therefore, the space-charge effect decreases with bunch momentum (unlike wakefield effects). Given the work in this thesis will solely relate to relativistic charged electron bunches, we will not consider the effects of space charge and assume them to be negligible when compared to the wakefields generated. The work in this thesis is focused on the effects of wakefields excited in DWAs, so it is relevant to solely include the effect of these fields on beam dynamics. Given space charge forces are independent of wakefields, these fields can be superimposed to create a consistent model of the EM fields in cases where space charge cannot be neglected [110].

The longitudinal and transverse wakefields, E_z and $\mathbf{F}_\perp$, generated by a charged particle are related by the Panofsky-Wenzel (PW) theorem,

$$\frac{\partial \mathbf{F}_\perp}{\partial z} = e\nabla_\perp E_z, \tag{3.2}$$

where e is the electron charge. This relation has been theoretically shown to hold for wakefields excited in DLWs [111]. If the longitudinal field is known,

$$F_x = e\int \frac{\partial E_z}{\partial x}dz, \qquad F_y = e\int \frac{\partial E_z}{\partial y}dz \tag{3.3}$$

hence if the 3D longitudinal field distribution is known the entire 3D field profile can be found. By applying the PW theorem it is clear that transverse fields can be minimised by reducing the transverse variation in longitudinal fields excited. This is investigated for a 3D bunch distribution in Section 3.3.2.

Using the PW theorem, it can be assumed that regions with minimised variation in longitudinal fields have minimised transverse fields. A witness bunch would be positioned so as to receive the maximum accelerating field behind the drive bunch, i.e. at a turning point where the transverse field is minimised. This is true for the fields generated by single point-like particles. The wakefield generated by a 3D particle bunch is given by the sum of these single particle fields so the transverse field at a witness bunch is not necessarily zero. If the fundamental wavelength of the wakefield is much greater than the bunch length it can be assumed that the transverse field is still minimised since all contributions to the wakefields will be close to the turning point. Therefore, when considering the effects of transverse fields, it is of greater importance to consider the effects on the drive bunch.

3.2 Single-Particle 3D Wakefield Calculations

The fields excited by a charged particle in a DLW follow Maxwell's equations, with boundary conditions at the dielectric-vacuum and dielectric-conductor boundaries. Maxwell's equations are given by

$$\nabla \times \mathbf{E} = -\frac{\partial \mathbf{B}}{c\partial t}, \tag{3.4}$$

$$\nabla \times \mathbf{B} = \frac{\partial \mathbf{D}}{c\partial t} - \frac{en\mathbf{V}}{c}, \tag{3.5}$$

$$\nabla \cdot \mathbf{B} = 0, \tag{3.6}$$

and

$$\nabla \cdot \mathbf{D} = -en \tag{3.7}$$

where

$$\mathbf{B} = \mu\mathbf{H}; \qquad \mathbf{D} = \epsilon\mathbf{E}. \tag{3.8}$$

In these equations the electric and magnetic fields are **E** and **H** and fluxes are **D** and **B** respectively, **V** is the average velocity of the particles, and n is the particle density. Considering a bunch of N electrons assumed to be point-like travelling at a constant velocity v at time t

$$n(x, y, z, t) = 4\pi N\delta(z - vt)\delta(y - y_0)\delta(x - x_0), \tag{3.9}$$

where (x_0, y_0) is the transverse position of the bunch. For a DLW inside a vacuum the relative permittivity and permeability are

$$(\epsilon, \mu) = \begin{cases} (1, 1) & -a \leq y \leq a \\ (\epsilon_r, \mu_r) & a < y \leq a + \delta \\ (\epsilon_r, \mu_r) & -(a + \delta) \leq y < -a \end{cases} \tag{3.10}$$

where ϵ_r and μ_r are the relative permitivity and permeability of the dielectric material respectively. The boundary conditions and the requirement that the **E** and **B** fields are continuous, make solutions for the fields non-trivial to solve.

For a planar DLW, with layout as shown in Figure 3.1, there are two sets of boundary conditions, at the conducting plates and at the vacuum-dielectric boundary. At the

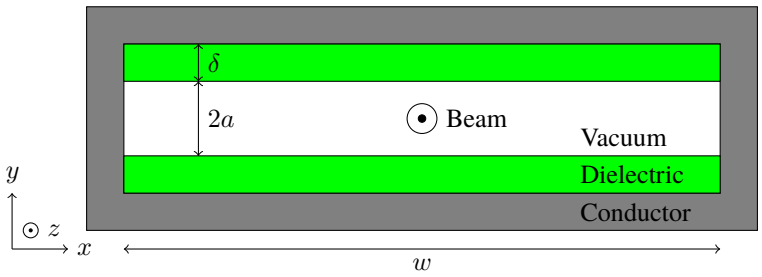

Figure 3.1. Schematic diagram of a transverse section of a planar dielectric lined waveguide with: half-gap a, dielectric thickness δ, and width w.

conducting plates

$$\begin{aligned} &E_y|_{x=0} = 0\,; \qquad E_y|_{x=w} = 0\,; \qquad \frac{\partial E_y}{\partial y}|_{y=\pm(a+\delta)} = 0\,; \\ &\frac{\partial H_y}{\partial x}|_{x=0} = 0\,; \qquad \frac{\partial H_y}{\partial x}|_{x=w} = 0\,; \qquad H_y|_{y=\pm(a+\delta)} = 0\,; \end{aligned} \tag{3.11}$$

and at the dielectric boundaries

$$\begin{aligned} &E_y|_{y=a\mp 0} = \epsilon_r E_y|_{y=a\pm 0}\,; \qquad H_y|_{y=a\mp 0} = \mu_r H_y|_{y=a\pm 0}\,; \\ &\frac{\partial E_y}{\partial y}|_{y=a\mp 0} = \frac{\partial E_y}{\partial y}|_{y=a\pm 0}\,; \qquad \frac{\partial H_y}{\partial y}|_{y=a\mp 0} = \frac{\partial H_y}{\partial y}|_{y=a\pm 0}\,. \end{aligned} \tag{3.12}$$

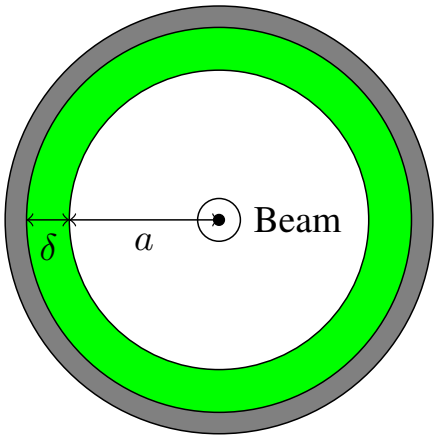

Figure 3.2. Schematic diagram of a transverse section of a circular dielectric lined waveguide with: radius a and dielectric thickness δ.

In the case of a circular DLW, as in Figure 3.2, the boundary conditions are simplified, such that the transverse fields are continuous at the dielectric boundary ($r = a$) and zero at the conducting plate boundary. Increased symmetry is given by the lack of two sets of boundaries. Given the symmetries in place, the simplest solution to the fields are for a circular DLW with the source particle at the centre.

The work in this thesis is focused on the fields in planar DLWs, so a complete derivation of the 3D fields in circular DLWs from Maxwell's equations will not be shown. Details of derivations of the fields generated in circular DLWs are given in [111]–[113]. When

discussing the fields generated, we will refer to the calculation of fields using the standard electric and magnetic components and forces ($E_{x,y,z}$, $H_{x,y,z}$, $F_{x,y,z}$), whilst for the final form we will use the wake potentials ($W_{x,y,z}$). The longitudinal component of the magnetic field is negligible assuming that the transverse velocity is much less than the longitudinal velocity. This holds for relativistic particles, so long as the bunch propagates with no tilt or yaw within the DLW. The wake potential is given by the field generated by a particle of unit charge, i.e. the EM force field produced by a particle with charge q is

$$\begin{pmatrix} F_x \\ F_y \\ E_z \end{pmatrix} \equiv q \begin{pmatrix} W_x \\ W_y \\ W_z \end{pmatrix}. \tag{3.13}$$

There are a number of methods to solve Maxwell's equations with the boundary conditions listed in Equations 3.11 and 3.12. With an impedance method, outlined for planar structures in [88], the field is calculated from the contribution of each mode. The dispersion equation, calculated from the boundary conditions, allows us to calculate the frequency of each mode. The shunt impedance (the magnitude) and quality factor (the power loss due to the conducting walls) of each mode is calculated and the wake potential is the sum of these modes. This method requires the assumption that the Coulomb field of the beam to be effectively constant, i.e. an ultra-relativistic electron beam. An alternative method is to treat Maxwell's equations as an eigenfunction problem. Maxwell's equations are manipulated into a form that allows for an eigenfunction solution, directly giving the form and amplitude of each mode. Finally, the geometry of the system can be exploited to give solutions to the transverse fields using a conformal mapping method. A conformal mapping method maps a particular DLW geometry and source particle position to a geometry with known solution. The inverse map can then be used to give the field profile for the required DLW and particle. Conformal mapping and transverse operator methods will be used in this thesis.

3.2.1 Conformal Mapping

Conformal mapping is a method of transforming the geometry of one system into another geometry space. The solutions in the desired geometry are space- and angle- preserving, i.e. there is no distortion of negligibly small shapes and the intersection of lines are not affected [114]. This does not mean individual lines are not curved or transformed. A conformal mapping method in the context of DLWs uses the field solution for a circular DLW with the source particle on-axis and was first suggested in [115].

Separating Maxwell's equations into longitudinal and transverse parts, the equations

can be reduced such that

$$\frac{\partial H_z}{\partial x} = \frac{\partial E_z}{\partial y}, \qquad \frac{\partial H_z}{\partial y} = -\frac{\partial E_z}{\partial x}. \tag{3.14}$$

This set of equations form Cauchy-Riemann equations for a function defined in the complex plane. Therefore, a conformal mapping method can be used to solve Maxwell's equations. The set of equations have solely transverse dependence so only require a transverse cross-section of the DLW. Given that the equations are in the form of Cauchy-Riemann equations, the function defined by

$$L = \frac{\partial E_z}{\partial \zeta} - i\frac{\partial H_z}{\partial \zeta} \tag{3.15}$$

can be considered a plane vector field with no sources or vertices and therefore the derivative of a complex potential, where ζ is the co-moving coordinate $\zeta = z - vt$. Defining $\chi = x + iy$ the derivative of the potential g_Z is

$$\frac{\partial g_Z}{\partial \chi} = L = \frac{\partial E_z}{\partial \zeta} - i\frac{\partial H_z}{\partial \zeta}. \tag{3.16}$$

Performing a Fourier transform on the equation for g_Z encourages us to consider the geometry of the system as a region with an arbitrarily smooth boundary and complex plane ω with source particle at ω_0. From Riemann's theorem it can always be assumed that a solution exists to map a geometry with a smooth boundary to a geometry defined by a circle with the source particle at the centre [114]. This circular plane will be defined as the χ-plane. In the χ-plane, $\chi = \chi(\omega)$ where $\chi(\omega_0) = 0$ at the source position. Considering the change in variables with respect to the charge and boundary conditions it can be found that

$$E_z - iH_z = -\frac{2Q}{a^2}\left(\frac{\partial \chi}{\partial \omega}\right)^* \frac{\partial \chi}{\partial \omega}\bigg|_{\omega=\omega_0}, \tag{3.17}$$

where * represents the complex conjugate. Using the equation for the longitudinal EM fields we can obtain that the perpendicular field potential is given by

$$W_\perp = \frac{4Q\theta(\zeta)\zeta}{a^2}\left(\frac{\partial^2 \chi}{\partial \omega^2}\right)^* \frac{\partial \chi}{\partial \omega}\bigg|_{\omega=\omega_0}, \tag{3.18}$$

where $\theta(\zeta)$ is the Heaviside step-function. It is important to note that these equations include the assumption that there is no longitudinal dependence for the longitudinal fields and transverse fields increase linearly with ζ. The perpendicular force on a test particle of charge q is given by $F_\perp = qW_\perp$. For ease of notation, $f(\omega, \omega_0) = \chi(\omega)$ will be used to refer to the function mapping the given geometry to a circle with the source

at the centre.

This method can be generalised to any geometry, once the solution is found to map the system to a circular DLW with particle on-axis. In the original geometry, the source particle is given by ω_0 and point within the structure given by ω. The total mapping is given by

$$f(\chi, \chi_0) = a^2 \frac{\chi - \chi_0}{a^2 - \chi\chi_0^*}, \tag{3.19}$$

where χ_0 is the mapping of the source to the centre of the circle and χ is the mapping of the point ω. The complete mapping from the original geometry is given by $f(\omega, \omega_0)$. A complete derivation of fields with the conformal mapping method is given in [116]. Note that the mapping function $f(\omega, \omega_0)$ depends on the specific geometry of the system and the position of the source particle, and therefore needs to be calculated for each individual case. However, once the mapping function is obtained, the resulting equations can be used to calculate the electromagnetic fields and forces on test particles in the system without the need for time-consuming numerical simulations.

The assumption that transverse fields increase linearly with longitudinal distance will only hold for small distances relative to the wakefield wavelength, which we will refer to as the self-fields. The same case is true for longitudinal fields, the assumption that longitudinal fields produced are constant will only hold over small distances. This limits the conformal mapping method to showing upper limits of fields generated for short bunches, and giving the transverse shape of fields.

3.2.2 Conformal Mapping for Planar and Circular DLWs

The conformal mapping method can be used to calculate the fields for circular and planar DLWs. For a circular structure, $\omega(r, \phi) = re^{i\phi}$ with source particle at the point $\omega_0 = r_0 e^{i\phi_0}$. From Equation 3.17, the longitudinal field is given by

$$W_z = -\frac{2Q}{a^2} \frac{a^8 - 2a^6 r r_0 \cos(\phi - \phi_0) + r^2 r_0^2 \cos[2\phi(\phi - \phi_0)]}{[a^4 + r^2 r_0^2 - 2a^2 r r_0 \cos(\phi - \phi_0)]^2}. \tag{3.20}$$

The transverse field can be similarly calculated using Equation 3.18 and

$$W_r = |W_\perp|, \qquad W_\phi = \arg(W_\perp), \tag{3.21}$$

where $||$ and arg are the magnitude and argument of $W_\perp$. The exact forms of the equations can be calculated using a mathematical equation solver such as Mathematica [117].

For a planar DLW, the original structure geometry in the complex plane is defined by $\omega(x, y) = x + iy$ with source particle at $\omega_0 = x_0 + iy_0$. Mapping to a circular structure

is performed with

$$\chi(\omega) = a\tan(\frac{\pi}{4}\frac{\omega^*}{a}) \tag{3.22}$$

and Equation 3.19 used to then map this geometry such that the source is at the centre of the circle, i.e.

$$f(\omega,\omega_0) = a\frac{\tan(\frac{\pi}{4}\frac{\omega}{a}) - \tan(\frac{\pi}{4}\frac{\omega_0}{a})}{1-\tan(\frac{\pi}{4}\frac{\omega}{a})\tan(\frac{\pi}{4}\frac{\omega_0^*}{a})}. \tag{3.23}$$

Given this mapping, using Equation 3.17

$$W_z = -\frac{2Q\pi^2}{8a^2}\frac{1+\cos\left(\frac{\pi x}{2a}\right)\cosh\left(\frac{\pi y}{2a}\right)}{[\cos\left(\frac{\pi x}{2a}\right)+\cosh\left(\frac{\pi y}{2a}\right)]^2}; \tag{3.24}$$

the analytical function for $W_\perp$ can be calculated from Equation 3.18 and

$$W_x = \Re\left[W_\perp\right], \qquad W_y = \Im\left[W_\perp\right], \tag{3.25}$$

where $\Re$ and $\Im$ are the real and imaginary components. Similarly to the circular case, the full form of the transverse components of the wake potential will not be given here.

With these equations the transverse variation in 3D fields has been explored. The magnitude of fields depends on longitudinal position and bunch charge, so when considering the distribution of fields it is more appropriate to consider the relative strength of wake potentials. Therefore, all potentials will be expressed in arbitrary units.

The vector transverse field maps, for circular and planar DLWs, with the source particle on-axis and offset $a/2$ towards the dielectric are shown in Figures 3.3 and 3.4.

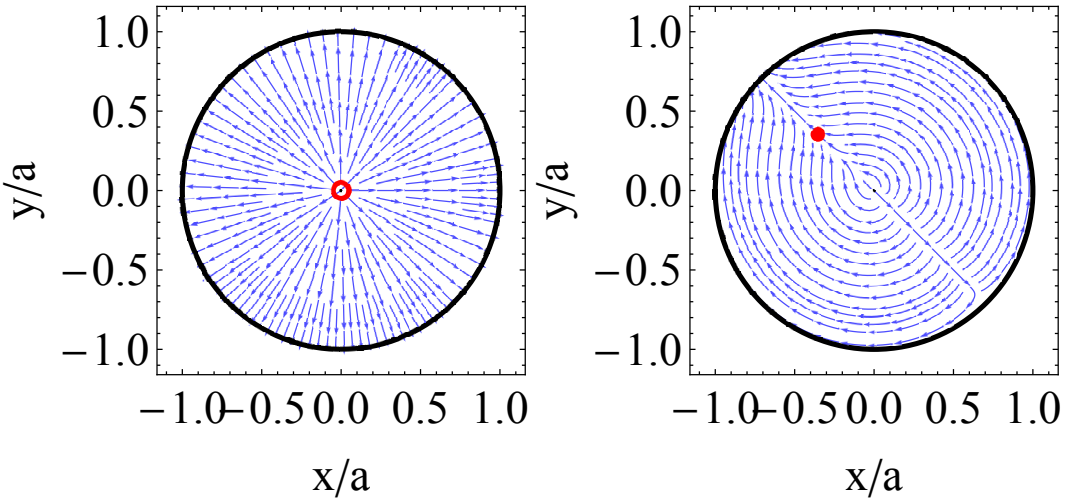

(a) Ring of source particles centred at $r_0 = 0$ (b) Point-like source at $r_0 = 0.5\ a$, $\phi_0 = -\pi/4$

Figure 3.3. Transverse vector field lines in a circular DLW with vacuum radius a for a source (red) on-axis and offset from centre.

In a circular DLW, when the source particle is located on-axis, no transverse fields are excited due to the inherent symmetry in all directions. To account for this, the

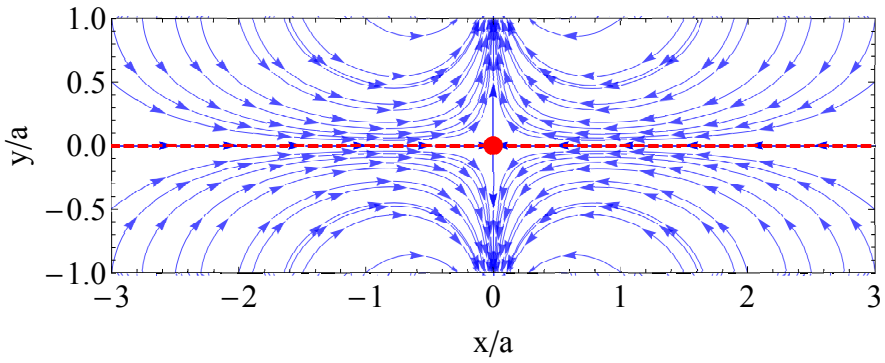

(a) $y_0 = 0$

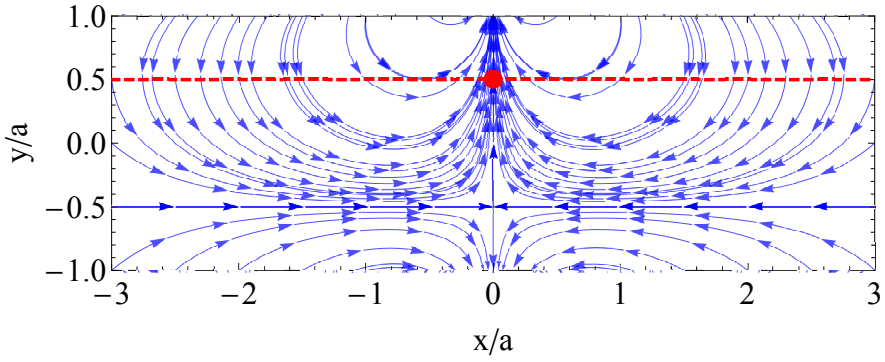

(b) $y_0 = 0.5\ a$

Figure 3.4. Transverse vector field lines for a single point-like particle in a planar DLW on-axis and offset from centre.

on-axis fields are modeled by considering a ring of source particles centered on-axis. By distributing the source particles in a ring shape, the model captures the circular symmetry and allows for an accurate representation of the on-axis fields. This is appropriate given the fields in a realistic DWA are given by the convolution of a 3D beam distribution and the point-like fields generated by each part of the bunch. A beam centred on-axis with azimuthal symmetry could be considered the sum of infinitely thin rings. For an off-axis particle, the field excited is overall towards the dielectric surface akin-to a dipole kick. The force field lines in Figure 3.3(b) show that the azimuthal field is focusing, with the field centred on the angular position of the source particle.

The field excited off-axis in a circular DLW and a planar DLW can be viewed similarly. One approach to modelling transverse fields is to perform a Taylor expansion; with this model dipole-like terms are constant, quadrupole-like linearly varying with transverse position and so on. For a planar DLW with source particle off-axis (in Figure 3.4b) the transverse field contains dipole-like terms towards the dielectric plate and focusing quadrupole-like terms in the orthogonal direction. Unlike with the circular DLW this field shape is seen for the source particle on-axis however in this case both sets of fields can be viewed as a quadrupole-like: defocusing towards the dielectric plate and focusing parallel to the plate.

Multipole Expansion of Planar DLW Fields

The field map in a planar DLW on-axis (Figure 3.4a) can be viewed as similar to the fields produced by a quadrupole magnet. With a source source particle off-axis, as in Figure 3.4b, the field lines are instead similar to a quadrupole magnet with a dipole component. A multipole expansion of the transverse fields allows for relevant comparisons to be made for beam dynamics purposes. For example, if a field is similar to a quadrupole magnet, it can be expected that the normalised emittance is preserved [118].

A multipole expansion is relevant along a particular axis, i.e. $W_y(y)$ and $W_x(x)$, with x and y being the distance between witness and source particles. Considering the vertical wake potential, $W_y(y)$, a Taylor expansion can be performed such that

$$W_y(y) = a + by + cy^2 + dy^3, \tag{3.26}$$

where a, b, c, d are the coefficients of the expansion, relating to dipole-like, quadrupole-like, sextupole-like, and octupole-like fields respectively.

The multipole expansion of the vertical wake potential is shown for a source particle on-axis in Figure 3.5 and with offset $y_0 = 0.2a$ in Figure 3.6. With the source particle on-axis, no dipole-like or sextupole-like fields are excited and the field is well approximated by the quadrupole-like component for small distances from the axis. Further from the DLW centre, the contribution of octupole-like fields increases. At this point, a quadrupole-like assumption no longer holds. With the source particle off-axis the transverse field is more complex, with the contribution of multiple field components non-negligible. A constant, dipole-like component is excited, providing a constant kick. A sextupole-like and octupole-like component to the field is evident. The quadrupole-like term is still evident and non-negligible and the contribution of higher-order terms (sextupole-like, octupole-like etc.) are greater than on-axis. For source particles away from the DLW centre the contribution of higher-order field components increases compared to the on-axis case.

It is often relevant to refer to the components of transverse fields by the equivalent magnet. Dipole-like fields will refer to a constant field, kicking a beam in a particular direction. Quadrupole-like fields focus/defocusing the transverse beam profile whilst maintaining emittance. Given that these fields are often sufficient to describe the transverse fields in most cases, other field contributions (sextupole-like, octupole-like etc.) will be referred to as higher-order terms when discussing the multipole expansion of transverse fields. It is worth noting that given that transverse fields are longitudinally varying, comparisons with equivalent magnets are only relevant at a given longitudinal position. For example,

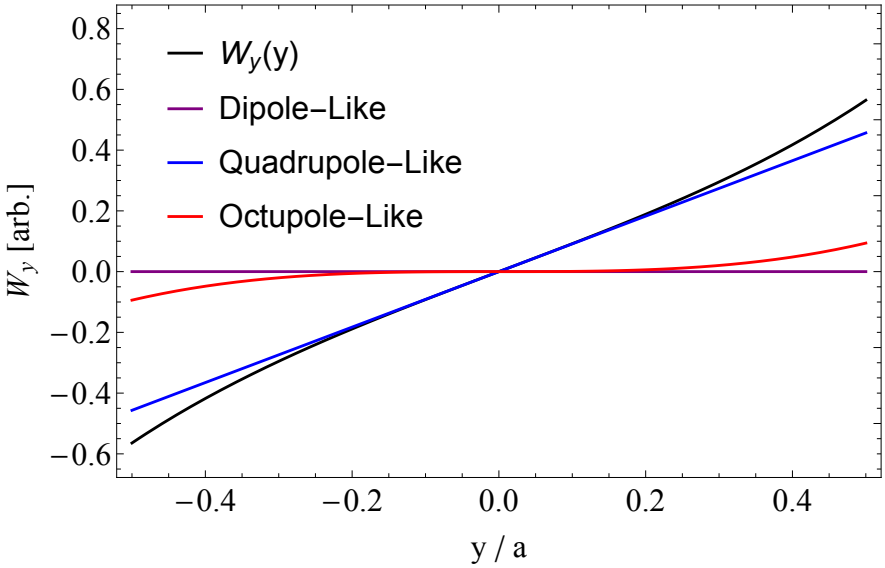

Figure 3.5. Vertical wake potential (black line) and multipole expansion (labelled coloured lines) as a function of witness position with source on-axis in a planar DLW.

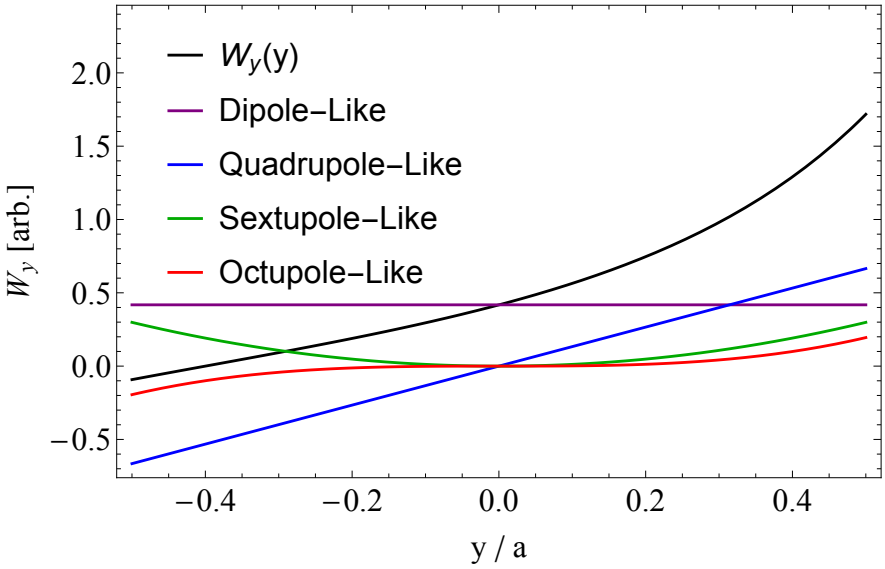

Figure 3.6. Vertical wake potential (black line) and multipole expansion (labelled coloured lines) as a function of witness position away from a source particle at $y_0 = 0.2a$ in a planar DLW.

whilst a quadrupole magnet maintains normalised beam emittance, a longitudinally varying quadrupole-like wakefield would maintain slice emittance but not necessarily projected emittance.

3.2.3 Single-Particle Field Distribution

Circular DLWs

The fields excited within a circular DLW are radially and azimuthally symmetric with respect to the source position. That is, the field produced with a source particle at $r = b, \phi = 0$ is equal to that at $r = b, \phi = \pi$, since the azimuthal source position simply

rotates the excited field. As shown in Figure 3.3, when a source particle is offset from the center, the transverse field excited has a stronger relative radial component than azimuthal (rotational) component. For the majority of the DLW ($0.05 < r_0/a < 0.8$), W_r increases exponentially with offset (Figure 3.7). The rate of exponential increase grows very close to the dielectric plate ($r_0 > 0.8\ a$). A beam with even a very small initial offset from the DLW center would be expected to be kicked towards the dielectric plate with an exponentially increasing field.

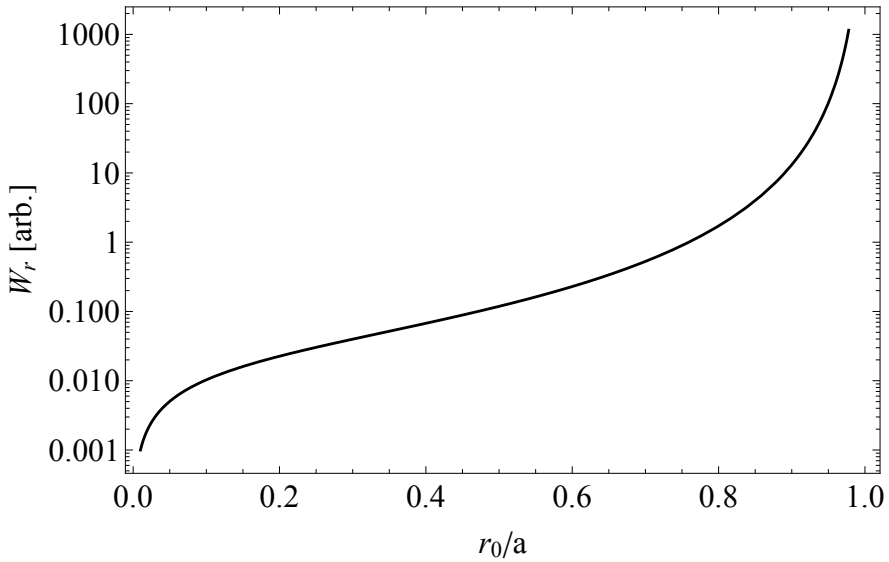

Figure 3.7. Radial wake potential as a function of source particle radius, r_0. The witness position is the same transverse position as the source particle.

For a source and witness particle offset from the DLW centre, the azimuthal force focuses a witness particle towards the source azimuthal position. As shown in Figure 3.8, the focusing field is directly proportional to the source-witness angular difference for small angles ($-\pi/4 < \Delta\phi < \pi/4$). The focusing azimuthal field increases with radius, similarly to the radial field, however the rate of increase is considerably shallower. The azimuthal field increases with radius, as shown in Figure 3.9.

For small offsets where the azimuthal field is greater than the radial field the beam would experience varying focusing (eventually towards a teardrop shape); for larger offsets the transverse force can be considered solely radial.

Planar DLWs

As shown in Figure 3.4(a), the transverse fields excited in a planar DLW exhibit a focusing effect parallel to the dielectric plate (due to W_x) and defocusing towards the dielectric plate (due to W_y). With the source particle away from the DLW axis (Figure 3.4(b)), the vertical force is instead dipole-like towards the dielectric with focusing effects still present parallel to the dielectric plates.

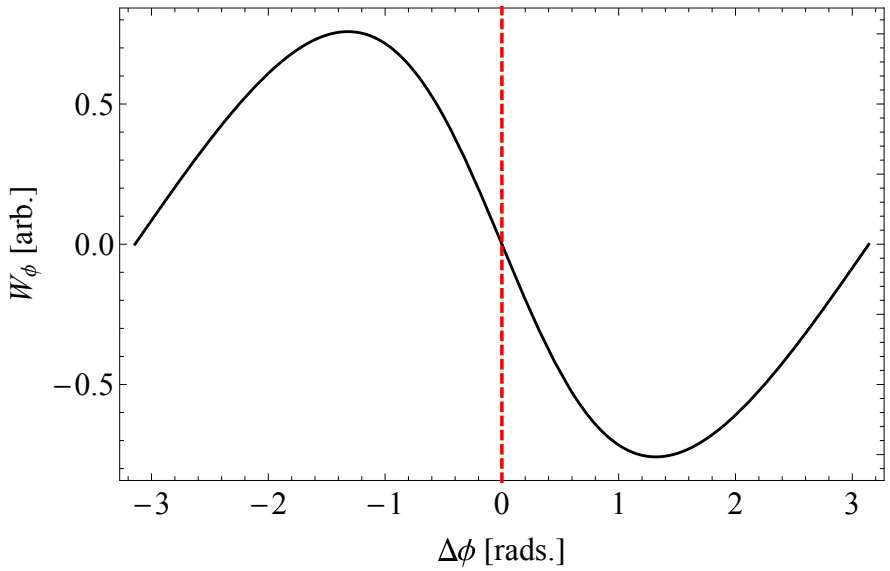

Figure 3.8. Azimuthal wake potential for varying angular difference between source and witness position, both at the same radius ($r_0 = 0.5a$).

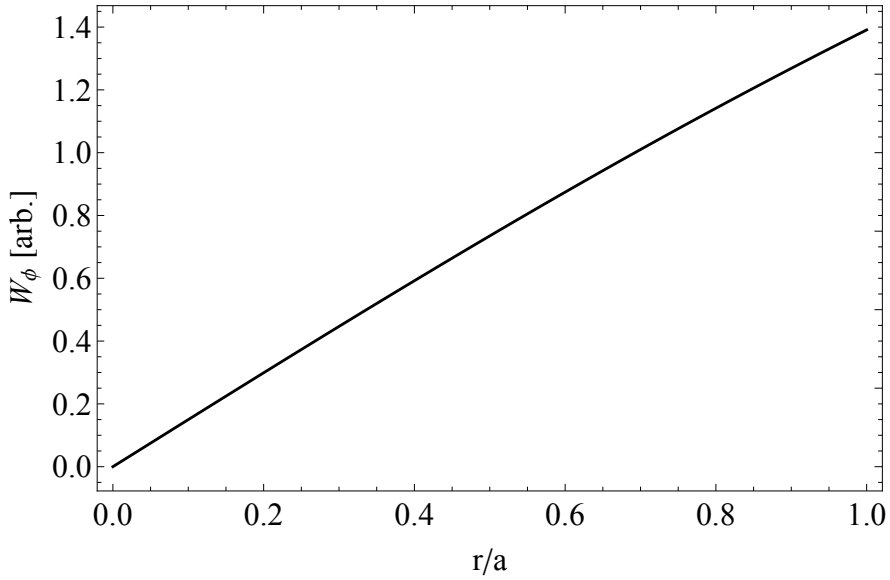

Figure 3.9. Azimuthal wake potential for varying witness radius. The phase difference between source and witness particle is $\pi/4$ and $r_0 = 0.5a$

The transverse wake potential components (W_x and W_y) exhibit symmetry for small distances from the DLW axis. In this region, both W_x and W_y increase approximately linearly with the distance from the axis, as depicted in Figure 3.10(a). This quadrupole-like behaviour opens the possibility of using multiple DLWs with alternating orientations to exploit this symmetry and cancel transverse fields, as in [84][88][90][91]. With increasing distance from the axis, the symmetry breaks down and W_y increases more rapidly than W_x (Figure 3.10(b)). The breaking of this symmetry imposes a limit on transverse beam size when using alternating DLW orientations.

For larger beams, non-linear effects are seen in the respective orthogonal transverse plane ($W_y(x)$ and $W_x(y)$). As shown in Figure 3.11, the vertical wake potential decreases

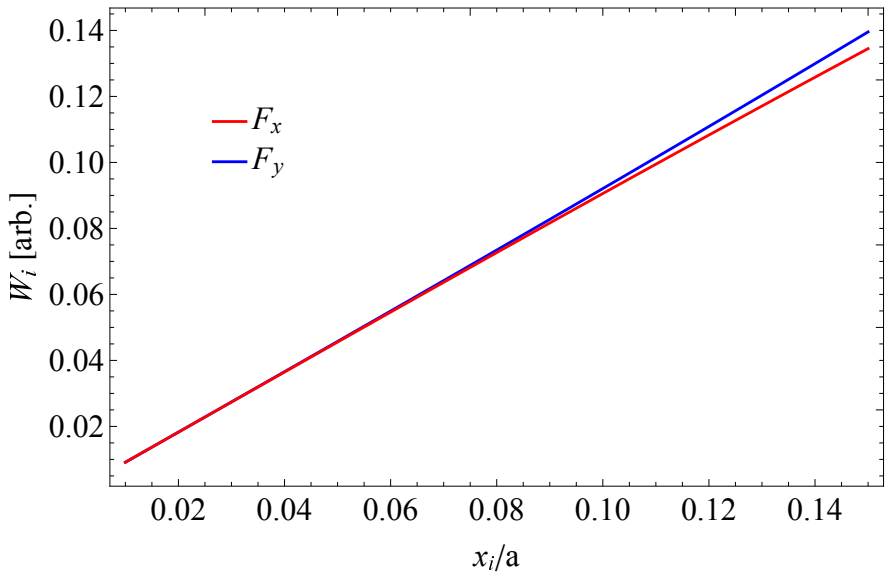

(a) Witness positions close to the DLW axis.

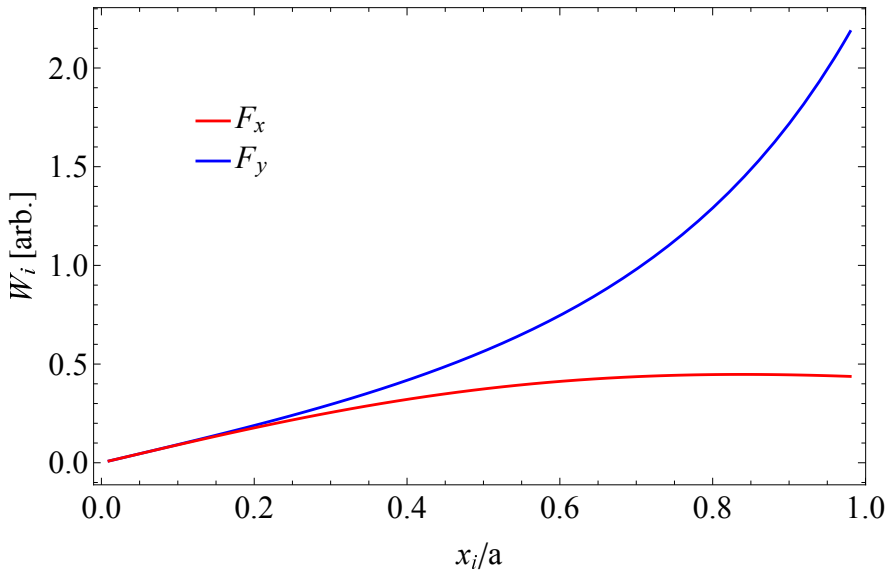

(b) Witness positions upto the dielectric boundary.

Figure 3.10. Vertical and horizontal wake potential, for a source particle at the centre of a planar DLW. The witness positions, (x, y), for the horizontal potential and vertical potential are $(x_i, 0)$ and $(0, x_i)$ respectively.

with increasing horizontal witness position. When $x \approx a$, the vertical potential is no longer defocusing but instead focusing towards the DLW axis. The beam optics implications of this would need considering if using a beam with large aspect ratio (i.e. larger horizontal beam size than vertical beam size). A non-linear relationship between wakefield strength and transverse position reduces the comparisons that can be made with quadrupole fields, leading to beam asymmetry growth in transverse planes and emittance dilution.

With the source particle off-axis, the vertical potential increases with both offset and witness vertical position. The vertical potential increases exponentially with offset,

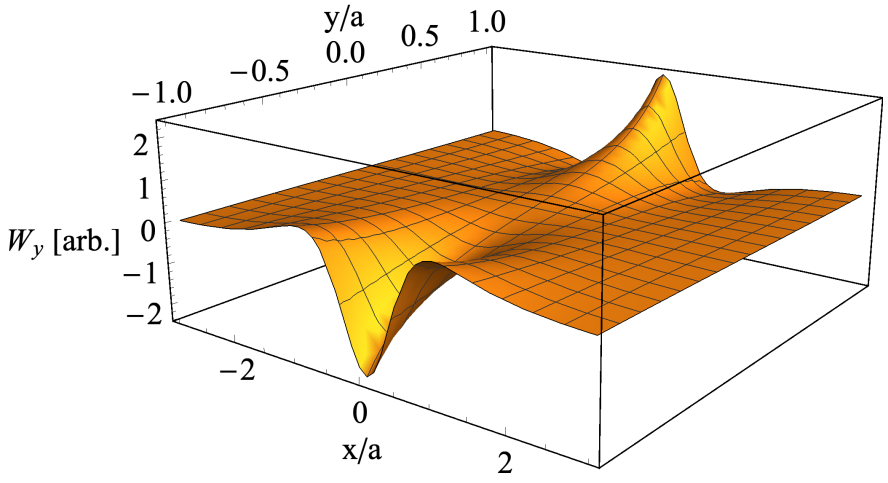

Figure 3.11. Vertical wake potential as a function of witness transverse position, with the source particle on-axis.

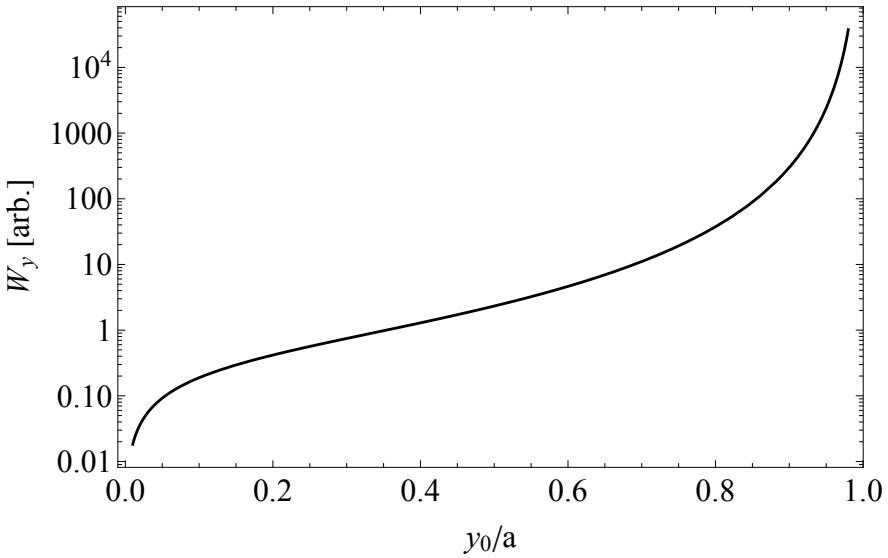

Figure 3.12. Vertical wake potential as a function of source and witness position, y_0.

shown in Figure 3.12, in the range $0.1 < y_0/a < 0.8$. For $y_0/a > 0.8$, the rate of increase in vertical potential increases beyond an exponential relationship. This is the same relationship seen with W_r for circular DLWs. The exponential relationship means that no initial offset is negligible and an off-axis particle will always be kicked towards the dielectric plate. Therefore, instability leading to single-beam breakup will always be a factor with both planar and circular DLWs. Given the exponential relationship, the kick received is very small initially however it can be assumed once a threshold offset is reached beam losses would increase rapidly with further propagation distance.

The longitudinal wake potential has a dependence on transverse position, shown in Figure 3.13. The variation is cos-like horizontally and cosh-like vertically as expected from Equation 3.24. The magnitude of W_z increases towards the dielectric plate vertically, and decreases with horizontal position. For larger beams in a DLW, both drive and witness, this would introduce energy spread across the beam transverse profile. For

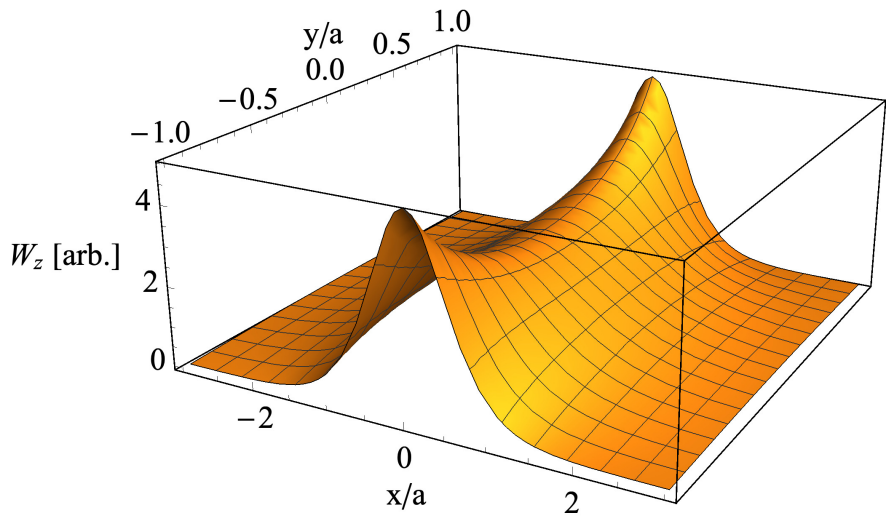

Figure 3.13. Longitudinal wake potential as a function of witness transverse position, with the source particle on-axis.

example, W_z varies by 2% within a 50 µm circle with $a = 500$ µm. From Equation 3.24 we know the transverse variation in W_z reduces with increasing a. Therefore, this energy spread becomes negligible for smaller beams and larger dielectric gaps.

3.2.4 Transverse Operator Method for Field Calculations

When the longitudinal variation in fields is required, for example to simulate drive-witness acceleration, the full 3D fields need to be solved. In this case the conformal mapping method is not appropriate given the assumption of a constant E_z and linearly increasing transverse wake potential. Maxwell's equations can be manipulated to an eigenfunction equation. The method detailed in [119] uses a transverse operator for Maxwell's equations to find solutions for the eigenmodes of the DLW system. This method does not require any assumptions on the self-field generated by the beam, so can be used independent of bunch energy at both high-energy and low-energy regimes.

Returning to Maxwell's Equations, using Equation 3.7

$$\nabla \cdot \mathbf{E} = -\left(\frac{E_y}{\epsilon}\frac{\partial \epsilon}{\partial y} + \frac{en}{\epsilon}\right), \tag{3.27}$$

and applying the curl operator to Equation 3.4 it is found that

$$\begin{aligned}\frac{\partial^2 E_z}{\partial z^2} &= \nabla_{xy}\mathbf{E} + \nabla\left[\frac{E_y}{\epsilon}\frac{\partial \epsilon}{\partial y}\right] - \epsilon\mu\frac{\partial^2 \mathbf{E}}{c^2 \partial t^2} \\ &= -e\left[\nabla\left(\frac{n}{e}\right) + \mu\beta\frac{\partial n}{c\partial t}\frac{\mathbf{V}}{|\mathbf{V}|}\right] + \frac{\partial \Lambda}{c\partial t},\end{aligned} \tag{3.28}$$

where it is defined that

$$\Lambda = \begin{pmatrix} H_z \frac{\partial \mu}{\partial y} \\ 0 \\ -H_x \frac{\partial \mu}{\partial y} \end{pmatrix} \tag{3.29}$$

and

$$\nabla_{xy} \equiv \frac{\partial^2}{\partial x^2} + \frac{\partial^2}{\partial y^2}. \tag{3.30}$$

Using the co-moving variable $\zeta = z - vt$, the equation for the the E_y component becomes

$$\frac{\partial^2 E_y}{\partial \zeta^2}(1 - \epsilon\mu\beta^2) + \frac{\partial^2 E_y}{\partial x^2} + \frac{\partial^2 E_y}{\partial y^2} + \frac{\partial}{\partial y}\left(\frac{E_y}{\epsilon}\frac{\partial \epsilon}{\partial y}\right) = \frac{-e}{\epsilon_0}\frac{\partial}{\partial y}\left(\frac{n}{\epsilon}\right). \tag{3.31}$$

At this point it is useful to define an operator, $\hat{T_E}$ such that

$$\hat{T}_E E_y = \frac{1}{(1 - \epsilon\mu\beta^2)}\left[\frac{\partial^2 E_y}{\partial x^2} + \frac{\partial}{\partial y}\left(\frac{1}{\epsilon}\frac{\partial}{\partial y}[\epsilon E_y]\right)\right], \tag{3.32}$$

from which Equation 3.31 can be rewritten as

$$\frac{\partial^2 E_y}{\partial \zeta^2} + \hat{T}_E E_y = \frac{-e}{\epsilon_0(1 - \epsilon\mu\beta^2)}\frac{\partial}{\partial y}\left(\frac{n}{\epsilon}\right). \tag{3.33}$$

In a similar manner, the magnetic components of Maxwell's equations can be manipulated, with the operator $\hat{T_H}$ defined such that

$$\hat{T}_H H_y = \frac{1}{(1 - \epsilon\mu\beta^2)}\left[\frac{\partial^2 H_y}{\partial x^2} + \frac{\partial}{\partial y}\left(\frac{1}{\mu}\frac{\partial}{\partial y}[\mu H_y]\right)\right] \tag{3.34}$$

leading to the equation for H_y,

$$\frac{\partial^2 H_y}{\partial \zeta^2} + \hat{T}_H H_y = \frac{-ev}{1 - \epsilon\mu\beta^2}\frac{\partial n}{\partial x}. \tag{3.35}$$

The two independent transverse operator equations, 3.33 and 3.35, provide equations for longitudinal section magnetic (LSM) and longitudinal section electric (LSE) propagating waves respectively. The eigenvalue equations for each are

$$\begin{aligned} &\hat{T_E}\Psi_E(x,y) = \lambda_E \Psi_E(x,y); \qquad \Psi_E(0,y) = 0; \\ &\Psi_E(w,y) = 0; \qquad \frac{\partial \Psi_E(x,y)}{\partial y}|_{y=\pm(a+\delta)} = 0; \end{aligned} \tag{3.36}$$

$$\hat{T_H}\Psi_H(x,y) = \lambda_H\Psi_H(x,y); \qquad \frac{\partial\Psi_H(x,y)}{\partial x}|_{x=0} = 0;$$
$$\frac{\partial\Psi_H(x,y)}{\partial x}|_{x=w} = 0; \qquad \Psi_H(x,\pm(a+\delta)) = 0; \tag{3.37}$$

where Ψ_H and Ψ_E are the eigenfunctions of each function with respective eigenvalues λ_H and λ_E. Since each eigenfunction relates to LSE and LSM modes, solving for the eigenfunctions provides a full mode decomposition of the fields.

The eigenfunctions for each set of propagating waves can be decomposed into a series expansion,

$$\Psi_E(x) = \sum_m X_E^m(x)Y_E^m(y) \tag{3.38}$$

$$\Psi_H(y) = \sum_m X_H^m(x)Y_H^m(y), \tag{3.39}$$

where m is the mode number. The solutions to the x component forms the set

$$\{X_E(x)\}_m = \{\sin(k_x^m x)\}_m, \{X_H(x)\}_m = \{\cos(k_x^m x)\}_m, \tag{3.40}$$

where $k_x^m = \pi m/w$ is the horizontal wave number. This orthonormal set is as would be expected given the single boundary in the x-direction. In the y-direction, the problem is more complicated, and there exists both symmetric and anti-symmetric solutions ($Y_{E,as}$,$Y_{E,s}$,$Y_{H,as}$, and $Y_{H,s}$). In the vacuum and dielectric regions the wavenumbers are defined as

$$k_{vac}^E = \sqrt{(1-\beta^2)\lambda_E + k_x^2}; \qquad k_{di}^E = \sqrt{(\epsilon_r\mu_r\beta^2 - 1)\lambda_E - k_x^2};$$
$$k_{vac}^H = \sqrt{(1-\beta^2)\lambda_H + k_x^2}; \qquad k_{di}^H = \sqrt{(\epsilon_r\mu_r\beta^2 - 1)\lambda_H - k_x^2}. \tag{3.41}$$

The dispersion relation for the asymmetric and symmetric solutions are

$$\epsilon_r k_{vac}^E \tanh(k_{vac}^E a) - k_{di}^E \tan(k_{di}^E\delta) = 0; \qquad \epsilon_r k_{vac}^E \coth(k_{vac}^E a) - k_{di}^E \tan(k_{di}^E\delta) = 0;$$
$$\mu_r k_{vac}^H \tanh(k_{vac}^H a) + k_{di}^H \cot(k_{di}^H\delta) = 0; \qquad k_{di}^H \tanh(k_{vac}^H a) + \mu_r k_{vac}^H \tan(k_{di}^H\delta) = 0. \tag{3.42}$$

The solutions, a product of trigonometric and hyperbolic functions and relating individually to the dielectric and vacuum regions, can be inserted into Equations 3.33 and 3.35 to calculate E_y and H_y for each mode. The solution is obtained by performing a Fourier transform and expanding the transverse electric and magnetic fields, the full derivation of which is provided in [119].

To ease the calculation of the fields for a point charge at (x_0, y_0), and simplify the

notation of fields, it helps to define the operator

$$I[f](y) \equiv \int f(y)dy, \tag{3.43}$$

and the vertical wavenumber

$$k_y(y) = \sqrt{[1-\epsilon\mu\beta^2]\lambda_E - (k_x^m)^2}. \tag{3.44}$$

The longitudinal wake potential excited by a point-like particle of unit charge is then given by

$$\begin{aligned} W_z(x,y,\zeta) = 4\pi \sum_m X_E^m(x_0) X_E^m(x) \Bigg[& \sum_{\lambda_E} \frac{k_y I[E_y^m][k_y(y)y]}{\lambda_E + (k_x^m)^2} \cos(\sqrt{\lambda_E}|\zeta|) \\ & -\mu\beta^2 \sum_{\lambda_H} \frac{(k_x^m)^2 H_y^m}{\lambda_H + (k_x^m)^2} \cos(\sqrt{\lambda_H}|\zeta|) \Bigg]. \end{aligned} \tag{3.45}$$

Substituting the above equation for W_z into the PW theorem - Equation 3.3 - the transverse fields can be calculated. The transverse wake potentials are found to be

$$\begin{aligned} W_x(x,y,\zeta) = 4\pi \sum_m X_E^m(x_0) \frac{\partial X_E^m(x)}{\partial x} \Bigg[& \sum_{\lambda_E} \frac{k_y I[E_y^m][k_y(y)y]}{\lambda_E + (k_x^m)^2} \frac{\sin(\sqrt{\lambda_E}|\zeta|)}{\sqrt{\lambda_E}} \\ & -\mu\beta^2 \sum_{\lambda_H} \frac{(k_x^m)^2 H_y^m}{\lambda_H + (k_x^m)^2} \frac{\sin(\sqrt{\lambda_H}|\zeta|)}{\sqrt{\lambda_H}} \Bigg] \end{aligned} \tag{3.46}$$

and

$$\begin{aligned} W_y(x,y,\zeta) = 4\pi \sum_m X_E^m(x_0) X_E^m(x) \Bigg[& \sum_{\lambda_E} \frac{(k_y)^2 E_y^m}{\lambda_E + (k_x^m)^2} \frac{\sin(\sqrt{\lambda_E}|\zeta|)}{\sqrt{\lambda_E}} \\ & -\mu\beta^2 \sum_{\lambda_H} \frac{(k_x^m)^2}{\lambda_H + (k_x^m)^2} \frac{\partial H_y^m}{\partial y} \frac{\sin(\sqrt{\lambda_H}|\zeta|)}{\sqrt{\lambda_H}} \Bigg]. \end{aligned} \tag{3.47}$$

Whilst mathematically complex, this method does not require repeated recalculation as the elements are constant for a given DLW structure. Once variables are calculated, the field at a given point is calculated from the analytical equations rather than needing to solve Maxwell's equations at each individual position.

3.2.5 Longitudinal Variation in Single-Particle Wakefields

The wakefields generated can be separated into two phases before and after the contribution of Cherenkov radiation. In the first phase, the only contributing fields are short-range wakefields. These wakefields are caused by the bunch generating Cherenkov radiation within the dielectric but this radiation has not reflected back into the vacuum region. Cherenkov fields contribute after the radiation is reflected back into the vacuum region, after which point the total wake potential is the sum of the self-field and reflected field. In the source rest-frame, the Cherenkov radiation is as shown schematically in Figure 2.3, with the Cherenkov radiation contributing in the vacuum regime after

$$\zeta[\mathrm{s}] > \frac{2\delta}{c}\sqrt{\epsilon_r - 1}, \tag{3.48}$$

where c is the speed of light in vacuum, δ is the dielectric thickness, and ϵ_r is the relative permittivity of the dielectric. Both longitudinal and transverse wake potentials, shown in Figures 3.14 and 3.15 respectively, show this point clearly. The self-fields are independent of δ with wake potentials equal up to the point at which Cherenkov radiation begins to contribute to the fields.

The wakefields generated are inversely proportional to the dielectric gap squared (Equation 3.24). As shown in Figure 3.16, the wake potential generated is solely a function of a^2 whilst the frequency is given by the dielectric thickness and relative permittivity. Normalising for both factors, whilst keeping the ratio of a to δ constant, as in Figure 3.16, the wakefields generated are constant.

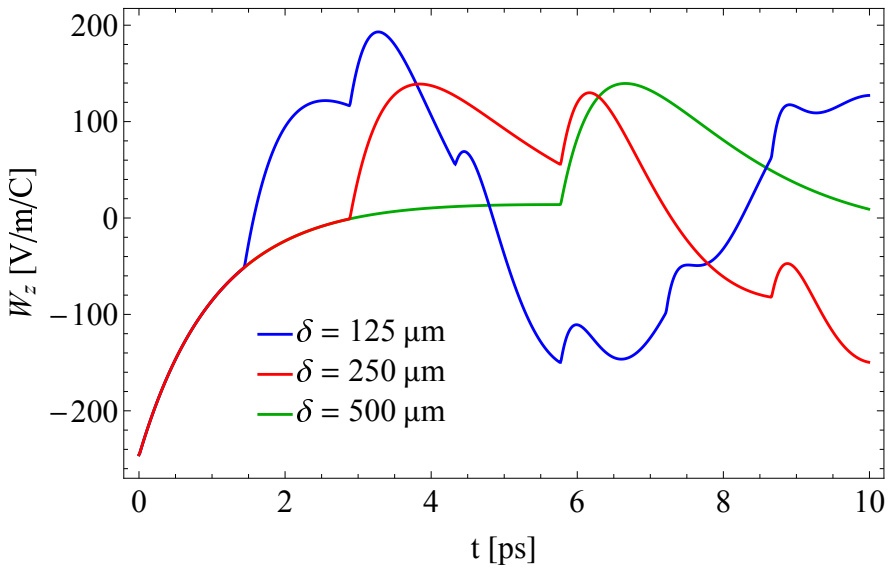

Figure 3.14. The longitudinal wake potential from a single point-like particle on-axis in a planar DLW with $a = 1000$ μm and quartz dielectric ($\epsilon_r = 3.75$) of varying thickness.

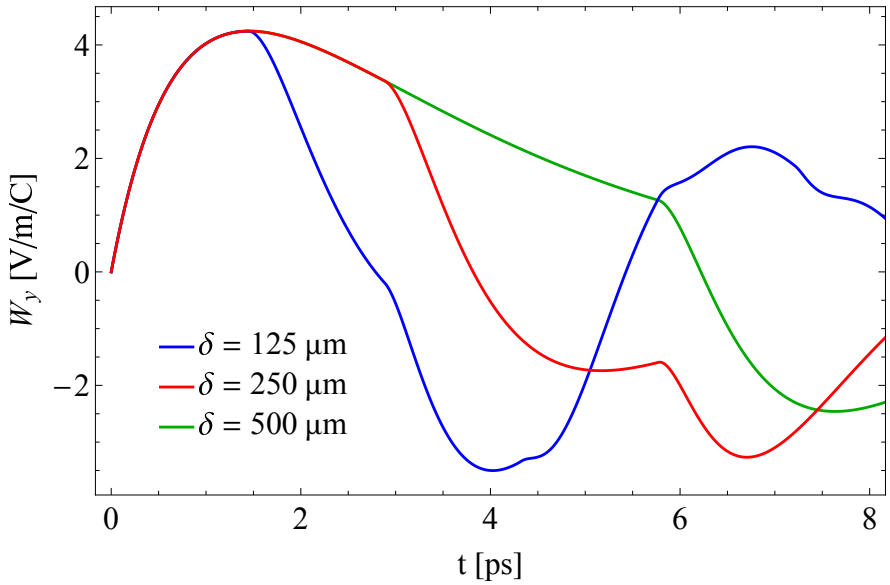

Figure 3.15. The vertical wake potential, as viewed 100 μm from centre, from a single point-like particle on-axis in a planar DLW with $a = 1000$ μm and quartz dielectric ($\epsilon_r = 3.75$) of varying thickness.

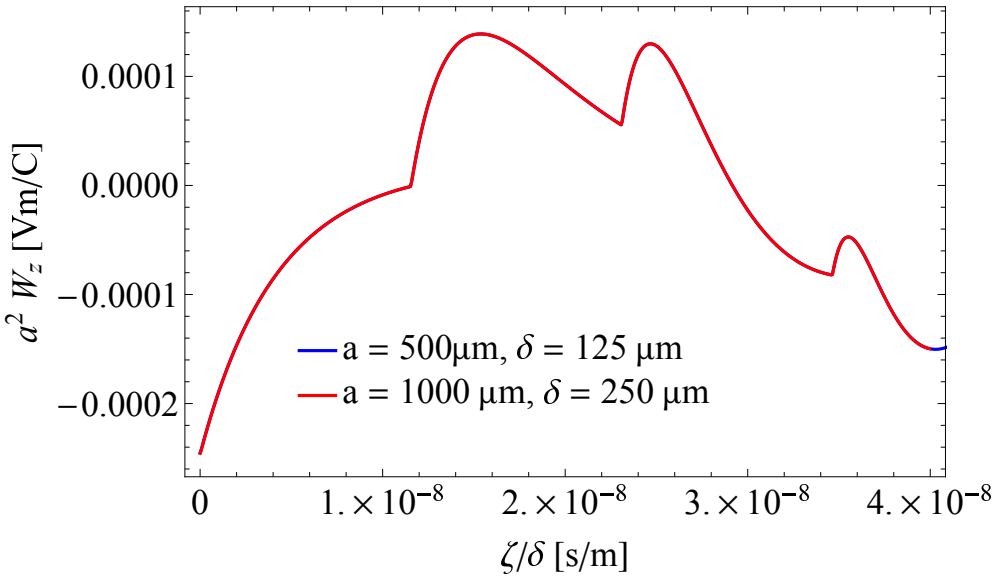

Figure 3.16. Longitudinal wake potential, multiplied by the dielectric gap squared, as a function of longitudinal position, normalised to the dielectric thickness.

3.2.6 Applicability of Theoretical Models to Finite Beam Distributions

Both conformal mapping and transverse operator methods allow for the calculation of wakefields solely within the region containing the beam, i.e. no requirement to calculate the fields at the dielectric boundaries. The conformal mapping method assumes a constant W_z and linearly increasing W_y, naturally limiting the scope of applications of the 3D field distributions to short bunches. The 2D transverse field profiles are applicable to any beam and is considerably quicker than a full implementation of the transverse operator method. As shown in Figure 3.17, the variation in fields calculated using the two methods is consistent.

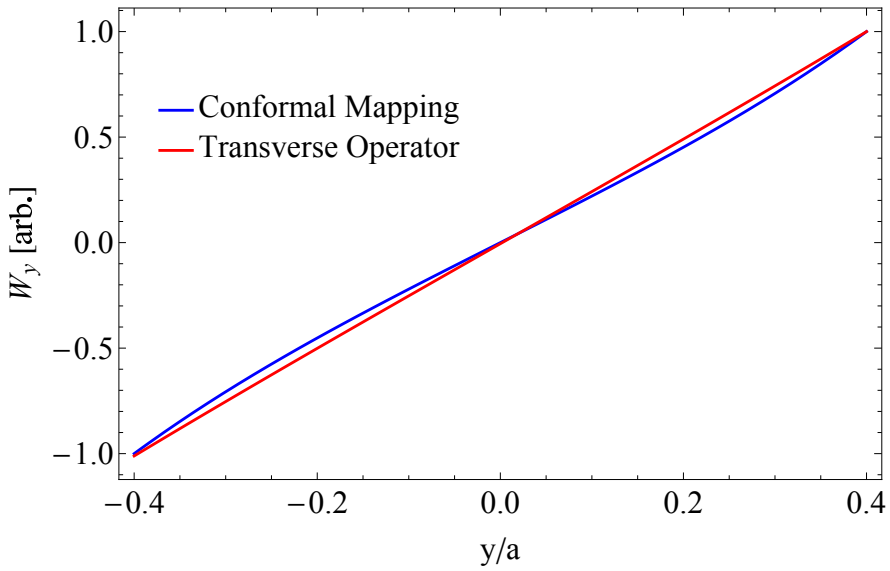

Figure 3.17. Vertical wake potential, W_y, as a function of vertical beam position normalised to dielectric gap calculating using conformal mapping and transverse operator methods. In both cases the wake potential is normalised to the field at $y = 0.2a$.

The assumptions made in the conformal mapping method, i.e. a constant W_z and linearly increasing $W_\perp$ with distance from the source, are clearly only valid for very small distances from the source particle. For the structure parameters used in Figures 3.14 and 3.15, W_z reduces by 10% within 100 fs and similarly the gradient of W_y reduces by 10% within 100 fs. Therefore, the conformal mapping method would only be appropriate for beams with bunch lengths sub-10 fs. For modelling the 3D fields produced by finite beams the transverse operator method will be used.

3.3 Shaping Wakefields with 3D Beam Distribution

The solutions to the fields given above are all for a point-like source particle. Every electron within a beam propagating in a DLW excites these fields; the resulting overall wakefield is the sum of all these individual wakefields. By shaping the electron beam entering the DLW, the contribution of each point-like source can be controlled, therefore shaping the wakefield produced. Rather than considering individual electrons, we define an electron bunch by a 3D distribution $\rho(x, y, z)$. At a witness position, the wakefield is given by the summation of the wake potential for a point-like source and the electron distribution, i.e. a convolution of the two functions. The field at the witness position (x_0, y_0, z_0) is given by

$$F_i = \int\int\int W_i(x, y, z, x_0, y_0, z_0)\rho(x, y, z)dxdydz, \tag{3.49}$$

where

$$Q = \int\int\int \rho(x,y,z)dxdydz \tag{3.50}$$

is the total bunch charge. The integral in z is performed between the head of the bunch and witness position due to causality.

The contribution of each part of the beam, weighted by the charge of that part, leads to the ability to shape the wakefields generated by shaping the drive beam. The wakefields can be shaped to increase the magnitude of accelerating field behind a drive bunch or reduce the transverse forces acting to erode the drive beam. One method of shaping is to use multiple short drive beams, with the spacing between each optimised to constructively interfere with the longitudinal field contribution of each single beam [120][121]. Alternatively, the longitudinal profile single longer drive beam can be optimised to maximise the efficiency of acceleration and/or reduce the effect of transverse fields. In this thesis a single drive beam has been investigated, with longitudinal and transverse shaping considered in turn.

Both the maximum field generated and average field are of interest. The efficiency of acceleration is commonly judged by the transformer ratio (T.R.) given by

$$\text{T.R.} = \frac{E_z^{acc}}{E_z^{dec}}, \tag{3.51}$$

where E_z^{acc} and E_z^{dec} are the maximum accelerating and decelerating field respectively. The maximum decelerating field may not be the most relevant value when determining the efficiency of acceleration given this does not take into account the energy loss by the rest of the drive beam (assuming the maximum decelerating field is within the drive bunch). When relevant, the weighted average field will be used for longitudinal and transverse fields, given for a field F_i by

$$\langle F_i \rangle = \frac{\int\int\int \rho(x,y,z)F_i(x,y,z)dxdydz}{\int\int\int \rho(x,y,z)dxdydz}. \tag{3.52}$$

The transverse field for a beam on-axis is symmetric about the axis so the average field will be $\approx$0. It will also be relevant to instead use the average absolute field strength. The average field will be a relevant value for a beam offset from the DLW axis.

The beam and structure parameters for fields calculated in this section are listed in Table 3.1, with exceptions used to demonstrate variation with respect to a given parameter. Whilst the exact values of each parameter are arbitrary, they are of the same order in magnitude of parameters used in the rest of this thesis.

Parameter	
Bunch Charge [nC]	1
Beam Momentum [MeV/c]	250
RMS Bunch Length [fs]	1000
RMS Beam Width [μm]	50
Skewness α	-4
Dielectric Half-Gap a [μm]	500
Dielectric Thickness δ [μm]	250
Relative Dielectric Permitivity ϵ_r	3.75
DLW Width w [mm]	10

Table 3.1. Default bunch and DLW parameters for simulations in Section 3.3.

3.3.1 Longitudinal Profile

Over the longitudinal profile of a drive bunch, the ideal longitudinal field would have constant decelerating E_z and large relative transformer ratio. Previous studies have shown that a bunch with large current at the tail achieves a more constant decelerating field, including triangular, 'door-step', or double-triangular bunches [51][122][77]. To model the effect of peak current placement relative to the bunch centre, we have employed a skew-Gaussian distribution such that

$$\rho(z) = \phi(z)\left[1 + \text{erf}\left(\frac{-\alpha x}{\sqrt{2}}\right)\right], \tag{3.53}$$

where the function $\phi(z)$ is the Gaussian distribution, erf(x) is the error function, and α is the skewness factor [123]. Example distributions for varying values of α are shown in Figure 3.18. Whilst the variance of a Gaussian distribution is given by σ^2, for a

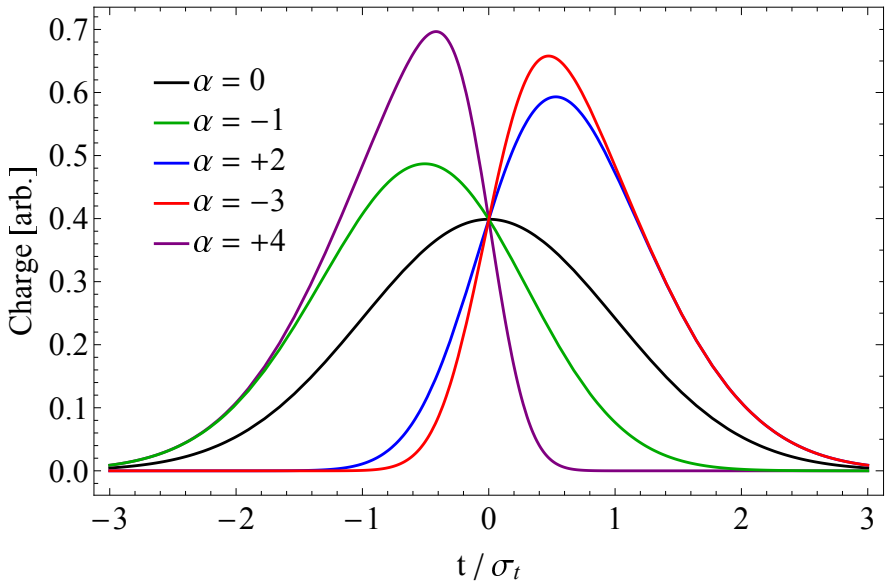

Figure 3.18. Probability distribution function (PDF) for skew-Gaussian bunches with equal mean (t =0) and width σ and varying skewness α.

skew-Gaussian distribution

$$\text{Variance} = \sigma^2 \left(1 - \frac{2\alpha^2}{\pi(1+\alpha^2)}\right). \tag{3.54}$$

The mean of a skew-Gaussian bunch does not equal the average position. Compared to a Gaussian distribution with the same mean, the change in average position is

$$\Delta\langle x\rangle = \frac{\sigma\alpha\sqrt{2}}{\sqrt{\pi(1+\alpha^2)}}. \tag{3.55}$$

Bunches with varying skew will be compared by keeping the longitudinal variance constant. The mean of skew-Gaussian bunches have been adjusted such that the average position is the same as respective Gaussian bunches, so field profiles can be directly compared.

A constant normalised energy spread before and after the DWA stage simplifies beam transportation into and out of the DWA, especially when using multiple DWA stages. Therefore, the ideal longitudinal field is constant within the drive bunch. For bunches with 1 ps RMS length, the longitudinal field produced with a large negative skew is closer to the ideal constant deceleration scenario, as shown in Figure 3.19. A negative skew provides the most advantageous field shape. A positive skew is clearly not desirable for a drive beam with increased variation in decelerating field compared to the Gaussian case.

The transverse fields excited with varying skewness (Figure 3.20) do not greatly differ. The peak F_y field is approximately constant for each bunch, with an approximately linear increase in field within the bunch. The gradient on F_y is decreased for increasingly negative values of α, however this is only particularly noticeable with $\alpha = +6$ where the position of the peak F_y value is within the bunch itself rather than at/after the tail as for the other cases.

With a constant beam profile shape, the bunch length determines the rate of wakefield excitation and period of time over which wakefields are excited. A very short bunch will have a wakefield similar to the wake potential, given the differences between parts of the bunch contributing are not large enough to cause interference to each component of the total wakefield. With a longer bunch, there is interference between the wakefields generated by the head and the tail of the bunch so the overall wakefield generated is shaped. As shown in Figure 3.21, the difference between maximum and average decelerating field decreases with bunch length. This can also be seen in the profile shapes in Figure 3.22. The strength of all longitudinal fields, including the accelerating field, decreases (as expected given the reduced current) however the transverse field

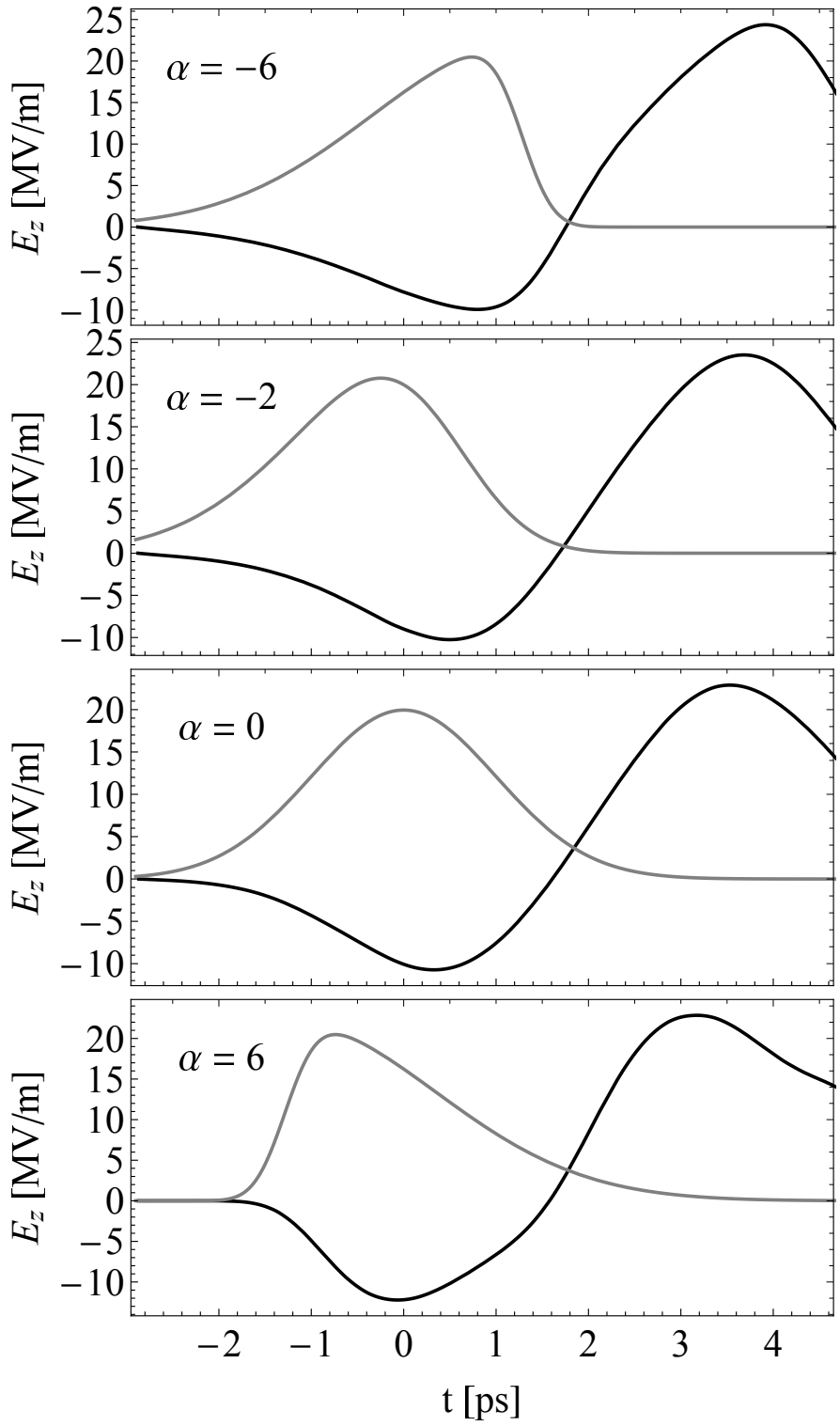

Figure 3.19. Longitudinal field generated by bunches with varying values of skewness, α, as a function of longitudinal position. Each bunch is shifted such that the mean longitudinal position for each bunch is $t = 0$.

(given in Figure 3.23) increases with bunch length up to $\sigma_t = 1$ ps at which point the field strength reduces with bunch length like E_z. The transformer ratio (using the average decelerating field) increases with bunch length, as shown in Figure 3.24. Therefore, whilst the field strength decreases with bunch length, the efficiency of acceleration increases. Ever increasing bunch length does raise two issues: accelerating field within

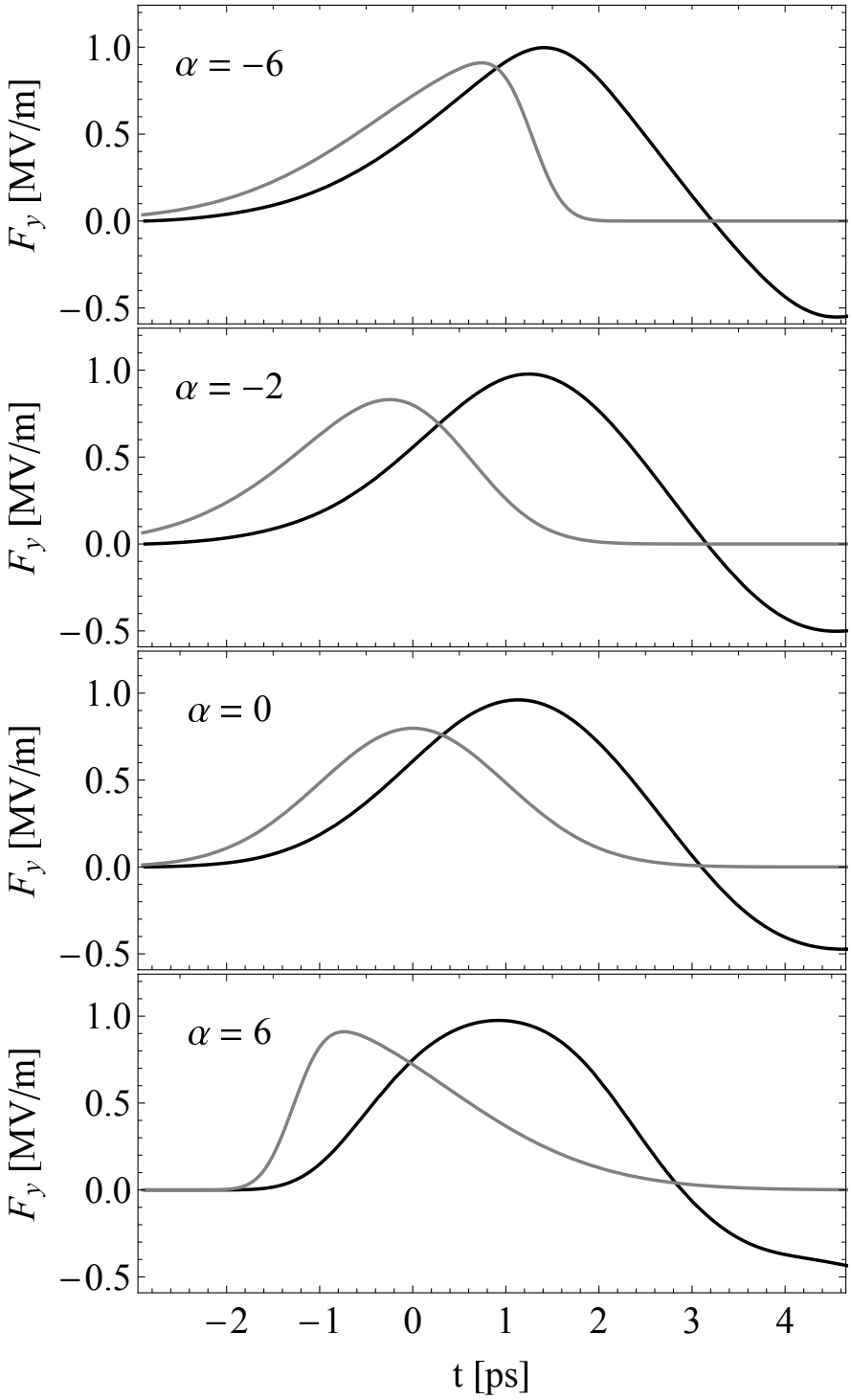

Figure 3.20. Vertical field generated by bunches with varying values of skewness, α, as a function of longitudinal position at $y = 50$ µm. Each bunch is shifted such that the mean longitudinal position for each bunch is $t = 0$.

the drive bunch and decreased relative distance between the drive bunch and peak accelerating field. These can be seen for $\sigma_t = 2$ ps in Figure 3.22 and can be seen as a limiting factor in increasing the transformer ratio obtainable.

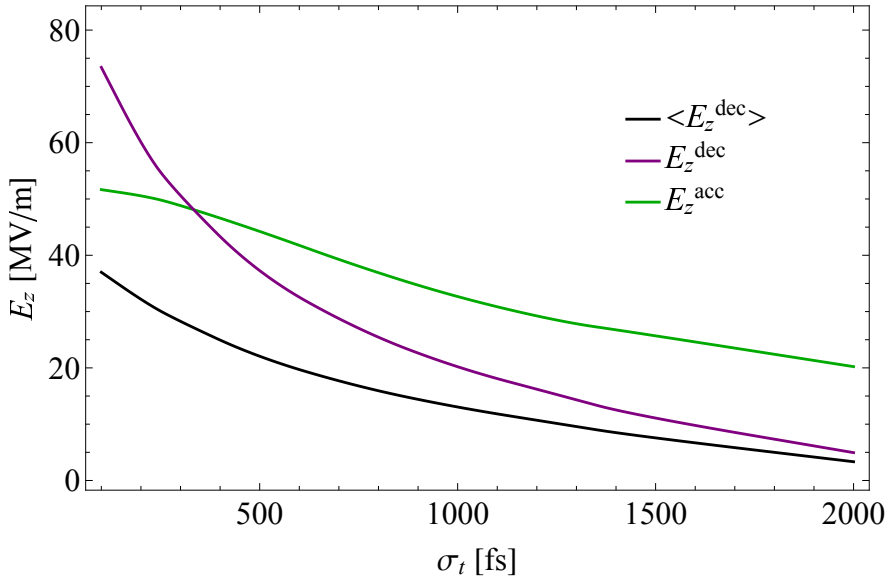

Figure 3.21. Peak accelerating and decelerating field generated and average decelerating field within the drive bunch as a function of bunch length.

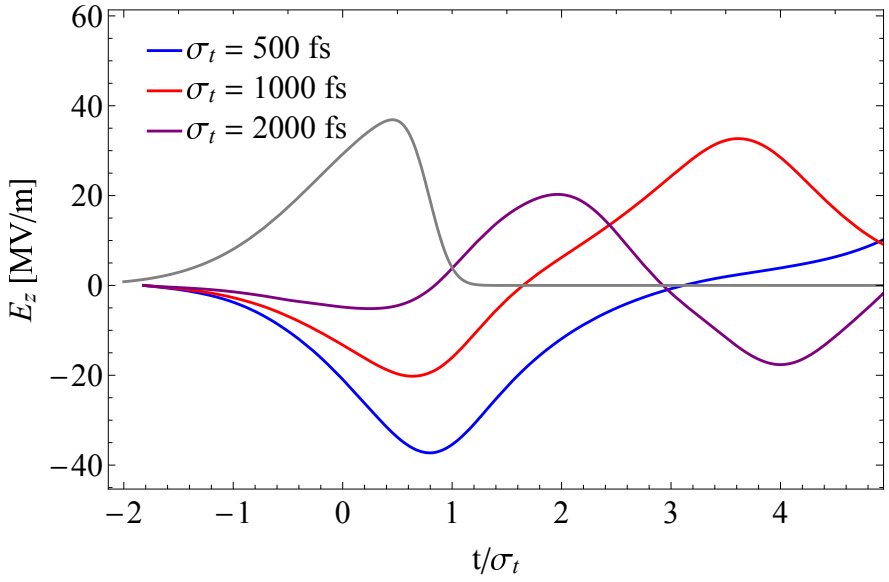

Figure 3.22. Longitudinal field profile as a function of longitudinal position for varying bunch lengths, normalised to bunch length.

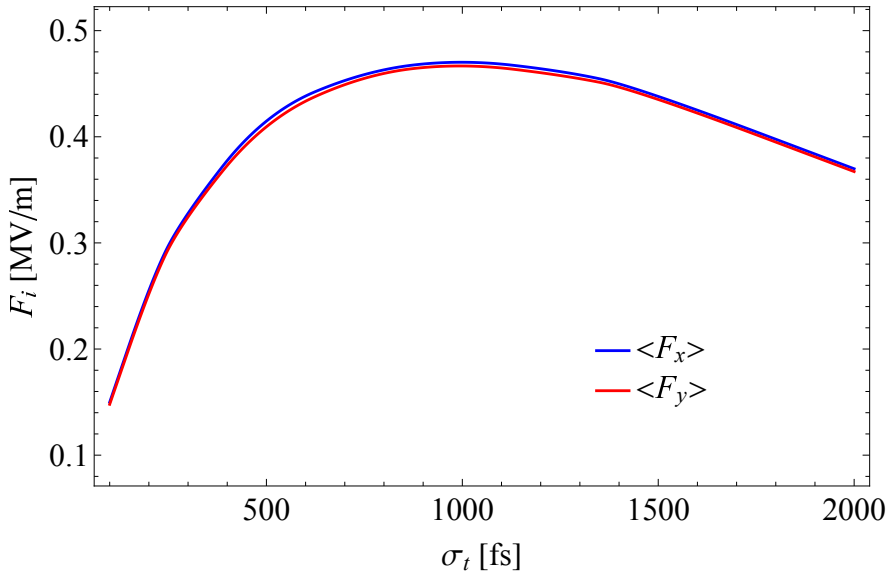

Figure 3.23. Average absolute transverse field within the drive bunch as a function of bunch length.

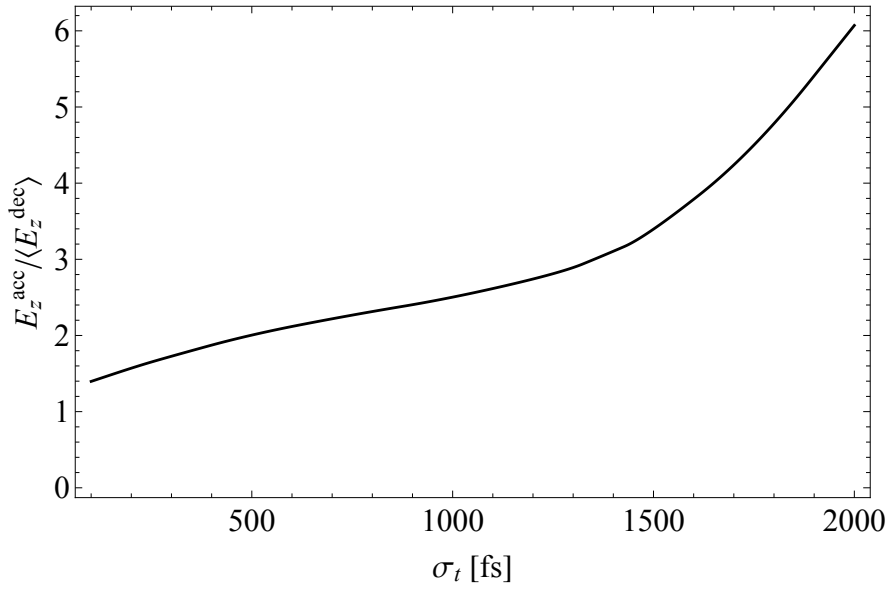

Figure 3.24. Ratio of the peak accelerating field behind the drive bunch to average decelerating field within the drive bunch as a function of RMS bunch length, σ_t.

3.3.2 Transverse Profile

From the PW theorem, for longitudinal variation in the transverse field to exist (i.e. any transverse field excited) there must be transverse variation in the longitudinal wakefield generated. An infinitely wide beam, in an infinitely wide DLW, will have no transverse dependence in the longitudinal field excited and therefore no transverse field excited.

For the specific planar DLWs considered in this thesis, the structure aspect ratio is very large (width ∼cm and a ∼mm). Bunches with RMS width σ_x ∼mm could be considered quasi-infinite relative to the vertical beam size (σ_y ∼10 μm) and would be expected to show highly reduced transverse fields. A full Fourier analysis of the

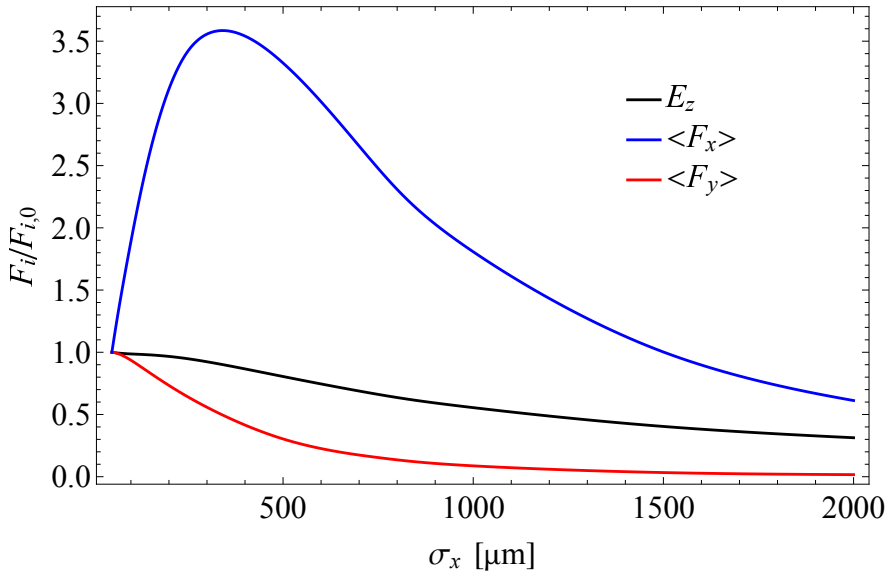

Figure 3.25. Peak longitudinal field and average transverse fields with increasing horizontal beam width $sigma_x$ and constant vertical beam, σ_y. Fields are normalised to the circular beam case where $\sigma_x = \sigma_y$ = 50 μm.

wakefields, detailed in [124], shows that the coupling of higher order modes decreases with bunch width. Higher-order modes, with smaller transverse wavelengths, have larger transverse gradients and therefore associated with increased transverse fields.

Investigating 3D Gaussian bunches with varying RMS beam width, σ_x, it is clear that the ratio of longitudinal to defocusing force increases with σ_x (Figure 3.25). Therefore, for a given accelerating field, the defocusing force in the drive beam is reduced for elliptical bunches [125]. This relationship has been shown experimentally in [126]. For increased, but not quasi-infinite, values of σ_x it can be seen in Figure 3.25 that horizontal and transverse forces do not follow the same trend. For small increases in σ_x the average focusing force increases. As σ_x tends towards the quasi-infinite case, $\langle F_x \rangle$ reduces with beam width in a similar manner to $\langle F_y \rangle$.

Differing magnitudes of focusing and defocusing forces is not necessarily problematic so long as the beam quality is not affected. As shown in Figure 3.26, the variation in focusing field is increasingly non-linear for increasing σ_x. This corresponds to the focusing field being increasingly non-quadrupole-like. Decreased focusing at the beam edge compared to the quadrupole-like beam centre would lead to an increased charge density at the beam centre compared to the edge. This would increase kurtosis in the transverse beam profile. Kurtosis is defined as the sharpness of a probability density function, given by the fourth moment of the distribution. The kurtosis of a purely Gaussian profile is zero. A quadrupole-like field would preserve a beam's emittance (for a given longitudinal slice) and allow for external beam optics to be used to maintain beam properties and quality. A non-quadrupole-like field, like those seen for larger σ_x, would likely degrade the quality of the beam and raises questions about the potential

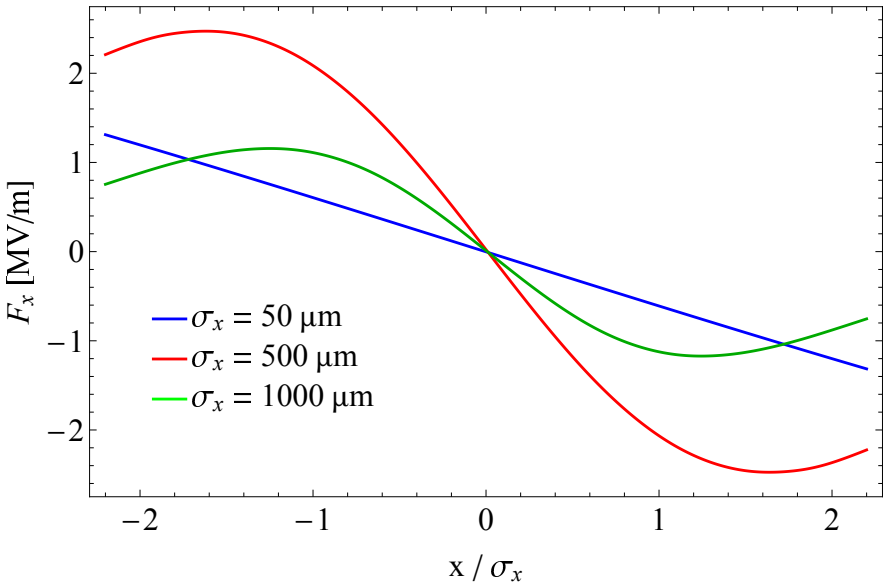

Figure 3.26. Variation in horizontal focusing force across a cross section of beams of varying horizontal widths. Horizontal position within the cross-section is normalised to the RMS beam width, σ_x.

suitability and stability of elliptical beams propagating over long distances in a DLW.

3.4 Summary

Two methods for calculating the wakefields generated by a point-like charged particle in a DLW have been evaluated. The conformal mapping method is useful for exploring the shape and relative strength of the fields generated by a particular DLW geometry. The method to calculate the fields is consistent irrespective of the geometry, with the only requirement that a conformal mapping from the geometry to a circular DLW be found. A transverse operator method, with a formal derivation required for each geometry, can be used over longer distances and includes a calculation of the mode composition of the wakefield generated.

Treating the fields calculated by a point-like particle as a wake potential, the field for a 3D particle distribution is calculated by the convolution of the wake potential and charge distribution. The 3D distribution can be shaped to generate an optimal wakefield for drive and witness bunches. The longitudinal distribution, both shape and length, allow for the generation of an accelerating field with higher efficiency. In particular, using a longer bunch with peak current towards the tail of the bunch ensure the variation in decelerating field is reduced over the drive beam profile and ratio of deceleration to accelerating field is maximised. The transverse beam distribution can be exploited to reduce the effective coupling to higher order modes in the wake potential which are associated with larger relative transverse forces. Shaping the bunch to be highly elliptical (large horizontal size), the ratio between transverse and longitudinal fields is

reduced, potentially increasing the stability of acceleration at a given gradient. Using elliptical beams does remove the symmetry in transverse fields present in circular beams, and the variation in transverse fields across the transverse bunch profile raises questions about the suitability of such beams over large distances, despite the attractive reduction in overall field strength. The question of the suitability of elliptical bunches will be addressed experimentally in Chapter 6 and in high-charge simulations in Chapter 7.

Chapter 4

Development of DiWaCAT: Dielectric Wakefield Calculator and Tracker

This chapter describes the development of a specialised simulation framework, **Di**electric **Wa**kefield **C**alculator **A**nd **T**racker (DiWaCAT) [127], for the calculation of wakefields from relativistic charged beams inside a DLW. This framework is used to simulate relativistic electron beams in planar DLWs in the rest of this thesis. The organisation and optimisation of the simulation framework is discussed. The fields calculated by DiWaCAT have been benchmarked against the commonly used commercial code CST.

4.1 Overview of Particle-In-Cell Methods

Typical particle-in-cell (PIC) simulation codes separate the calculation of electromagnetic (EM) fields and tracking particle motion due to these fields. For a generic particle motion integrator, the method for calculating the EM fields is irrelevant to the algorithm being implemented. Object-Oriented Programming (OOP) methods can be used to increase the efficiency and flexibility of calculations. Rather than directly solve Maxwell's equations for every scenario, a PIC code could use existing analytical formulae for the fields in a given context to simplify calculations and reduce the computational load of simulations. Analytical equations could be used for specific applications, increasing the flexibility of a code written with OOP methods.

Fields are typically calculated by setting a large number of macroparticles onto a discrete mesh of "cells", as in Figure 4.1, and calculating the field at those discrete mesh points. The charge density is given by the probability density function (PDF) of macroparticles and can be applied to simulations in two ways: either with the density of macroparticles or the charge assigned to each macroparticle. With fixed-weights, the distribution of macroparticles is described by the PDF whilst for variable-weight macroparticles the charges/weights are instead described by the PDF and the distribution of the particles is

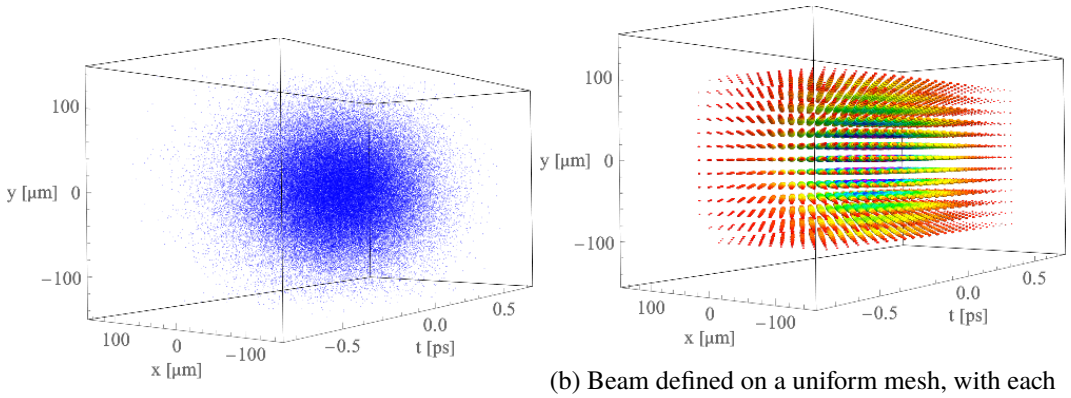

(a) 3D beam distribution of 10000 fixed-weight macroparticles.

(b) Beam defined on a uniform mesh, with each mesh point having variable charge/weight. The highest charge mesh points are purple and lowest charge points are red.

Figure 4.1. 3D distribution consisting of the a) full selection of uniform charge macroparticles and b) set onto a uniform mesh.

typically uniform. Tracking the charge of each variable-weight macroparticle, including updating the macroparticle charge when relevant, is more computationally expensive than 6D tracking of fixed-weight macroparticles. Simulating variable-weight macroparticles is typically only necessary when particle-particle interactions need to be included, new particles are being generated within the simulation, or there is a need to control the density of macroparticles to avoid stochastic noise effects [128]. Using a mesh with variable-weights is a compromise solution; fields are calculated from charge deposition on to a uniform grid - forming a set of 'variable weight' charge locations - and individual fixed-weight macroparticle motions are tracked.

There are two methods, and assumptions, when calculating the electromagnetic fields for simulations. The most commonly used method in generalised codes, is to assume the EM fields dynamically change during the simulation timeframe. As a result of this assumption, EM fields need to be regularly recalculated. This is relevant for cases such as plasma-based problems, given the EM fields change with changing plasma density (i.e. a time-dependent problem) [129]. In the case of a DLW, we can instead make the assumption that the field profile as a function of position within a bunch is constant, at least over time-scales in which the beam properties do not change. Therefore, recalculating the EM fields generated as a dynamic problem would be an inefficient use of computational time. The field applied to each macroparticle is the value of the constant field profile at the macroparticle position. Once the field profile is calculated, the simulation problem is reduced to a particle tracking problem. The field applied to each particle may change, as will be discussed later, but the 3D field distribution will not, provided there are not substantial changes to the 3D spatial distribution of the beam or that substantial beam losses occur.

4.1.1 EM-PIC methods

Generalised EM-PIC codes, such as those typically commercially available, cannot make the assumption that fields are constant so must use an algorithm with time dependent EM fields that are recalculated at each step. A typically used algorithm for dynamic cases is the "Boris pusher" [130], which can be simplified to the "Vay pusher" for relativistic particles [131]. These methods use a leapfrog method, solving Maxwell's equations for the EM fields in one time interval, and applying those fields to particles in the next. This process is typically considered a single time interval that has been split in half. The position of macroparticles are given at half-time intervals, and velocity at integer time intervals used to advance macroparticles. Compared to a more complex numerical integration, such as a Runge-Kutta method, the Boris pusher preserves phase-space volume over long distances, accounts for small-scale gyration in particle motion, and conserves particle energy when no electric field is applied [132][133]. With a Boris pusher, the particle motion is treated at discrete time steps ($n, n+1$, etc.) using the forms

$$\frac{\mathbf{x}^{n+1/2} - \mathbf{x}^{n-1/2}}{\Delta t} = \frac{\mathbf{u}^{n}}{\gamma^{n}} \tag{4.1}$$

and

$$m\frac{\mathbf{u}^{n+1} - \mathbf{u}^{n}}{\Delta t} = q(\mathbf{E}^{n+1} + \bar{\mathbf{u}} \times \mathbf{B}^{n+1}). \tag{4.2}$$

In these equations **x** and **v** refer to the vector position and velocity, and **u** = γ**v** where γ is the Lorentz factor. $\bar{\mathbf{u}}$ is an average velocity between the two time intervals. For particles propagating outside of a vacuum, $\bar{\mathbf{u}}$ on the right-hand side in Equation 4.2 is replaced by the effective velocity. The EM fields are calculated at discretised regular mesh points, with the resultant field at each macroparticle position estimated using an interpolation method. When macroparticles are advanced, the beam is re-meshed to account for changing charge density over time.

The right-hand term in Equation 4.2 is the force applied to the particles. In cases where the EM force field is known, such as from a wakefield in a DLW, Equation 4.2 is simplified to

$$m\frac{\mathbf{u}^{n+1} - \mathbf{u}^{n}}{\Delta t} = \mathbf{F}^{n+1}. \tag{4.3}$$

Given $\mathbf{x}^{\mathbf{0}}$ and $\mathbf{u}^{\mathbf{0}}$ are known, this equation can be used to iteratively push individual macroparticles. This process is outlined in Figure 4.2.

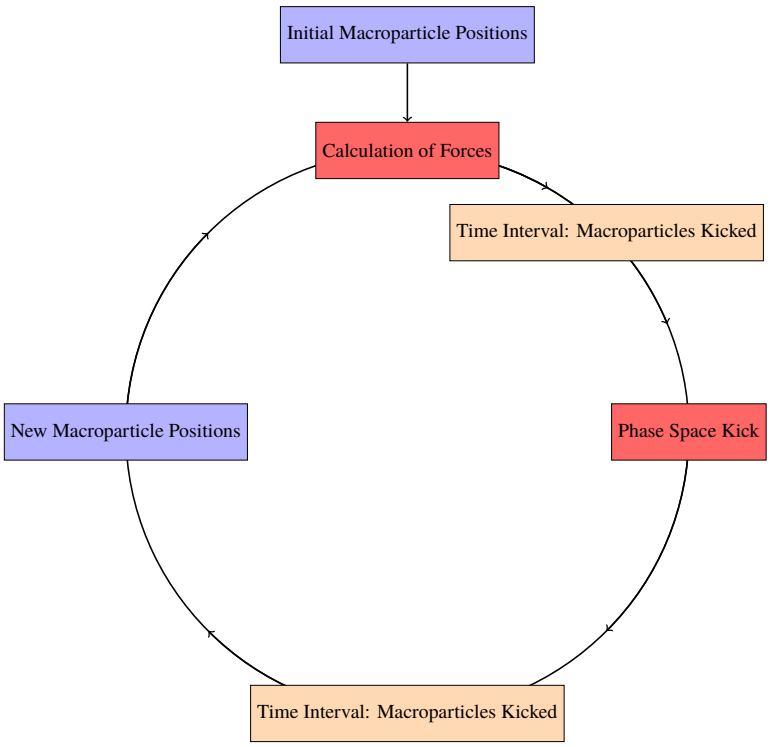

Figure 4.2. Flowchart for a typical particle kicker algorithm.

4.2 DiWaCAT, A Simulation Framework for Dielectric Lined Waveguides

Using a particle pusher method, a simulation framework, DiWaCAT, has been developed to calculate the fields excited and track relativistic charged beams inside a planar DLW. This code has been explicitly designed to allow for integration with other beam dynamics simulation codes. As a result, certain parts can be performed by external software. Particular attention has been paid to ensure integration is possible with SimFrame, the in-house start-to-end (S2E) simulation framework for the CLARA/VELA beamline at Daresbury Laboratory [134]. This framework has been designed to work with beams from ASTRA [135], Elegant [136], GPT [137], and CSRTrack [138]. Beams from any of these can be used as inputs, or idealised beams can be generated using in-house code. These idealised beams are generated using 6D distributions, with beam emittance and longitudinal energy chirp as allowed input variables. These allow for a specific beam envelope to be generated for DLW simulations. DiWaCAT is used to create a cubic grid of non-uniform charge mesh points, at which the field is calculated. There is the option to add mesh points beyond the bounds of the beam. This is useful in cases where the field behind the beam is required, such as a drive/main beam system.

Calculating the field at the mesh points is completed in two steps: the wake potential (Green's function) calculation for a planar DLW, and convolution of the Green's function

with mesh point charges to generate the 3D field. Separating these steps, using an OOP method, allows for the separation of DLW specific calculations which can later be extended for arbitrary geometries. The wake potential is calculated from a sum of discrete eigenmodes using the transverse operator method, as outlined in Chapter 3.

The Green's function is constant for a given DLW, so does not need to be recalculated. The 3D wakefields can be recalculated by the convolution of the constant Green's functions with changing charge density, without the need for a full re-calculation of all steps. Applying the fields to the full sample of fixed-weight macroparticles can be performed outside the DLW simulation code, allowing for the addition of other fields if required. One such example would be surrounding a DLW with external magnetic fields, as in [77][84].

The DiWaCAT code can be viewed as a linear process shown in Figure 4.3: read in the beam and DLW parameters, calculate the number of modes needed for convergence, calculate the Green's function (`CalcWakeElement`), calculate the 3D fields (`TotalForceMesh`), and finally apply that field to the individual macroparticles for particle tracking (`InterpolationKicker`). Particle tracking can be further broken down, following the process outlined in Figure 4.2. Two of these processes are iterative, the mode convergence and particle tracking. The details and implementation of each process will be discussed in turn in Section 4.3.

Mode convergence is completed to a given tolerance. The 3D Green's function is calculated for the outer-most mesh point (to ensure the transverse components are non-zero) with a given number of modes, and also with 5 fewer modes. The tolerance for each of the 3 Green's functions (W_x, W_y, and W_z) is

$$\text{Tolerance}(nX) = \frac{W_i(nX, nY) - W_i(nX - 5, nY)}{W_i(nX - 5, nY)} \tag{4.4}$$

and

$$\text{Tolerance}(nY) = \frac{W_i(nX, nY) - W_i(nX, nY - 5)}{W_i(nX, nY - 5)}, \tag{4.5}$$

where W_i is the Green's function, calculated at the transverse mesh point closest to the dielectric plate. This point is chosen as this is where the highest order modes will have the greatest contribution. Convergence for each set of modes is assumed to be reached when the final 5 modes contribute less than the given tolerance for W_x, W_y, and W_z.

Particle tracking, performed by the `InterpolationKicker` function, follows the method shown in Figure 4.2. For each macroparticle, the field is calculated using an interpolation of the field at the mesh points and each macroparticle is tracked by applying that field. Over small propagation distances, it can be assumed that the field at the mesh

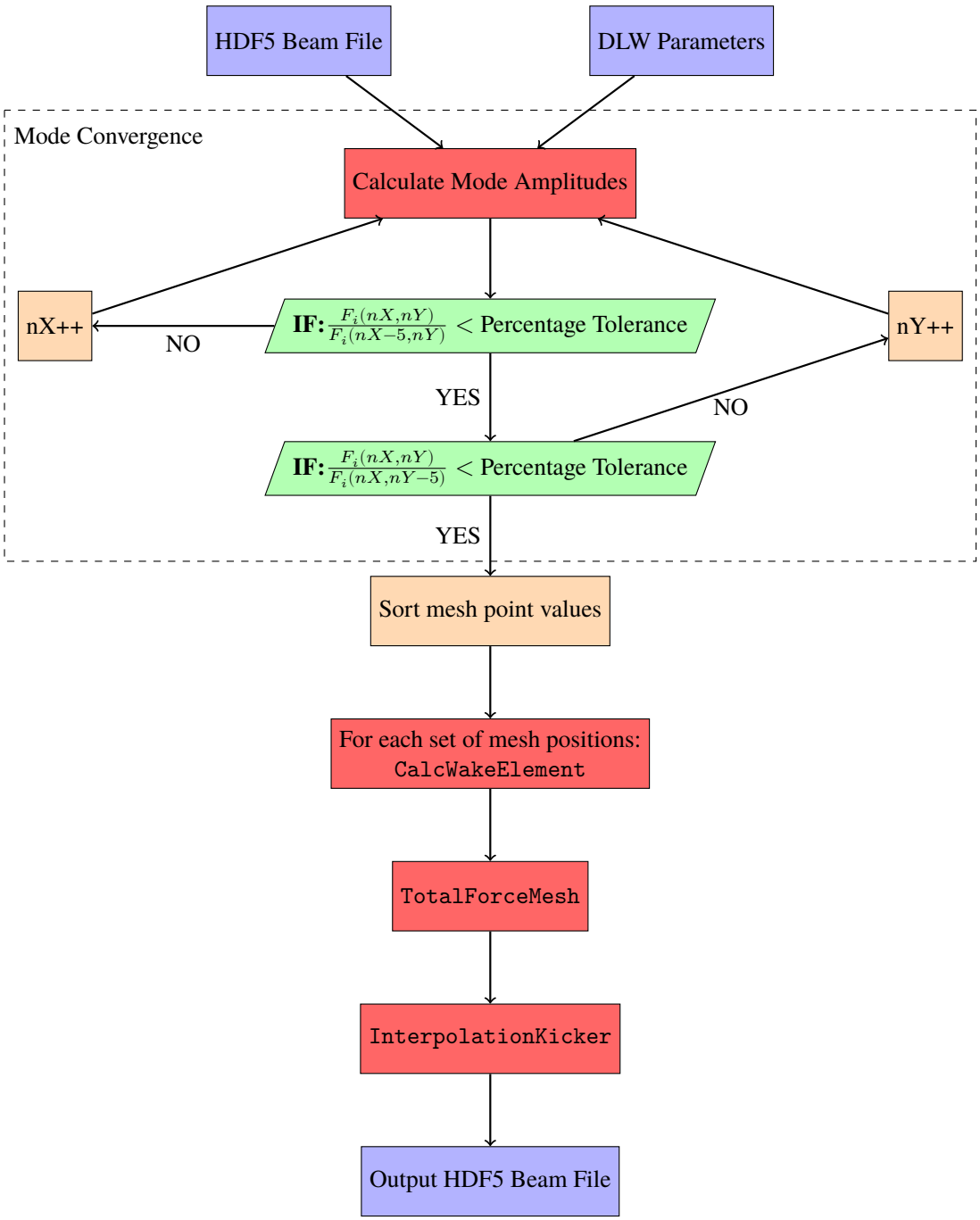

Figure 4.3. Functional flowchart for DiWaCAT. Beam and structure files are represented by purple, data organisation by orange, logic tests by green, and computational processes by red boxes.

points varies by a negligible amount, so the same fields are then used to interpolate the field for subsequent time steps. When macroparticles are lost at the boundaries of the DLW, the charge is set to zero (rather than deleting the macroparticle). This ensures individual macroparticle labels are consistent and individual macroparticle tracking can be performed. When dealing with longer propagation distances, the field requires recalculation. In such instances, the output beam can serve as the input for subsequent field calculations, effectively transforming the entire process into a self-consistent loop.

4.3 Organisation and Optimisation of DiWaCAT

In this section, the optimisation of each method (red in Figure 4.3) will be discussed in detail in reverse order. The different algorithms required for accurate simulations will be discussed, with a focus on maintaining computational efficiency. The interpolation of the 3D field distribution to individual macroparticles (`InterpolationKicker`) is discussed in Section 4.3.1, the particle tracking (also `InterpolationKicker`) in Section 4.3.2, mesh organisation (relevant for `TotalForceMesh` and `CalcWakeElement`) in Section 4.3.3, and tolerance for mode convergence in Section 4.4.

For these test studies, fields are calculated with parameters listed in Table 4.1, and offsets from the DLW centre y_0 = 0 and 750 µm. These parameters were chosen to give a suitably wide range of field strengths that would have a noticeable effect on beam properties. With the off-axis beam, the transverse field is ∼0.5 MV/m which will give a measureable kick after a few centimetres of propagation. The bunch length is long enough that the peak decelerating field is within the bunch, so the maximum field - and any non-linearities - within the field shape can be observed.

Parameter	
Beam Momentum [MeV/c]	200
Total Charge [pC]	250
Beam Width, $\sigma_{x,y}$ [µm]	50
RMS Bunch Length, σ_t [fs]	200
Beam Emittance, ϵ_n [mm mrad]	3
DLW Half-Gap, a [µm]	1000
Dielectric Thickness, δ [µm]	250
Dielectric Permittivity, ϵ	4
DLW Width, w [mm]	10

Table 4.1. Beam and DLW parameters for DiWaCAT field calculation studies.

4.3.1 Interpolation Methods

The field is directly calculated on a regular grid of non-uniformly charged mesh points. The field at the position of each individual macroparticle is estimated using a 3D interpolation from these mesh points. A more accurate interpolation method allows for fewer mesh points to be necessary in the simulation, reducing the time for the computationally expensive Green's function calculation.

In 1D, an n^{th}-order interpolation requires $n + 1$ points around the point at which the field is being estimated [139]. A nearest-neighbour (NN) interpolation, a 0th-order interpolation, only requires the single closest point. All higher-order terms require weighting based on relative distance from mesh points to the calculation point. Each dimension is considered independently, so the theory of a 1D interpolation is no different

to a 3D extension. Linear interpolation, being a 1-st order interpolation, uses the two nearest mesh points: the value at each mesh point is weighted by the fractional distance to each. A cubic interpolation considers the points surrounding the two closest mesh points to calculate a spline function. The layout of this system, for mesh cells with unit length separation is shown in Figure 4.4. The fractional difference between the two closest points (x_i and x_{i+1}) is given by u.

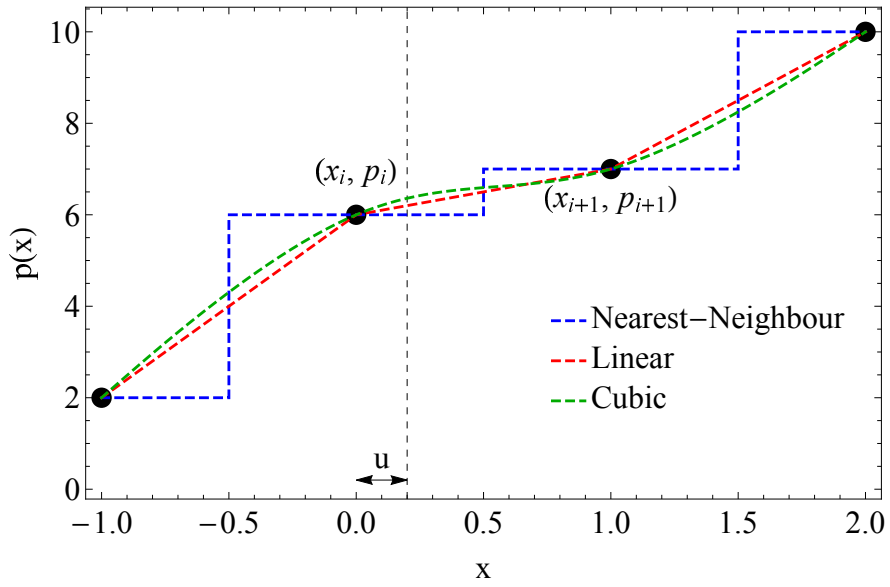

Figure 4.4. Example nearest-neighbour, linear, and cubic interpolations for a generic 1D function with changing gradient between mesh points, with point values chosen at random.

Using a linear interpolation, one assumes that the overall profile of a function is described by the values at the mesh points. This assumes the second derivative of the function is negligible between mesh points, and the change in function is assumed to be linear. For a generic function, $p(x)$, known at mesh points i and $i+1$ with unit distance between mesh points, the value at the point u is

$$p(u) = p_i + u(p_{i+1} - p_i). \tag{4.6}$$

Extending a linear interpolation to 3D can be performed in 2 ways: either use a weighted sum of all 9 surrounding points, or perform a 1D interpolation in each axis in turn. The later method can be simplified to improve computational efficiency. The equations required to extend a linear interpolation to trilinear (3D) interpolation is given in [139].

If the second derivative of the function is non-negligible between mesh points, a method to estimate the change in function gradient is required. In order to estimate the second derivative, it is necessary to consider the cube of the nearest points around the calculation point, as well as the cubes of points surrounding each of these closest points. The estimated spline function can be calculated using an interpolating curve. One example of an interpolation curve would be the Catmull-Rom cubic function which is expressed

by a matrix formula. The equation,

$$p(u) = \begin{bmatrix} u^3 & u^2 & u^1 & 1 \end{bmatrix} \begin{bmatrix} -0.5 & 1.5 & -1.5 & 0.5 \\ 1 & -2.5 & 2.0 & -0.5 \\ -0.5 & 0 & 0.5 & 0 \\ 0 & 1 & 0 & 0 \end{bmatrix} \begin{bmatrix} p_{i-1} \\ p_i \\ p_{i+1} \\ p_{i+2} \end{bmatrix}, \tag{4.7}$$

weights the function by distance to the closest point, as with a linear interpolation. Extending this to 3D, the method of which is listed in [140] is non-trivial and requires a large mesh sample. A formal tricubic interpolation requires the calculation point to have 64 surrounding mesh points (i.e. 4×4×4). A cascading interpolation method is used, with 16 interpolations performed in the first dimension, 4 in the second, and a single interpolation in the third dimension. Therefore, a tricubic interpolation requires 21 calculations, compared to a 7 calculations for a trilinear interpolation [140][139]. When a formal tricubic interpolation is not possible at a given mesh point, the typical method is to use a nearest-neighbour approach and assume the value of the next mesh. For example, if in a tricubic interpolation the point x_{i+2} is beyond the bounds of the mesh, it would be assumed that p_{i+2} = p_{i+1}. For a trilinear interpolation, one method is to assume the gradient between the final two mesh points remains constant beyond the limit (i.e. extrapolation) or reduce the interpolation order to nearest-neighbour.

With an increasingly fine mesh the target function is well-described by the function values at the mesh points and higher-order interpolations are not required to estimate the profile shape in great detail. With a suitably fine mesh, interpolation functions rapidly converge after a first-order interpolation. Trilinear and NN interpolations have been considered as methods for the `InterpolationKicker` function in DiWaCAT. It is assumed that a mesh fine enough to accurately describe the bunch charge density shape will also accurately define the wakefield shape so requires only trilinear or NN interpolation. Explicitly this assumption is that the second derivative of the fields do not change drastically between mesh points, so a higher-order interpolation is not required. NN interpolation would be increasingly unattractive with larger variation in field between mesh points: physically this would be simulations with longer bunch lengths and increasing offset away from DLW centre.

Given the layout of DiWaCAT, individual macroparticle tracking allows for direct comparison of the Trilinear and NN interpolation methods. The variation in momenta for each macroparticle is defined as

$$\Delta p_y = p_y^{\textbf{NN}} - p_y^{\textbf{Trilinear}}. \tag{4.8}$$

The RMS difference in Δp_y increases with transverse field strength; larger variation in p_y is seen for both longer bunches and increased offsets in Figures 4.5 and 4.6, respectively. For both on-axis and off-axis simulations, the variation in p_y is the summation of two Gaussian functions with a symmetric mean and identical widths. This is to be expected given the differences between linear and nearest-neighbour interpolations. In Figure 4.4, the linear interpolation between two mesh points results in values that are higher than the nearest-neighbor value for half the distance between the mesh points, and lower for the remaining half. The point at which the two interpolation methods meet is at the halfway mark between the mesh points, resulting in each Gaussian having an equal width. The double-Gaussian variation can be clearly seen off-axis, in Figure 4.6, for both bunch lengths. For on-axis simulations, the variation in F_y between grid points is reduced. This reduces the mean for each Gaussian distribution, leading to an overall distribution with a single peak and high kurtosis.

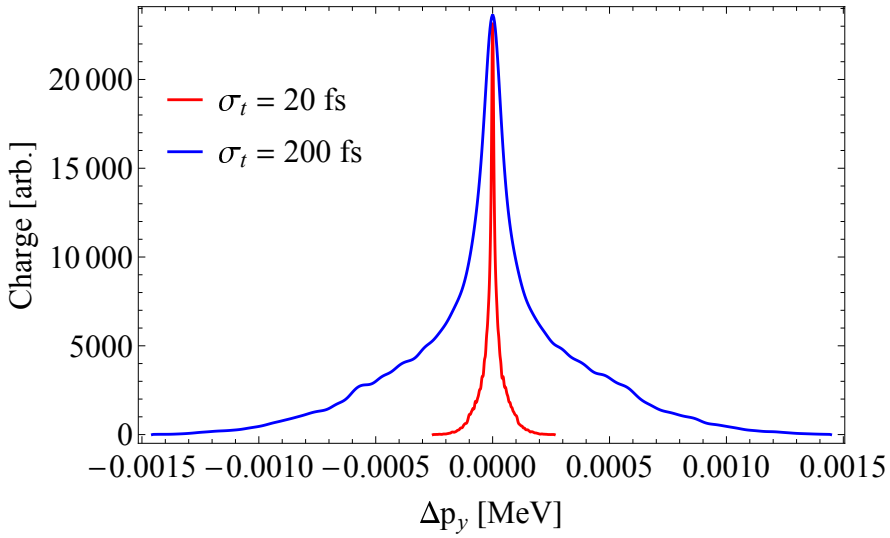

Figure 4.5. Difference in vertical momentum of individual macroparticles, using nearest-neighbour and trilinear interpolation. The field at the regular mesh points is the same for each and calculated on-axis with a = 1 mm.

Overall beam profiles are unaffected by interpolation method, given the Gaussian nature of individual macroparticle variation. The vertical beam profiles 5 m downstream, shown in Figure 4.7, are identical for the two methods despite the variation in macroparticle vertical momenta. The variation in kick received is always smaller than the difference between the nearest two mesh values. The over-estimation and underestimation cancel over a large beam sample, leading to no visible difference in beam profiles. Individual macroparticle behaviour is necessary to understand certain beam behaviours, and is an advantage of labelling individual macroparticles, so using the highest order interpolation where possible is preferable. The unaffected behavior of the ensemble macroparticle beam allows for accurate conclusions and simulations regardless of the interpolation order. Since higher order interpolations converge and the overall beam behavior remains

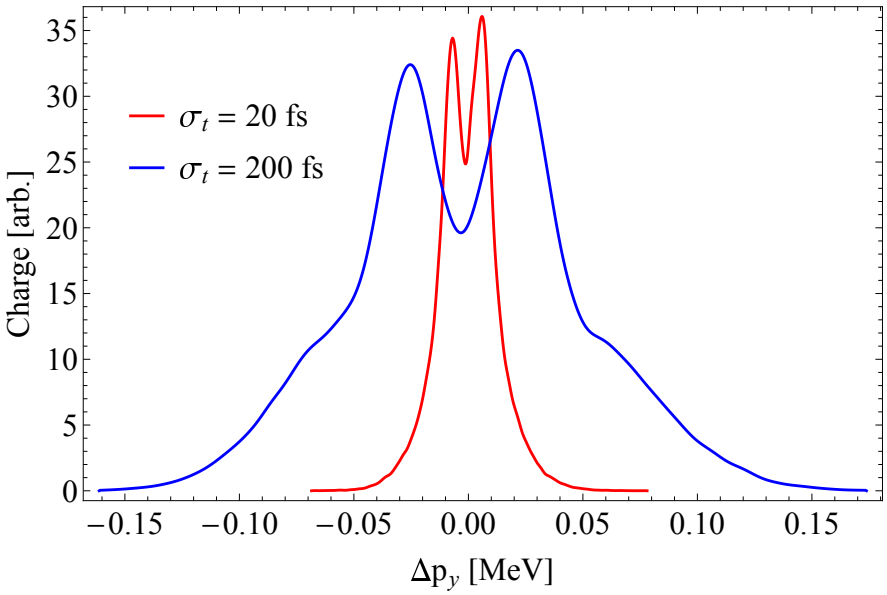

Figure 4.6. Difference in vertical momentum of individual macroparticles, using nearest-neighbour and trilinear interpolation. The field at the regular mesh points is the same for each and calculated with a = 1 mm, and y_0 = 750 µm.

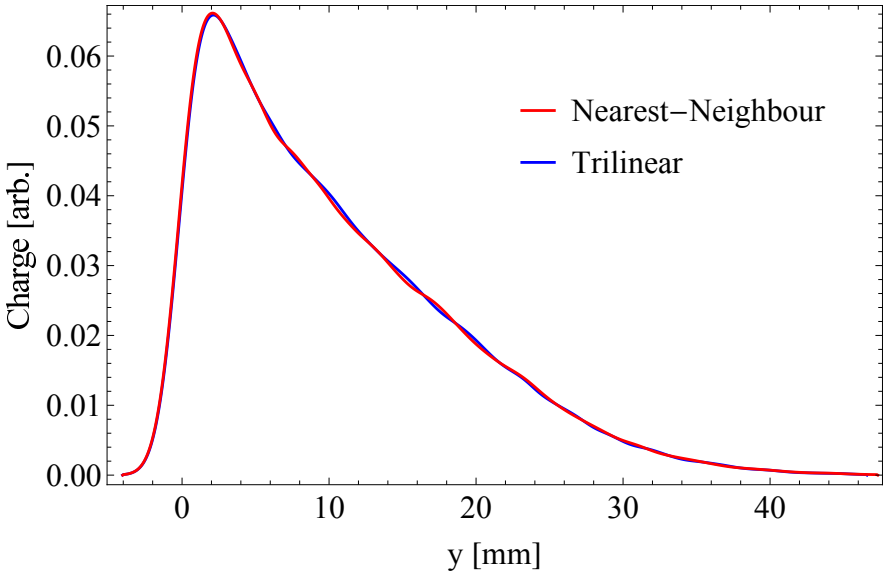

Figure 4.7. Vertical profile, at a screen 5 m downstream from the DLW, with individual macroparticle kicks calculated using a nearest-neighbour and trilinear interpolation. The field at the regular mesh points is the same for each and calculated with a = 1 mm, and y_0 = 750 µm.

consistent, it is sufficient to use first-order interpolation.

4.3.2 Time Intervals

To accurately integrate the equations of motion using the particle pushing technique, the time interval between steps must be sufficiently small to minimise variations in phase space. The specific point at which these variations become noticeable depends on the applied kick and initial phase space of the particles. When the kick is negligible or the beam is propagating in free space, larger time intervals can be used. On the other

hand, a strong or changing field requires smaller time intervals to accurately capture non-linear beam behavior. For example, when a constant field is applied to a particle the particle undergoes quadratic motion. Therefore, if a beam experiences a large wakefield over an extended distance and undergoes a substantial angular kick compared to the initial particle angle, the motion is expected to be quadratic. To accurately represent this motion using the particle pusher method, more steps are required. Similarly, if the field profile varies as the beam propagates, small time steps are required to ensure an accurate field is applied to each macroparticle.

With a field profile at mesh points calculated and assumed constant, particles are tracked using Equation 4.3 with varying time intervals Δt. At each time interval the field applied to each macroparticle is derived from the mesh using a linear interpolation. The beams simulated have parameters as listed in Table 4.1. Only a selection of macroparticles are tracked for these simulations: those creating an ellipse of points in phase space with radii $\pm 2\sigma_y$ and $\pm 2\sigma_{py}$. For these macroparticles, $x = p_x = t$ = 0.

As expected, the time step required depends on the change in momentum (i.e. field integrated over the time interval). Particle paths for the beam on-axis are shown in Figure 4.8, and with y_0 = 200 μm in Figure 4.9. Over small propagation distances (i.e. less than 5 cm or 160 ps) where the change in momentum is very small, there is negligible difference between any of the step sizes. There are no noticeable differences between particles paths for Δt = 30 and 3 fs. For on-axis beams, differences are evident for L >60 cm, and with y_0 = 200 μm for L > 40 cm. Fields are lower when the beam propagates on-axis, and this is reflected in the ability to use larger time intervals without loss in accuracy and variation in particle paths only evident at larger distances.

It is also worth considering that by the time that variation in seen in Figures 4.8 and 4.9, the width of the beam had increased by a factor of 2. At this point, new field calculations would be required given the beam parameters have significantly changed. Up to the point at which fields are no longer constant, the macroparticle phase space paths are consistent in all cases.

Beam tracking can also be considered for a single macroparticle. With a small enough time interval, the change in the field gradient between time steps will be negligible and the macroparticle paths will converge. This has been explored for the on-axis and off-axis cases for a particle with an initial position of $y = 25$ μm and $p_y = 0$. As shown in Figure 4.10, convergence is seen for both cases for $\Delta t < 30$ fs, matching the results from the phase space plots in Figures 4.8 and 4.9. Given that the particle pusher method results in a converged solution, we can state that it is a suitable method of solving for particle motion.

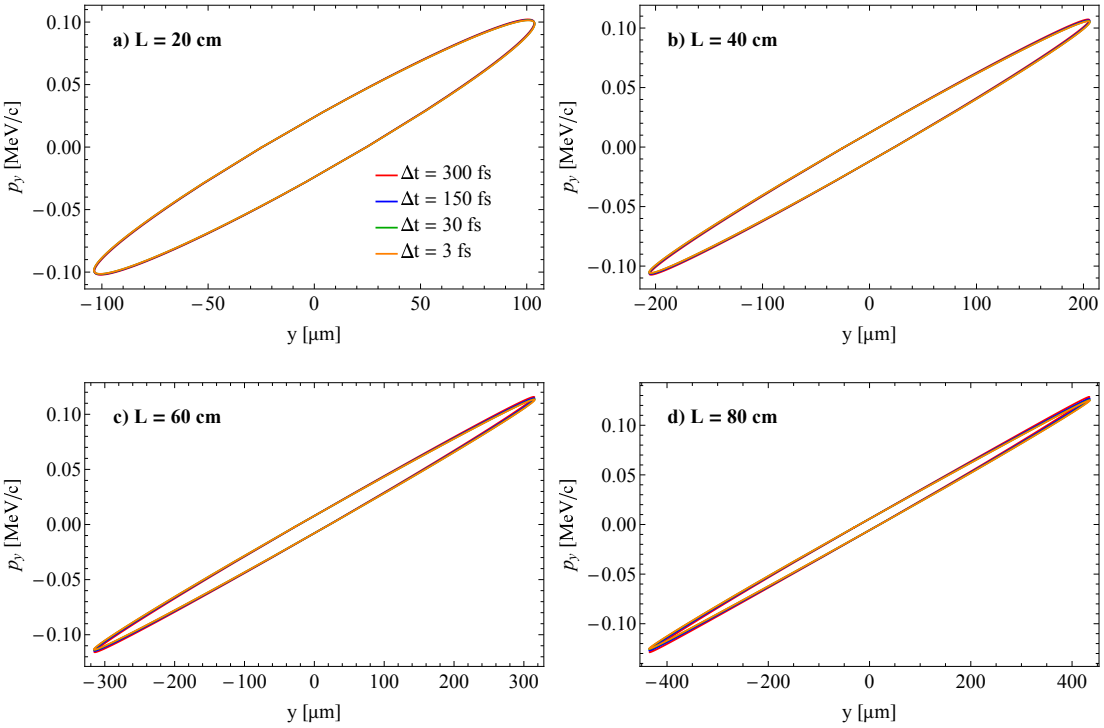

Figure 4.8. Phase space ellipse at varying distances within a planar DLW, for beam on-axis. Macroparticles are kicked at varying time intervals.

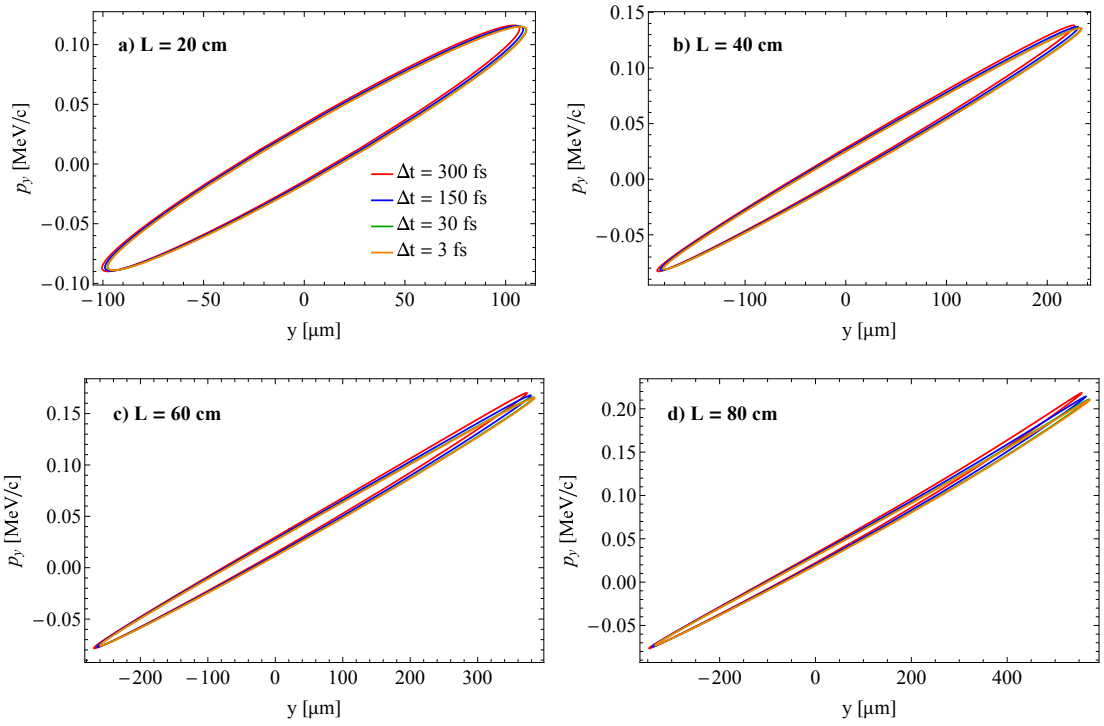

Figure 4.9. Phase space ellipse at varying distances within a planar DLW, for beam with y_0 = 200 μm. Macroparticles are kicked at varying time intervals.

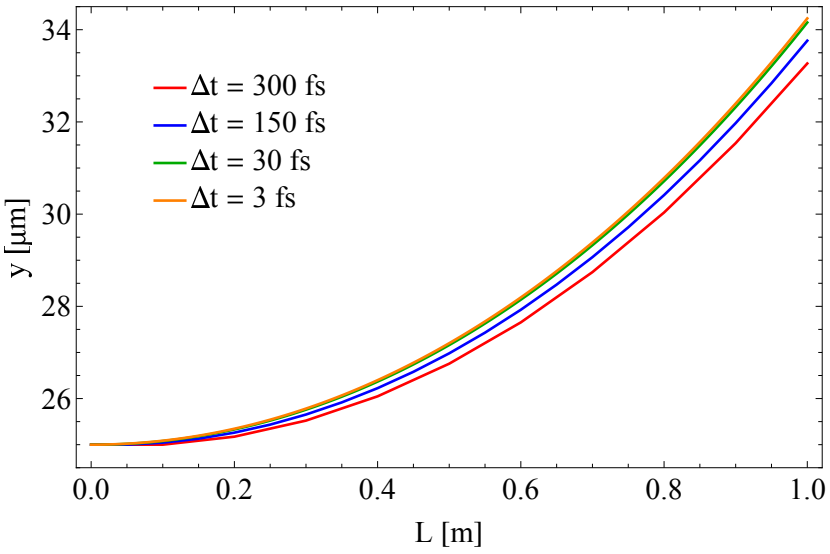

(a) $y_0 = 0$ µm

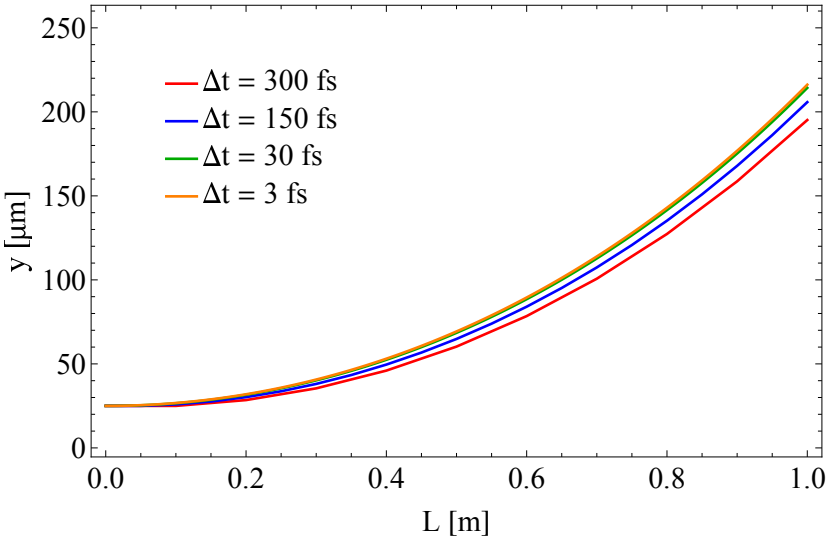

(b) $y_0 = 200$ µm

Figure 4.10. Vertical position of a macroparticle as a function of distance within a planar DLW. The initial vertical position is 25 µm from the beam centre and macroparticles are tracked with varying time intervals.

4.3.3 Mesh Density

An interpolation function ensures that each individual macroparticle receives an accurate momentum kick from the field. The accuracy of the field at the grid points is determined by the size and layout of the grid. The 3D grid is defined with the number of grid points, n_{Grid}, per RMS width, σ, in each direction. The number of calculations is directly proportional to the number of mesh points; therefore a factor of 2 increase in mesh density in all 3 dimensions results in an $8\times$ increase in field calculation time. For a Gaussian distribution the entire beam is assumed to be defined by the region incorporating $\pm 3\ \sigma$. We would expect a converging result with increasing grid points, with the optimum solution being the one which provides an accurate solution with as few grid points as possible.

To investigate the effect of the mesh layout, there should be significant variation in transverse fields across the beam profile. A larger transverse beam size, σ_r = 150 µm, was chosen for these simulations (all other parameters are listed in Table 4.1). The maximum $E_z(t)$ will often be situated within the beam, and ensuring a grid point is close to the turning point of $E_z(t)$ is important, especially given a linear interpolation is used to apply the field to macroparticles. This can be seen in Figure 4.11, more mesh points give a closer representation of the field shape, and a higher order interpolation would not be required. Using 1 grid point per $\sigma_{x,y,t}$ does not accurately describe the field shape or magnitude, whilst the higher number of grid points only provides increasing accuracy. The same behaviour is seen with the transverse field. The vertical variation in F_y, for a beam on-axis and offset 500 µm from a DLW with a = 1 mm, are shown in Figures 4.12 and 4.13. As with the longitudinal profile, it is clear that more than 1 grid point per $\sigma_{x,y,t}$ is required however the field shape is effectively captured with fewer grid points. The difference between fields with n_{Grid}/σ = 2 and 5 are within 4% and 5% for y_0 = 0 and 500 µm respectively. Using fewer transverse grid points significantly reduces calculation time. For example, for fields accurate to 5%, $n_{Grid}(x, y, t)$ = (2 per σ_x, 2 per σ_y, 3 per σ_t) would be suitable. This reduces the number of grid points by 55% compared to using 3 grid points per $\sigma_{x,y,t}$. The shape of the distributions are accurately depicted by a linear interpolation, further demonstrating the lack of need for a higher-order interpolation. A higher order interpolation would increase computational efficiency if the field strength, but not shape, was accurately calculated with fewer mesh points. However, this is not the case so a linear interpolation with suitably high mesh density is preferable.

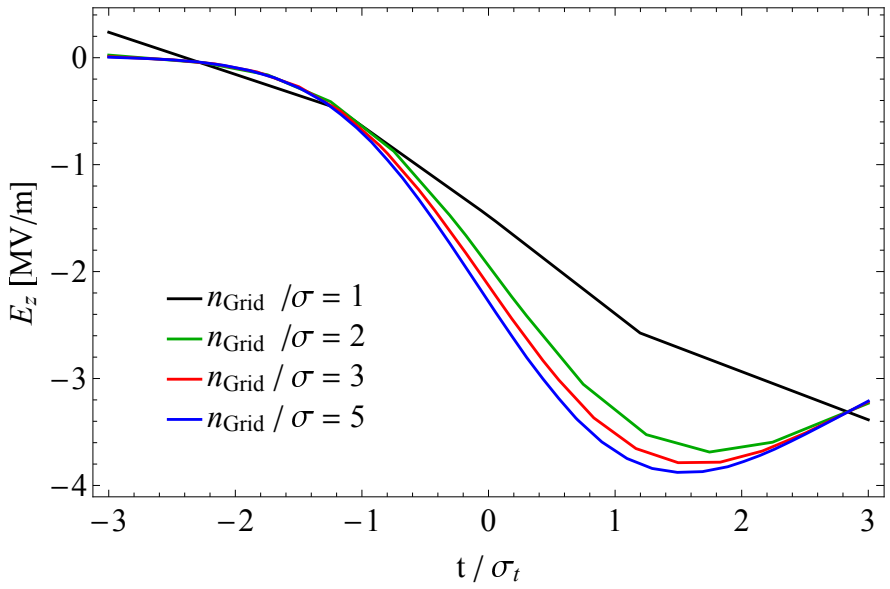

Figure 4.11. Longitudinal field profile calculated using varying mesh point separations, for beams on-axis.

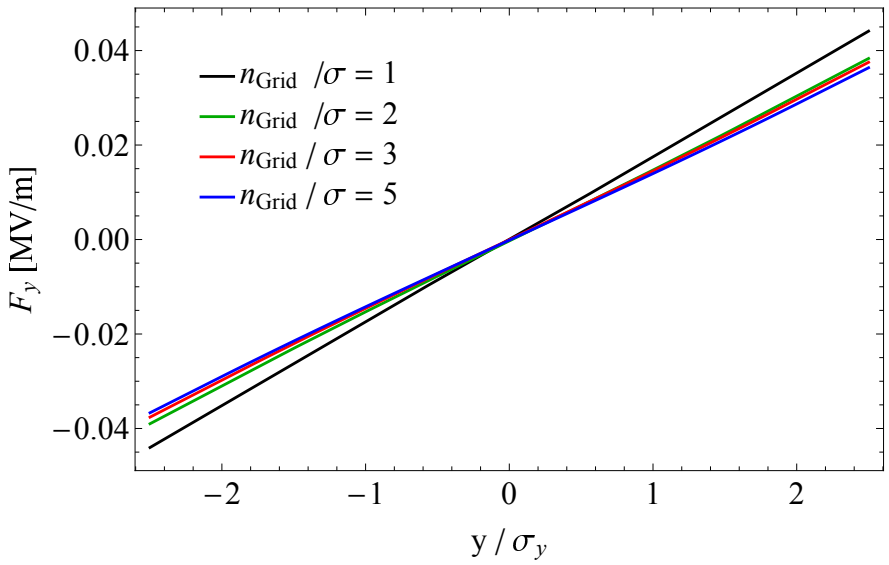

Figure 4.12. Transverse F_y field profile, calculated using varying mesh point separations, for beams on-axis.

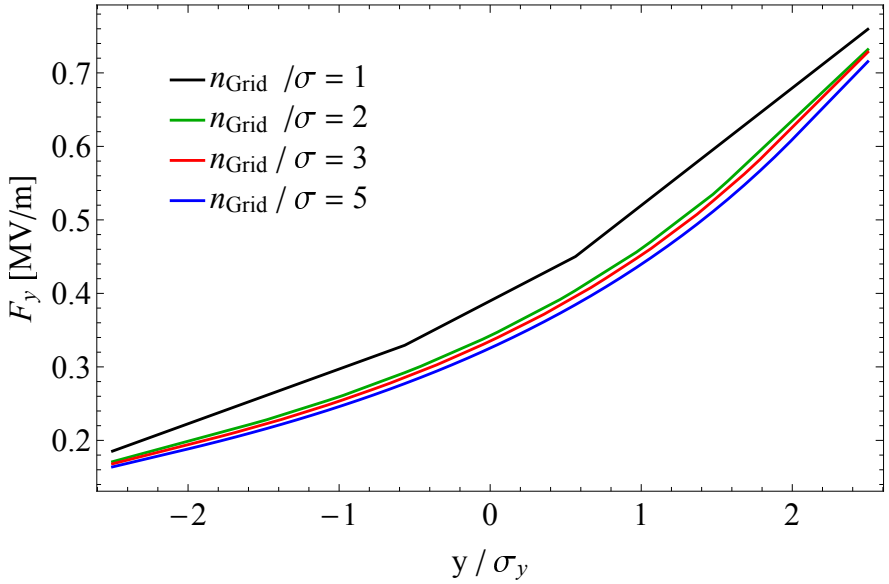

Figure 4.13. Transverse F_y field profile, calculated using varying mesh point separations, for beams with y_0 = 500 µm.

4.4 Mode Composition and Field Convergence

The fields excited by an electron beam in a DLW, as discussed in Chapter 3, can be expressed as a series of longitudinal-section magnetic (LSM) and longitudinal-section electric (LSE) modes. Each mode can be calculated using the transverse operator method. The two wave numbers, corresponding to horizontal and vertical modes, k_x and k_y, excite modes with amplitudes that converge at different rates. The convergence rates are dependent on both the beam parameters and DLW parameters.

Accurately calculating the wakefields excited in all cases requires either determining the number of modes required, or using a large number of modes for all cases. The latter

would add unnecessary computational time to all but the most complex simulations. To calculate the number of modes required, an iterative process is used, as outlined in the mode convergence section of Figure 4.3. The contribution of horizontal and vertical modes converge at different rates, so must be independently considered.

When plotting and discussing mode amplitude, only contributions to the longitudinal field at the centre of the bunch (transversely and longitudinally) are given as an arbitrary reference point. Beam parameters are listed in Table 4.1, with exceptions used to demonstrate variation with respect to a given parameter.

4.4.1 Percentage Tolerance for Convergence

When considering mode convergence, the contribution of modes to the Green's function in all 3 dimensions are considered. The Green's function is calculated, using the `CalcWakeElement` function, at a given point-like source and witness position. Higher order modes are excited closest to the dielectric plate and higher-frequency terms contribute to the wake potential to a greater extent over smaller longitudinal distances. With this in mind, the position of the source particle is chosen to be the mesh point corresponding to the centre of the bunch (transversely) and head of the bunch longitudinally. The witness position is chosen to be the first longitudinal mesh point and maximum vertical and horizontal mesh points. Higher-order modes contribute to a greater extent closer to the dielectric plate, so choosing this position ensures convergence in $W_{x,y}$. Longitudinal detail is required over a time frame equal to the difference in mesh points, therefore this choice of position ensures modes are included with the frequency range required for convergence.

In some cases, mode convergence may not be perfectly smooth with the amplitude of an individual mode weak, leading to premature convergence. To exclude any discrepancy from a single mode, the final 5 modes are compared to the Green's function with all modes included. The Green's functions are for mode convergence purposes solely functions of the number of horizontal and vertical modes, i.e. $W_i(nX, nY)$. The tolerance is calculated for the 3D Green's function using Equation 4.4.

The full mode spectra, across two frequency ranges, is shown in Figure 4.14. It appears by eye that suitable convergence has taken place even with a 50% tolerance. If judging the convergence of modes by eye, the number of modes chosen would be fewer than those needed for 5% tolerance; this would be a significant underestimation of the wakefields. An automated convergence calculation is preferable to avoid this.

Contributions of individual vertical modes, for $nX = 0$, and horizontal modes, for

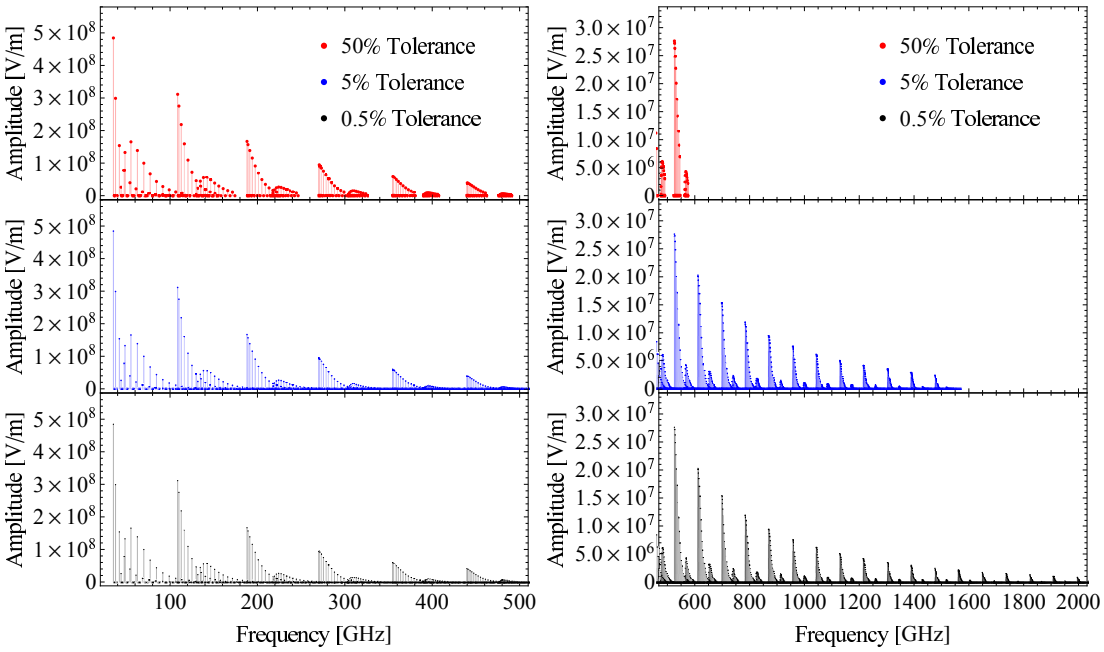

Figure 4.14. Contribution of all LSE and LSM modes, on-axis, with varying levels of convergence. GHz and THz scale frequencies are shown separately given the order of magnitude difference in amplitude.

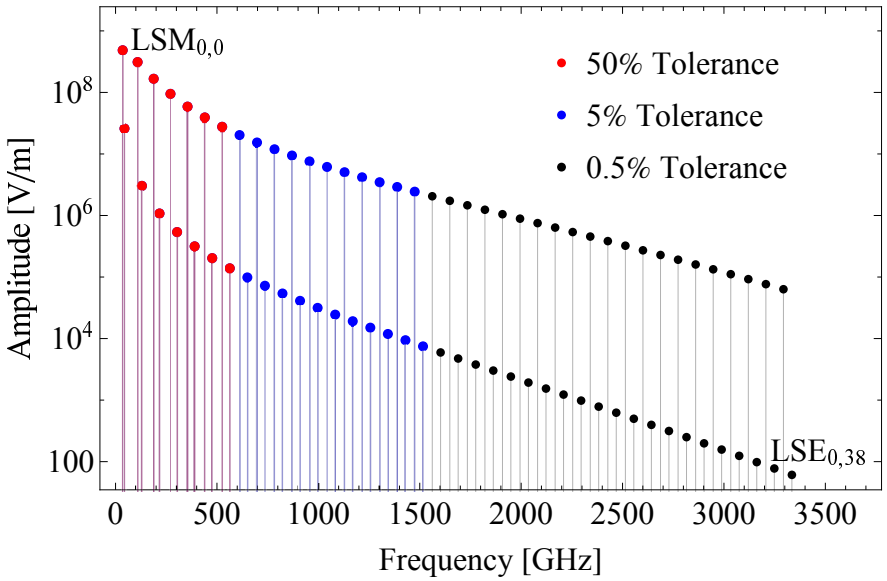

Figure 4.15. Contribution of the $\mathrm{LSE}_{0,nY}$ and $\mathrm{LSM}_{0,nY}$ modes, on-axis, with varying levels of tolerance.

$nY = 0$, are shown in Figures 4.15 and 4.16 respectively. Vertical modes set the overall frequency range with large differences in frequency between mode numbers. Each vertical mode has a corresponding set of horizontal modes, providing a sub-spectra with smaller difference in frequency between modes. For each set of modes, the mode amplitude exponentially decreases with increasing mode number (and frequency).

Given horizontal modes can be seen as sub-structure, including all combinations of $[nX, nY]$ modes leads to the inclusion of modes with very small amplitudes. For example, with the final vertical mode, the mode amplitude of the $nX = 0$ mode is already orders of magnitude lower than the fundamental mode and final nX mode has

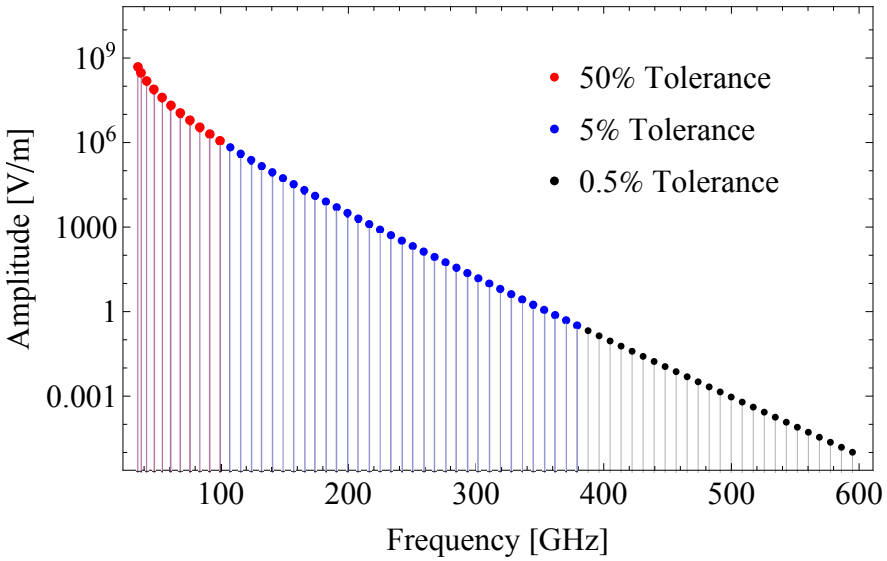

Figure 4.16. Contribution of the $\text{LSM}_{nX,0}$ modes, on-axis, with varying levels of tolerance.

an amplitude orders of magnitude lower than this. Each $[nX, nY]$ pair includes both the corresponding LSE and LSM mode. For a DLW with $w >> a$, as is the case for DLWs in this thesis, LSE modes have amplitudes approximately an order of magnitude lower than the equivalent LSM mode. Therefore, more LSE modes are included than needed for a desired convergence. One way to improve computational efficiency would be to separate the convergence calculation of LSE and LSM modes.

4.4.2 Mode Distribution as a function of DLW Parameters

The number of modes required for a given simulation is dictated by the frequency range and frequency gap of excited modes. The maximum possible frequency of the modes excited by an electron bunch is independent of the DLW, instead depending on the electron bunch longitudinal distribution [124]. The number and composition of modes excited in a DLW determine the shape and characteristics of the wakefields generated. The frequency range from the fundamental mode to the maximum mode is populated by a varying number of modes, and the specific composition of these modes depends on the DLW width, structure gap, and dielectric parameters. The relationship between these parameters and the number of modes necessary for an accurate representation of the wakefields is discussed in the following sections.

DLW Width

For all planar DLWs used in this thesis, the DLW width is much greater than the beam width, i.e. $w >> \sigma_x$. The field excited does not depend on the DLW horizontal width, so long as this condition holds [124]. This is seen for both horizontal and vertical forces,

as shown in Figure 4.17, with the magnitude of each field increasing once $w \sim \sigma_x$.

The DLWs considered in this thesis either fit the condition that $w >> \sigma_x$ or do not have a horizontal boundary (i.e. w can be considered infinite). This condition also holds for previous DWA experiments outlined in Chapter 2. The anomalous behaviour seen for small w is therefore not relevant to typical DWA studies. It is likely that this behaviour is a result of calculating F_x and F_y at a constant position relative to the DLW centre and constant longitudinal position. With $w >> a$, the transverse field is dependent on the transverse position relative to the dielectric gap (x/a and y/a) [116]. As outlined in [116], the field in a DLW with finite width can be considered as a superposition of the field of a DLW with infinite width and from imaginary charges. Therefore, the transverse field will depend on both absolute and relative distance to the metal wall. This is only relevant when w is no longer much greater than both the structure gap and beam width.

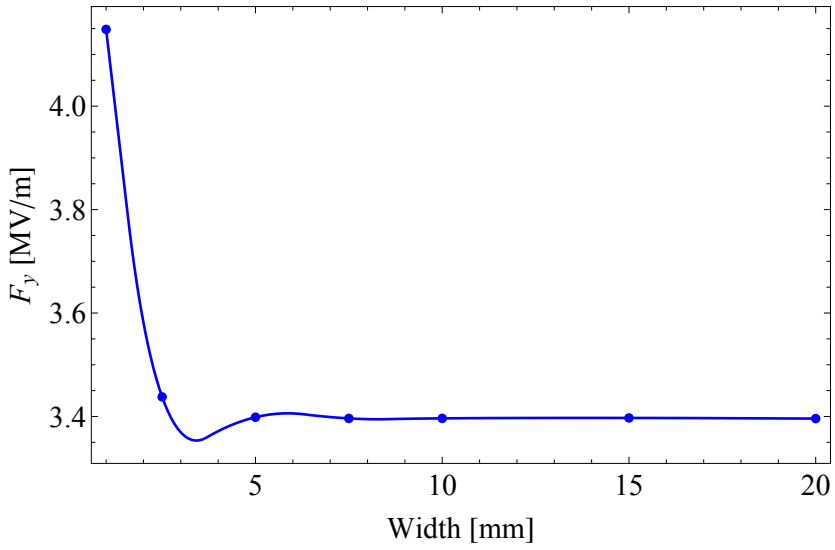

(a) F_y

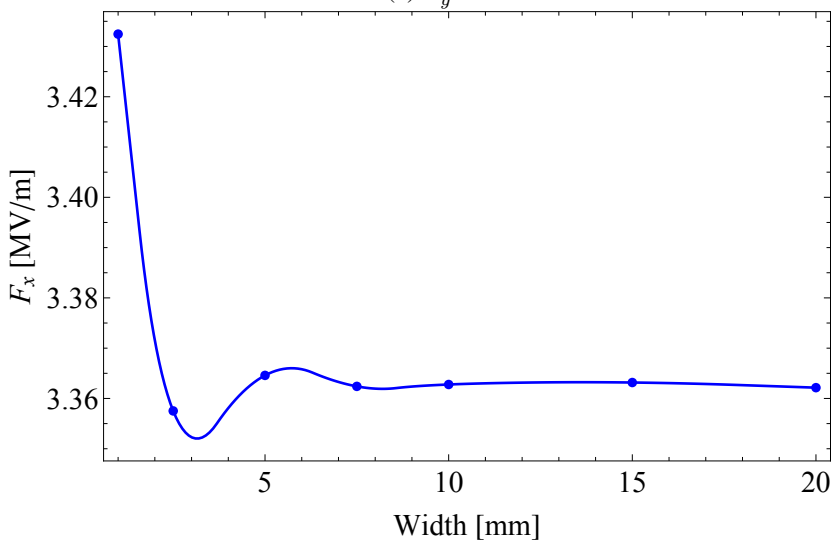

(b) F_x

Figure 4.17. Transverse field, at (x, y, t) = (-2σ_x, +2σ_y, +1σ_t), for varying DLW horizontal width, with $\sigma_x = \sigma_y = 50$ µm.

The frequency gap between each horizontal mode decreases with increasing width, so a wider structure requires an increasing number of modes to accurately model the wakefield. This is seen in Figure 4.18. There is no change in the required number of vertical modes as function of w. To investigate the frequency spectra, it is only worth considering one set of horizontal modes, arbitrarily chosen as the $\mathrm{LSM}_{m,0}$ modes. Comparing the spectra for $w = 5$ and 10 mm, as in Figure 4.19, the frequency range is the same. The varying amplitudes are due to the number of modes excited. The total field strength is the same from the summation of these modes (Figure 4.17), given that twice the number of modes are excited with w = 10 mm, the respective amplitude of each mode must be lower.

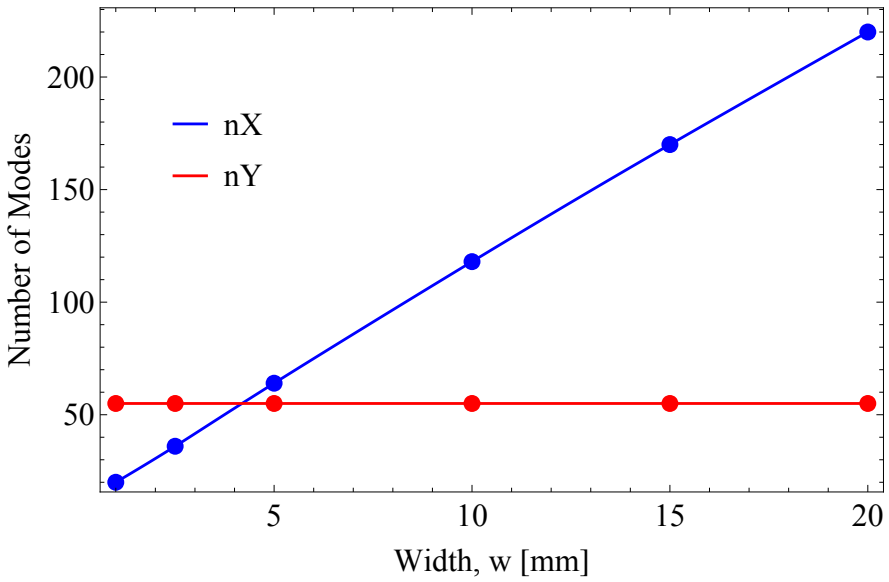

Figure 4.18. Total number of nX and nY modes required for convergence to 1% with varying DLW width.

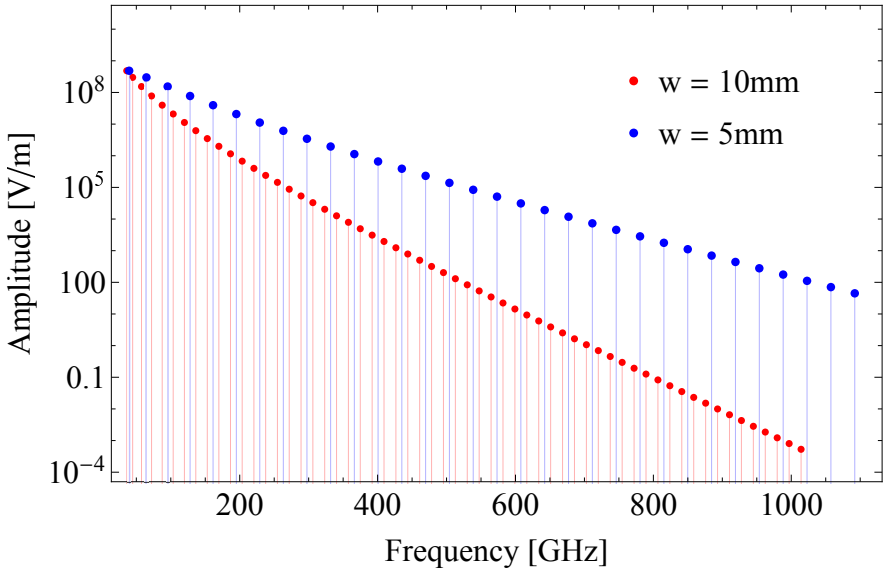

Figure 4.19. Contribution of $\mathrm{LSE}_{m,0}$ modes, on-axis, for DLW width of 5 and 10 mm.

Dielectric Thickness

As discussed in Section 3.2.5, the frequency of the wake potential scales with the dielectric thickness. Therefore, in a similar manner to the structure width, the number of nY modes required to model the wakefields accurately will increase with dielectric plate thickness. The horizontal size of the DLW is unchanged so the number of nX modes are constant. The number of modes required for convergence to 1% follows this expectation, and shown in Figure 4.20.

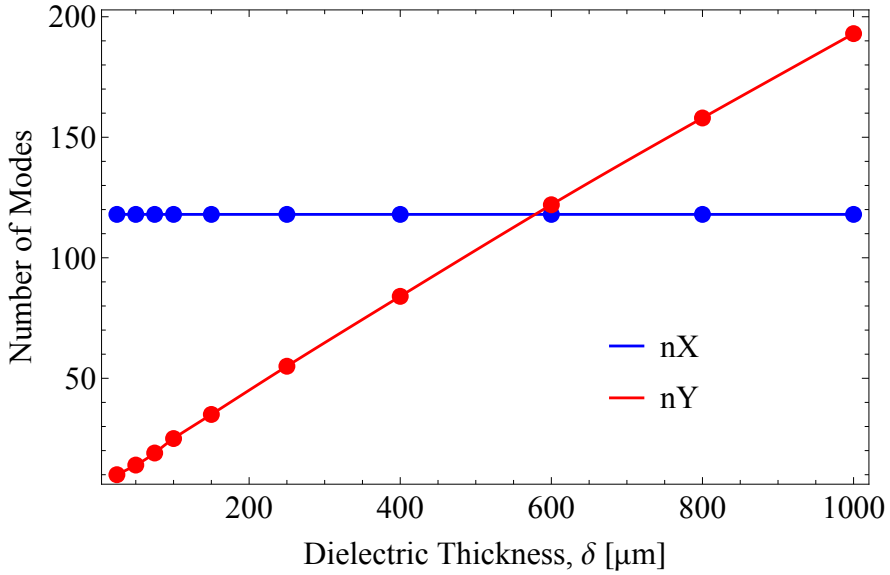

Figure 4.20. Total number of nX and nY modes required for convergence to 1% tolerance with varying dielectric thickness.

The frequency of vertical modes are calculated by solving the dispersion equation in Equation 3.42. The argument given for changing structure width (in the case $w_x \gg \sigma_x$), that the field remains constant with changing width, does not hold for changing dielectric thickness. Unlike DLW width, the field magnitude does depend on dielectric thickness, given that in most cases $a \sim \sigma_y$. The mode distribution shown in Figure 4.21 for two values of δ does not show changing mode amplitude with dielectric thickness. The same frequency range is excited in both cases, requiring more modes for a thicker dielectric. However, the mode amplitude of overlapping modes does not changing so, for these two values of δ the field strength increases with dielectric thickness. This relationship does not generalise since the mode composition and amplitude of each mode is a function of both a and δ.

4.5 Benchmarking of DiWaCAT against CST

CST is a commercially available PIC code [141], commonly used for DLW simulations. CST has been validated against DWA experimental results in multiple publications (such

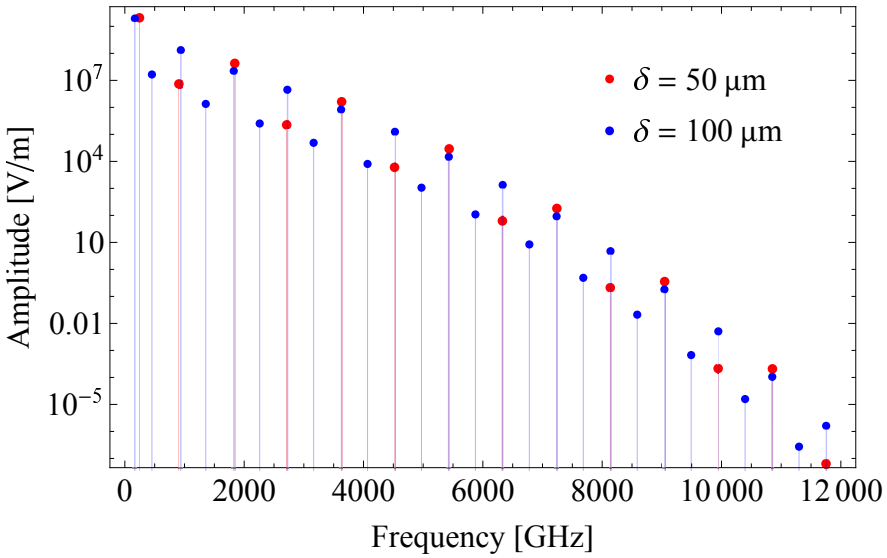

Figure 4.21. Contribution of $\mathrm{LSM}_{0,n}$ modes, on-axis, for a dielectric thickness of 50 and 100 µm.

as in [56] and [142]), and is widely used for simulation studies, so can be assumed to accurately calculate the wakefields excited within DLWs. The transverse operator method, used to calculate the wakefield in DiWaCAT, has been validated against CST for a single case in [119], however a comprehensive comparison has not been published to the author's knowledge. The transverse operator method has been benchmarked against another widely used commercial code, VSim [143], the details of which are in [102].

Simulations with CST required a dedicated high-performance desktop with GPU cores allocated to CST simulations. The use of GPU acceleration limits the boundary conditions which can be used in the CST solver. Namely, the DLW boundaries were assumed to be perfect electrical conductors. This did not significantly impact the physics simulated for this benchmarking study as the same assumption is made within DiWaCAT. CST simulations took multiple hours to complete. In contrast, DiWaCAT simulations took ∼0.5 hours on a personal laptop running in serial on a single CPU core. Due to the different architecture (GPU and CPU), a direct comparison of core hour time and simulation efficiency was not made. The parameters for these simulations are listed in Table 4.2.

Parameter	
Beam Momentum [MeV/c]	35
Total Charge [pC]	100
Beam Width, $\sigma_{x,y}$ [µm]	150, 300
RMS Bunch Length, σ_t [fs]	300, 800
Beam Emittance, ϵ_n [mm mrad]	5
DLW Half-Gap, a [µm]	700
Dielectric Thickness, δ [µm]	200
Dielectric Permitivity, ϵ	4
DLW Width, w [mm]	20

Table 4.2. Beam and DLW parameters chosen for CST and DiWaCAT comparisons.

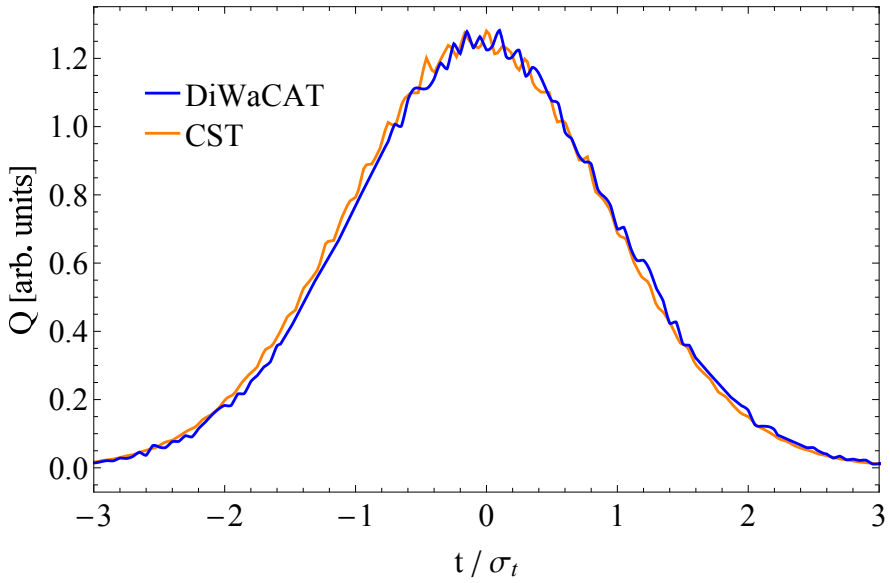

Figure 4.22. Longitudinal macroparticle distributions for particle beams simulated using CST and DiWaCAT.

The mesh used in CST and DiWaCAT were not equal. To contain the DLW boundaries within the CST simulation window and avoid excessively long simulation times, the number of mesh points containing the beam is limited. Transversely the mesh density in CST and DiWaCAT was 1 per $\sigma_{x,y}$ and 3 per $\sigma_{x,y}$, respectively. Given the lower mesh density within the bunch, and different methods used to calculate each field, consistency is presumed when agreement is given to 5%.

A number of test cases were chosen to compare the two codes:

- Test #1: Beam centred on-axis in the DLW, $y_0 = 0$. Beams were simulated with two beam sizes, σ_r = 150 and 300 µm.
- Test #2: Beam offset from axis, with y_0 = 200 µm.
- Test #3: Changing beam offset

These are all for Gaussian bunches with two RMS bunch lengths, σ_t = 300 and 800 fs. When using CST, simulations tend to contain two phases: an initialisation stage followed by a phase with stable fields not affected by longitudinal DLW boundaries. Fields were extracted at the later steady state stage. DiWaCAT simulations do not contain a transient phase, fields calculated do not consider any boundary effects at the DLW entrance/exit. With a CST simulation, the charge distribution is defined over the entire 3D simulation window, whereas with DiWaCAT the charge distribution defines the simulation window. Therefore, the first step for comparing simulations is to ensure the charge distributions are aligned as shown in Figure 4.22.

The fields calculated match for all test cases, with a selection of results given here.

Fields are plotted with 5% regions to test consistency of results; the region containing 5% in both x and y-axes. In each case, the longitudinal field, E_z, is given on-axis and transverse field, F_y, at the position $\Delta y = +1\sigma_y$. Results for Test #1 are shown in Figure 4.23. Consistent results are seen for the two beam widths, and for a beam on-axis both transverse field magnitude and the variation in transverse fields are consistent. In Figure 4.23(d), non-linearity is seen in the transverse variation in F_y using DiWaCAT which are not seen for CST. This can be explained by the lower mesh density used in CST; the transverse field variation is plotted from 4 transverse points with CST and 12 with DiWaCAT allowing for more detail. The inclusion of the entire DLW transverse cross-section means CST simulations do not suffer from the field shape issues at the beam edge seen in Figure 4.12 for 1 mesh point per $\sigma_{x,y}$ in DiWaCAT. The small variation in F_y can therefore be accounted for and the fields still assumed consistent.

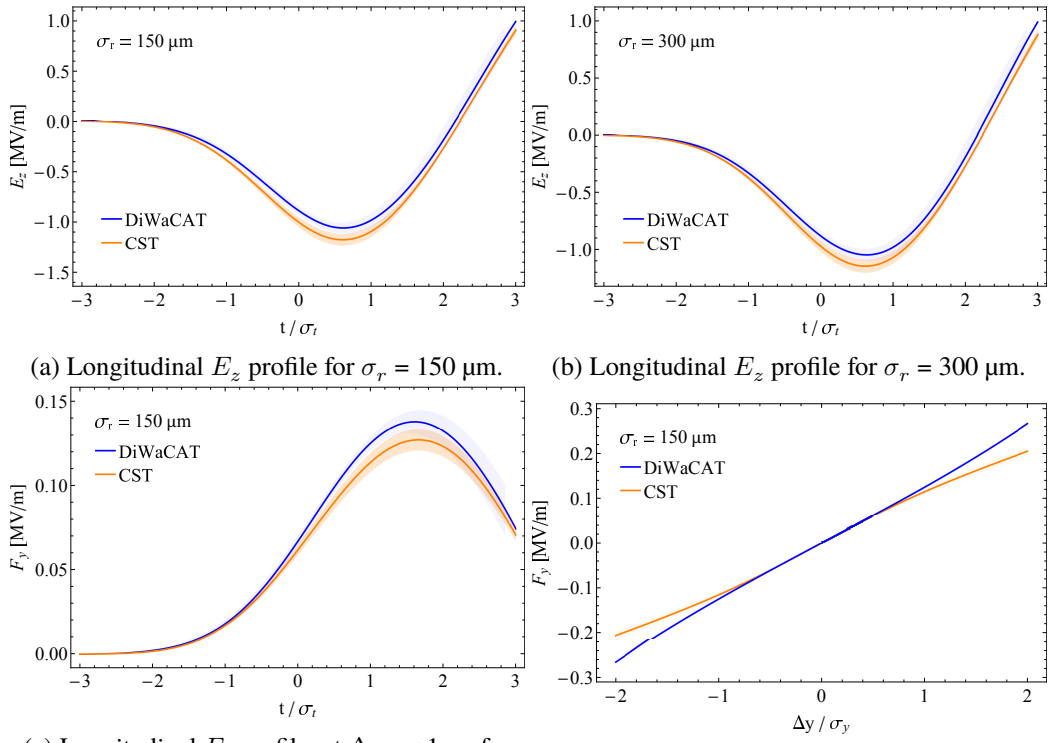

(a) Longitudinal E_z profile for σ_r = 150 µm.

(b) Longitudinal E_z profile for σ_r = 300 µm.

(c) Longitudinal F_y profile, at $\Delta y = +1\sigma_y$, for σ_r = 150 µm.

(d) Vertical F_y profile for σ_r = 150 µm.

Figure 4.23. Comparison of fields calculated for beams on-axis calculated using CST and DiWaCAT. Simulations are for Gaussian beams with σ_t = 800 fs, and two beam widths.

Results for Test #2 - bunches offset from axis - are shown in Figure 4.24. The transverse fields are consistent for shorter and longer bunches. The variation in F_y against vertical position (Figure 4.24(d)) is greater than for the beam on-axis. Variation is seen closer to the dielectric boundary. Non-linear field variation requires an increased mesh density so, as with the beam on-axis, we can assume that the likely reason for this inconsistency is the mesh layout in CST. The transverse fields across the range $\Delta y = \pm 1\sigma_y$ are consistent.

The transverse variation in fields are consistent between the codes for all cases across

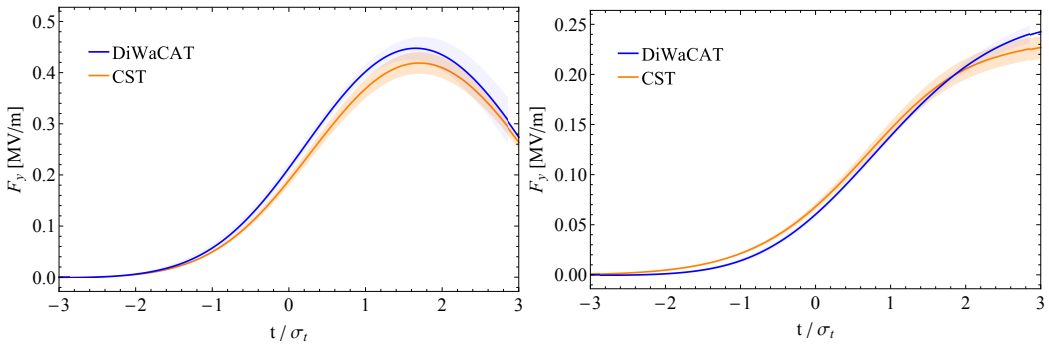

(a) Longitudinal F_y profile, for the beam centre, with σ_t = 800 fs.

(b) Longitudinal F_y profile, for the beam centre, with σ_t = 300 fs.

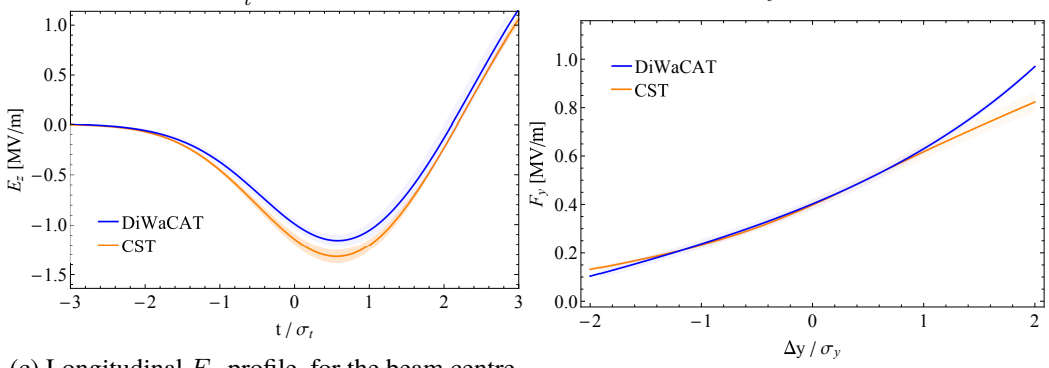

(c) Longitudinal E_z profile, for the beam centre, with σ_t = 800 fs.

(d) Vertical F_y profile with σ_t = 800 fs.

Figure 4.24. Comparison of fields calculated for beams with y_0 = 200 µm, calculated using CST and DiWaCAT. Simulations are for Gaussian beams with σ_t = 800 and 300 fs.

the range $\Delta y = \pm 1\sigma_y$. This is true for varying offset, i.e. Test #3, as shown in Figure 4.25. Almost exact matching are seen across this transverse range, with similar results at varying longitudinal positions. As in previous cases, a higher degree of agreement is seen with σ_t = 800 fs compared to 300 fs, however fields in both cases match to 5% tolerance.

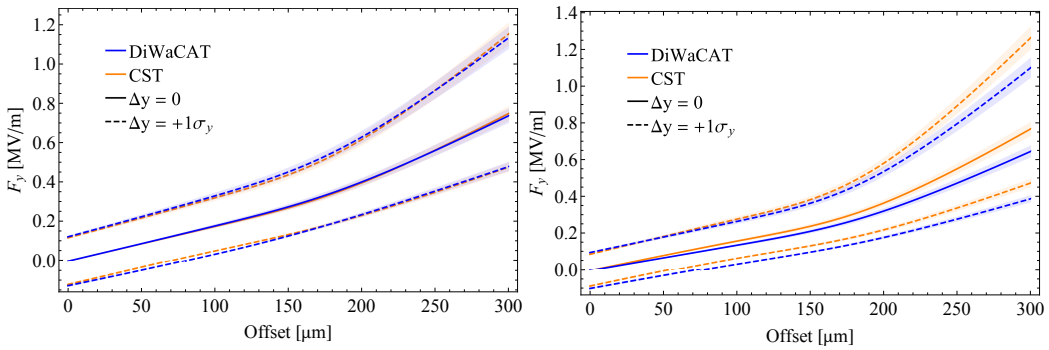

(a) σ_t = 800 fs.

(b) σ_t = 300 fs.

Figure 4.25. F_y at the beam centre and $\Delta y = \pm 1\sigma_y$ for varying beam offset, y_0.

Overall, we can conclude that the results given by DiWaCAT and CST are sufficiently consistent. DiWaCAT gives an accurate representation of simulated wakefields. Deviations between the codes in fields are seen at beam edges and likely explained by differences in mesh layout for these simulations. The reduction in simulation time with

DiWaCAT required to match the simulation detail of CST also provides a clear example of the advantage of using specialised code.

4.6 Extensions and Future Applications of DiWaCAT

As previously mentioned DiWaCAT has been specifically designed for integration with other accelerator codes. Input and output beam file formats have been designed to integrate with SimFrame [134], so can therefore integrate with other accelerator codes such as ASTRA, Elegant, GPT, or CSRTrack. This functionality is not shown in this thesis, however has direct applications for DLW based beam manipulation devices (e.g. the DLW dechirper to be installed on CLARA [103]) and beam diagnostics (such as DLW streakers discussed later in Chapter 8). This functionality also allows for detailed studies of the feasibility of dielectric wakefield acceleration and simulated DWA experiments. Without S2E simulations, long-distance simulations of DWA are often limited by the use of idealised beams. Simulations of a complete accelerator beamline should also include methods to model instabilities which are seen in real facilities. Modelling the effect of these instabilities and methods generate drive/witness beam pairs are required in future DWA studies.

4.7 Summary

In summary, a specialised simulation code has been developed for relativistic beams inside dielectric lined waveguides. With this, the 3D fields excited can be extracted, and beam dynamics within the DLW is tracked. Integration of this code with other accelerator software has been explained, with the specific context of the CLARA online model given as an example. This integration can be generalised, allowing for S2E simulations of DWA experiments and studies with realistic beam parameters. S2E simulations of DWA experiments allows for the optimisation of experiments with the diagnostics and beam optics available at a particular facility. Comparisons of experimental data with detailed simulations also allows for more detailed conclusions to be made and the effects of specific field elements isolated.

The simulation parameters for accurate field and beam dynamics simulations have been studied. The methods for field interpolation, and particle pushing algorithms have been studied to ensure accurate methods were chosen. The fields with varying beam and structure parameters have been explored and the modal composition of the wakefields excited has been explained. The number of modes required for each simulation has been optimised whilst minimising simulation time, ensuring that the frequency range

and field profiles are accurately calculated. DiWaCAT has been benchmarked against a commercially available code, CST, with agreement between the two shown across a number of test cases. It has been shown that DiWaCAT accurately calculates the theoretical wakefields excited in a DLW, so is an appropriate method for simulations throughout this thesis. Benchmarking with experimental results is required to show the applicability of theoretical expectations; such benchmarking is detailed in Chapter 6.

Future work will be focused on a full integration of DiWaCAT with other simulation codes, to produce a complete DLW simulation package that can be utilised for a variety of applications, for example for design of passive beam manipulation in a Free Electron Laser, or in High Energy Physics collider design.

Acknowledgement

The author would like to thank Dr. Andrew Vint for performing simulations using CST to compare with DiWaCAT results. Thanks are also given to Dr. Stanislav Baturin of ITMO University, for kindly providing our research group with a C++ function to calculate the Green's function for a planar DLW, which became the foundation for the DiWaCAT code.

Chapter 5

Experimental Setup at CLARA

5.1 Overview of the CLARA/VELA Beamline

The work presented in Chapter 6 describes experimental results obtained using the Compact Linear Accelerator for Research and Applications (CLARA) at Daresbury Laboratory (see Figure 5.1). At the time of experiments, the CLARA Front End (CLARA FE) had the capability to accelerate electrons up to a maximum achieved 50 MeV/c momentum for injection into the VELA (Versatile Electron Linear Accelerator) beamline [144].

During DWA experiments, the CLARA FE contained a 3 GHz RF gun, 2 m long linac, and beam optics before injection into the VELA beamline. The photoinjector used for the CLARA FE was a 2.5 cell S-band structure operating at 10 Hz with a copper photocathode. At the exit from the injector, the electron beam reached a momentum of 5 MeV/c. The copper cathode was illuminated at an angle of 4° by the third harmonic of an 800 nm infared laser light (266 nm) via an aluminium coated mirror. The laser pulse duration on the cathode was variable within 2-8 ps FWHM. A 2 m long S-band linac, after the injector, accelerated electrons to the final momenta (set by varying the RF power supplied to the linac and the beam off-crest phases). Beams were injected into the VELA beamline via a double-bend achromate (dog-leg) where longitudinal compression took place [144]. The combination of the CLARA FE and VELA beamlines allowed for the transportation of beams with varying parameters to Beam Area 1 (BA1).

Design and operational beam parameters delivered to BA1 during the experiments described in this thesis are listed in Table 5.1. Operational parameters were chosen to prioritise a reproducible beam over multiple days of experimental time. At the time of our experiments, the available bunch charge was reduced due to combined effects of reduction in the cathode quantum efficiency and photoinjector laser beam transport efficiency [144]. A conservative value of 100 pC bunch charge was chosen for setting up the machine. A maximum momentum of 50 MeV/c could be achieved, however using 35.5 MeV/c allowed for a wider range of off-crest accelerating phases (and therefore

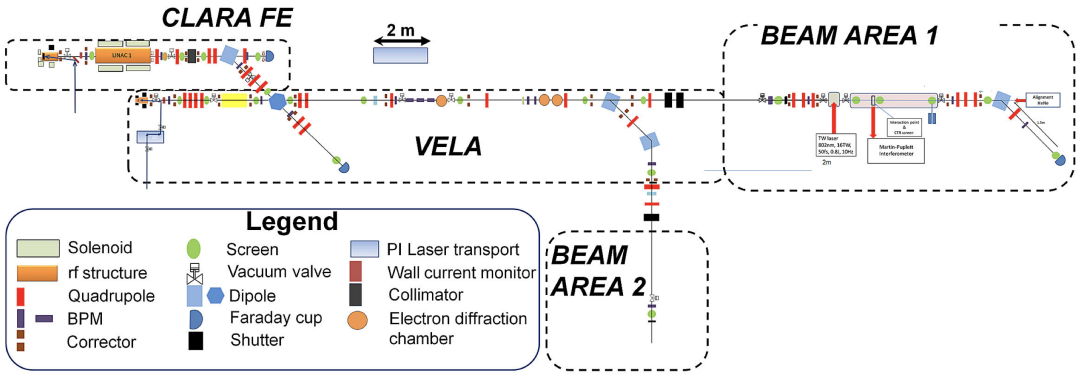

Figure 5.1. Schematic diagram of the CLARA/VELA beamline. A more detailed schematic of Beam Area 1 is given in Figure 5.2

Parameter	Design Value	Operated Value
Bunch Charge [pC]	250	100
Momentum [MeV/c]	50	35.5
RMS Bunch Length [fs]	>200	300-5000
Normalised Emittance $\epsilon_{x,y}$ [mm mrad]	~2	~5
Horizontal RMS Beam Size σ_x [µm]	Minimum <100	100 - 1500
Vertical RMS Beam Size σ_y [µm]	Minimum <100	100 - 300
RMS Momentum Spread [%]	Variable up to 5	0.5-2
Bunch Repitition Rate [Hz]	10	10

Table 5.1. Beam parameters in Beam Area 1 as designed and delivered [144].

bunch lengths) to be used while keeping momentum constant. Keeping a constant momentum removed the need to adjust the transverse beam optics whilst changing the linac off-crest phase.

The amount of compression through the dog-leg set the bunch length delivered to BA1. Varying the linac phase, and therefore the energy chirp, varies the compression ratio. The bunch compression to second-order is governed by the following expression

$$\delta z_f = \delta z_i + R_{56}\frac{\delta p_z}{p_z} + T_{566}\left(\frac{\delta p_z}{p}\right)^2, \tag{5.1}$$

where δz_i is the initial longitudinal position of the electron (with the mean longitudinal position $\delta z_i = 0$), δz_f is the final longitudinal position, p is the average momentum, δp_z is the difference from the mean electron momentum, and R_{56} and T_{566} are the linear and non-linear longitudinal dispersion components of the dogleg section [145]. The dog-leg has a fixed $R_{56} = -78$ mm and requires positive energy chirps for bunch compression (i.e. higher energy at the head). In addition, there is a large non-linear component ($T_{566} = -2.794$ m) which adds curvature to the longitudinal phase space of beams injected into VELA. These values are determined by the lattice of the dogleg through simulation [144].

The chosen maximum and minimum compression used during DWA experiments were given by linac off-crest phases of -6° and 0° corresponding to RMS bunch lengths of 370

and 800 fs respectively. During DWA experiments the bunch length and profile were estimated by wakefield streaking [16][108] and the previously reported relationship between bunch length and off-crest phase at CLARA [146]. Details of this are given in Section 6.3.1.

5.1.1 Beam-Area 1 Description

DWA experiments were conducted in BA1, a schematic of which is shown in Figure 5.2. BA1 contained a 2.3 m long experimental chamber (between vacuum valves VALV-04 and VALV-05) which could house multiple experimental targets and diagnostics. The quadrupole triplet (Q-01 to Q-03) was used to set the horizontal and vertical envelopes through the chamber and the required beam size at the interaction point (IP). Upstream from the experimental chamber (between VALV-02 and and VALV-04), a TW laser light box was located for other user experiments. The laser box increased the distance from quadrupole magnets to the IP (increasing the minimum beam size at the IP). The beam pipe at the light box (with 10 mm inner diameter and 100 mm length), required for differential pumping for LWFA related gas jet experiments, limited the beam envelopes that could be set through BA1 without beam losses.

For one set of experiments, beams were required with various horizontal widths (up to 1.5 mm RMS) and an approximately constant vertical width. This was difficult to achieve with BA1 quads alone and therefore also required adjustment of quadrupoles in the VELA beamline.

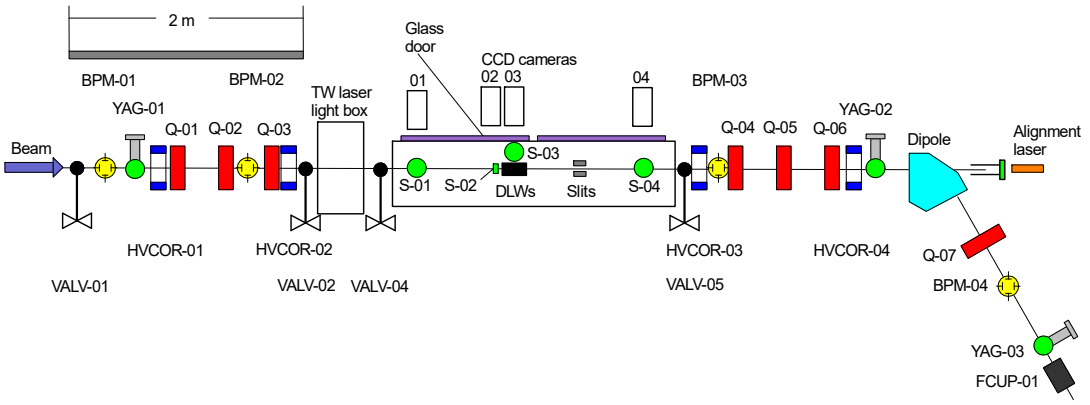

Figure 5.2. Schematic of the beamline within BA1. Red boxes are quadrupole magnets, dark blue are trajectory correctors, light blue is the dipole magnet for the spectrometer, and green circles are YAG screens.

Downstream from the experimental chamber, a quadrupole triplet (Q-04 to Q-06) was used to minimise the horizontal β_x function at the energy spectrometer (YAG-03) and focus beams with large transverse sizes onto YAG-02. For beams with a large momentum spread, Q-07 was used to control the horizontal dispersion, D_x. The size of the horizontal

spectra at YAG-03 is

$$\Delta x = \frac{D_x \Delta p}{p}, \tag{5.2}$$

where Δp is the full momentum spread and p is the average momentum [118]. In the case of beams with a large momentum spread, the horizontal spectra can extend beyond the size of the screen. Increasing the focusing strength of Q-07 reduces D_x and the spectra width. Conversely, to increase the momentum resolution for a beam with small momentum spread, Q-07 current is reduced to increase D_x and the spectra width. The dependence of horizontal dispersion on Q-07 current is shown in Figure 5.3. An iterative process of minimising β_x using the quadrupole triplet and setting the dispersion allowed for accurate measurements of the energy spectra. The resolution of energy measurements is estimated by the minimal resolvable detail in the measured YAG-03 spectra. From Equation 5.2, the minimum spatial detail Δx relates to the momentum resolution Δp which during operation was approximately 20 keV. A Faraday cup after YAG-03 (with this YAG screen removed from the beam path) was used to measure the charge transported through BA1 and monitor beam losses within DLWs.

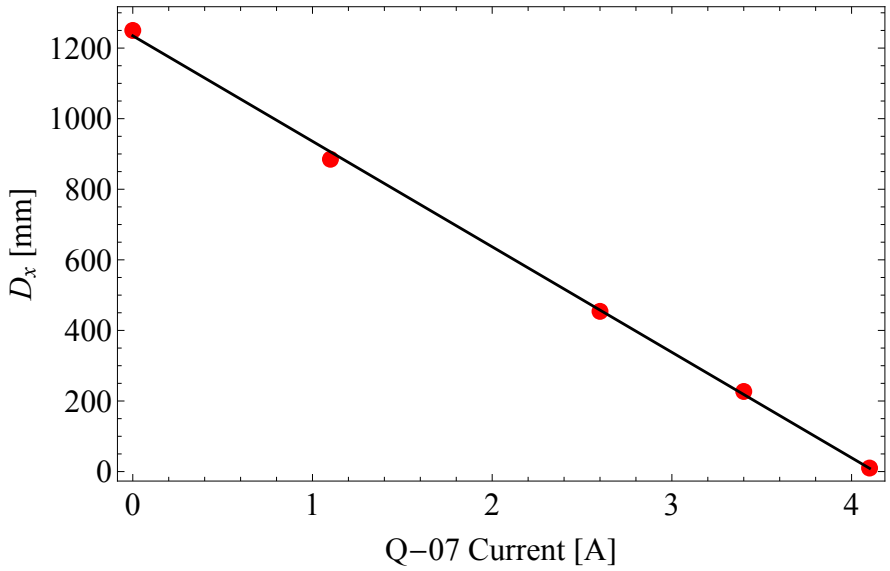

Figure 5.3. Horizontal dispersion D_x at YAG-03 as a function of Q-07 quadrupole current, I. The line of best fit is $D_x = 1240 - 300I$.

The beam trajectory within BA1 was adjusted using two correctors upstream of the experimental chamber (HVCOR-01 and HVCOR-02) and two downstream (HVCOR-03 and HVCOR-04). The first pair set the beam trajectory through the chamber on the beamline axis, and the second pair ensured the beam was centred at the dipole magnet entrance.

5.2 BA1 Experimental Chamber and Bunch Diagnostics

A photograph of the BA1 experimental chamber with DWA structures installed is shown in Figure 5.4. Within the chamber, 3 circular YAG screens (with 30 mm diameter, and 300 µm thickness) were installed to measure the transverse profile of the beam (S-01, S-03, and S-04 in Figure 5.2). A screen with the same parameters was installed at YAG-02; the increased distance from the IP allowed for measurements of the beam envelope (with the quadrupole triplet Q-04 to Q-06 turned off). With the quadrupole-triplet turned on, large beam sizes at YAG-02 could be focused to the size of the screen for transverse profile measurements. Reticules included in the mounting structures (with assembly as in Figure 5.5) of each YAG in the chamber were used to calibrate camera images. The required field of view (i.e. camera zoom) and therefore calibration was individually set for each YAG-screen. For example at the IP small beam sizes down to 100 µm and below were required so the field of view was smaller than on up/downstream YAGs. The calibration factor and distance of each YAG screen to the IP is given in Table 5.2. All screens and other components within the chamber were mounted on motorised translation stages to enable full withdrawal from the beam path. Alignment of components to the beamline axis was performed with an alignment laser positioned behind the energy spectrometer dipole with the glass window at the end of the beam pipe (Figure 5.2). The gate valve VALV-05 was also equipped with a glass window thus enabling the alignment to be performed in-air.

The beam envelope through BA1 was estimated by measuring the beam sizes on each

Camera	Calibration Factor [µm/pix.]	Distance to IP [m]
YAG-01	51	3.20
S-01	30	0.84
S-03	5.65	0
S-04	33	1.05
YAG-02	32	3.10
YAG-03	21	5.20

Table 5.2. Calibration in µm per pixel for each YAG screen camera in BA1 and distance to the IP.

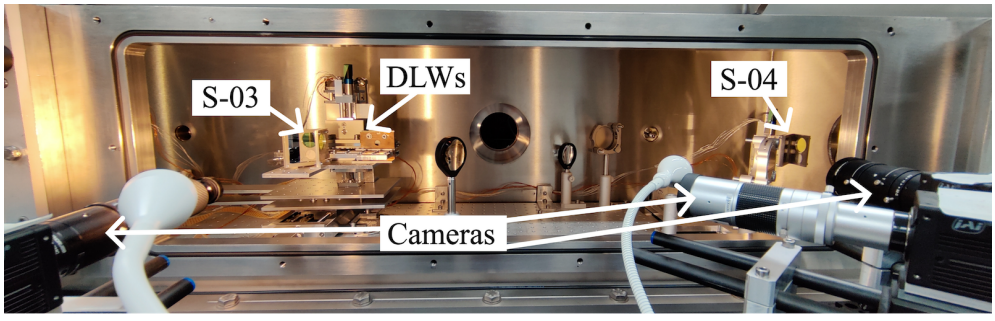

Figure 5.4. Photograph of the BA1 experimental chamber with the side window open. The beam propagates left to right.

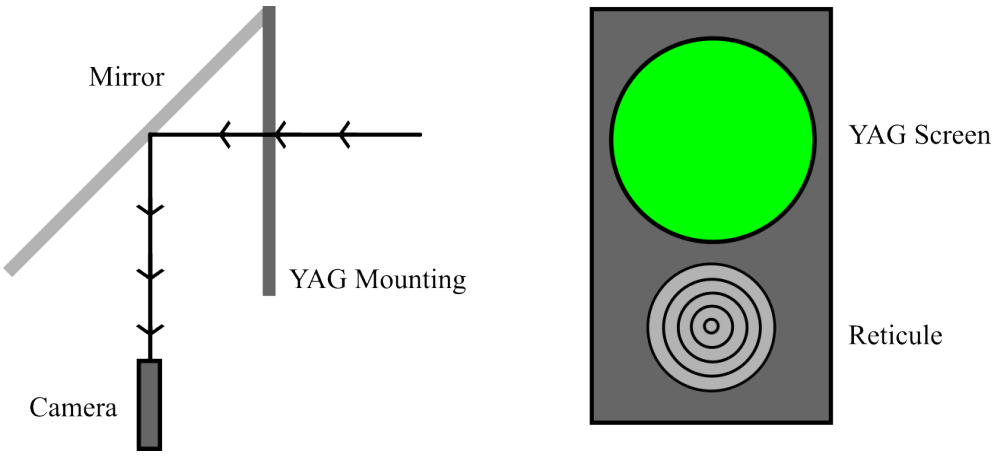

Figure 5.5. Schematic of the YAG setup and mounting system.

YAG screen. Beam envelopes were necessary to determine the beam trajectory into DLW structures and enable accurate comparison of measurements with simulations. In drift space the beam envelope follows

$$\sigma(l) = \sigma_0 \sqrt{1 + \left(\frac{\epsilon(l - L_0)}{\sigma_0^2} \right)^2}, \tag{5.3}$$

where l is the longitudinal position, σ_0 is the beam size at the waist, L_0 is the waist position, and ϵ is the geometric emittance [118]. The envelope fit involves fitting 3 free variables (ϵ, σ_0, and L_0) from 4 measurements (beams sizes at S-01, S-03, S-04, and YAG-02). Positioning of screens was not optimal for envelope measurements, therefore, the resultant fit can only be taken as an estimate of the envelope. The accuracy can be improved by measuring one of the variables, such as emittance. Setting the waist closer to one of the YAG screens, ideally S-03, also improves the accuracy of envelope measurements given σ_0 and L_0 are approximately known in this case. The transverse beam size can be measured from YAG screen images in two ways: using the width from a Gaussian fit of the profile or using the second moment of the distribution. During operation it was found that the beam was not purely Gaussian, instead formed from several smaller beamlets. Each of these beamlets had different beam dynamics through CLARA FE to BA1, thus leading to non-Gaussian, in most cases, transverse distributions. For non-Gaussian profiles, measurement of the second moment of the distribution was the more appropriate method to measure the transverse width. An example of this, for a beam with Gaussian vertical profile and non-Gaussian horizontal profile is shown in Figure 5.6. The horizontal and vertical envelopes for two typical settings (one highly elliptical and one circular examples) are given in Figure 5.7. As these were only ever used for estimating the position of the waist, no error bars are shown and comments on fit quality would not be appropriate.

The beam transverse emittance was measured using a slit-scan method, with horizontal

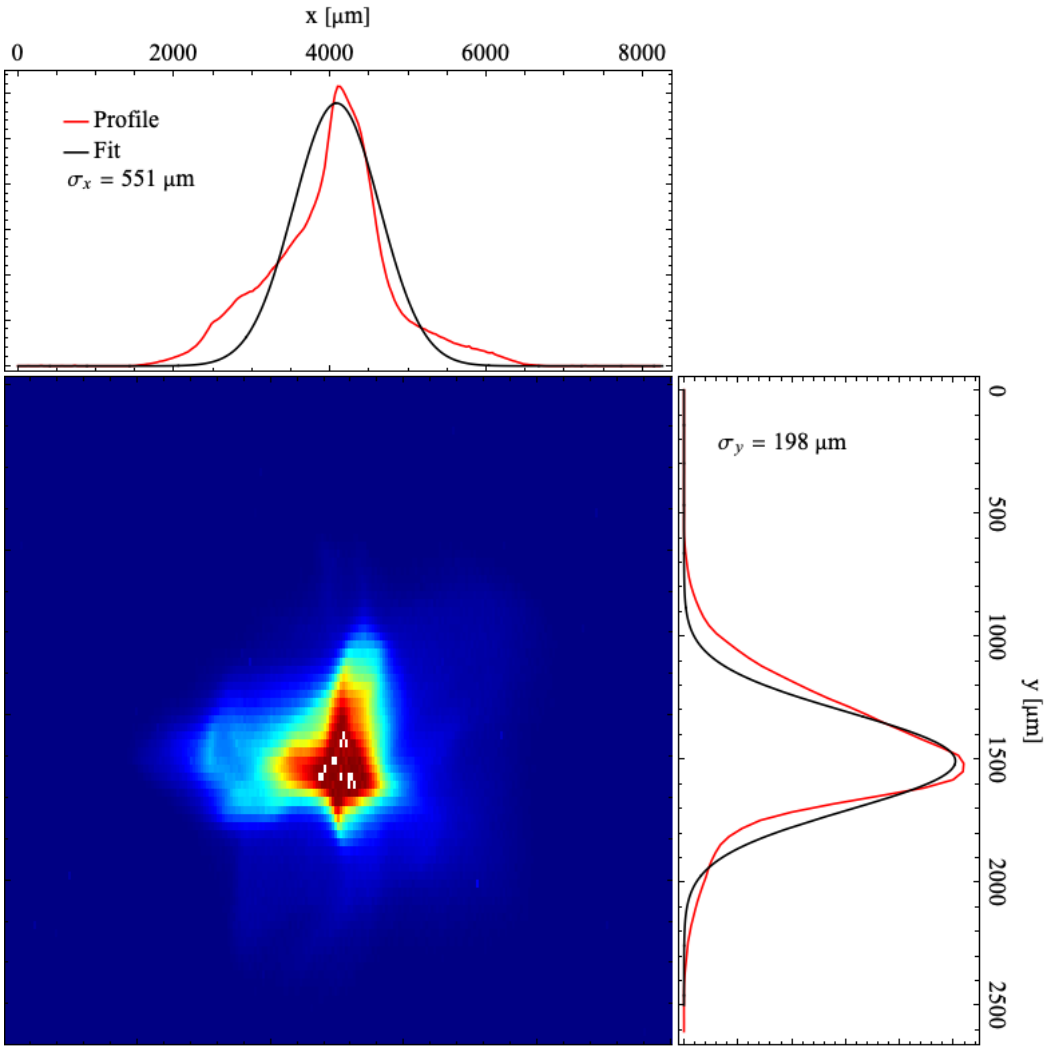

Figure 5.6. Example transverse profile measurement using the YAG-DOWN screen. Image has been rescaled for an aspect ratio of 1. A Gaussian fit was used to measure σ_y whilst the second moment was used for σ_x.

and vertical slits, each of 50 μm width, to measure vertical and horizontal emittance respectively. Shot-to-shot beam position jitter was negligible, allowing for the beam to be characterised by moving a single-slit across the beam profile. Vertical and horizontal slits were positioned within the experimental chamber (between S-03 and S-04 in Figure 5.2), 0.5 m from the IP, and slit beamlets were imaged on YAG-02. To measure horizontal emittance, the vertical slit was moved horizontally across the beam with each resulting beamlet on the downstream screen measured at each slit position as shown in Figure 5.8. The beamlet is highly collimated, with minimal charge in the beamlet, so the size on the downstream screen is dominated by the emittance rather than space charge. Therefore, the measured downstream beamlet horizontal profile is a good estimate of the upstream angular distribution [147], [148]. By combining all beamlet angular distributions, the horizontal phase space of the entire beam can be reconstructed.

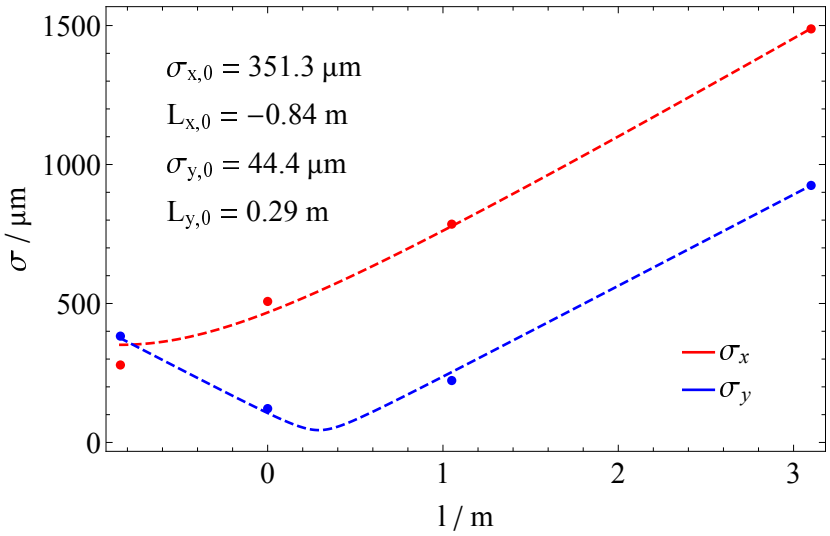

(a) Envelope for a highly elliptical beam.

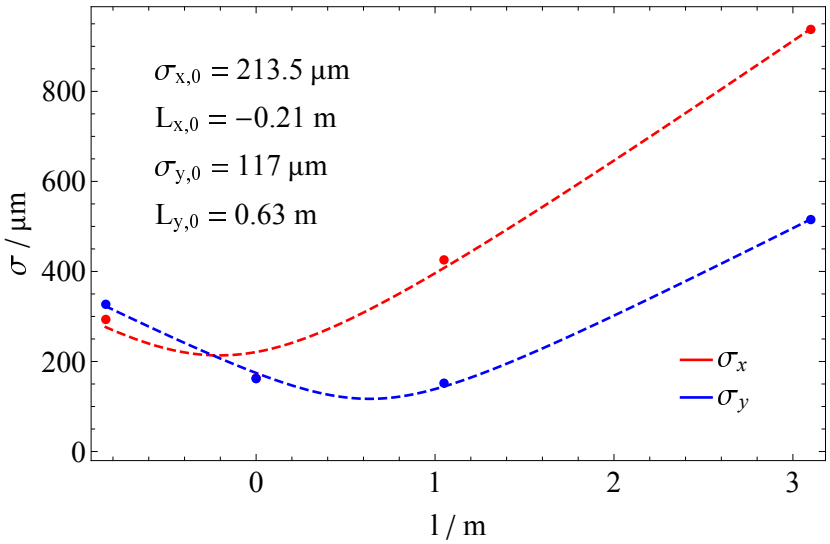

(b) Envelope for an approximately circular beam at the IP.

Figure 5.7. Example fitted transverse envelope using the 4 YAG screens for two example beams.

The total RMS horizontal emittance is given by

$$\epsilon_x = \sqrt{\langle x^2 \rangle \langle x'^2 \rangle - \langle x x' \rangle^2}, \tag{5.4}$$

where x and x' are the position and angle of particles respectively and $\langle\rangle$ represents averaging over all particles. Given a slit of negligible width, dividing the beam into a series of beamlets is a suitable replacement for averaging over individual particles. The charge of each beamlet is proportional to the measured integrated image intensity.

Let denote the total charge/intensity of all N beamlets as Q, q_i is the charge of the i-th beamlet and x_i is the i-th position of the slit. Note that slit positions are usually chosen to avoid overlapping beamlets so Q is less than the total bunch charge. At the downstream screen, each beamlet profile is centred at X_i and has RMS width $\sigma_{x,i}$. Positions x_i and X_i are taken relative to the centroid of each beamlet. The average centroid of all

beamlets is given by $\bar{x}$. Using the distance between the slit and screen, L, the mean and RMS variance in divergence/convergence can be calculated, with

$$x'_i = \frac{X_i - x_i}{L} \tag{5.5}$$

and

$$\sigma_{x',i} = \frac{\sigma_{x,i}}{L}. \tag{5.6}$$

Each term in Equation 5.4 can be calculated with

$$\langle x^2 \rangle = \frac{1}{Q} \sum_i^N q_i (x_i - \bar{x})^2, \tag{5.7}$$

$$\langle x'^2 \rangle = \frac{1}{Q} \sum_i^N q_i [\sigma^2_{x'i} - (x'_i - \bar{x'})^2], \tag{5.8}$$

where $\bar{x'}$ is the correlated beamlet divergence/convergence, and

$$\langle xx' \rangle = \frac{1}{Q} \left(\sum_i^N q_i x_i x'_i \right) - Q \bar{x} \bar{x'}. \tag{5.9}$$

In each equation the sum is over all N beamlets. The vertical emittance is measured in the same manner, using a horizontal slit scan. Full details of the derivation of each term is given in [148]. Images were taken with regularly spaced slit positions, allowing for a semi-automated process:

1. The imaging camera sensitivity was adjusted such that the brightest beamlet image had no saturated pixels.
2. The maximum and minimum slit positions were found by finding the positions at which no beam was measurable above the standard background.
3. An automated script was then used to take images at a set number of slit positions between these two edge points.

5.3 DWA Experimental Setup

For DWA experiments, various DLWs were installed at the IP position. The DLWs (shown and labelled in Figure 5.9) consisted of two circular DLWs and a variable gap planar DLW. The planar DLW is a single section of the CLARA dechirper [103], to be installed in phase two of the CLARA facility. The parameters for each DLW used, with variables as in Figures 3.1 and 3.2 for planar and circular DLWs respectively, are listed

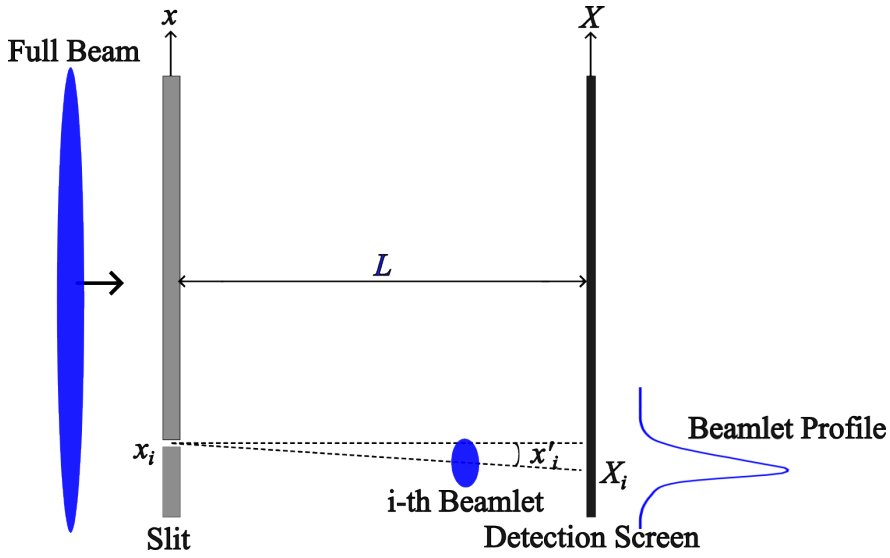

Figure 5.8. Schematic of a single slit measurement. A full slit scan would involve taking an image of each beamlet as the slit is moved across the face of the beam.

in Table 5.3. The smaller circular DLW (#2) was not used for experiments as beam losses could not be prevented. Small YAG-screens (5x5 mm with 300 µm thickness) were glued near the entrance of the circular and planar DLW structures to facilitate approximate centering of the beam on the DLWs entrance. S-03 was positioned in the middle of 200 mm long DLWs thus providing a beam size measurement within the structures and, in combination with the envelope measurements as described above, provides information on beam size variation within the structure.

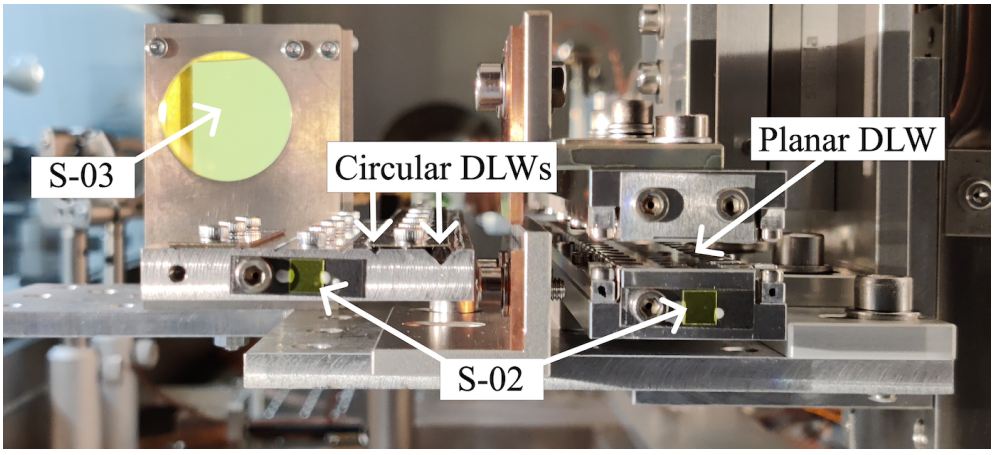

Figure 5.9. Photograph of the DLW structures installed at the interaction point in BA1.

Parameter	Planar DLW	Circular DLW #1	Circular DLW #2
Dielectric Gap/Diameter, $2a$ [µm]	500-4000	2000	900
Dielectric Thickness, δ [µm]	200	200	200
Relative Dielectric Permitivity, ϵ_r	3.75	3.75	3.75
Length [m]	0.2	0.2	0.2
Width [mm]	10	N/A	N/A

Table 5.3. Parameters for DLWs used in BA1 experiments.

All DLW structures were mounted onto a platform, a schematic of which is shown in

Figure 5.10. The entire assembly could be moved transversely using horizontal and vertical motorised remotely controlled translation stages. These stages also ensured that DLW structures could be easily moved out of the beam path. A small stage controlling the gap of the planar DLW was mounted on the vertical stage (enabling gap and beam offset variation). The gap between dielectric plates in the planar DLW could be adjusted with sub-μm precision. Note that the gap was controlled by moving only one (upper) DLW plate. Re-centering the beam therefore required additional vertical movement of the structure (i.e. increasing the gap by x required the structure to be moved down by $x/2$).

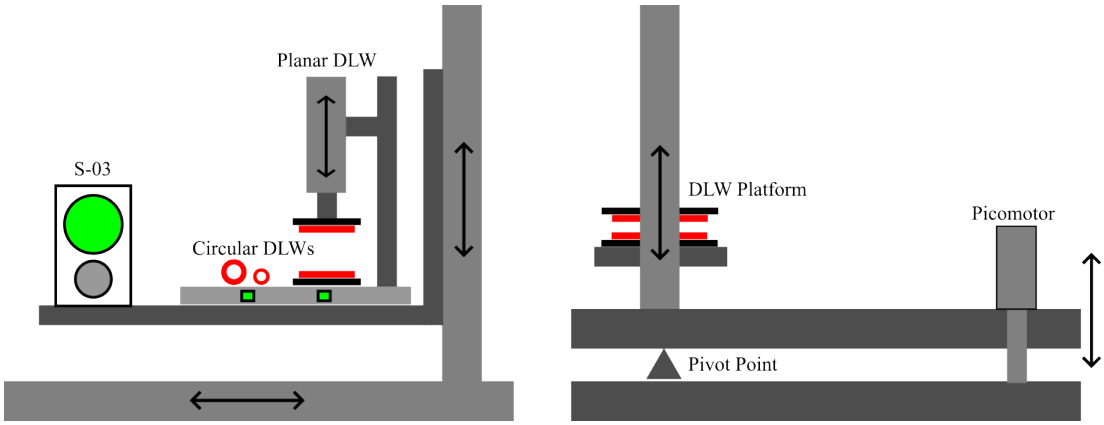

Figure 5.10. Schematic of the DLW stage (left:) at the face of the DLW entrance and (right:) with the electron beam travelling left to right. Dielectric structures are represented in red, YAGs in green, and arrows represent available stage motion.

To compensate for tilt, the platform was secured at one end and adjustable at the other using a picomotor, which allowed for precise fine-tuning of the tilt around the platform pivot point. Ideally, the pivot point should have been located at the entrance of the DLWs to ensure that adjustments in tilt did not affect the beam's entry point into the DLWs. However, due to the necessity to keep the assembly centre of mass close to the pivot point, setting the tilt was an iterative process. To set the tilt in the planar DLW, the following steps were taken:

1. The dielectric gap was minimised to ensure beam losses always occurred.
2. The centre of the DLW was found by maximising charge transport.
3. The tilt was adjusted in the direction of increasing charge transportation.
4. Steps 2 and 3 were repeated until adjusting the tilt in either direction decreased the charge transported.

The tilt of the circular DLW was set using the same method, as the circular DLWs were attached to the same platform. However, the yaw of the DLW platform could not be adjusted, so the beam trajectory had to be adjusted to match the yaw of the structure

using the two upstream correctors. The same principle of maximising charge transport used to set the DLW tilt was used to set the beam yaw.

The centre of each DLW was determined using the charge transport through the DLW. Beam losses occur either at or symmetrically around the centre (assuming the tilt is correctly set). Using the planar DLW with $2a = 500$ µm we always observed beam losses, so the position of the greatest charge transported was when the beam was at the DLW centre. For the circular DLW, beam losses were symmetric around the centre. An example of setting the centre of the circular DLW is shown in Figure 5.11. With circular DLWs, the beam centre had to be determined in both vertical and horizontal planes, whilst for the planar DLW, the centre only needed to be determined in the vertical direction, as the DLW had no horizontal boundary.

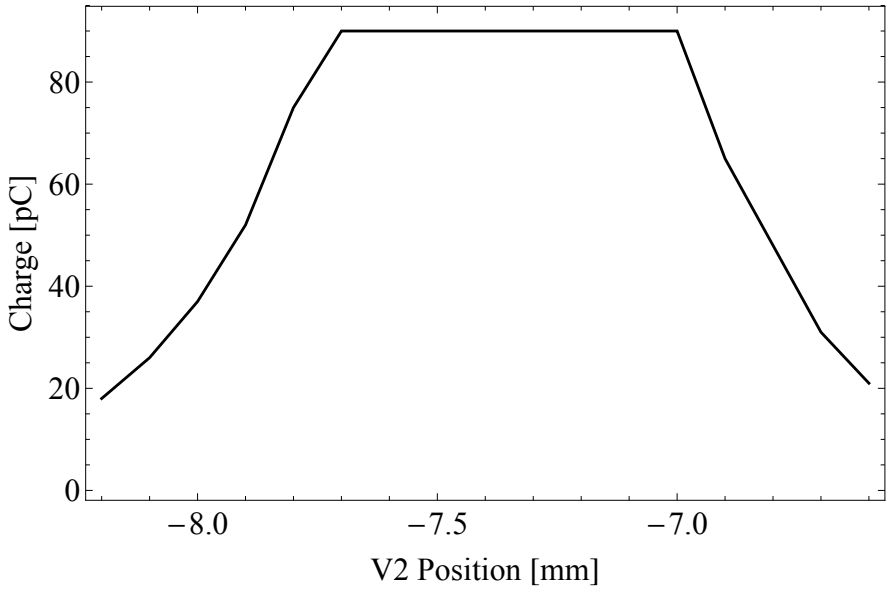

Figure 5.11. The charge transported, measured using the Faraday cup FCUP-01, through the 2 mm circular DLW with varying vertical stage V2 position. The centre of the DLW is at V2 = -7.35 mm.

When taking measurements, beam energy jitter was not significant ($< 0.1\%$) but shot-to-shot energy spectra jitter was observed, limiting the ability to directly compare single-shot measurements with the DLW in/out. Where possible, YAG-03 images were taken by averaging over multiple shots (typically 10-20) rather than single-shot measurements.

5.4 Summary

In summary, the beam transported from CLARA/VELA into BA1 has been thoroughly characterised, and a specific set of machine parameters has been selected to ensure a reproducible beam for dielectric wakefield acceleration (DWA) experiments. The chosen machine parameters were designed to provide two distinct bunch lengths, namely 370

and 800 fs, while maintaining equal bunch charge and momentum.

The experimental area, BA1, has been carefully designed and equipped to facilitate the DWA experiments. The experimental chamber itself comprises three YAG-screens, which are utilised for beam diagnostics. Furthermore, horizontal and vertical slits are available for emittance measurements and phase space reconstruction. The set of YAG screens, slits, and energy spectrometer allowed for 5D beam measurements (transverse phase space and longitudinal momentum).

Within the chamber, both a variable gap planar DLW and a circular DLW were installed. To ensure precise alignment of the dielectric structures with the beam path, robust experimental procedures have been developed. These procedures are crucial for accurate positioning of the dielectric structures, which are essential components for the DWA experiments discussed in the subsequent chapter.

In conclusion, the beam transport system from CLARA/VELA into BA1 has been characterised, and meticulous attention has been given to machine parameters, experimental chamber design, and alignment procedures. These efforts are aimed at providing a well-defined and reproducible beam environment for conducting DWA experiments in BA1.

Chapter 6

Experimental Study of Wakefields in Dielectric Wakefield Accelerators

6.1 Experimental Measurements and Field Calculations

Experimental measurements were taken using YAG-screen images. For the majority of results, measurements are compared with the beam propagating in free path (no DLW inserted). In some cases, such as when the beam is set offset from the DLW centre, comparisons are instead made to the on-axis measurement (where the on-axis position is calculated as outlined in Section 5.3). This assumes the beam is well centred in each DLW for the on-axis measurements.

Average transverse fields were measured by the change in average beam position at S-04 and/or YAG-02 and average longitudinal field was measured at YAG-03. The average transverse field, calculated at each screen, is given by

$$\langle F_i \rangle = \frac{p\Delta x_i}{Ll_s}, \tag{6.1}$$

where Δx_i is the change in average position due to transverse fields, L is the distance between the IP and screen, l_s is the length of the DLW (0.2 m), and p is the longitudinal momentum (35.5 MeV/c). At YAG-03, using Equation 5.2, L is replaced by the horizontal dispersion to convert the change in average horizontal position on the screen to change in energy. Average fields in simulations are calculated using the 3D field profiles and defined as

$$\langle F_i \rangle = \frac{\int\int\int \rho(x,y,z)F_i(x,y,z)dxdydz}{\int\int\int \rho(x,y,z)dxdydz}, \tag{6.2}$$

where $\rho(x,y,z)$ and $F_i(x,y,z)$ are the beam and field distributions.

Quadrupole-like transverse fields change the transverse beam distribution rather than beam position. Therefore, quadrupole-like fields were evaluated using the change in

beam size at a S-04 and/or YAG-02. The change in beam size was defined by

$$\sqrt{\Delta\sigma_i^2} = \sqrt{\sigma_{i,m}^2 - \sigma_{i,0}^2}, \tag{6.3}$$

where $\sigma_{i,m}$ and $\sigma_{i,0}$ are the measured beam sizes with the DLW in and free-path respectively. The effect of quadrupole-like fields were also measured using the beam divergence between screens. The divergence is given by

$$\Theta_i = \frac{\sigma_i(\mathrm{YAG}-02) - \sigma_i(\mathrm{S}-04)}{2.05}, \tag{6.4}$$

where the beam size, σ_i was measured at S-04 and YAG-02 and the distance between the two screens was 2.05 m. This equation assumes that the beam is either purely diverging or converging between the screens, i.e. the beam waist is upstream of S-04 or downstream of YAG-02.

6.2 Variation of Wakefield Strength with Structure Gap

For the first set of experiments, the planar structure gap was varied with the free path beam envelope for each linac off-crest phase kept constant. The range of structure gaps were chosen such that no charge was lost within the DLW. S-04 screen images with and without the planar DLW in the beam path are shown in Figure 6.1. A comparison of the images with and without the planar DLW in the beam path reveals noticeable changes in transverse beam dynamics. Differences are observed between the free path and the presence of the DLW, as well as among different structure gaps in the DLW. However, it is challenging to immediately determine the magnitude and strength of the transverse fields solely based on the observed changes in beam sizes. The impact of transverse fields relies on the beam's convergence or divergence when subjected to the applied field.

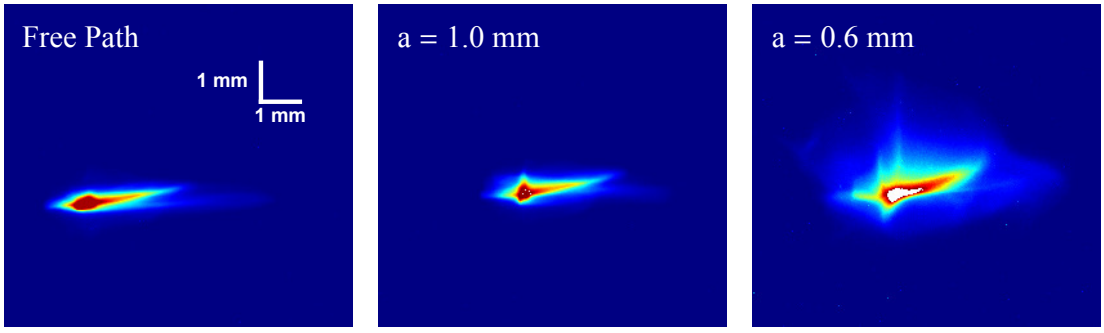

Figure 6.1. S-04 images with free path and beams centred in the planar DLW set with a = 1.0 and 0.6 mm. Bunch length is 370 fs.

Simulated beam envelopes for varying planar gaps at 3 waist positions are shown in Figure 6.2. In each simulation, the beam size at the waist was set such that the beam size in each transverse plane matched, to the best of our ability, the free-path measurements at S-01, S-03, S-04, and YAG-02. Quadrupole wakefields focusing the beam horizontally decrease in strength with increasing structure gap. With the waist positioned upstream of the DLW centre (at $s = -0.1$ m), weaker focusing reduces divergence after the waist, reducing the downstream beam sizes. Stronger focusing at smaller planar gaps bring the beam to a second sharper waist, therefore increasing the divergence and downstream beam size. With the waist downstream of the DLW centre, the wakefield focusing at each gap increases the beam convergence, therefore increasing the divergence after the waist and increasing the beam size downstream. The opposite is true for defocusing forces: decreased convergence if the waist is downstream and increased divergence if the waist is upstream of the DLW. It was determined that for $\sigma_t = 370$ fs the horizontal waist was at $s = 0.2$ m and vertical waist at $s = 0.5$ m and for $\sigma_t = 800$ fs the horizontal and vertical waists were both approximately at the DLW entrance ($s = -0.1$ m).

The difference in waist position in each transverse plane leads to differences in the change in beam size, as evident in Figure 6.3, despite symmetric focusing/defocusing in the x and y-plane respectively. Although the beam envelope was not precisely measured (as explained in Section 5.2), an estimated envelope provides a good agreement between experimental results (data points) and simulations conducted with DiWaCAT (solid lines) in Figure 6.3. The match between experimental and simulation results is more pronounced in the vertical plane compared to the horizontal plane. This difference can be attributed to the waist position being closer to the DLW center in the horizontal plane. Within the DLW, errors in the waist position would have a larger impact on downstream divergence or convergence. The effect of this means that the error in expected results from simulations is likely larger than the measurement errors shown in Figure 6.3. However, for reasons given in Section 5.2, the exact size of these errors cannot be quantified.

Transverse fields in planar and circular structures cannot be directly compared due to the different symmetries of each scheme. In a planar DLW the fields are always focusing parallel to the dielectric plate and defocusing towards the dielectric. In a circular DLW, any beam asymmetry will introduce defocusing in the direction of greater beam size. Downstream profiles do allow for some conclusions on the strength of the fields to be made. Smoothed horizontal profiles at S-04 for each bunch length used are shown in Figure 6.4. For each structure, the beam size is larger than free path. When considering a bunch length of $\sigma_t = 370$ fs, the change in beam size for the circular DLW is approximately equivalent to the planar DLW with $a = 0.8$ mm. Conversely, for

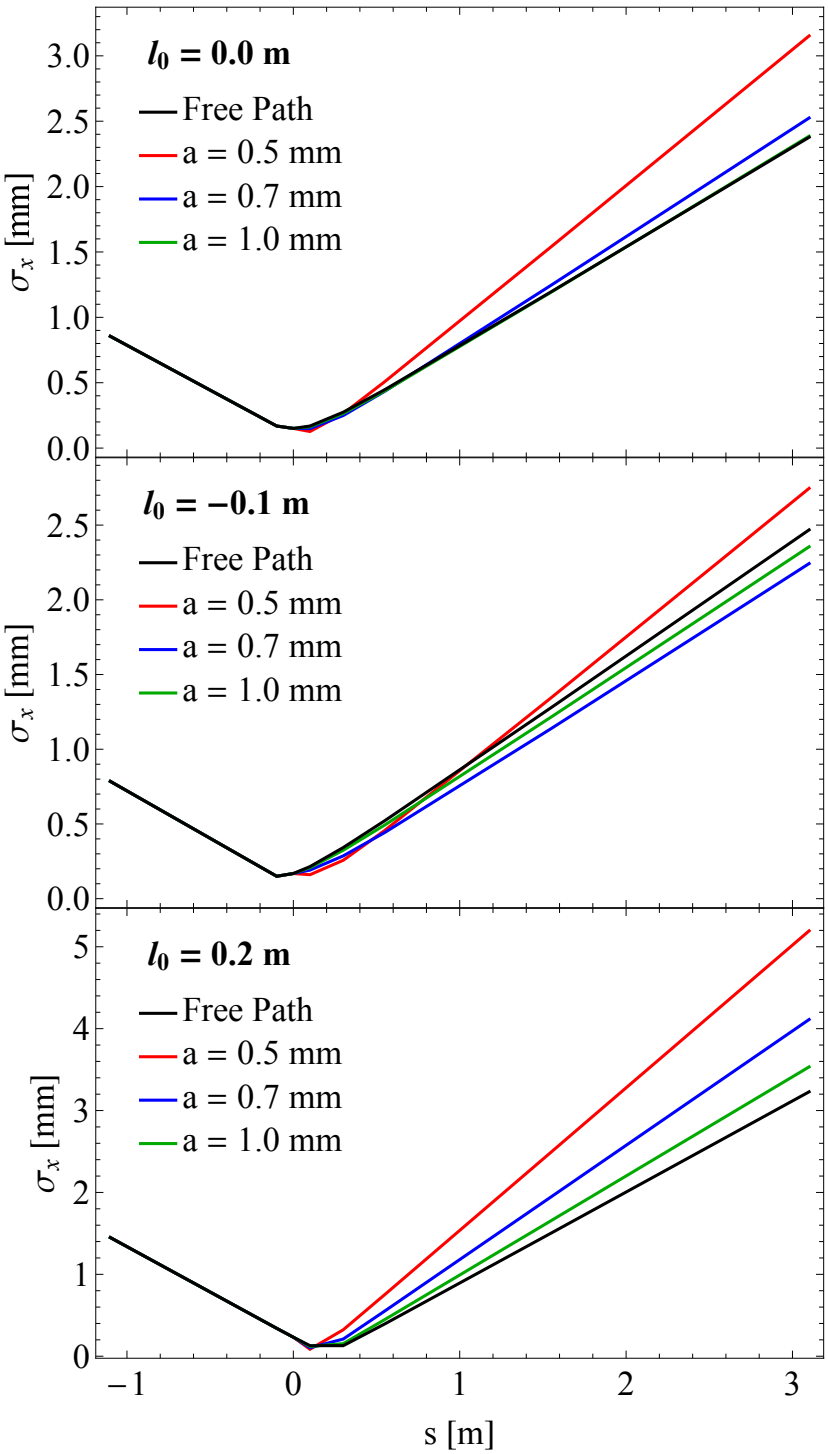

Figure 6.2. Simulated horizontal beam envelopes for varying free path waist positions, l0, and planar dielectric gaps. The DLW is positioned between -0.1< s <0.1 m. The beam size at the waist position was set such that the beam sizes at each screen position matched the free path case. Bunch length is 370 fs.

the longer bunch length of $\sigma_t = 800$ fs, the change in beam size for the circular DLW is smaller than that for the planar DLW with $a = 1.0$ mm. These profiles suggest some quadrupole-like fields, similar to in planar DLWs were excited in the circular DLW for the shorter bunch. The beam size in free path shows asymmetry between horizontal and vertical RMS beam size (approximately 230 and 150 μm respectively) at S-03 for the 370 fs RMS bunch, whilst for the 800 fs bunch the beam sizes are approximately

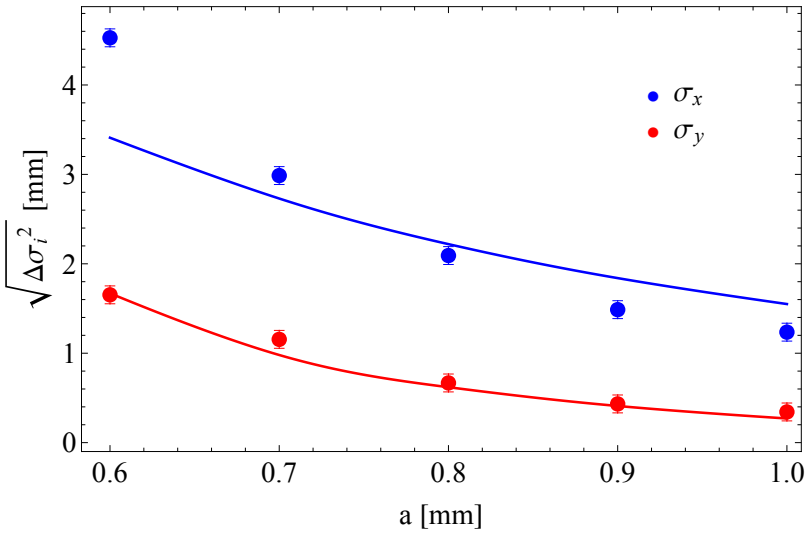

Figure 6.3. Variation in transverse beam size as a function of the planar structure gap. Solid lines represent simulated results. Bunch length is 370 fs.

140 μm in both transverse directions. Beam astigmatism will excite different radial field distributions as a result of the beam in each transverse plane, presenting as the total field appearing quadrupole-like. The exact characteristics of these wakefields necessitate detailed simulations similar to those conducted for planar DLWs using DiWaCAT.

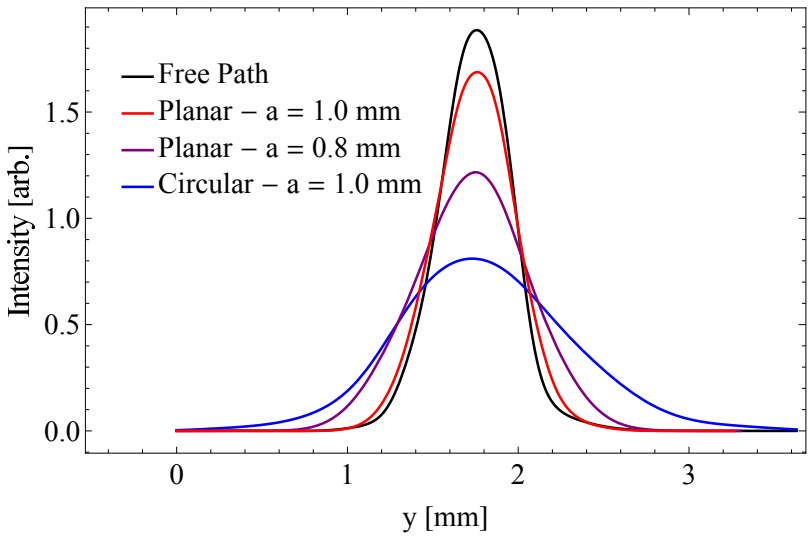

(a) $\sigma_t = 370$ fs

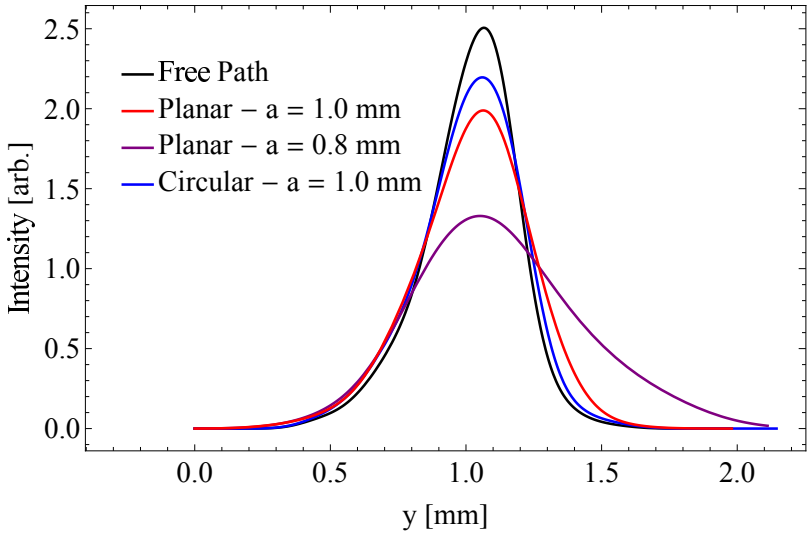

(b) $\sigma_t = 800$ fs

Figure 6.4. Vertical beam profiles at S-04 for various planar structure gaps and circular DLW at both bunch lengths.

The change in energy spectra allows for inferences on the longitudinal E_z profile. The CLARA beam has a positive chirp in BA1, i.e. the tail of the bunch has lower energy. Non-linear components to the LPS do not allow for the energy spectra to be directly used to reconstruct $E_z(t)$. Non-linear components to the LPS also mean that DiWaCAT can only be used to compare average longitudinal fields, rather than directly compare with energy spectra. Energy spectra for the free path and planar dielectric at each structure gaps are shown in Figure 6.5. The spectra and average momentum (shown with vertical lines) indicate deceleration with both gaps. The average change in beam energy with the two strucutre gaps are, to measurement accuracy, equal (0.338 MeV). This can be explained by the bunch length, 800 fs, which both decelerates and accelerates the bunch as shown in Figure 6.7. Acceleration may be inferred from the energy spectra with $a = 0.8$ mm however the difference from the highest energy of the free path spectra makes this inconclusive.

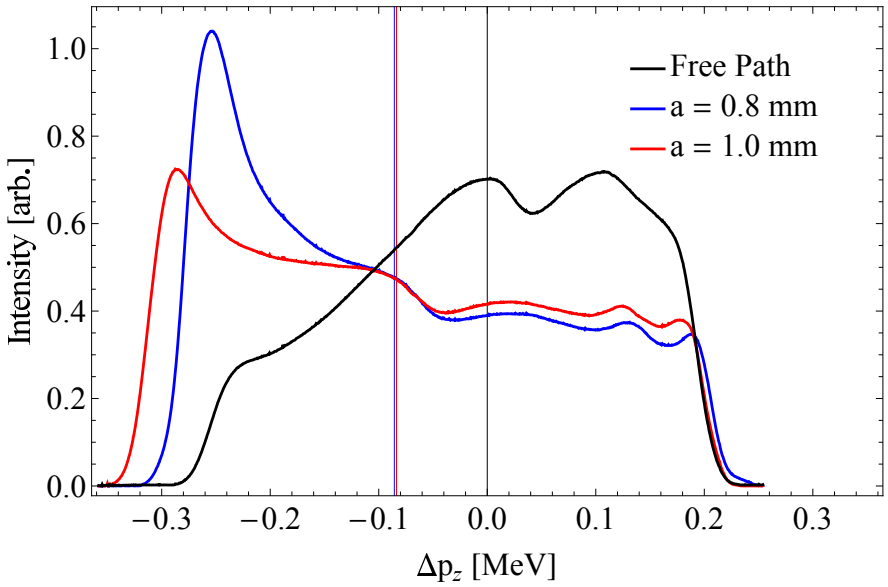

Figure 6.5. Averaged YAG-03 energy spectrometer data for free path and planar DLW with two structure gaps. The plot is normalised to integrated intensity and the average energy of each case given by vertical lines. Bunch length is 800 fs.

With $\sigma_t = 800$ fs, acceleration and deceleration complicates evaluating the strength of longitudinal fields using energy spectra data. It is more appropriate to use the data from bunches with $\sigma_t = 370$ fs instead. Average longitudinal fields are shown in Figure 6.6. Simulations using DiWaCAT (solid line) show good agreement with experimental data. The circular DLW (red point) with $a = 1.0$ mm is positioned on the horizontal axis where the point fits on the planar trend line, the point $a = 0.775$ mm. This result is corroborated by the E_z profiles in Figure 6.7, with approximately equal profiles measured for the circular and planar structures with this gap/aperture pair. The ratio of average E_z in planar and circular structures with the same dielectric gap ($a = 1.0$ mm) is 0.6 ±0.1 in good agreement with the theoretically predicted value of 0.62 [115][149]. These simulated field profiles also support the conclusion from Figure 6.5 that the peak deceleration is within the bunch.

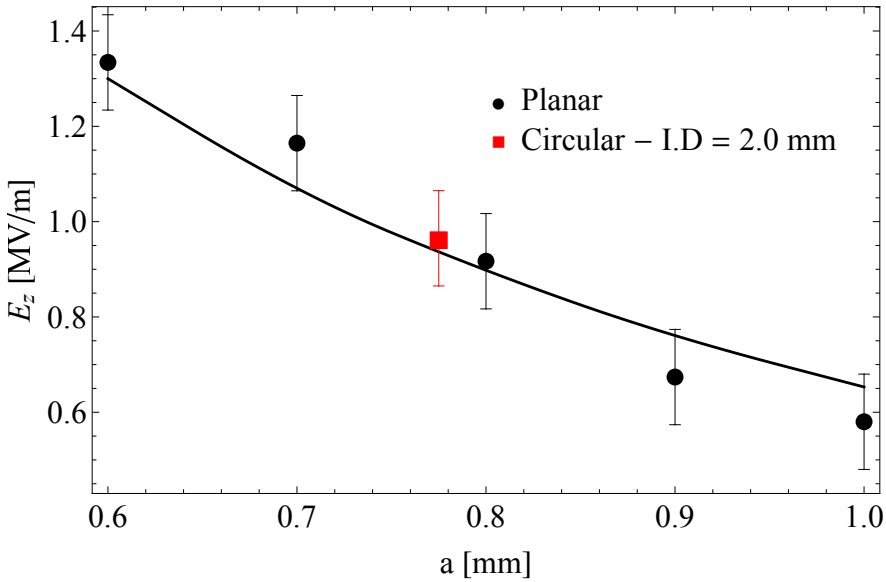

Figure 6.6. Average longitudinal field as a function of planar dielectric gap, with the result for the circular DLW given in red at an effective planar gap of 0.775 mm. Bunch length is 370 fs.

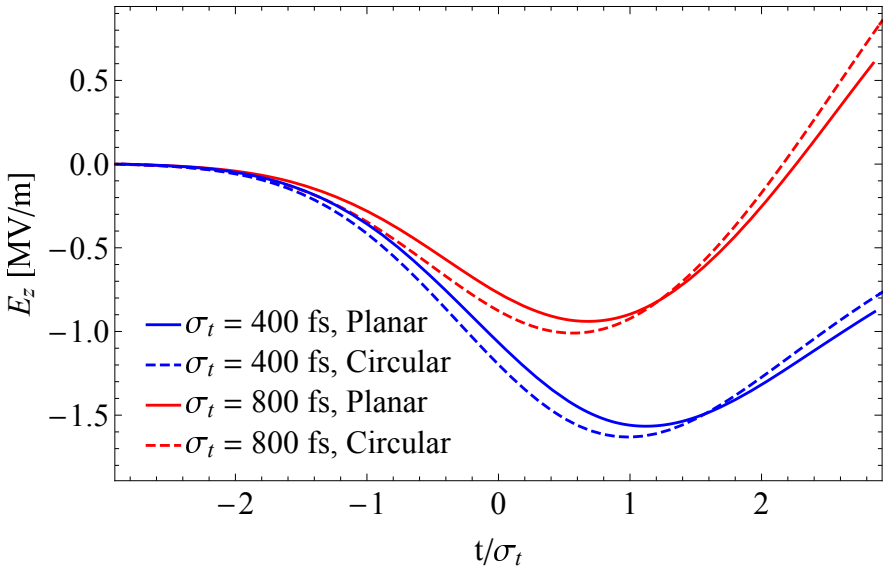

Figure 6.7. Simulated Ez profile for an 800 and 400 fs Gaussian bunches with planar DLW with a = 0.775mm and circular DLW with a = 1.0 mm. Fields for the circular DLW were calculated using the analytical equations in [113].

6.3 Variation of Wakefield Strength with Beam Offset

In practical DWAs, the drive bunch is not expected to travel exactly on-axis over multiple metres of deceleration due to orbit jitter and DLW misalignment. Beams propagating offset from the DLW axis excite dipole-like wakefields in planar and circular DLWs which in turn lead to the development on single-beam breakup instability (BBU) [77]. Accurate modelling of these effects are necessary for future realisation of DWAs.

Examples of how these dipole-like fields affect the beam in planar and circular DLWs are shown in Figures 6.8 and 6.9 respectively. The beam size increases with offset in both structures. Screen images at YAG-03 show vertical position as a function of beam momentum. Given the positive chirp of the CLARA beam this is therefore vertical position as a function of longitudinal beam position, with the left hand-side being the head of the bunch. YAG-03 images (Figures 6.8(b) and 6.9(b)) indicate a dipole-like field that is longitudinally varying. With the beam on-axis the vertical position is constant for all horizontal screen positions, indicating zero kick is applied. With the beam offset from the DLW centre, the vertical position is a function of horizontal position, indicating a dipole-like field with strength increasing along the bunch. The length of the streak can be measured by the beam size and indicates the maximum vertical force, which increases with offset as shown in Figure 6.10.

The beam behaviour in the vertical plane of the planar structure is dominated by the dipole-like wakefield that streaks the image on the downstream screen with appreciable contribution from the vertical quadrupole-like fields due to relatively large transverse beam size. In the horizontal plane, the longitudinal slices close to the head of the bunch are focused to a waist while further slices towards the tail of the bunch are strongly overfocussed. Similar behaviour is observed with the circular structure thus indicating that both dipole-like and quadrupole-like fields are excited when the beam propagates off-axis in circular DLWs. With $y_0 = 1.4$ mm in the planar DLW and 0.6 mm in the circular DLW, the beam is 0.6 mm from the dielectric surface. The vertical streaks in both are approximately the same total length, as shown in Figure 6.11 so approximately equal maximum F_y is excited in the two DLWs. Given the field is longitudinally dependent, the horizontal profile as a function of vertical position is the equivalent of the horizontal focusing as a function of longitudinal position. Quadrupole-like fields can be isolated in the horizontal plane; the strength of horizontal focusing can be evaluated by the vertical position at which the horizontal profile is at a waist. Similar horizontal behaviour is seen in both planar and circular DLW screen images (Figures 6.8(a) and 6.9(a)) with the beam focused to a waist at a vertical position in both structures, suggesting quadrupole-like fields are excited horizontally in both structures. The vertical position the waist is greater

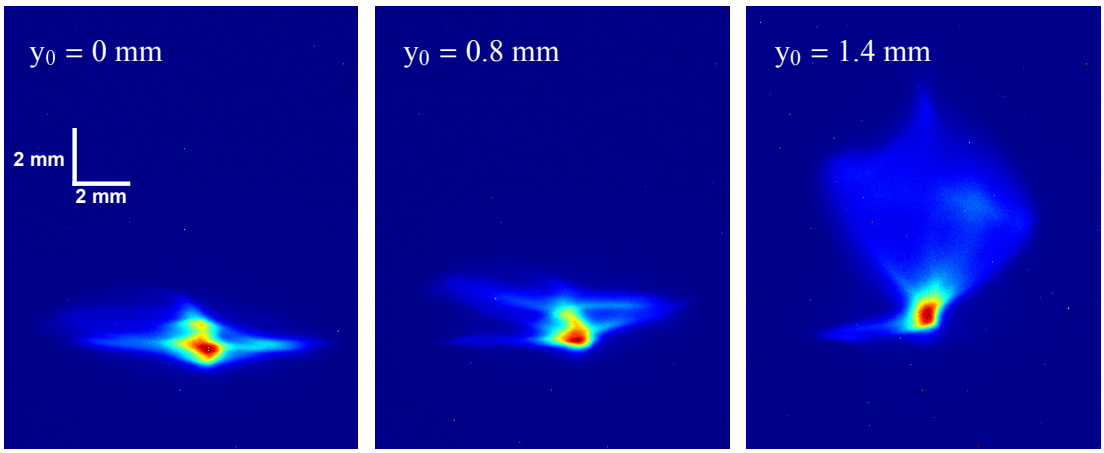

(a) YAG-02

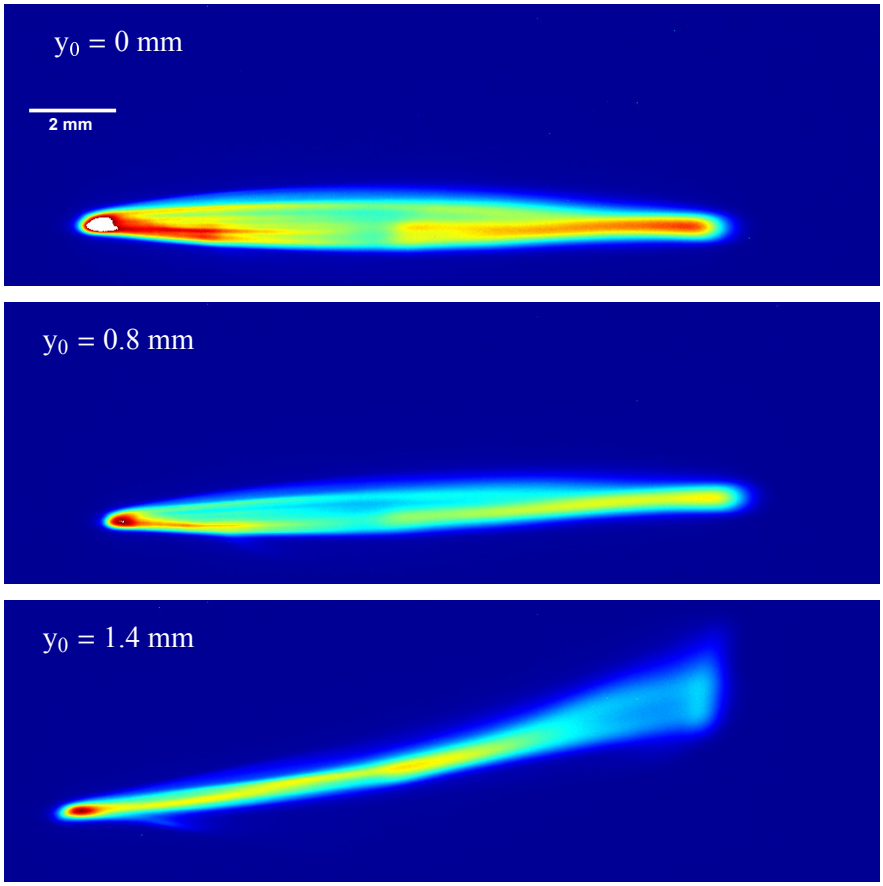

(b) YAG-03

Figure 6.8. Downstream screen images for varying offsets in the planar DLW with a = 2.0 mm. Bunch length is 800 fs.

in the circular DLW than the planar DLW, indicating weaker focusing in the circular DLW. Quadrupole-like fields vertically defocus each longitudinal slice. This can only be seen where the maximum kick is applied, so can be evaluated by the length of the tail in the vertical beam profile. The tail of the vertical profile in Figure 6.11 is longer for the planar DLW, indicating a larger contribution of vertical quadrupole-like fields.

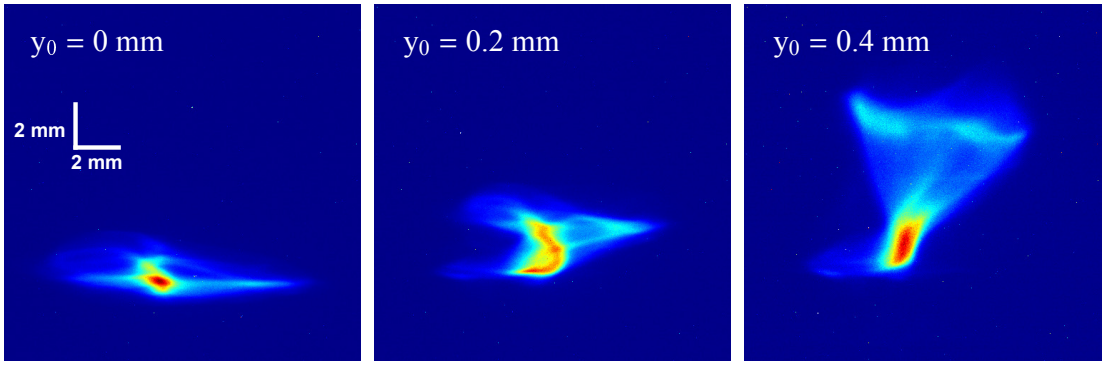

(a) YAG-02

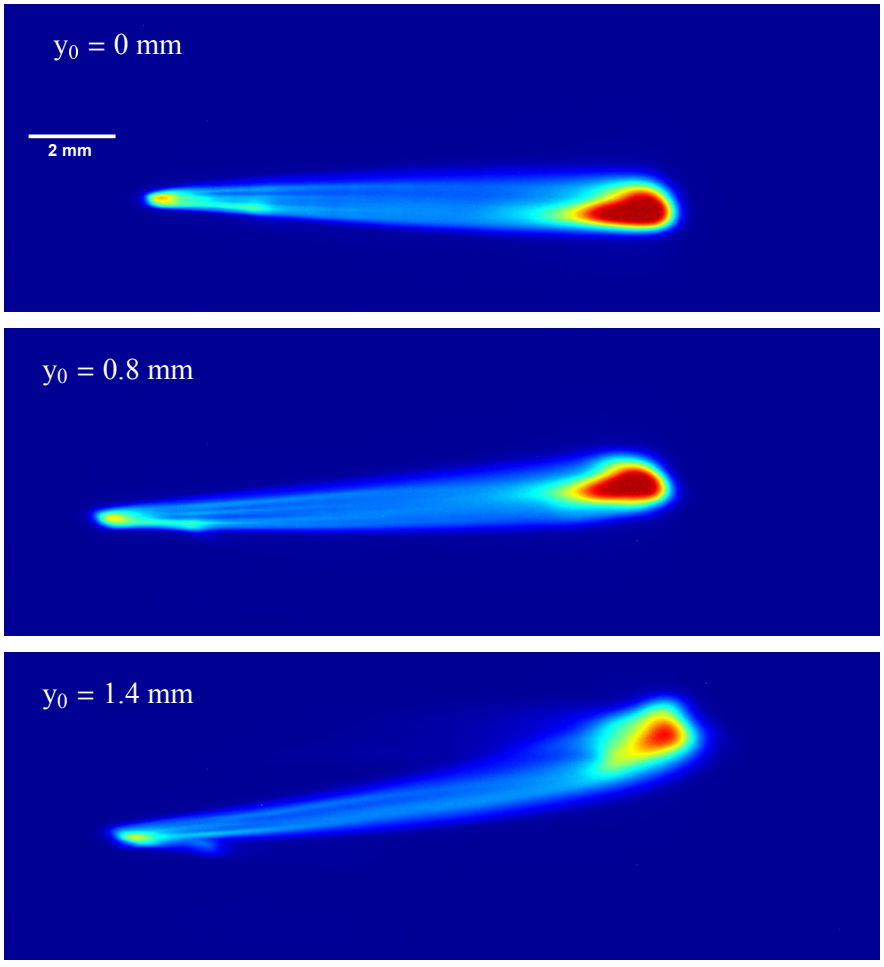

(b) YAG-03

Figure 6.9. Downstream screen images for varying offsets in the circular DLW. Bunch length is 800 fs.

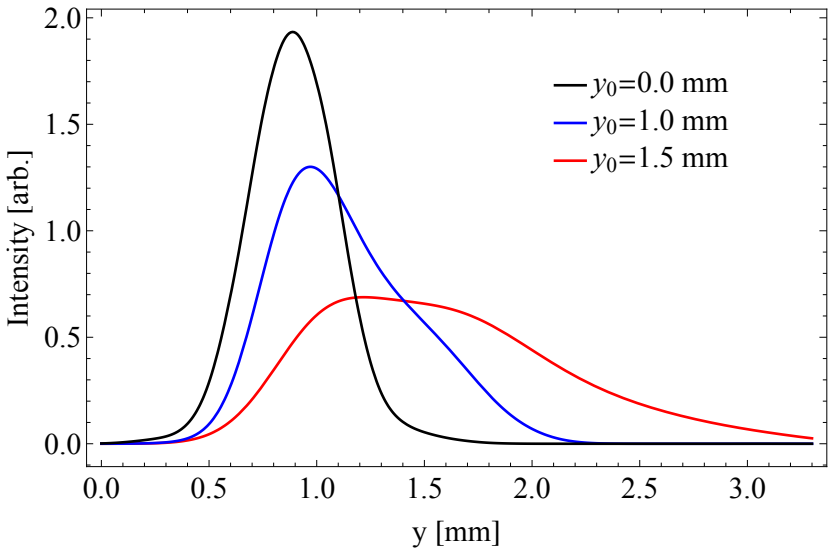

Figure 6.10. Smoothed vertical beam profile at S-04 for varying offsets in the planar DLW with a = 2.0 mm. Bunch length is 800 fs.

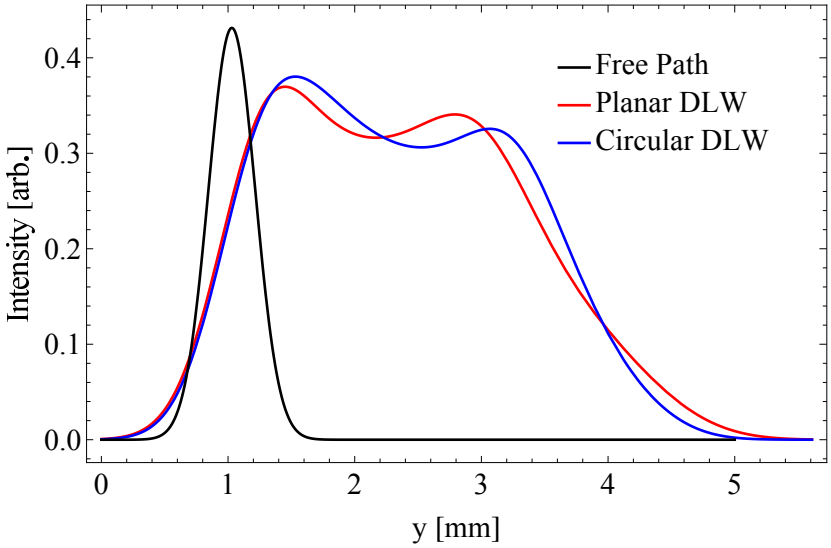

Figure 6.11. Smoothed vertical screen profiles at S-04 for the free-path and beam offset 0.62 mm from the dielectric surface in the circular DLW and planar DLW with $a = 2.0$ mm. Bunch length is 800 fs.

The average vertical wakefield, $\langle F_y \rangle$ was measured for two bunch lengths in each structure, and shown in Figures 6.12 and 6.13. DiWaCAT simulations are shown for the planar DLW. Similar simulations cannot be undertaken for circular DLWs at this time using DiWaCAT so the solid line is a fit shown to aid the eye. Behaviour is symmetric about the DLW centre, as expected, and planar results match expectations from simulations. Both results show non-linear increases in $\langle F_y \rangle$ with beam offset, however the non-linear behaviour is greater in the planar case. The circular DLW results follow previous results, which showed that transverse fields can be modelled using a combination of dipole and quadrupole terms [16]. The contribution of higher-order terms appears greater in planar DLW, the contribution of which increases with offset, given that the planar trendline cannot be modelled with linear (dipole) and quadratic (quadrupole) terms.

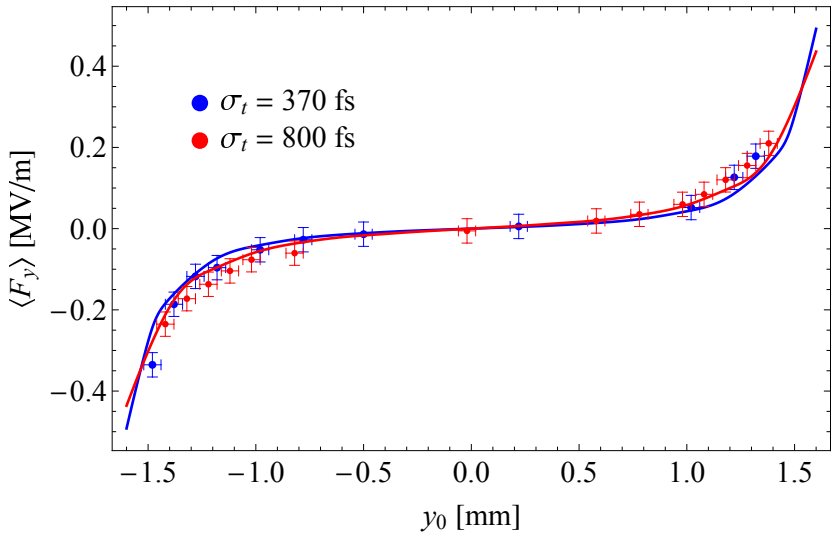

Figure 6.12. Average vertical force for each bunch length, calculated from the change in screen image central moment, as a function of offset in the planar DLW with a = 2.0 mm. Solid lines represent simulation results.

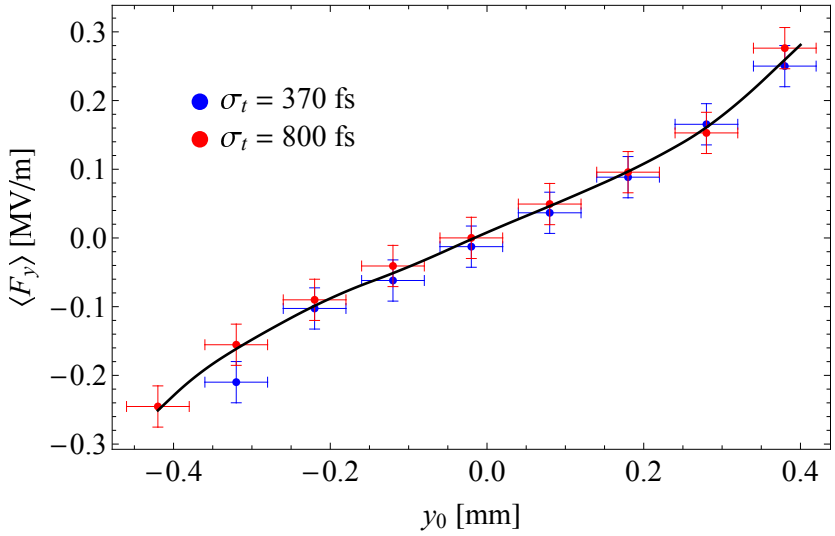

Figure 6.13. Average vertical force for each bunch length, calculated from the change in screen image central moment, as a function of offset in the circular DLW with a = 1.0 mm. Solid line shows a quadratic fit to the complete dataset.

The results for $\sigma_t = 370$ and 800 fs are approximately equal, despite a factor of more than 2 difference in bunch length. This can be explained using the F_y profiles in Figure 6.14. The shorter bunch has a larger peak F_y but it is reached behind the bunch where the beam current is zero. The peak F_y for the 800 fs bunch is lower, but contained within the bunch. Therefore, the average F_y fields do not differ significantly. The simulated dependence of $\langle F_y \rangle$ on bunch length at two offsets for the planar DLW is shown in Figure 6.15. The difference between 400 and 800 fs bunches is only 15%, within the accuracy of measurements. For bunches shorter than 300 fs, the dependence on $\langle F_y \rangle$ with bunch length is approximately linear due to F_y peaking farther away from the bunch. The wavelengths of higher-order modes are lower, therefore the F_y field is more likely to peak within longer bunches at larger offsets. At smaller offsets, where the contribution

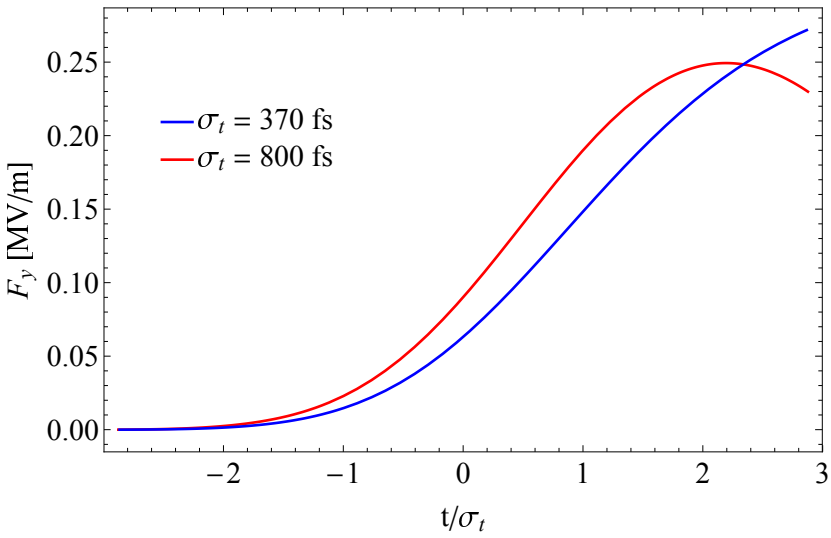

Figure 6.14. Simulated F_y profile for each bunch length with $y_0 = 1.6$ mm and $a = 2.0$ mm.

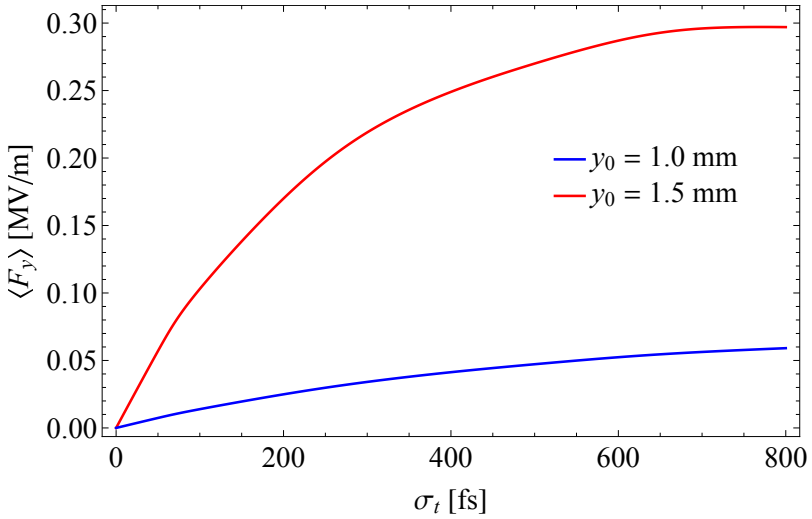

Figure 6.15. Simulated average vertical wakefield strength, $\langle F_y \rangle$, as a function of Gaussian RMS bunch length at two offsets with $a = 2.0$ mm.

of higher-order modes is smaller, the average field increases with bunch length, contrary to larger offsets, at the expense of field strength.

Close to the dielectric plate it can be assumed that the wakefield is similar to a single dielectric plate irrespective of the structure geometry. It can be assumed that for large offsets, the variable of interest is distance to the dielectric plate rather than offset from the DLW centre. The data from Figures 6.12 and 6.13 are replotted as a function of distance to the dielectric plate in Figure 6.16(a). The change in beam size, a measurement of the length of the streak is shown in 6.16(b). The measured fields in planar and circular DLWs converge close to close of the single dielectric plate. Further away from the dielectric plate direct comparisons between the two structures are less relevant due to the different structure gap/aperture.

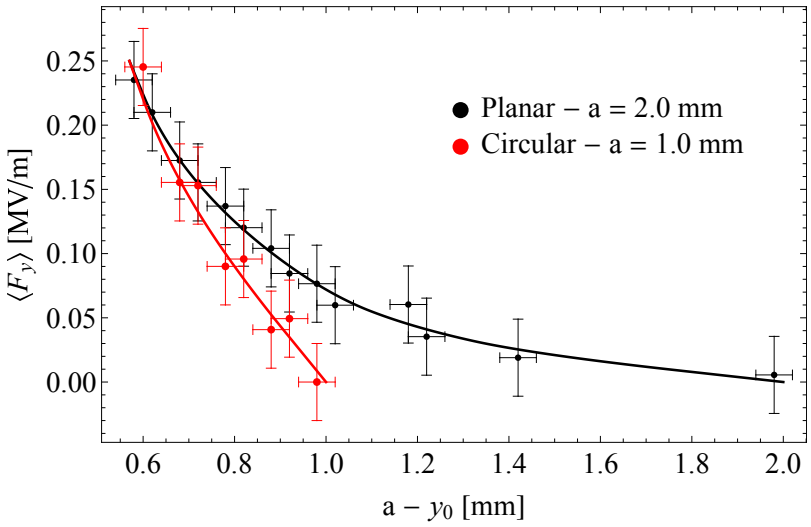

(a) Average vertical force.

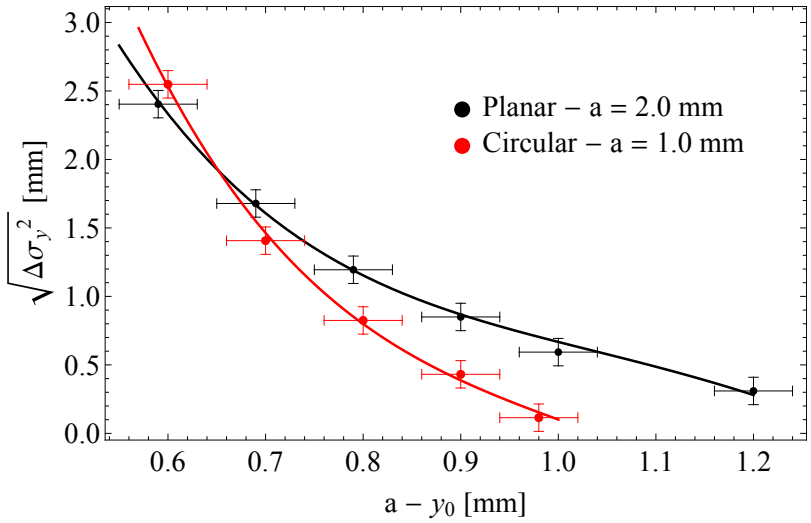

(b) Change in vertical beam size.

Figure 6.16. Vertical beam measurements as a function of distance to the dielectric plate for planar and circular DLWs. Bunch lengths is 800 fs.

6.3.1 Longitudinal Profile Estimation with Streaked Beams

The RMS bunch length is determined by the linac-beam off-crest phase, with the relationship between the two at CLARA given in [146]. For shorter bunches it would be possible to verify this bunch length using the average wakefield strength, however as shown in Figure 6.14 the variation in average F_y is within measurement accuracy for these bunch lengths.

For a given offset in the DLW, the wake potential is constant and wakefield is given by the convolution with the bunch profile. The downstream beam profile then relates to the shape of the transverse wakefield. The longitudinal profile can be reconstructed by finding the longitudinal profile that excites a transverse wakefield which maps that profile to the measured downstream image. An iterative method was used to reconstruct the

bunch profile; the downstream transverse profile was mapped to a longitudinal position using the wakefield calculated from a test profile. The wakefield is calculated from this longitudinal profile and used to remap the downstream profile, converging on a solution where the wakefield from a longitudinal profile maps the downstream profile to the same longitudinal profile. This method is similar to that detailed in [108][150].

The initial test profile is chosen as a Gaussian bunch with RMS length given by the off-crest phase. The final measured profile depends on the bunch length used for the test profile. The optimal longitudinal profile is found by altering the bunch length of the test profile. The measured longitudinal profile for each bunch length is tested by simulating the downstream profile, which is compared to the measured profile. The solution is given by the profile which gives the best agreement with the measured profile and the variation in agreement allows for the error in bunch length to be estimated. An alternative reconstruction process, using the forward propagation of a test beam profile is outlined in Chapter 8.

The reconstruction process for the bunch with off-crest phase of -6° is shown in Figure 6.17. The large error in RMS bunch length is explained by the small difference in the wakefield strength with changing bunch length. The profile can be approximated by a skew-Gaussian with skew-factor $\alpha = -2.25$.

The same process is shown with the off-crest phase at 0° in Figure 6.18. For the longer bunch at large offsets, the peak F_y value is contained within the bunch. In this case there are two longitudinal positions which receive the same kick and therefore measured at the same position at a downstream screen. A smaller offset is used instead to avoid this, at the expense of wakefield strength. The offset in this case is negative, so the magnitude of the vertical position was used for reconstructed. The reconstructed profile (Figure 6.18(c)) is estimated by a skew-Gaussian with $\alpha = -2$.

Simulations using these bunch profiles and lengths show agreement with experimental results. This suggests that the reconstruction provides a reasonable estimate of the longitudinal bunch profile.

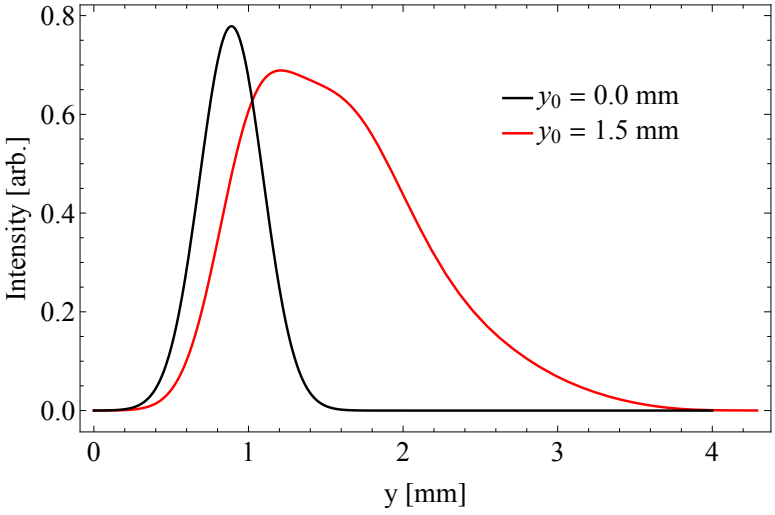

(a) Smoothed beam profile at S-04 with $y_0 = 0$ shown for comparison.

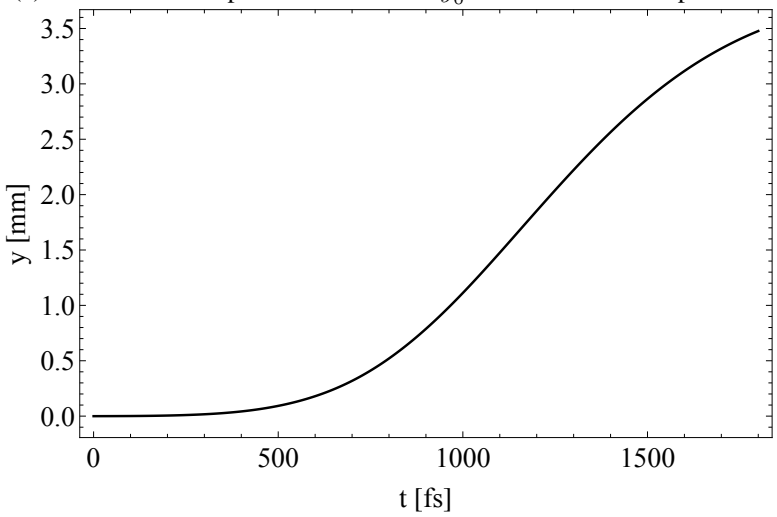

(b) Simulated vertical kick at S-04 as a function of longitudinal position within a Gaussian bunch with 370 fs RMS bunch length. The head of the bunch is at t = 0.

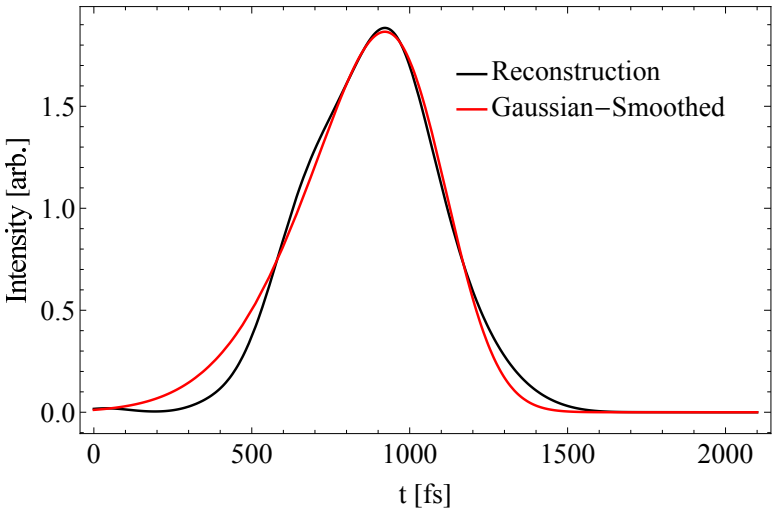

(c) Reconstructed longitudinal profile (black), and skew-Gaussian fit (red).

Figure 6.17. Input and output longitudinal profiles from the reconstruction of the bunch produced with an off-crest linac phase of -6°. The bunch length was determined to be 370 $\pm$ 60 fs.

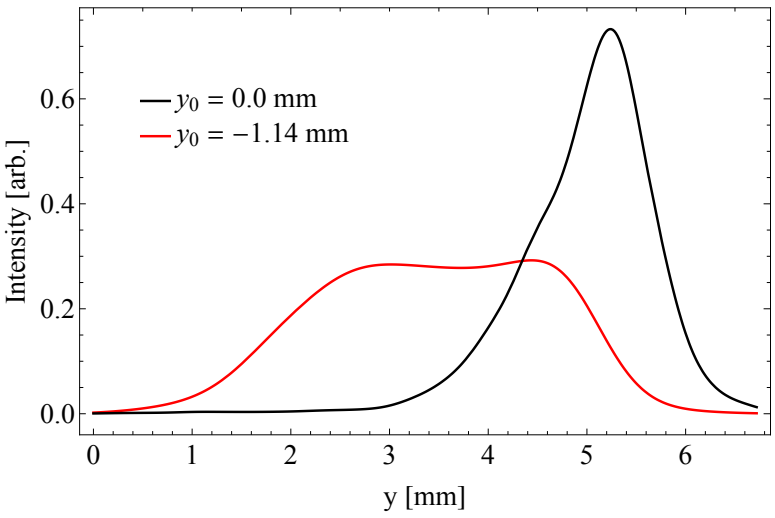

(a) Smoothed beam profile at S-04 with $y_0 = 0$ shown for comparison.

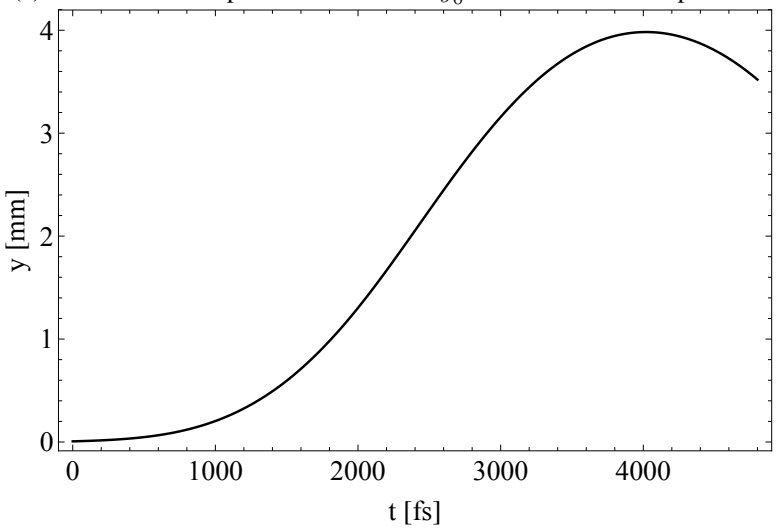

(b) Simulated vertical kick at S-04 as a function of longitudinal position within a Gaussian bunch with 800 fs RMS bunch length. The head of the bunch is at t = 0.

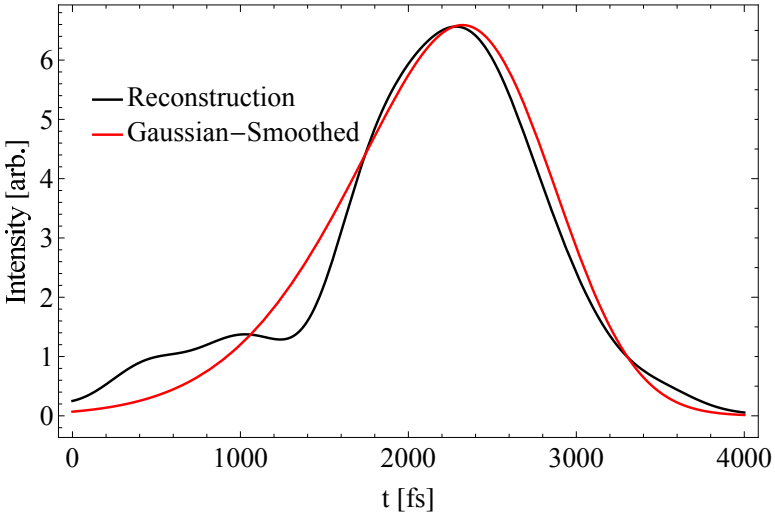

(c) Reconstructed longitudinal profile (black), and skew-Gaussian fit (red).

Figure 6.18. Inputs and outputted longitudinal profile from the reconstruction of the bunch produced with an off-crest linac phase of 0°. The bunch length was determined to be 800 ± 100 fs.

6.4 Variation of Wakefield Strength with Beam Ellipticity

6.4.1 BBU Suppression

The BBU instability caused by the development of dipole-like fields off-axis can be reduced by using a highly elliptical bunch, as previously discussed in Section 3.3.2 and reported experimentally in [126]. The bunch ellipticity is given by the ratio of horizontal to vertical beam size (aspect ratio). In this experiment, the horizontal beam size was varied whilst keeping the vertical beam size, $\sigma_y = 150 \pm 20$ µm, approximately constant. A circular beam is defined with an aspect ratio ≈ 1. The quoted horizontal beam size is the RMS size measured at S-03.

The dependence of the average vertical wakefield with beam offset is shown for a number of horizontal beam sizes in Figure 6.19. While the dependence for the approximately circular beam ($\sigma_x = 180$ µm) follows the non-linear trend in Figure 6.12, the dipole-like wakefields which would lead to BBU are greatly reduced with increased horizontal beam size. The non-linear behaviour also reduces with beam width, with the dependence for $\sigma_x = 750$ and 1500 µm more closely resembling quadratic and linear relationships. This supports the theoretical reasoning for BBU reduction, that higher-order modes are suppressed with an increasingly elliptical beam.

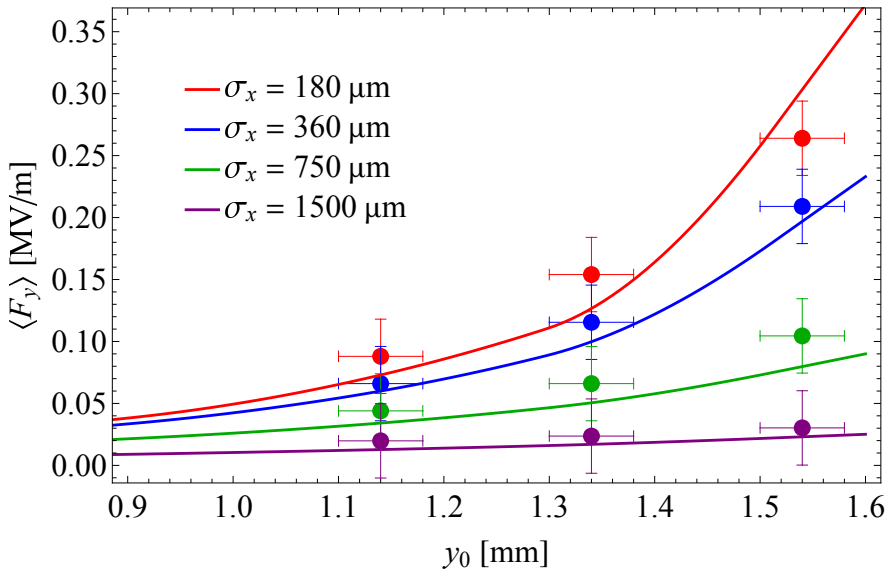

Figure 6.19. Average vertical force as a function of offset for various beam widths. Solid lines show simulation results. Bunch length is 800 fs.

The suppression of BBU with elliptical beams relies on the transverse and longitudinal fields scaling with $1/\sigma_x^3$ and $1/\sigma_x$ respectively. This relationship was observed experimentally for the short and long bunches, as shown in Figure 6.20. The measured average longitudinal and transverse fields show good agreement with the theoretical expectations from simulations. Whilst the longitudinal field decreases with the horizontal beam size,

the transverse field decreases at a faster rate as theoretically expected [125]. This result is in agreement with previous measurements in [126], in which transverse fields were measured using beam position monitor (BPM) data rather than using full screen images as here.

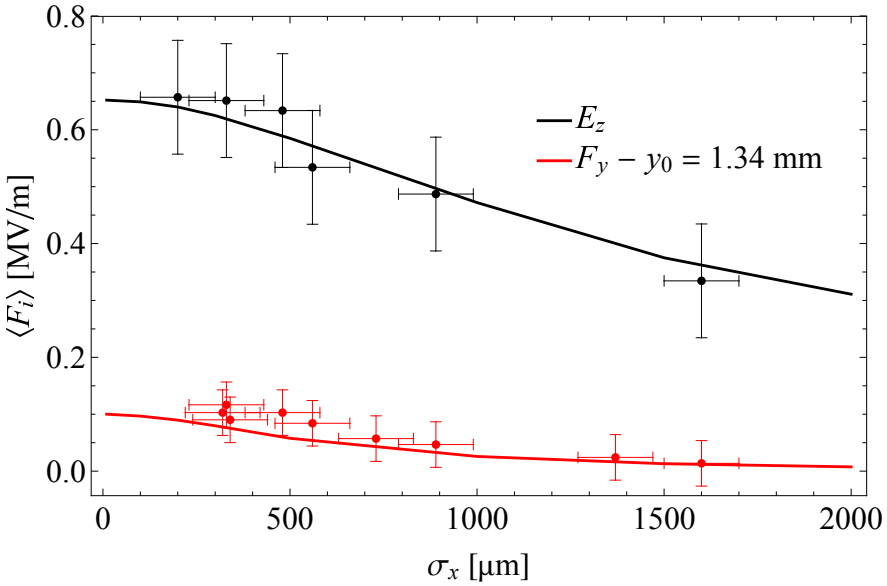

(a) $\sigma_t = 370$ fs

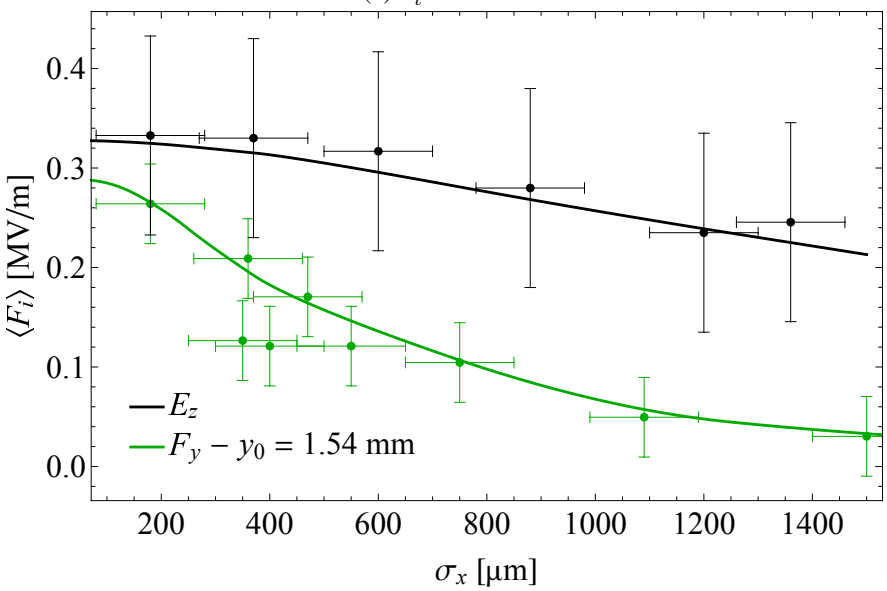

(b) $\sigma_t = 800$ fs

Figure 6.20. Average vertical force and longitudinal field as a function of RMS beam width. Solid lines show simulation results.

The magnitude of the suppression was measured at different beam offsets, shown in Figure 6.21. The amount of suppression with offset is larger when the beam has a larger initial offset. By normalising the simulation data to a beam with negligible size, as in Figure 6.22, this effect is clear. With a circular beam, the contribution of higher-order modes increases with offset so the suppression of higher-order modes is more observable at larger offsets.

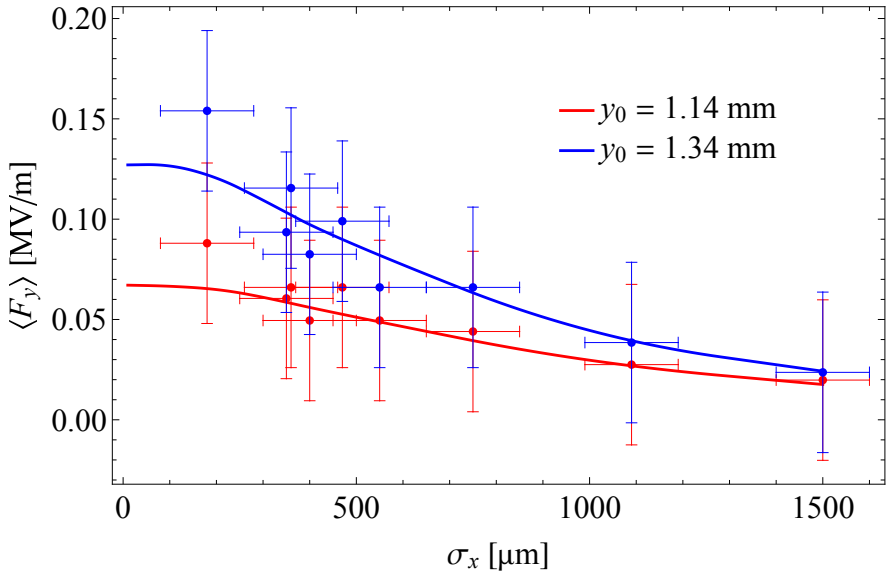

Figure 6.21. Average vertical force at two offsets as a function of RMS beam width. Solid lines show simulation results. Bunch length is 800 fs.

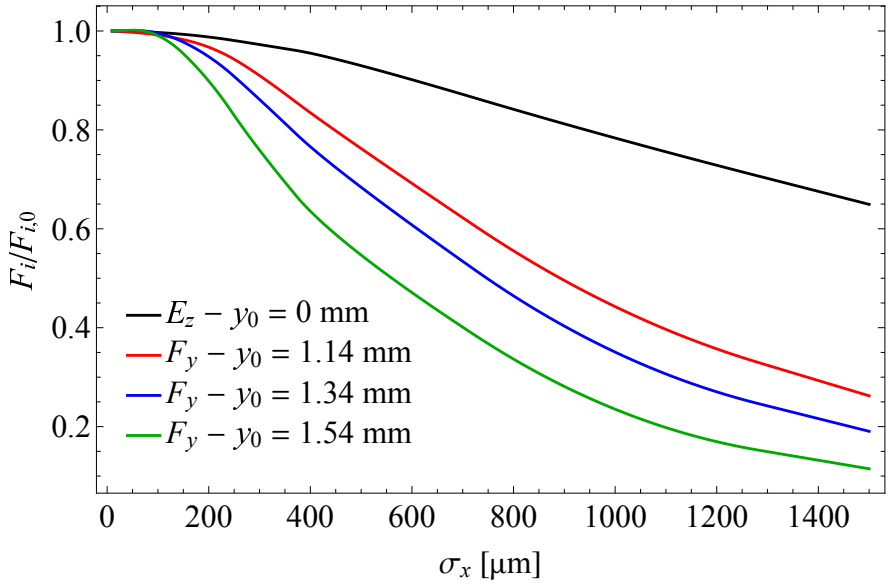

Figure 6.22. Simulated relative strength of the longitudinal field on-axis and vertical field at various offsets as a function of RMS beam width. Fields are normalised to sigmax = 0. Bunch length is 800 fs.

6.4.2 Transverse Beam Quality

As discussed in Section 3.3.2 the transverse field distributions raise questions about the beam quality of elliptical beams. Whilst the reduction of dipole-like fields has been experimentally validated in [126], the transverse beam quality of elliptical beams in DLWs has not been investigated. Figure 6.23 shows horizontal and vertical divergence for varying beam width and planar structure gap. In the vertical plane the defocusing force increases divergence at all structure gaps and the change in divergence compared to the free path case reduces with increased beam width. In the horizontal plane the behaviour is more complex. Strictly speaking, data presented in Figure 6.23 can be

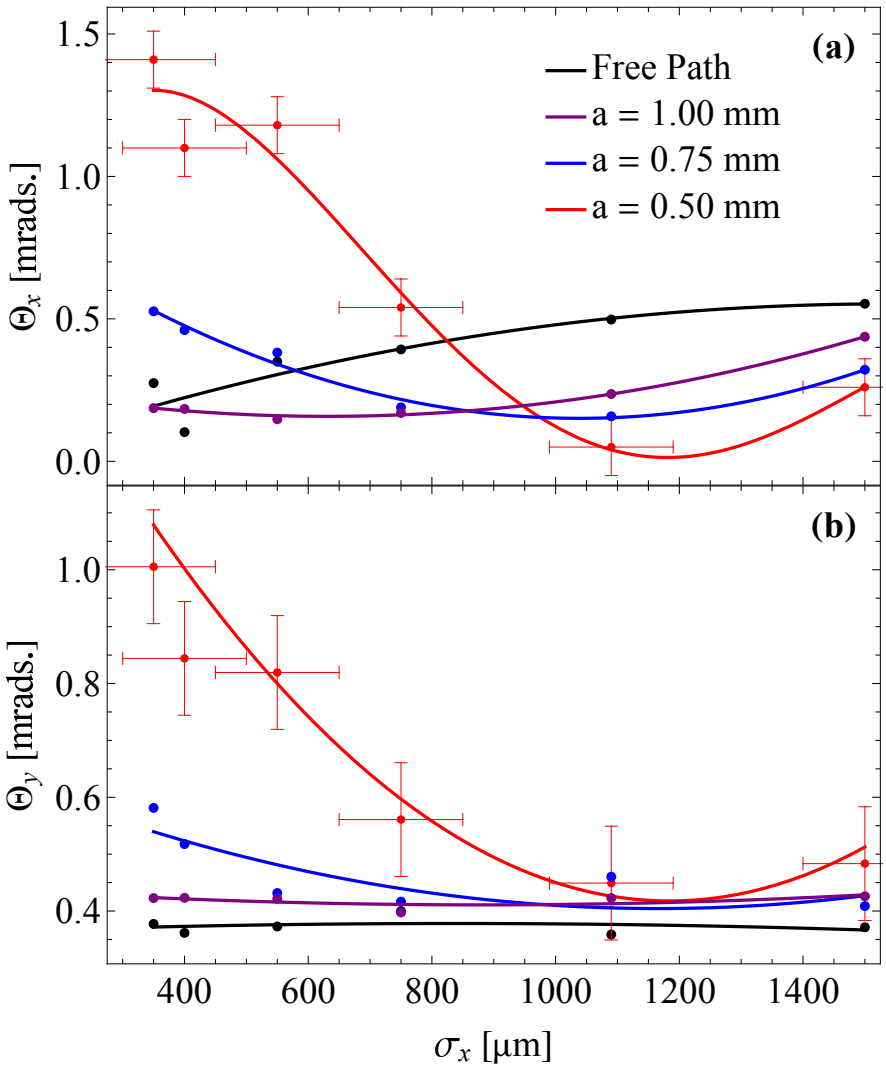

Figure 6.23. Beam divergence in the (a) Horizontal and (b) Vertical plane as a function of RMS beam width on-axis with varying dielectric gap. Solid lines show polynomial fits to the data. Error bars shown for $a = 0.5$ mm are indicitive of errors at other structure gaps and have not been shown to aid legibility. Bunch length is 800 fs.

interpreted as divergence only if the beam waist is upstream of S-04. With $a = 0.5$ and 0.75 mm the trend crosses the free path case suggesting that indeed for some values of σ_x the waist is between the two screens.

Complex behaviour of the transverse beam dynamics in the horizontal plane is further illustrated in Figure 6.24 where the beam sizes on screens S-04 and YAG-02 are given as a function of beam width at the DLW (S-03). The beam here is always divergent from the structure position in a free path but this changes when the DLW is inserted. Small σ_x bring the beam to a horizontal waist upstream of S-04 and the waist moves onto S-04 at $\sigma_x = 0.72$ mm. Further increase in σ_x moves the waist towards YAG-02 which is reached at $\sigma_x = 1.1$ mm. After that, the beam size on YAG-02 is approaching the free path beam size. This behaviour provides a clear indication that the average horizontal field, $\langle F_x \rangle$, diminishes while the beam size at DLW increases.

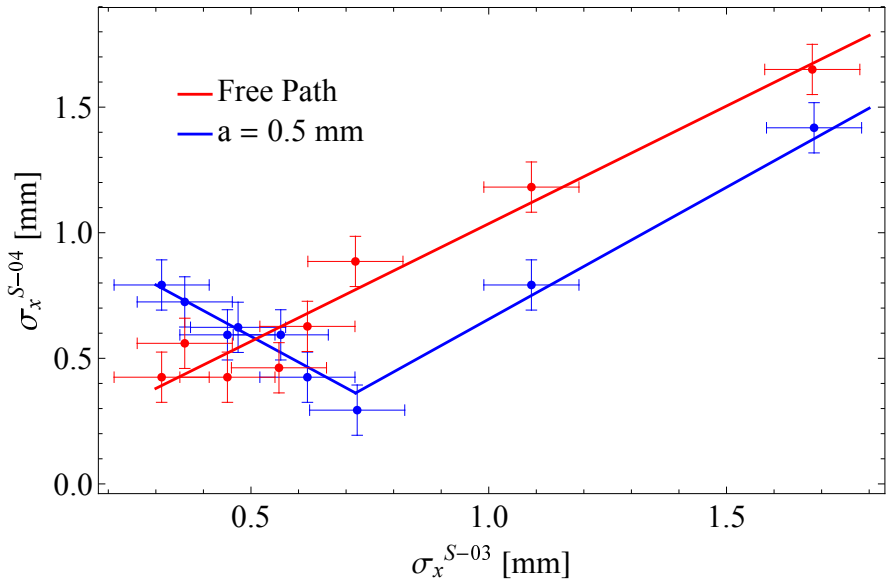

(a) S-04

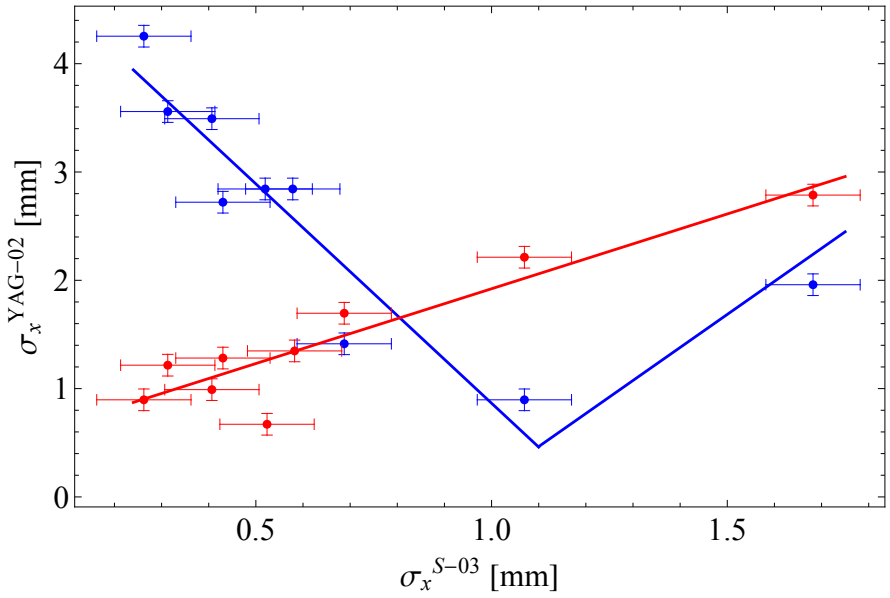

(b) YAG-02

Figure 6.24. Horizontal beam width downstream as a function of beam width at S-03 in the free path case and on-axis in the planar DLW with a = 0.5 mm. Bunch length is 800 fs.

The beam focal length is the propagation distance at which the total beam size is minimised. The simulated focal length as a function of σ_x for 3 structure gaps is shown in Figure 6.25. With $a = 0.5$ mm, the beam is at the waist at S-04 and YAG-02 with σ_x = 750 and 1200 µm respectively. This supports the results in Figure 6.24. Scaling the focusing force to multiple nC, as required to reach practical accelerating gradients, the beam waist would be after a short propagation distance for all values of σ_x and a. This may have important implications for the practical design of a DWA using elliptical beams, a topic explored in Chapter 7.

Both slice and projected emittances are conserved when the beam propagates through conventional quadrupole magnets. In DLWs, the quadrupole strength varies longitudi-

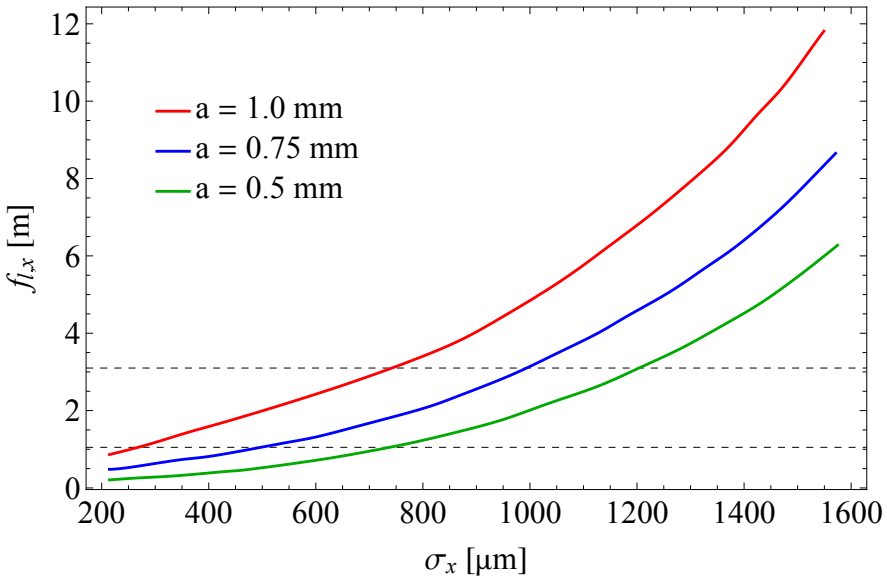

Figure 6.25. Simulated horizontal focal length as a function of RMS beam width for varying dielectric gap. Dashed lines show the distance to S-04 and YAG-02 from the centre of the DLW. Bunch length is 800 fs.

nally (zero at the head and increasing within the bunch). Each longitudinal slice receives a constant quadrupole-like field so slice emittance is conserved (if the field is perfectly quadrupole-like) however projected emittance is not preserved. Emittance dilution as the beam propagates diminishes the ability to control a beam with conventional quadrupole magnets, for example to keep a drive bunch elliptical over long distances. Examples of the horizontal phase space, reconstructed from slit scans, with the beam propagating in free path and in the DLW with $a = 0.5$ mm are shown in Figure 6.26. The focusing quadrupole-like wakefield clearly transforms the main body of the beam from divergent to convergent. The transverse phase space also show that F_x is non-linear across the wider beams (in particular $\sigma_x = 0.75$ mm) and toward the beam edge. Projected emittance growth is seen with the DLW in for all beam widths, with the dependence of the projected emittance on horizontal beam width shown in Figure 6.27. As expected from simulations, the emittance growth increases with beam size.

6.5 Conclusions and Discussion

The work presented in this chapter provides extensive experimental benchmarking of the wakefields given by analytical functions in [119] and implemented in DiWaCAT against the experimentally measured results. Benchmarking of DiWaCAT with experimental results demonstrates the applicability of a lightweight code in modelling the transverse beam behaviour in DWAs at higher charge and energies required at future DWAs.

Cylindrical DLWs may be advantageous for DWA, since stronger longitudinal wakefields

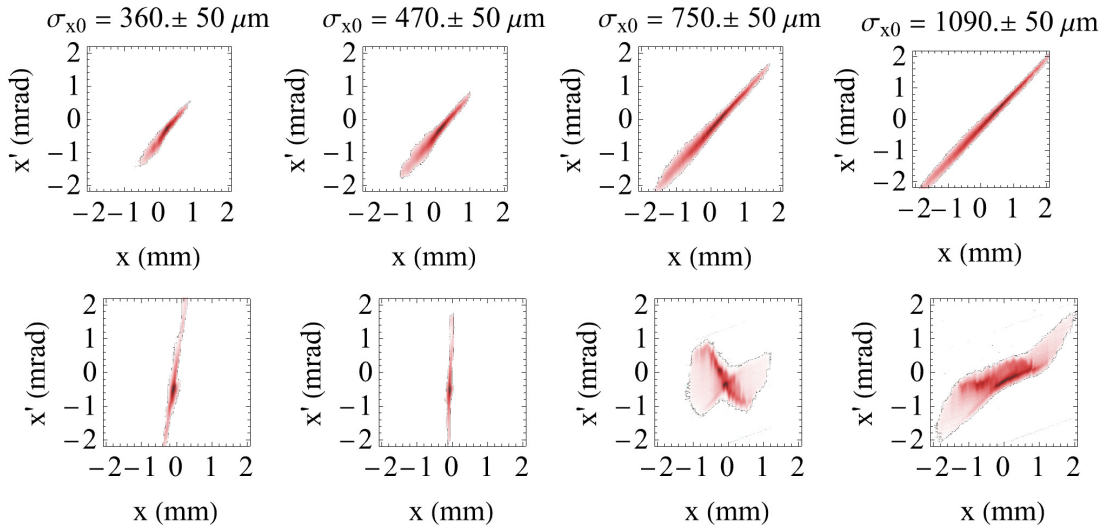

Figure 6.26. Reconstructed horizontal phase space of the beam propagating in the free path (top) and through the planar DLW with a = 0.5 mm (bottom) for various RMS beam widths. Bunch length is 800 fs.

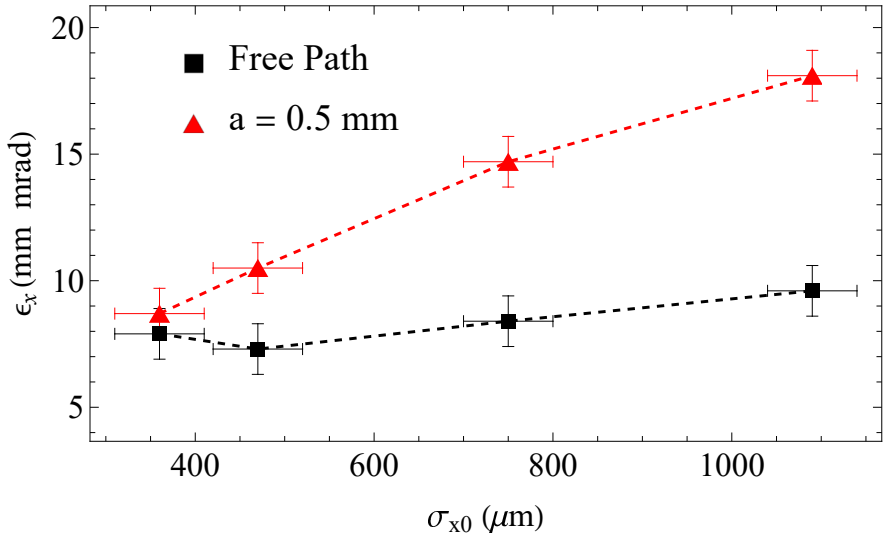

Figure 6.27. Horizontal projected emittance as a function of RMS beam width. Bunch length is 800 fs.

are excited in DLWs of the same size. Measurements presented in this chapter showed agreement, within measurement accuracy, to the theoretical ratio of fields excited in planar and circular DLWs [149][115]. Dipole-like fields are excited with the beam off-axis in planar and circular DLWs and approximately equal in strength as the beam propagates closer to the dielectric plate, suggesting a negligible difference in BBU development between planar and circular DLWs.

Transverse wakefields on-axis in circular DLWs require further study, with quadrupole-like wakefields a potential further cause of instability alongside dipole-like fields for a beam offset from the DLW centre. Beam asymmetry would have implications for currently suggested methods of BBU suppression in circular DLWs such as the use of a quadrupole wiggler [77].

Planar DLWs are known to excite strong quadrupole-like wakefields and the strength

of these fields with varying DLW structure gap and beam offset have been shown. The effect of these fields can be negated by using a series of orthogonally orientated DLWs [111][90][91][92][89]. Simulations of the behaviour of this DWA geometry are presented in the following chapter.

Transverse wakefields are reduced in planar DLWs when using an elliptically shaped beam. The suppression of higher-order modes with elliptical beams has been shown to match theoretical expectations and demonstrated by increased suppression at increased beam offsets. However, the quadrupole-like fields excited are still present even if reduced. Projected emittance growth, due to horizontal focusing, increases with ellipticity due to non-linear $F_x(x)$. Over long distances, this will degrade beam quality. Non-symmetric and non-linear focusing/defocusing limits the application of elliptical drive beams to a single DLW stage. Scaling the average focusing to the charge of proposed future DWAs, the overall beam profile would be brought to a waist after a short propagation distance. In reality the focusing is longitudinally varying so the question of beam behaviour in this regime is more complex. This question motivates the study of a DWA with 'practical' beam parameters, the results of which are presented in the following chapter.

Acknowledgement

The author would like to thank the entire CLARA facility project team, with particular thanks to Y Saveliev, T Pacey, B Muratori, N Joshi, N Thompson, M King, and S Mathisen for support during machine shifts.

Chapter 7

BBU Suppression in a Practical Dielectric Wakefield Accelerator

7.1 Introduction

The work presented in Chapter 6 experimentally investigated the transverse wakefields for a 100 pC bunch with 35.5 MeV/c momentum. The relatively low charge ensured energy spread did not significantly change through the DLW and low momentum ensured transverse field effects were observable. This combination allowed us to take precise measurements of beam properties and the effects of transverse fields in a planar DLW and benchmark DiWaCAT against experimental results. Whilst the results can be scaled to higher charge beams (which would be required for a practical DWA), studies of these higher charge beams are required to evaluate the effectiveness of transverse field suppression methods. DiWaCAT offers a simulation toolkit for conducting such studies, allowing for the tracking of beam dynamics within a DLW, including individual macroparticles and beam slices. The toolkit accurately calculates fields and enables detailed investigations efficiently.

In this chapter, simulations of high charge and high energy drive beams are discussed in the context of two methods for suppression of transverse fields in planar DLWs: elliptical beams and DLWs with alternating orientations. This work will primarily focus on studying the development of the single-beam breakup instability (BBU) caused by an initial small beam offset. Additionally, it will investigate the effect of quadrupole-like wakefields on beam losses and beam quality.

The work presented here only considers a drive beam, rather than the drive-witness beam system required for acceleration. One of the significant challenges for a practical DWA is the transportation of the drive beam over long distances. Stable transportation is crucial to ensure maximum energy extraction from the drive beam and maintain overall accelerator efficiency. Efficient acceleration relies on extracting the maximum energy

from the drive bunch, which necessitates transporting the bunch over multiple metres without significant beam degradation or susceptibility to instabilities.

7.2 Parameters for High Charge Simulations

Two transverse distributions for drive beams have been considered, an elliptical beam (i.e. $\sigma_x > \sigma_y$) with the aim of suppressing BBU and a circular beam (i.e. equal σ_y and σ_x) with small initial transverse size. Beam parameters have been chosen to be reasonably achievable at current facilities, and listed in Table 7.1. One such facility able to produce multi-nC charge electron bunches, with parameters comparable in order to those in Table 7.1, is FACET-II [151]. In order to isolate the effect of transverse wakefields, and minimise the otherwise asymmetric 'natural' divergence, the emittance of the elliptical beam was set to the negligible value of 1 nm rad. For the circular beam case an emittance of 1 mm mrad was chosen as both the effect of the beam optics and transverse wakefield should be considered.

The DWA structure parameters were chosen to excite ~ 100 MeV/m fields for the beam parameters listed. A larger vacuum gap is preferred - to reduce the relative contribution of higher order modes -but this could be reduced if a greater accelerating field were desired. A quartz-like (ϵ_r = 4) dielectric with thickness readily available from suppliers was chosen to demonstrate the feasibility of DWA with conventional materials and manufacturing techniques.

Parameter	Elliptical	Circular
Bunch Charge [nC]	10	
Beam Momentum [GeV/c]	1	
RMS Bunch Length, σ_t [ps]	1	
Longitudinal Skewness	-4	
Vertical Beam Width, σ_y [µm]	50	20
Horizontal Beam Width, σ_x [µm]	500	20
Normalised Emittance, $\epsilon_{x,y}$ [mm mrad]	0.001	1
Dielectric Half-gap, a	1 mm	
Dielectric Thickness, δ	250 µm	
Relative Dielectric Permittivity	4	

Table 7.1. Beam and DLW structure parameters for elliptical and circular high charge bunch simulations.

The transformer ratio (accelerating to decelerating field ratio) can be increased with an optimally shaped longitudinal profile. This increases the efficiency of acceleration, coming at the expense of maximum accelerating field [75]. As discussed in Section 3.3, beams with higher charge towards the tail of the bunch are associated with transformer ratios greater than 2. For a maximal transformer ratio (> 5), a longer bunch with a 'double-triangular' or 'doorstop' shape would be used and bunch length optimised [77][51]. We have chosen to simulate a skewed-Gaussian, with probability density

function given by

$$\rho(t) = \frac{1}{\sqrt{2\pi}} \exp\left(\frac{-t^2}{2\sigma^2}\right)\left[1 + \text{erf}\left(\frac{\alpha t}{\sigma\sqrt{2}}\right)\right], \tag{7.1}$$

where α is the skewness factor, σ is RMS width, and erf(x) is the error function [123]. For these simulations, α = −4 is chosen to estimate a highly triangular bunch, so any beam losses at the tail are immediately evident.

7.3 High Charge Elliptical Beam

7.3.1 Transverse Dynamics

Using an elliptical beam reduces transverse fields, as shown theoretically in Chapter 3 and experimentally demonstrated in Chapter 6. Experimental results highlighted concerns regarding quadrupole and higher-order fields in practical DWAs and their effects over long propagation distances.

For the elliptical beam and DWA structure with parameters in Table 7.1, the maximum accelerating gradient is 105 MeV/m. The transformer ratio, given by the ratio of maximum accelerating to decelerating field is 1.2. However, the maximum decelerating field is outside the bunch; using the decelerating field at the tail of the bunch the transformer ratio increases to 1.44. The longitudinal profile has not been optimised for maximal transformer ratio given the focus of the chapter on transverse dynamics. Optimisation would increase the transformer ratio at the expense of maximum accelerating gradient [75].

Over long propagation distances, with a quadrupole-like field applied, the horizontal beam size of the bunch longitudinal slices should oscillate between a waist and initial beam width. The beam size at the waist is a function of the transverse emittance, and frequency of oscillations is given by the strength of the quadrupole field. To observe this effect, the beam is simulated without the vertical force applied, ensuring long distance propagation without beam losses. The magnitude of the F_x focusing force varies longitudinally, as shown in Figure 7.1(c), so the frequency of beam size oscillations varies longitudinally.

The longitudinal variation of the strength of the focusing force has some important implications for the beam dynamics. A constant quadrupole strength would imply the entire beam is brought to a waist at the same focal length. However, here the focal length is a function of longitudinal position so each longitudinal slice of the beam oscillates

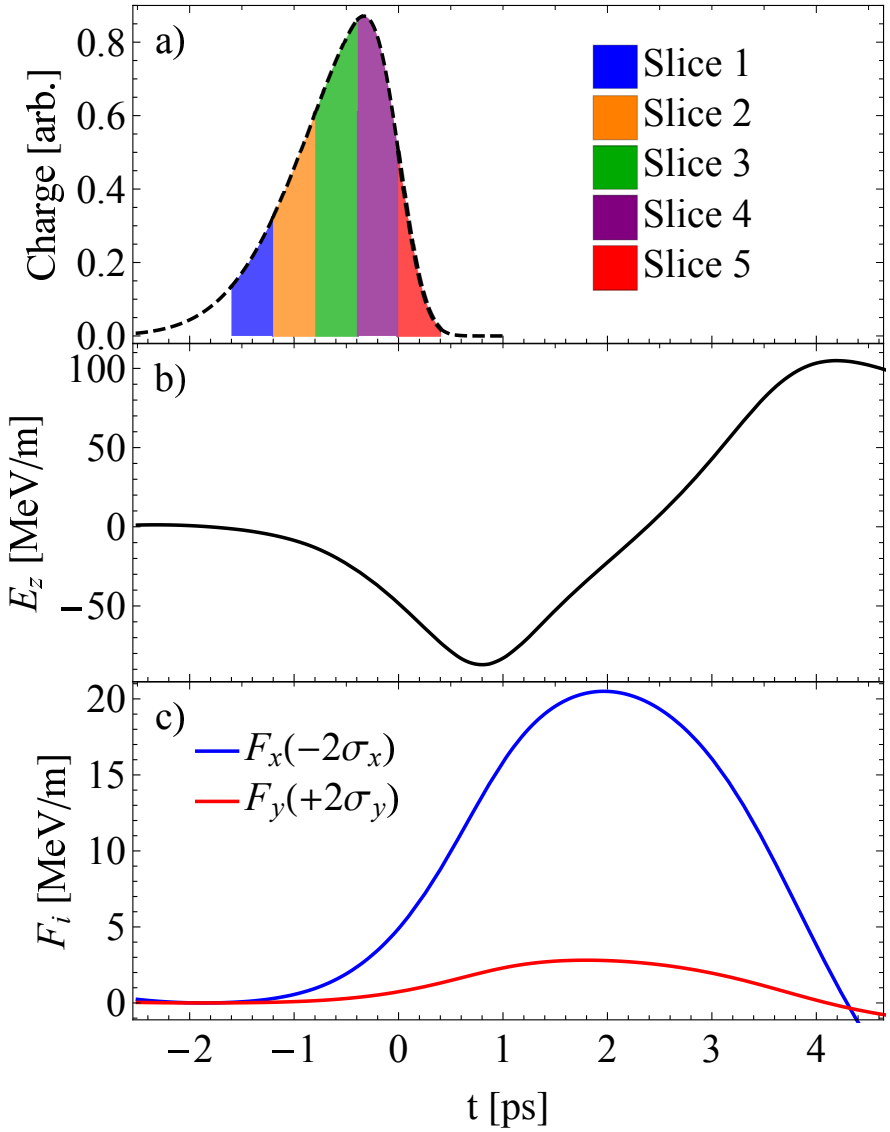

Figure 7.1. Longitudinal (a) charge distribution, (b) longitudinal field, and (c) transverse field profiles for the elliptical beam. The beam head is positioned at the left-handside of the plot.

sinusoidally about a waist with different frequencies. With a perfect quadrupole-like (linear) field, slice emittance would be preserved (for an infinitely thin longitudinal slice) whilst projected emittance would grow due to the longitudinally varying focusing. On a macroscopic scale, the beam width, σ_x is the sum of the beam width of all longitudinal slices. This is also true for the beam width of a longitudinal slice with a finite length, as the beam only oscillates with a constant frequency for an infinitely thin slice. Taking the limit as the slice width tends to zero, this beam width becomes the integral of sinusoidal waves with longitudinally varying frequency. Modelling this for a perfect quadrupole-like field, the strength of which linearly increases from the head, the oscillations can be modelled as

$$p(s, z) = \sin(asz), \tag{7.2}$$

where p is the beam width, s is the propagation distance/time, z is the longitudinal position within the 'bunch', a is an arbitrary number (the gradient of the frequency

increase). A discrete sum of sinusoidal waves would produce a beating wave as the waves constructively and destructively interfere. Instead the integral of $p(s,z)$, P, over a longitudinal slice $a < z < b$ is given by

$$P(s,a,b) = \int_a^b \rho(z)p(s,z)dz, \tag{7.3}$$

where $\rho(z)$ is the bunch distribution. This function is shown for a arbitrary triangular distribution ($\rho(z) = z$) for 3 slice widths in Figure 7.2. In each case the phase difference across the slice width increases over time. With a thin slice, this difference is very small so the beam size continues to oscillate with some reduced amplitude over time. A thicker slice, with large phase difference across the slice exhibits overall damping within some beat wave features. With the largest slice no beating frequency is seen; since the phase difference across the slice is very large after small s the amplitude of the oscillations are strongly damped.

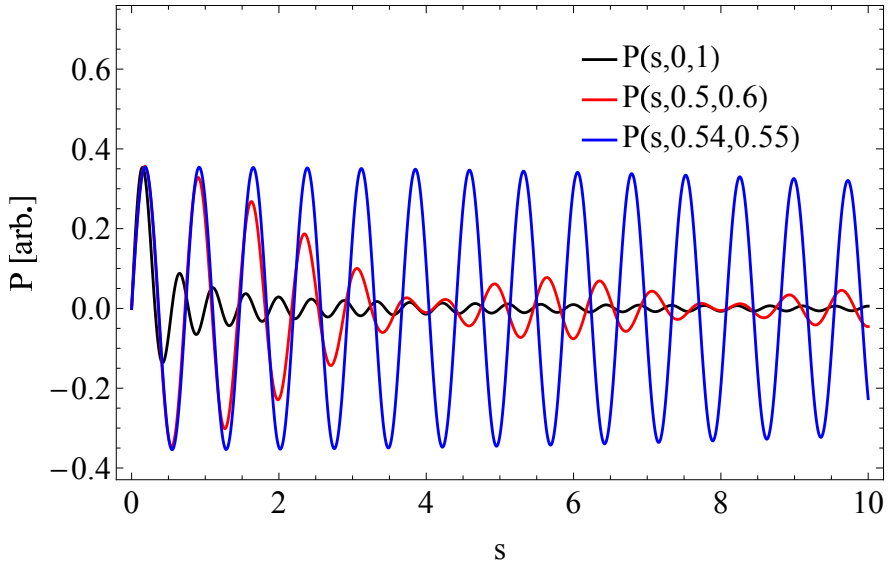

Figure 7.2. Integral of a sinusoidal function with longitudinally varying frequency, given by Equation 7.3, with 3 slice widths.

The behaviour seen with an arbitrary function above can be applied to a beam and beam slices. The evolution of beam width with propagation distance is shown in Figure 7.3, for the entire beam and the longitudinal slices in Figure 7.1(a). For slices towards the tail of the bunch, where F_x is larger, the beam width oscillates with a higher frequency and each slice oscillates with increased damping. This make the total beam width appear over-damped with a constant value of σ_x observed after 1 m.

To maintain a Gaussian horizontal profile within a longitudinal slice, and preserve normalised slice emittance, the horizontal focusing force would need to increase linearly with horizontal position. This would be akin to a ideal quadrupole magnet. The actual horizontal F_x distribution is not perfectly quadrupole-like, with higher-order octupole-

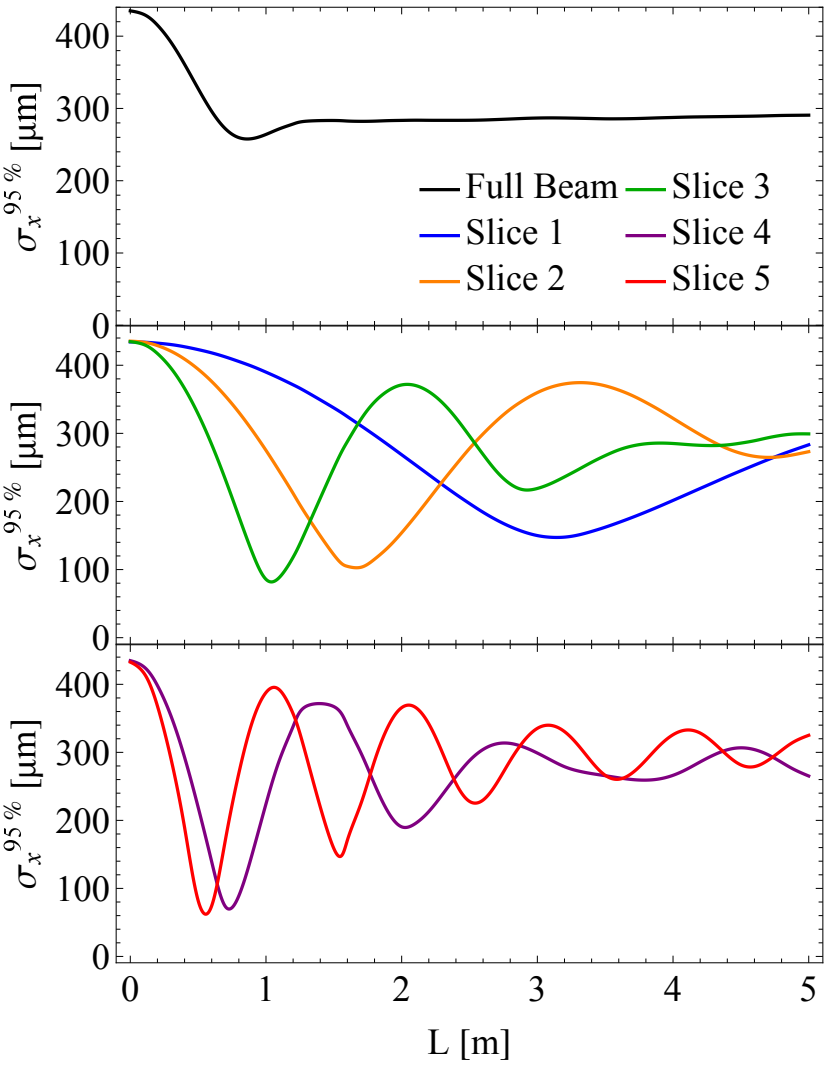

Figure 7.3. RMS beam width, for the 95% innermost macroparticles, for the full elliptical beam and longitudinal slices. The vertical field, F_y, is not applied.

like fields observed, as shown in Figure 7.4. At the beam edge, the horizontal field is reduced compared to the ideal quadrupole at the beam centre. Whilst an ideal quadrupole shears the horizontal phase space, keeping the total phase space volume constant, the reduced F_x at the beam edge will lead to a more spiral phase space shape. This effect is evident when tracking individual macroparticles. In Figure 7.5, the phase space of individual macroparticles with only the F_x force applied is shown. For small values of initial horizontal position, Δx, the force is quadrupole-like so the particle maintains an orbit of constant radius. For larger Δx, the macroparticle does not maintain a constant radius, instead oscillating with changing radii. The closer to the beam centre, the closer these oscillation resemble circular orbits as the offset from a quadrupole field is small, whilst at the beam edge these oscillations are more extreme.

For the entire beam, the damped behaviour seen in Figure 7.3, and deviations from quadrupole-like behaviour contribute to increase both the emittance and kurtosis of the horizontal projected beam profile. After a small propagation distance, the kurtosis

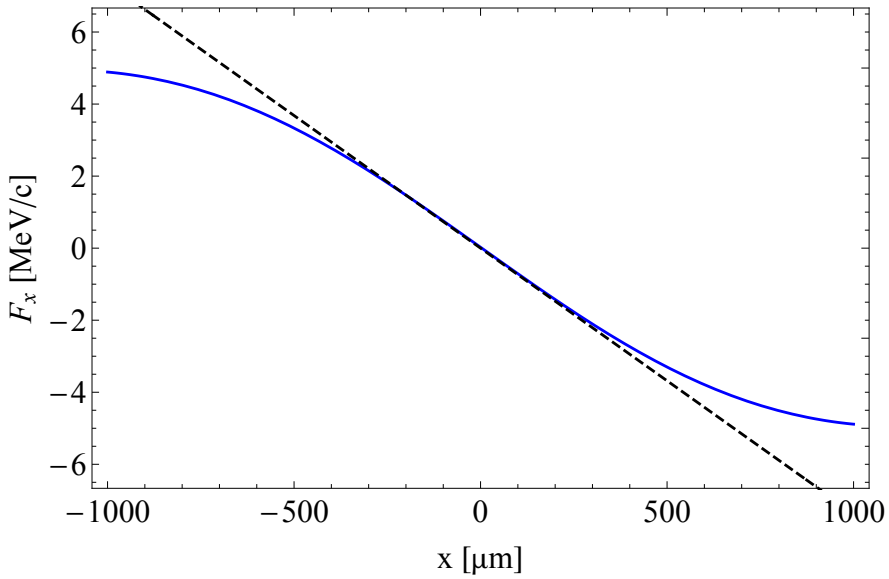

Figure 7.4. Horizontal variation in F_x across the elliptical beam at t = 0. The dashed black line shows the quadrupole field with the same gradient as F_x at x = 0. The RMS beam width is 500 μm.

increases (i.e. higher central charge than for a Gaussian distribution), as shown in Figure 7.6. The $F_x(x)$ profile shown in Figure 7.4 will curve the phase space of an infinitely thin slice over time due to transversely varying focal length. This can be seen with a thin slice (-2$<t<$-1.9 ps), shown in Figure 7.7. The reduced focusing at the beam edges increases the RMS width compared to a perfectly linear field. Considering a Gaussian profile with width equal to the RMS slice width, the centre of the bunch is focused more and beam edge focused less. Therefore, the density of macroparticles at the centre of the slice increases relative to the beam edge so the slice kurtosis increases.

As a result of the transversely and longitudinally varying F_x force, and nature of the F_x force changing the beam profile and increasing emittance, it would not be reasonably feasible to use conventional magnets to control the beam horizontally. A large energy chirp would be required to account for the longitudinally varying transverse fields. As the drive beam energy decreases as the beam propagates through the DWA stage this chirp would change, complicating the beam dynamics. Non-linear (i.e. octupole-like) components to the focusing field would cause both projected and slice emittance growth, further complicating the optics that would be required. Therefore a single elliptical bunch would only be able to be used over a single DWA stage, with multiple elliptical drive bunches required for long distance acceleration.

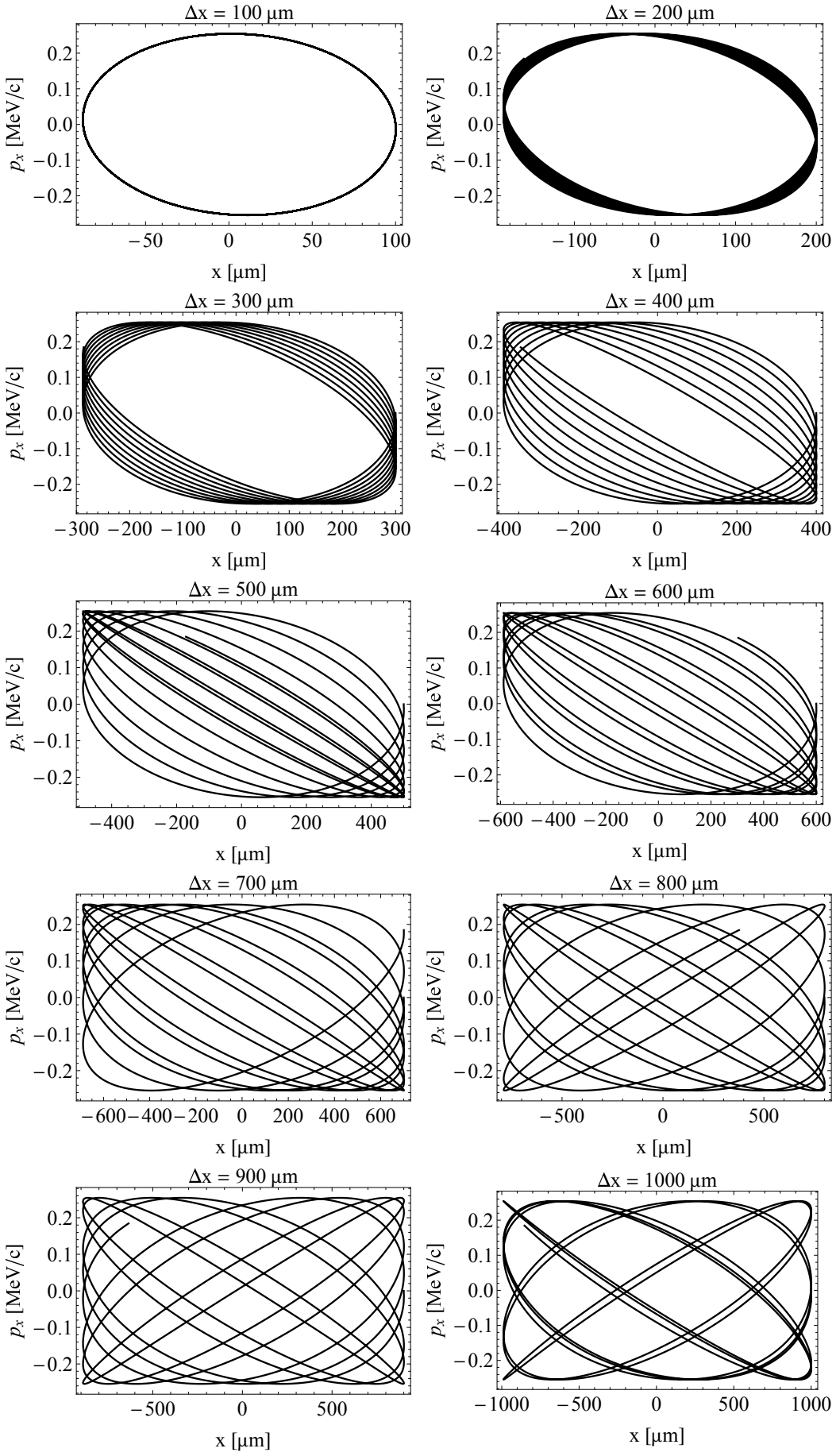

Figure 7.5. Phase space over 20 m for individual macroparticles with initial $(x, y, t, p_x, p_y, p_z) = (\Delta x, 0, 0, 0, 0, 1\ \mathrm{GeV/c})$. Particles are tracked with only the F_x field applied.

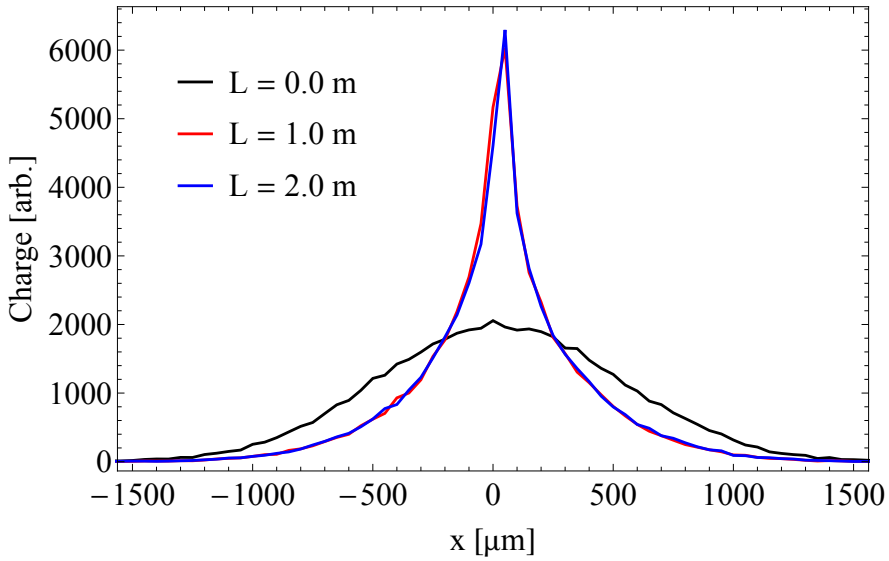

Figure 7.6. Horizontal beam profile, for varying propagation distances within the DLW. Vertical field, F_y is not applied to macroparticles.

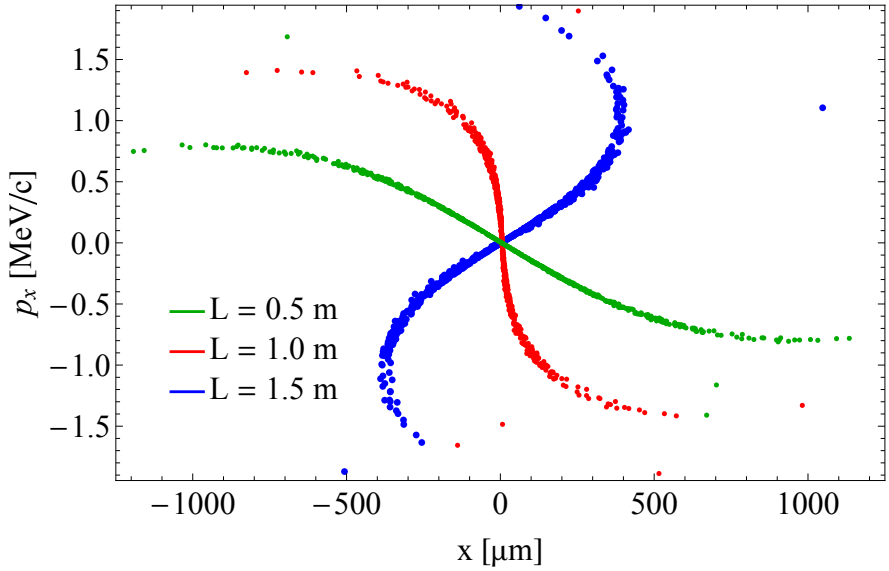

Figure 7.7. Horizontal phase space positions for macroparticles with longitudinal position -2< t <-1.9 ps, for varying propagation distances within the DLW. The vertical field, F_y is not applied to macroparticles.

7.3.2 Charge Losses and BBU

Charge losses are caused by two factors: the beam defocusing until the beam reaches the dielectric boundary, or a small initial offset from the beamline axis leading to the beam kicked towards the dielectric plate. The cause of such offsets would be for example beam pointing jitter and/or DLW misalignment. In both cases the direct cause of beam losses are vertical fields towards the dielectric plate. To simulate a small initial offset, y_0 = 50 μm was chosen. This offset is comparable to the vertical beam size and small relative to the overall beam size, so a reasonable estimate of beam positioning accuracy in a DWA.

The amount of charge transported along the DLW is shown in Figure 7.8 with $y_0 = 0$ and 50 µm, with the circular bunch also shown. For the elliptical beam in both cases, charge losses start at $L \sim 1$ m. The contribution of higher-order modes, suppressed by an elliptical beams, increase close to the dielectric plate. With the beam off-axis, the beam centroid is streaked towards the dielectric plate increasing the excitation of these higher-order modes. In comparison, when the beam defocuses whilst on-axis the beam centroid remains on-axis so the contribution of higher-order modes remains smaller. As a result of this, elliptical beams suppress BBU to a greater extent than they suppress beam losses due to on-axis defocusing. With y_0 = 50 µm, the amount of beam lost at L = 1.5 m is reduced by 50% (2.4 nC compared to 4.8 nC) whilst for the beam on-axis the reduction is $\approx$ 20% (0.82 compared to 1.05 nC).

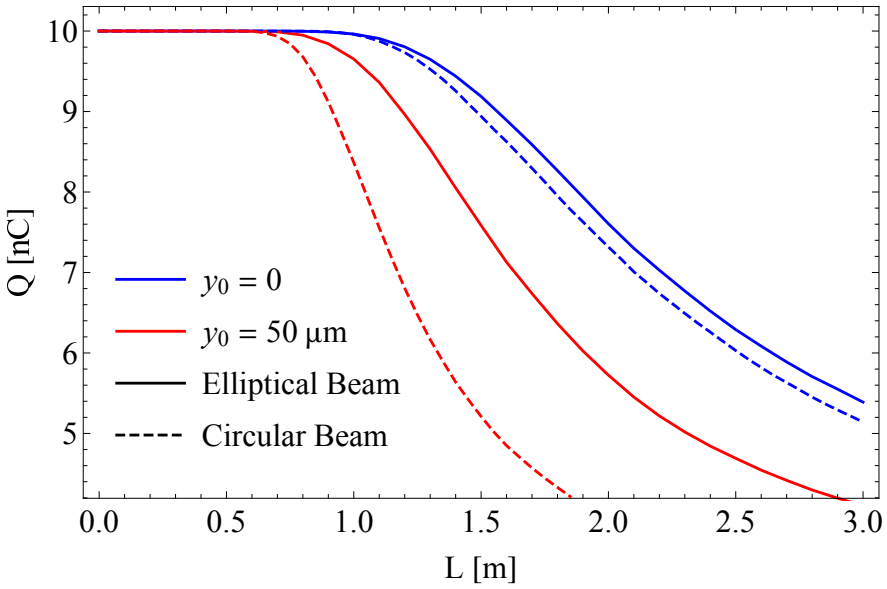

Figure 7.8. Total charge transported for elliptical (solid line) and circular (dashed line) within a DLW on-axis and with initial vertical offset 50 µm from centre.

Transverse forces cannot solely be considered independently, i.e. focusing forces effecting beam quality and defocusing/kicking forces cause beam losses. Instead each force is dependent on the 3D position within the bunch, i.e. $F_x(x, y, z)$ and $F_y(x, y, z)$. As discussed in Chapter 3, $F_y(x)$ is maximised towards the centre of the bunch. The focusing force therefore reduces the bunch ellipticity, reducing transverse force mitigation, and pushes particles towards regions of higher defocusing/kicking fields. To isolate the impact of the focusing forces, simulations were conducted with the F_x applied and set to zero in all places. Charge losses in both cases with the beam propagated on-axis and offset in the DLW are shown in Figure 7.9. In both cases, charge losses are greater with F_x applied.

With F_x applied, the beam is focused towards the beam centre reducing the beam width and therefore reducing the ellipticity of the beam. This reduces the mitigation of F_y, increasing the rate of charge loss. $F_y(x)$ is also maximised towards the beam centre so

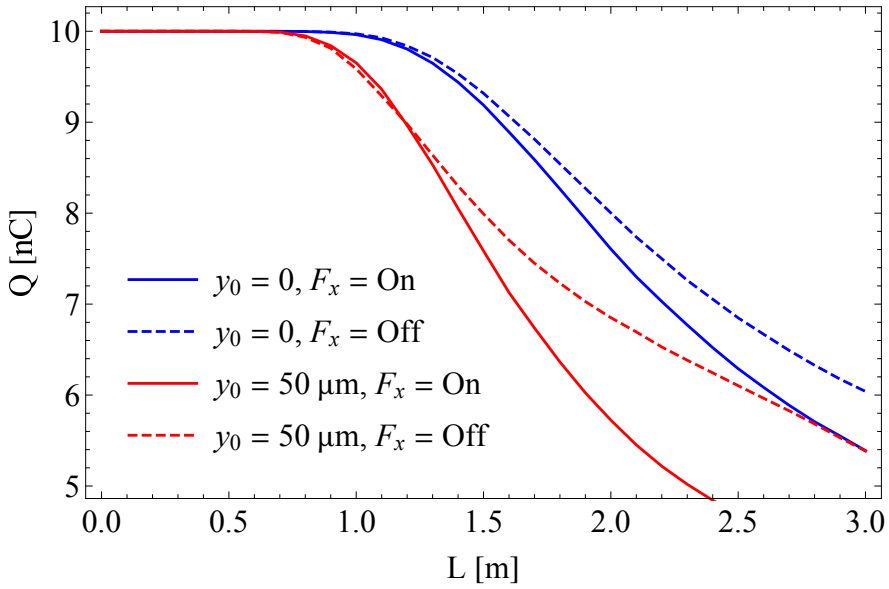

Figure 7.9. Bunch charge as a function of propagation distance within the DLW, on-axis and offset 50 µfrom centre, with the horizontal force applied and with $F_x(x, y, t) = 0$.

the focusing force kicks particles towards a region of higher F_y, also increasing the rate of charge loss compared to the case where no horizontal kick is applied.

The beam profiles for the bunch on-axis and with y_0 = 50 µm are shown in Figures 7.10 and 7.11 respectively. Given F_y is largest at the tail of the bunch, beam losses are first seen here. Two forms of beam losses can be clearly seen in the two particle distributions; on-axis the beam losses are symmetric and always present, caused by defocusing quadrupole-like fields, whilst with a small offset the BBU instability causes the beam to be kicked towards the dielectric plate in the direction of the offset.

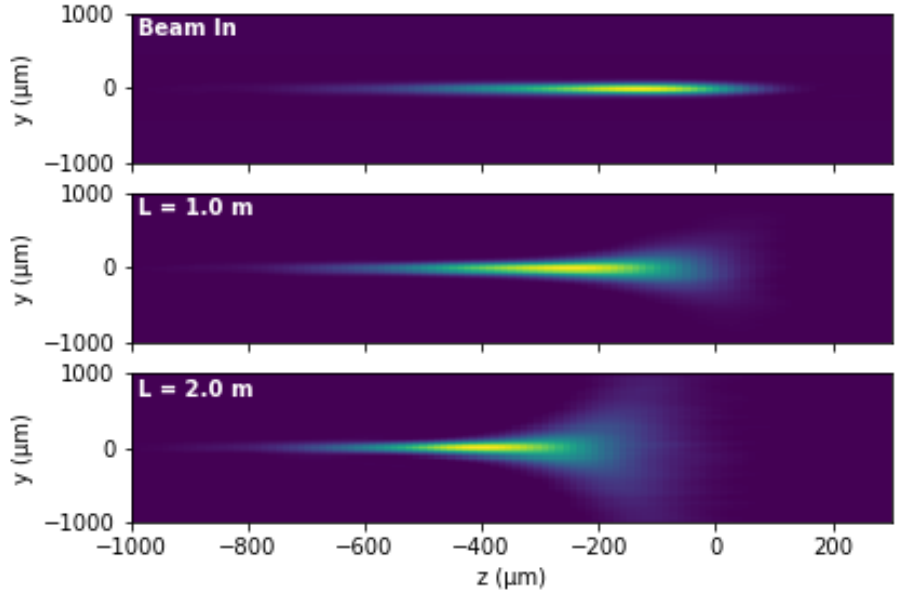

Figure 7.10. Longitudinal-vertical bunch profile, for elliptical bunch on-axis in a DLW, at various propagation distances.

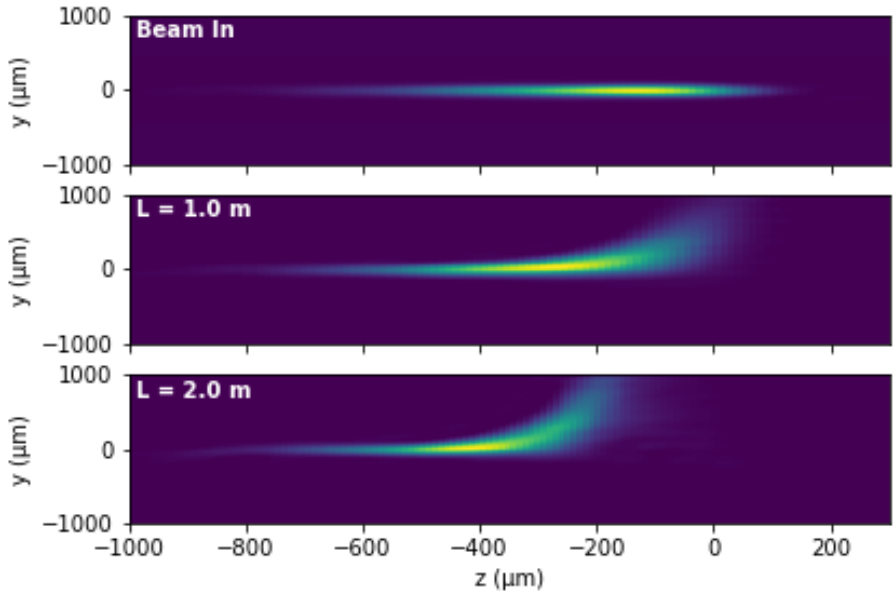

Figure 7.11. Longitudinal-vertical bunch profile, for elliptical bunch with initial vertical offset 50 µm from DLW centre, at various propagation distances.

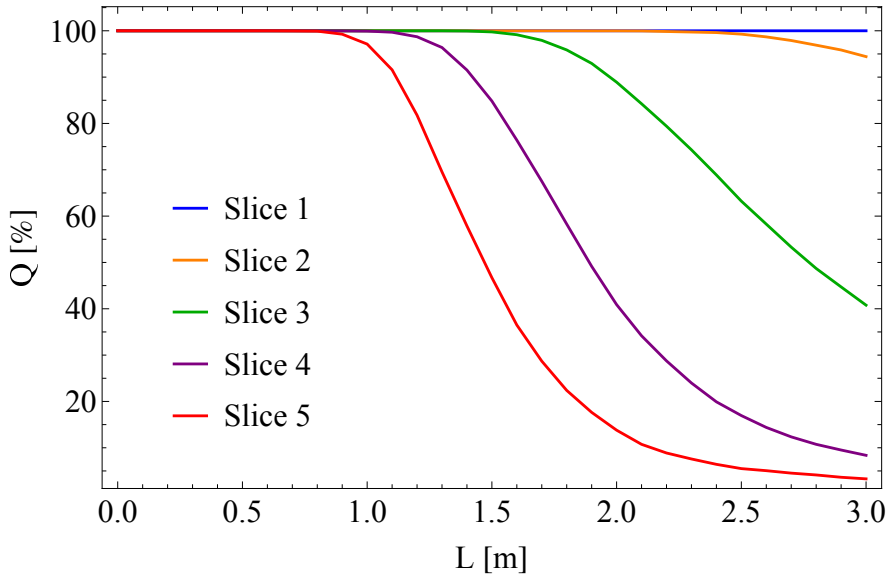

Figure 7.12. Percentage charge transported in longitudinal slices, defined in Figure 7.1(a), for an elliptical beam on-axis in a DLW.

Beam losses for each longitudinal beam slice are shown in Figure 7.12. Greater beam losses are seen at the bunch tail, with the slices at the tail completely eroded by ≈ 2 m of propagation. Charge losses reduce the accelerating field excited behind the bunch and shorten the bunch length. The beam has lost $\sim$50% of the initial charge by 3 m of propagation. However, at this point slices 4 and 5 (shown in Figure 7.12) have been completely eroded. Therefore, the total bunch length has been reduced by 40%.

An elliptical beam with $\sigma_x = 500$ µm would not be suitable for DWA over long propagation distances, and alternative methods to reduce transverse fields and BBU effects must instead be considered. Further increase in σ_x would increase the propagation distance

by further suppressing transverse fields, however this would be at the expense of longitudinal field strength and introduce further non-linearity into the focusing quadrupole-like fields. The 2D transverse wakefields, $F_y(x, y)$ and $F_x(x, y)$, are a significant source of losses including on-axis. This reduces the propagation distance of an elliptical drive beam, setting a limit on the energy extraction from a drive bunch and therefore overall DWA efficiency.

7.4 Transverse Field Cancellation with Alternating DLW Orientation

For the beam and structure parameters used in this Chapter, beam losses caused by on-axis transverse fields start within 1.5 m of beam propagation for both elliptical and circular bunches (Figure 7.8). Therefore, on-axis transverse fields must be compensated to achieve acceleration of a main bunch over multiple metres.

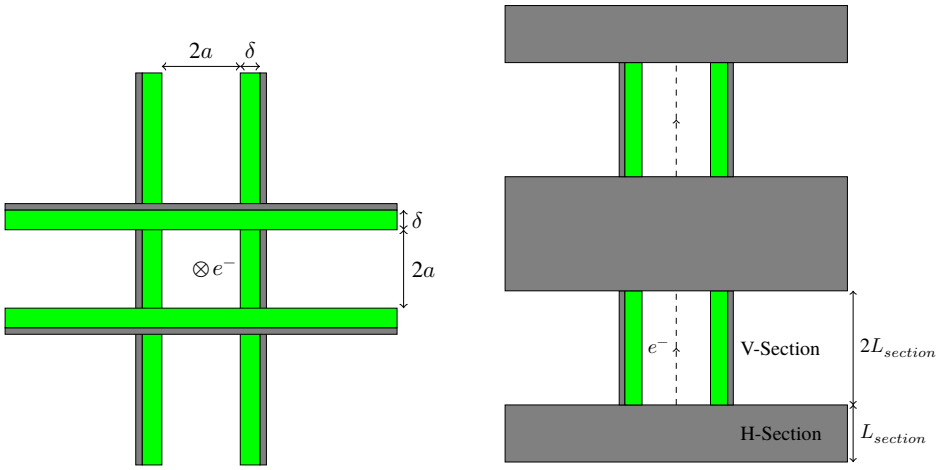

(a) Beam propagating into the page.

(b) Beam propagating from top to bottom of the page.

Figure 7.13. H+V layout with two orientations.

A circular beam propagating on-axis in a planar DLW, with beam size small compared to the structure gap, will excite approximately symmetric focusing and defocusing forces.

The on-axis transverse quadrupole-like fields can be cancelled using a series of alternating orthogonal horizontal and vertical DLWs (H+V), with layout as in Figure 7.13 [88], [90], [91][152]. The symmetry of the quadrupole-like fields are therefore used to maintain transverse beam properties over long propagation distances. Simulations here have been conducted with the parameters listed in Table 7.1. An accelerating gradient of 112 MeV/m is excited behind the drive bunch, with the same transformer ratio as with the elliptical bunch, as shown in Figure 7.14.

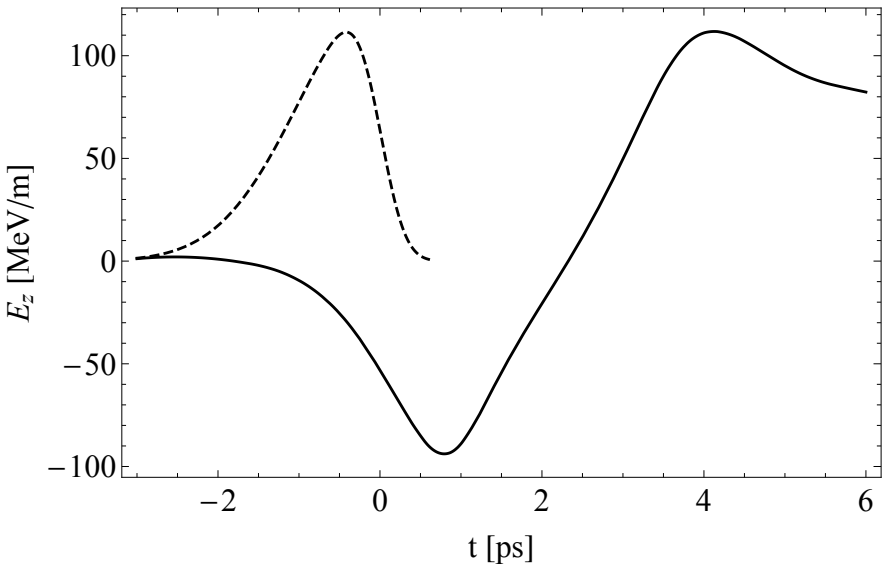

Figure 7.14. Longitudinal profile produced by the circular bunch, with beam and DLW parameters as in Table 7.1. The longitudinal profile is given by the dashed line.

For clarity, each DLW will be referred to as a single section orientated horizontally (H-section) or vertically (V-section). These sections will be combined to form one 'cell', with beam properties equal in/out of each cell. These cells will then be combined in series to form an acceleration stage/module, multiple metres in length.

The length of each cell must be set to cancel both the transverse field and change in beam size. In each section, the transverse fields increase/decrease the transverse momentum of each particle. A simplified case is constant field applied to a single particle. Sections of equal length effectively cancel the change in transverse momentum, as shown in Figure 7.15(a). However, in this case the momentum is changing beam position in one direction. As shown in Figure 7.15(c), the particle position increases quadratically in the first section and the gradient decreases linearly in the second section. Whilst the momentum has been cancelled, the beam has only been kicked in one direction so the effect of the field has not been cancelled. A second V-section kicks the particle in the opposite direction, the effect of which is cancelled in a final H-section. With this layout both momentum and position equal at the start and end, as shown in Figures 7.15(b) and (d). Rather than H+V+H it is sensible to consider this setup as a cell of 4 sections H+V+V+H (with V+V being formed of one contiguous piece) instead so each section length is equal.

For the simple setup in Figure 7.15 the force applied was constant so the only criteria was that the length of the second section be twice the length of the first (H+V+V+H). In reality, the transverse force is a function of transverse position and beam size; variation in beam size between sections will lead to the force applied in one section not equalling the force applied in the next. If the section length is too long, the initial (de)focusing will

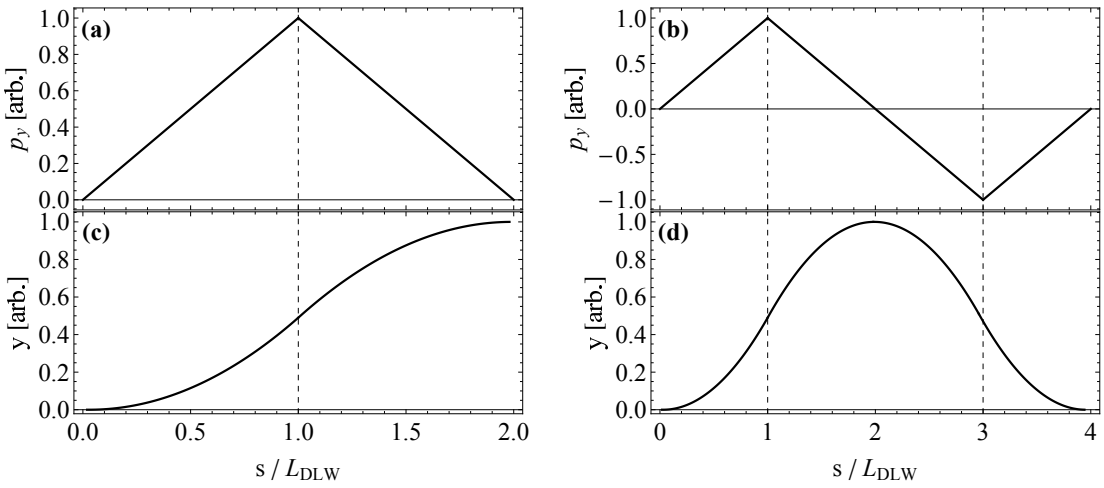

Figure 7.15. Transverse momentum and position of a single particle as a function of propagation distance, normalised to the length of the first section. A constant force is applied which changes sign with changing structure orientation, shown by dashed lines in each plot. (a) Transverse momentum with two DLWs of equal length (H+V). (b) Transverse momentum for 3 sections with the second twice the length of the first and last (H+V+V+H). (c) Transverse position with two DLWs of equal length (H+V). (d) Transverse position for 3 sections with the second twice the length of the first and last (H+V+V+H).

not be completely cancelled by the following section. This is a function of the transverse field strength and therefore structure gap. For effective cancellation, the force applied by each section must equal the force applied by the previous section. Taking the example of the initial horizontal focusing force, after the beam is focused in the H section the beam size at the subsequent V-section will be reduced. The subsequent $F_y(y)$ is smaller close the DLW centre so the defocusing will also be reduced. In the vertical transverse plane, initial defocusing would lead to a slightly elliptical beam at the start of the subsequent section. Ellipticity in the plane parallel to the dielectric plate reduces transverse fields in both planes and reduces the amount of cancellation that occurs. This would lead to an overall focusing/defocusing effect given by the orientation of the first section. The ideal scenario would be for the phase space of each particle to orbit in a circular motion. This is achieved by minimising the change in beam size over each section with a shorter section length, as shown in Figure 7.16. A perfectly circular orbit cannot be completely achieved however shorter sections minimises the effect to negligible amounts, especially when considering the initial transverse momentum distribution of a real beam. With each section length 10 cm, the change in beam size over one cell is 1.07 μm. By halving the section length the change is negligible, 38 nm. Extending this to even shorter sections, the design and manufacture of each cell becomes more complex. Alternatively, cancellation could be achieved by changing the length/gap of each section along an accelerating stage however this would require optimisation across the entire stage and likely impractical.

For simulations over longer distances, a section length of 5 cm has been chosen. A long distance DWA stage/module could be arranged as in Figure 7.17, with all sections

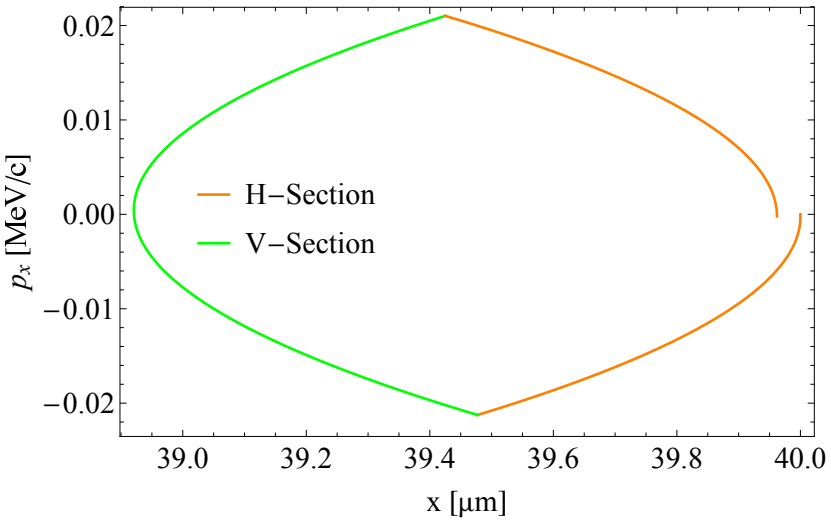

(a) $L_{section}$ = 5 cm

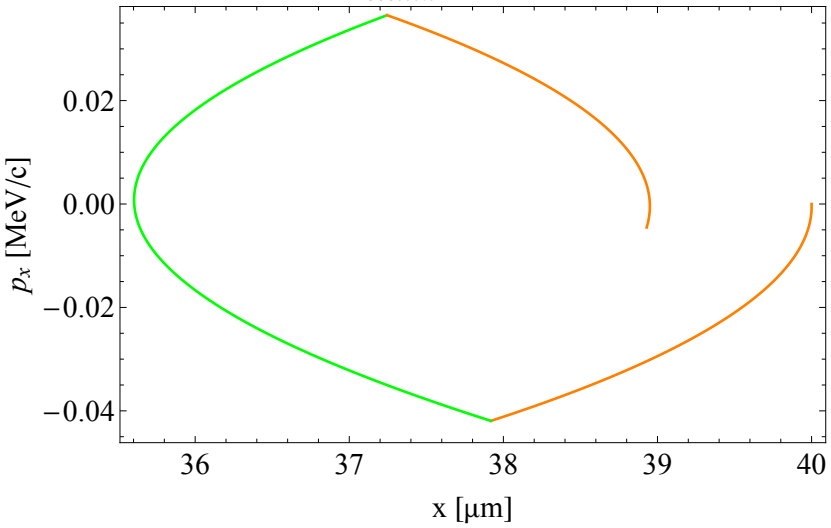

(b) $L_{section}$ = 10 cm

Figure 7.16. Phase space of a single particle, with initial (x, p_x) = (40 μm, 0), over a complete H+V section. A complete section in this context is a H-section of length $L_{section}$, followed by a V-section of length $2L_{section}$, and a final H-section of length $L_{section}$.

with the same orientation connected and controlled collectively. This approach has also been chosen for experiments with a H+V setup at AWA reported in 2023 [92]. With such a setup, all horizontal and vertical sections can be aligned with each other, and all sections would require the same gap, so control of each section would not be required. Alignment to the beam would take place once in each plane and the beam centred on-axis in horizontal and vertical directions.

The beam parameters over a metre-scale stage should be compared to the initial beam in free path. As shown in Figure 7.18, horizontal and vertical beam sizes are kept approximately equal to the initial beam drifted an equal distance. The same can be said of the projected emittance, as shown in Figure 7.19. Emittance increases by 20% to 1.2 mm mrad at the end of the DWA stage. The projected emittance changes within a section as a consequence of the longitudinally dependent focusing, which causes a

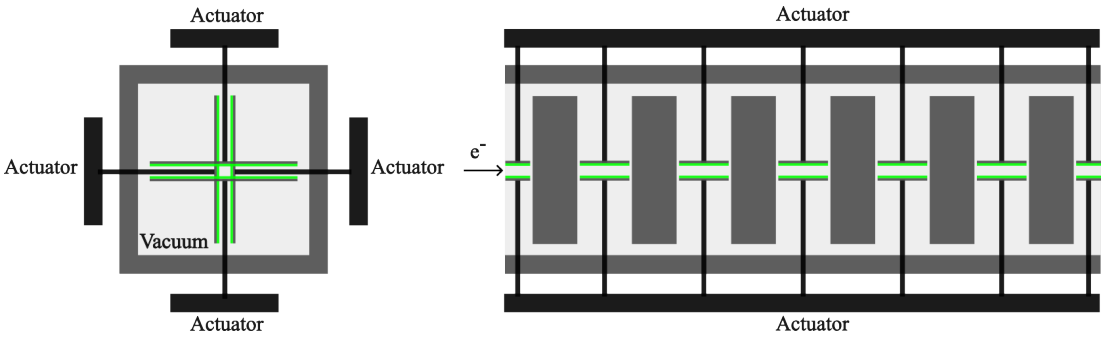

Figure 7.17. Schematic of a DWA module, consisting of multiple H+V DLW sections. DLWs with the same orientation are controlled by a single set of actuators to control the dielectric gap and on-axis position of each section.

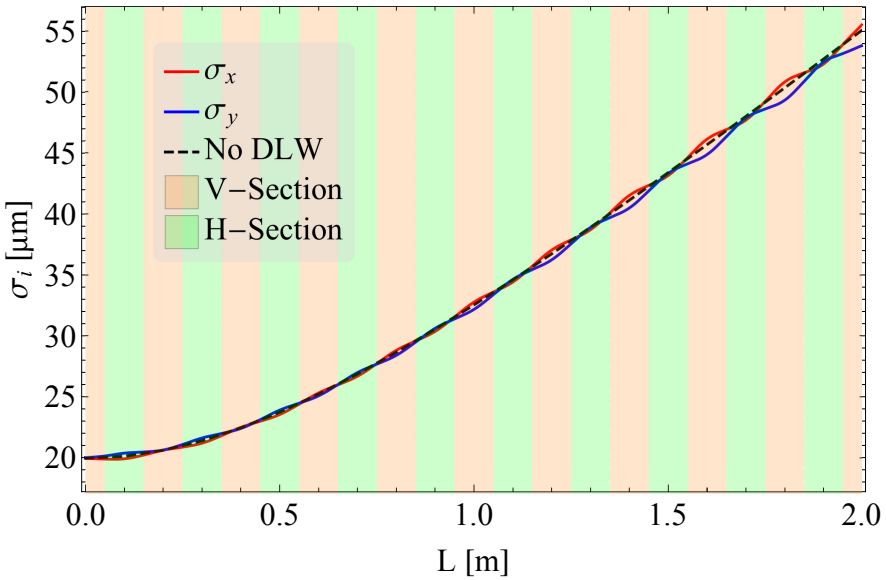

Figure 7.18. Horizontal and vertical RMS beam size, within a 2 m DWA stage consisting of multiple H+V sections. The beam size for the beam drifting equal distance is shown with a dashed line.

longitudinal variation of the slice Twiss parameters. The variation in projected emittance within each section does increase over time; over the first 1 m the variation in normalised emittance is 0.1 mm mrad whilst in the final section the variation is 0.65 mm mrad. Given simulations are with a perfectly symmetrical Gaussian transverse profile, and the initial beam is set with a waist at the entrance of the DWA stage, the increase in variation over each section has been given further consideration.

The increase in projected emittance over the 2 m can be attributed to non-linear transverse fields, as was the case for elliptical beams. This effect is much smaller than with elliptical beams; the variation from a linear quadrupole-like field for circular beams (Figure 7.20) is much smaller than an elliptical bunch (Figure 7.4). The variation from a linear quadrupole-like field increases with beam size. Therefore, as the beam size increases due to natural divergence as the beam propagates in a H+V setup, the variation from a perfect quadrupole-like field increases. Since these fields are not fully cancelled the rate of projected emittance growth increases with propagation distance.

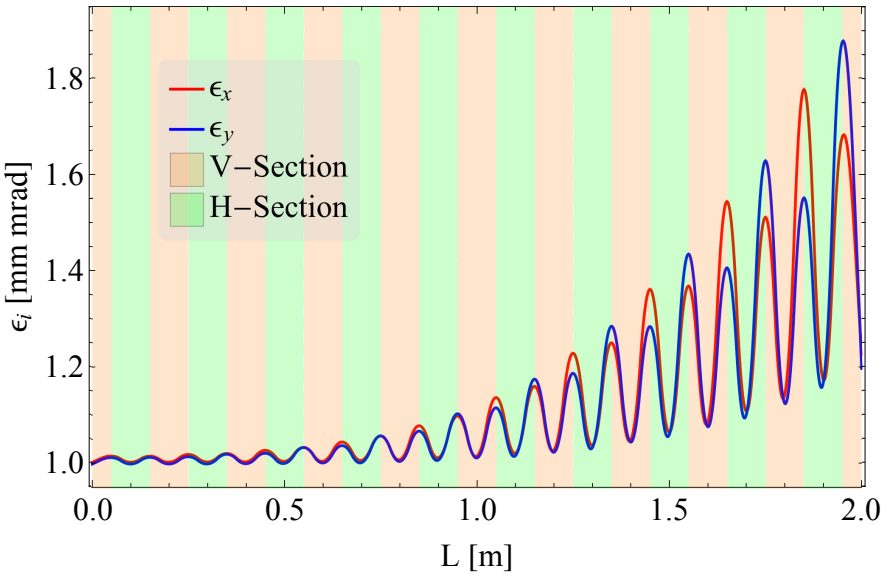

Figure 7.19. Normalised horizontal and vertical emittance, within a 2 m DWA stage consisting of multiple H+V sections.

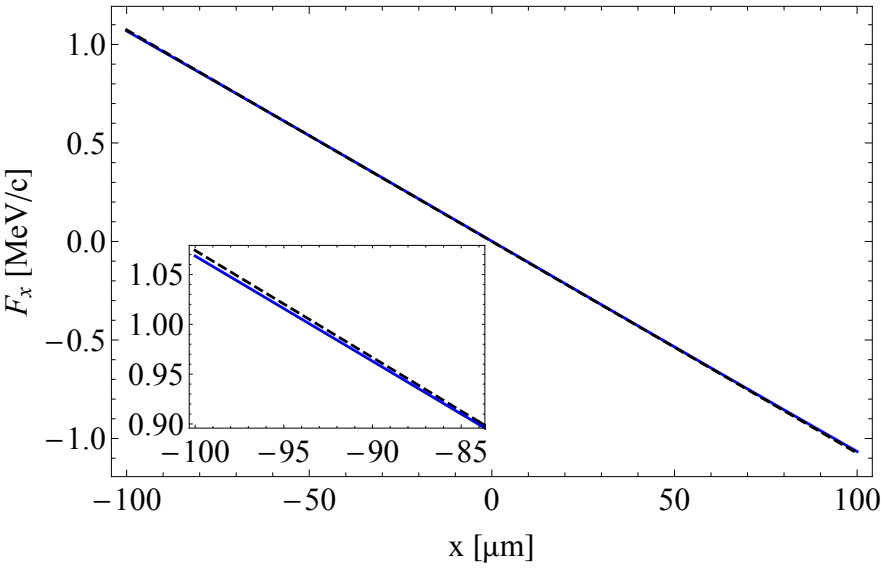

Figure 7.20. Horizontal variation in F_x in a H-section at $t = 0$. The dashed black line shows the quadrupole field with the same gradient as F_x at $x = 0$.

To demonstrate the origins of projected emittance increase, three scenarios are compared after 2 m of propagation: no DLW (i.e. free path), a 2 m long horizontal DLW, and a H+V setup with each cell as before (5 cm section length). As shown in Figure 7.21, the horizontal and vertical phase spaces are approximately equal in the free-path and H+V setup. With a single horizontal DWA stage, not only is the beam defocused vertically (as seen in the vertical phase space) leading to beam losses, but the horizontal phase space shows varying degrees of focusing, manifesting in a non-elliptical horizontal phase space. This can be seen for the total beam profile in Figure 7.21 and at each longitudinal slice in Figure 7.22. Over multiple H+V cells the phase space is constant for each slice which is not the case with a single horizontal DLW. There are small deviations in vertical phase space between the free path and beam after the H+V stage, seen at the beam

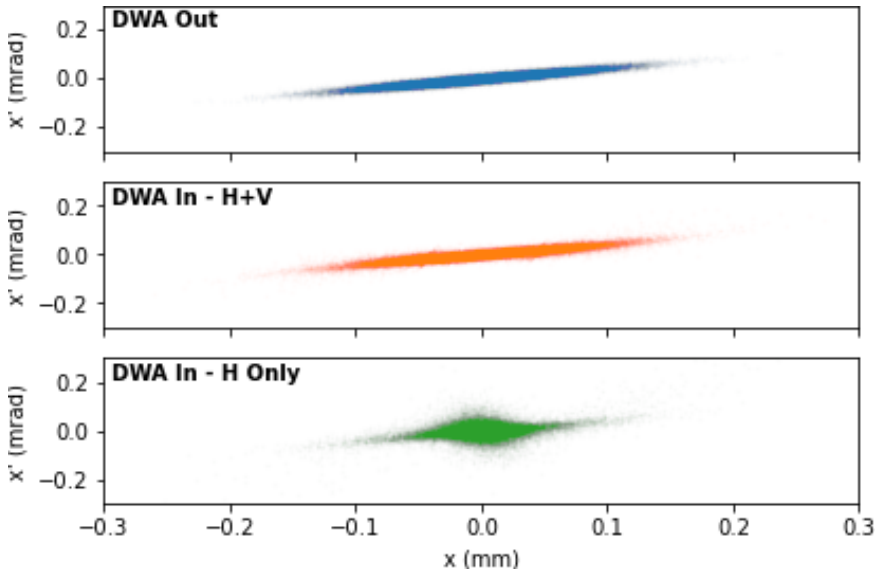

(a) Horizontal phase space.

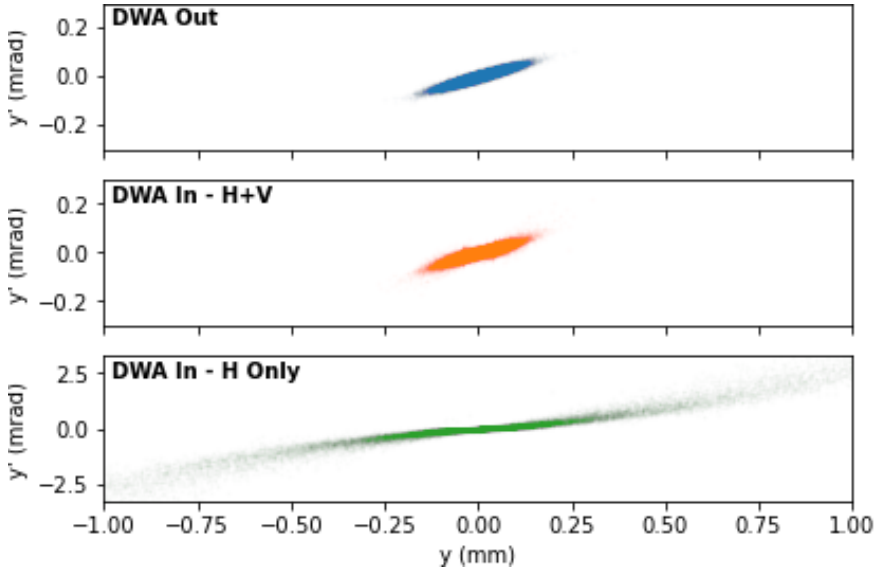

(b) Vertical phase space.

Figure 7.21. Phase space of the initial beam propagating 2 m in drift-space, multiple H+V sections, and a single horizontal DLW.

edge, which explains the small growth in emittance through the H+V stage. The beam parameters are effectively conserved and listed for the 3 cases in Table 7.2, with an average momentum loss of 48 MeV/c over the 2 m. A smaller average momentum loss is observed for the horizontal DLW, as particles at the tail are lost first and these receive the greatest decelerating field (shown in Figure 7.14).

Given the H+V sections only cancel the effects of each other, the total DWA stage cannot replace the role of conventional magnets in a beamline. Beam divergence and beam size must still be controlled using quadrupole magnets, as is the case with an RF linac at a conventional accelerator. Given the physical size of the DLWs these could either surround the waveguides or be placed before/after each DWA stage. The exact design of the beam lattice would need to take into account the longitudinally

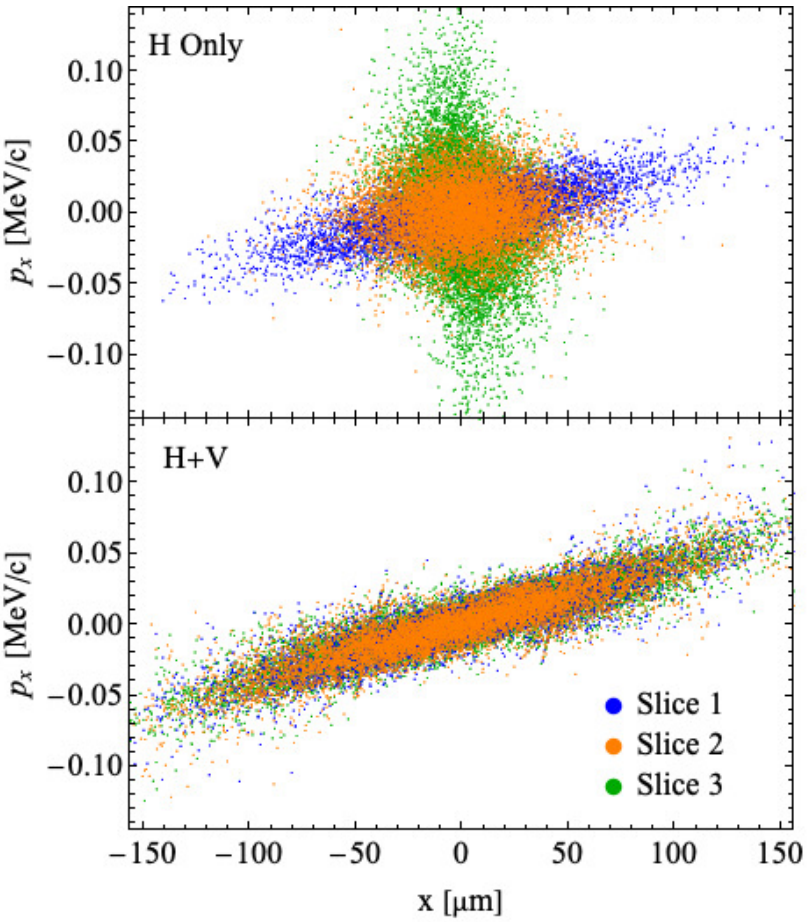

Figure 7.22. Horizontal phase space after 2 m propagation in multiple H+V sections and a single horizontal DLW for each longitudinal slice. Each slice position is given in Figure 7.1(a)

Beam Parameter	No DWA	H+V Stage	H Only Stage
Beam charge [nC]	10	10	7.3
Average Beam Momentum [GeV/c]	1	0.952	0.976
RMS Bunch Length σ_t [ps]	1	1	0.562
Vertical Beam Width, σ_y [μm]	54.8	53.8	302.7
Horizontal Beam Width, σ_x [μm]	55.1	55.5	44.6
Vertical Normalised Emittance, ϵ_y [mm mrad]	1	1.22	116.4
Horizontal Normalised Emittance, ϵ_y [mm mrad]	1	1.20	5.19

Table 7.2. Beam parameters after 2 m with no DWA stage, a H+V stage, and single H stage. Initial beam and DLW parameters are listed in Table 7.1.

varying deceleration. No field is excited at the head of the beam whilst the rest of bunch decelerates as the bunch propagates. The longitudinal profile can be shaped to produce a more monotonic deceleration however the head of the bunch will still have approximately constant longitudinal momentum. Multiple DWA stages could be used with a single drive beam to maximise energy extraction, with optics used to match the beam entering each stage (taking into account the reduced energy over propagation distance). Given the beam parameters have been preserved in/out of this 2 m long simulations, there is no reason to suggest this setup could not be extended to multiple 10s of metres, providing the energy of the drive beam is large enough.

7.5 BBU Suppression with Alternating DLWs

When a beam propagates off axis in a DLW it receives a longitudinally varying transverse kick. An example of this 'streaked' beam can be seen in Figure 7.11. As discussed in Section 7.3, beam losses will begin at the tail of the bunch where the kick received is greatest.

The transverse field at a position within the bunch is excited by the particles in front of that position (as must be true given causality). Quadrupole-like fields are centred on the beam centroid position with focusing forces steering the beam towards the beam centroid. If a beam is streaked, due to an initial offset, in the first H-section, the beam centroid will be longitudinally varying. This is shown in Figure 7.23, with the beam centroid always closer to the axis than the change in beam position at each longitudinal position. Therefore, the beam is offset compared to the quadrupole zero-cross point. Instead of being a purely focusing force the field will steer particles towards the central beam position, as in seen when propagating off-axis in a quadrupole magnet. Given the change in beam position in the H-section will likely be smaller than the initial offset and quadrupole-like fields on-axis are typically weaker than dipole-like kicks off-axis, this effect is likely to mitigate for BBU effects rather than completely eliminate them.

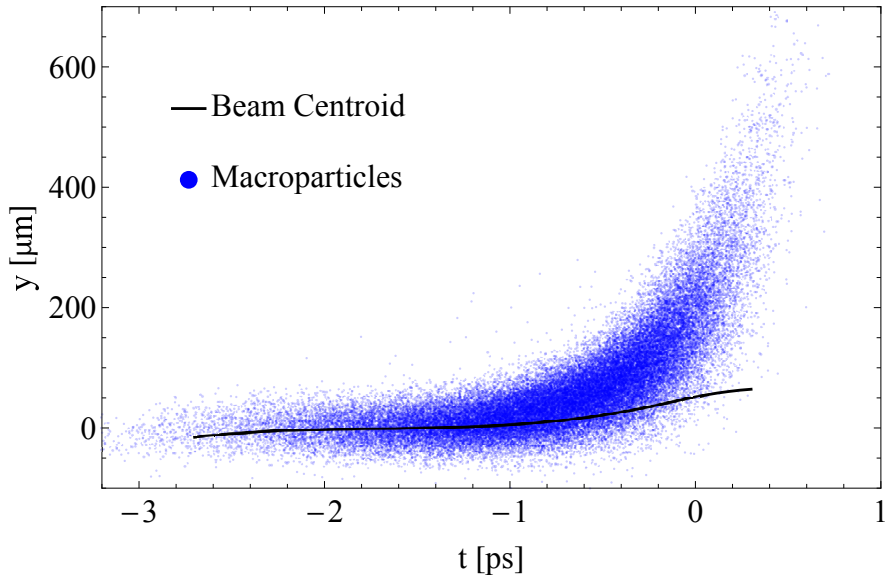

Figure 7.23. An example streaked beam, with the beam centroid, defined as the mean vertical position of all macroparticles towards the head, given by the solid line. The black line is the zero-point of the quadrupole-like focusing force in the following section.

To evaluate this effect and determine whether BBU suppression occurs, two scenarios have been considered. Using a circular beam, with parameters listed in Table 7.1, and H+V setup with 5 cm section length, beams have been simulated with an initial vertical offset of 10 and 50 µm. This will streak the beam vertically in the H-sections. Without the H+V setup, beam losses began at $L = 0.45$ m, as shown in Figure 7.8. When referring

to longitudinal slices, these will match those referenced in Figure 7.1(a).

Directly comparing the charge transported over 2 m stage, as in Figure 7.24, partial BBU suppression is observed. With y_0 = 50 µm, charge losses begin at 1 m, double the distance with a single DLW. Beam losses begin after the same length of horizontally orientated DLW, however without the vertically orientated DLWs the addition of drift space between each section would cause beam losses to occur earlier. For y_0 = 10 µm, beam losses amount to 0.2 nC over 2 m and do not begin until L = 1.75 m.

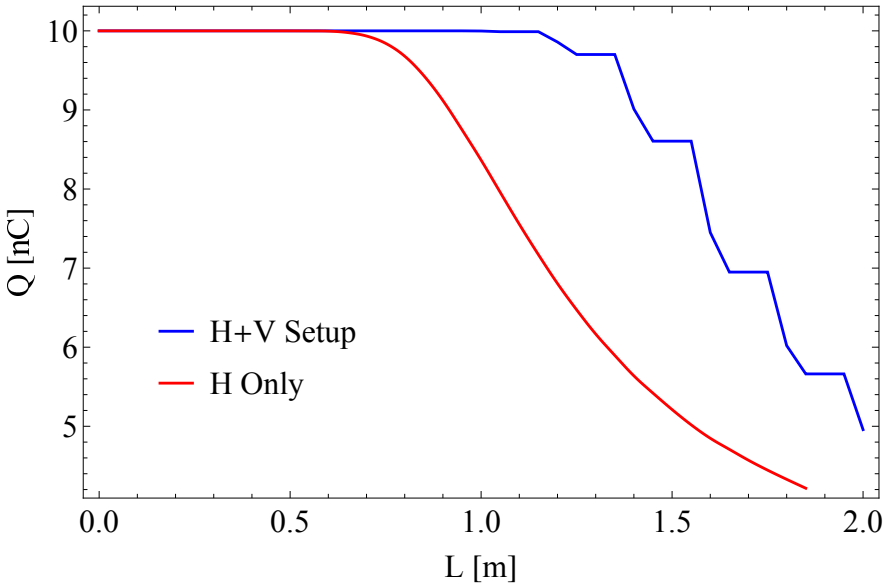

Figure 7.24. Charge transported in a single DLW and multiple H+V sections, with an initial vertical offset 50 µm from the DLW centre. For the H+V setup, no charge is lost in vertical sections.

The mean particle position and momentum, for the entire beam and each slice (Figures 7.25 and 7.26), illustrates how the suppression occurs over the first 1 m. As expected, the vertical (/correcting) section reduces but does not cancel the initial kick. Instead, the focusing force decreases the rate at which $\langle y \rangle$ increases with propagation. This is evidenced by the average vertical momentum of the beam and each slice in Figure 7.26; the average momentum is reduced by the vertical sections (therefore suppressing BBU) but never reduces the vertical momentum below zero. Therefore, at no point is the beam travelling away from the dielectric plate in the horizontal sections. Given higher momentum particles are lost first, the average momentum of the whole beam in Figure 7.26(b) does not increase once slices 4 and 5 are lost.

The correction each vertical section applies is proportional to the kick, as shown by the increasing amplitude of momentum oscillations over distance in Figure 7.26. This is a result of the distance from the focusing zero-cross point increases as $\langle y \rangle$ increases. The BBU suppression caused by a H+V layout increases the allowed beam alignment and jitter tolerances at the start of each DWA stage without charge losses.

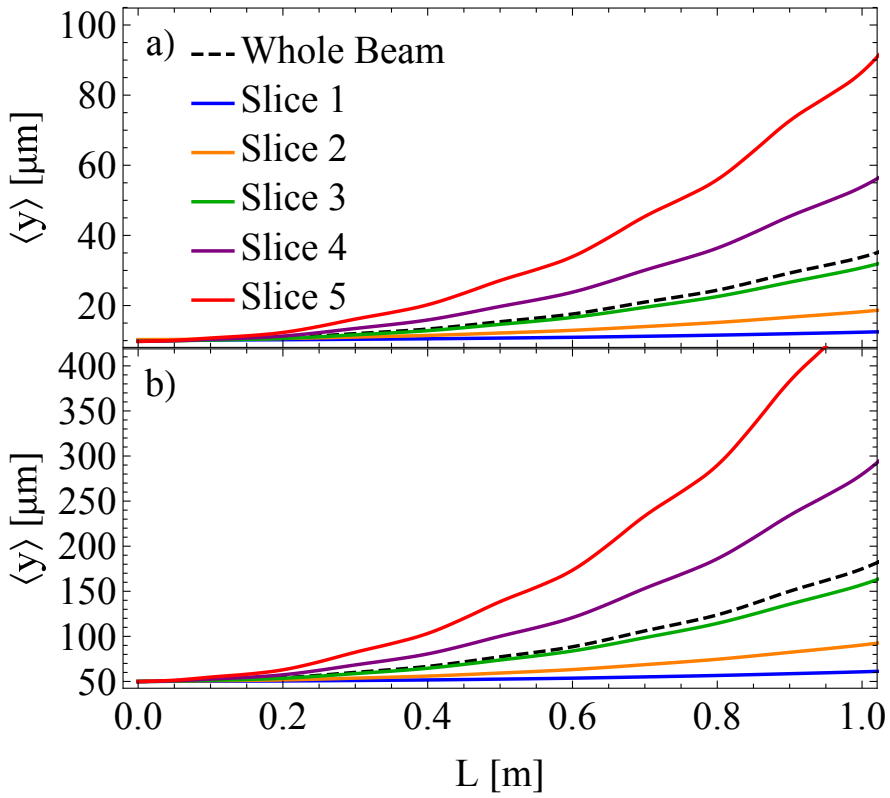

Figure 7.25. Average vertical position for the whole beam and each longitudinal slice for (a) y_0 = 10 μm and (b) y_0 = 50 μm.

7.6 Summary and Conclusions

7.6.1 Summary of Findings

Beam losses in a planar DWA are caused by both off-axis dipole-like fields and on-axis quadrupole-like fields. Both of these fields must be considered for DWA to be feasible over multiple metres. An elliptical beam does suppress the deflecting fields leading to BBU, however it has been shown that quadrupole-like fields reduce this effect and limit the length of DWA stages with an elliptical drive beam. Conversely, a H+V setup can control the quadrupole-like fields but provides comparatively limited suppression of deflecting forces.

From experimental results in Section 6.4 it was concluded that quadrupole-like fields would limit the propagation of elliptical beams over long distances. These conclusions have been confirmed with higher charge simulations. Longitudinally varying quadrupole-like fields, which deviate from a linear relationship with transverse position, degrade the beam quality over time and increase both projected and slice emittance. Defocusing fields for a beam on-axis still lead to beam losses and are suppressed less than off-axis fields. Focusing fields reduce BBU suppression as an elliptical beam propagates and contribute to increased beam losses. These beam losses limit the potential propagation

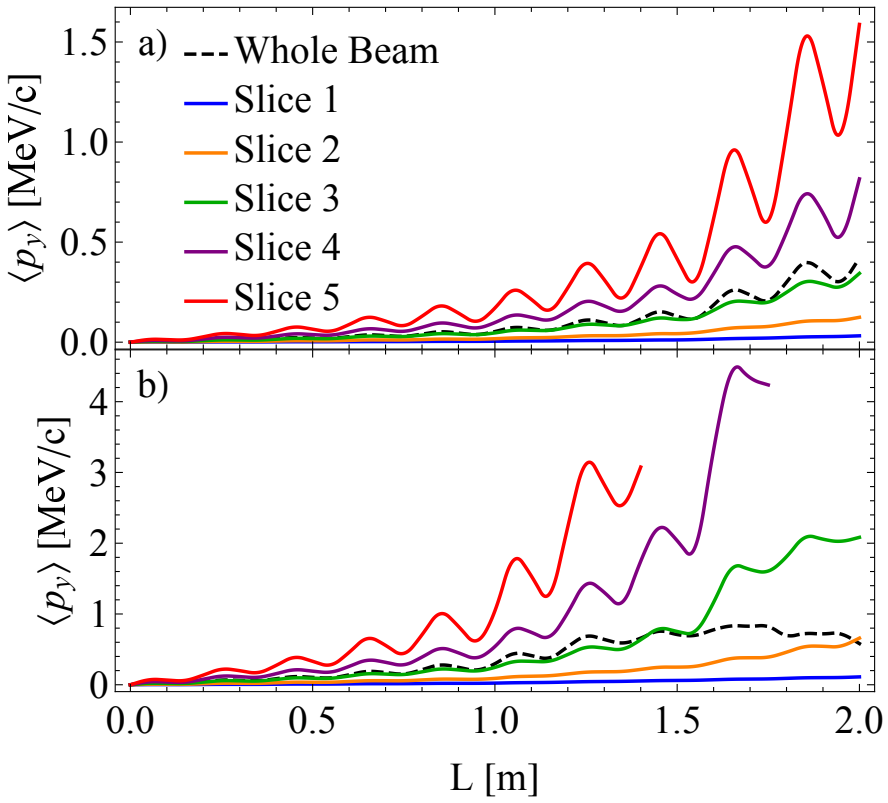

Figure 7.26. Average vertical momentum for the whole beam and each longitudinal slice for (a) y_0 = 10 µm and (b) y_0 = 50 µm. In (b), lines stop when there are no macroparticles in the particular slice.

length of an elliptical drive bunch, limiting the energy transfer possible from an elliptical drive bunch to a witness/main bunch.

Alternating DLWs in a H+V setup can be used to exploit the quadrupole-like fields and minimise beam losses due to defocusing towards a dielectric plate. It is possible to set the parameters of each DLW section to keep the beam properties approximately unchanged compared to the beam in free path.

For a beam propagating on-axis, a H+V setup effectively cancels the transverse fields. The alternating field polarity also mitigates for off-axis kicks caused by small offsets in beam position from the beamline axis. This does not eliminate BBU effects caused by small initial offsets, but does provide a level of BBU mitigation. For the beam and DLW parameters in this chapter, the tolerance in initial beam position would be less than 10 µm to ensure no charge losses over 2 m of propagation. With these beam and DLW parameters a witness/main bunch could be accelerated by ∼200 MeV over this distance. Higher accelerating gradients would decrease tolerances given increasing transverse fields with smaller gaps and/or increase drive bunch charge. Further research into this effect, including experimental study, would provide tolerances required to operate a DWA over long distances and maximal drive beam energy extraction.

The work presented in this chapter shows the importance of a flexible and scalable simulation tool like DiWaCAT to accurately model non-linear fields and small changes

in field profiles due to change in the beam profile over long and small time intervals. Conventional simulation tools are typically used over small time intervals (with increased field detail) or larger time intervals with assumptions on fields (such as perfectly quadrupole-like fields) that cannot capture required details. The advantages of an efficient and scalable code, such as DiWaCAT, include being applicable across a range of beam parameters, whether low-charge and low-momentum beams such as in Chapter 6 or beam and DLW parameters indicative of future applications of DWA technology as in this Chapter.

7.6.2 Extensions and Future Development

Future work on methods to increase the stable propagation distance could include investigations of maintaining natural/free path beam size within DWA stages. Previous work on this topic has focused on the effects on BBU, rather than beam quality. The study of circular DLWs are also of interest: we showed that transverse fields are excited in circular DLWs in Chapter 6. The strength of these compared to planar DLWs should be a topic of research to directly compare the feasibility of each DLW geometry.

Methods presented here only mitigate, rather than completely eliminate, charge losses from BBU. The transverse fields which streak the beam are longitudinally varying, so a traditional corrector magnet could not be used after the DWA stage to correct the streak. Future work could be focused on methods to correct the beam streak with a longitudinally varying transverse field, such as a conventional RF deflecting cavity, or with the beam purposefully off-axis in a DLW as in a dielectric streaker. The effect could be further mitigated by surrounding the DWA stage with quadrupole magnets, in a FODO layout, and using a drive beam with large energy chirp, as in [77].

Chapter 8

Longitudinal Bunch Diagnostics with a Dielectric Streaker

8.1 Introduction

In recent years, passive diagnostic and beam manipulation devices, including structure-based wakefield streakers, have been investigated and installed at accelerator facilities. Examples of experimentally demonstrated wakefield streakers are given in Section 2.3.2. A charged particle beam in a wakefield streaker excites a longitudinally varying transverse field which converts a longitudinal particle position to a downstream transverse position. The downstream transverse profile can be used to reconstruct the initial longitudinal profile in a similar manner to a conventional RF transverse deflecting cavity (TDC).

With a planar DLW, such transverse streaking forces are excited by a beam propagating off-centre towards the dielectric plate (i.e. $y_0 > 0$ in Figure 3.1). The transverse fields in planar DLWs have been explored experimentally with results given in Chapter 6.

There are relatively few streakers under operation so a detailed investigation of such a diagnostic across a range of beam parameters is required, and is presented in this chapter. Limiting factors for dielectric wakefield streakers include reduced field strength at shorter bunch lengths and higher energy beams, and non-monotonic streaking fields for longer bunches [16]. These limitations have implications for two different types of beams specific to different facilities. A streaker at an accelerator technology test facility, would be expected to operate over a wide range of bunch lengths and with various longitudinal profiles. In this case, the important factors would be ensuring a streak profile is monotonic and ensuring there is a unique solution when reconstructing the longitudinal profile from the streaked profile. A facility such as a free-electron laser facility would be expected to work with shorter bunch lengths and at a higher energy. As the bunch length decreases, the transverse wakefields within the bunch also decrease and the angular kick applied is inversely proportional to beam momentum.

8.2 Theory of Longitudinal Bunch Reconstruction

In a passive streaker, as with a TDC, the longitudinal profile is given by using the mapping of longitudinal position to downstream transverse position, $y(t)$. When $y(t)$ is independent of the bunch itself, such as in a TDC, a coordinate transform applied to the measured transverse profile returns the longitudinal profile. The transverse force in a DLW is a function of the 3D bunch profile, the convolution of the bunch profile and Green's function. Therefore, both $y(t)$ and the measured transverse profile are functions of the longitudinal profile. The transverse force, and therefore downstream position, is also a function of initial transverse position. The transverse force can be seen as a series of dipole-like and higher-order fields. The dipole-like term is purely dependent on longitudinal position and higher-order terms introduce transverse variation in the field. The relative contribution of higher-order terms increases with distance from the DLW centre, increasing the contribution of non-dipole fields.

Using a simplified model with only dipole-like fields, the angular kick applied to a particle at longitudinal position t is given by

$$K_y(t) = \frac{l_s F_y(t)}{E_b}, \tag{8.1}$$

where E_b is the beam energy, l_s is the length of the streaker, and $F_y(t)$ is the dipole-like transverse force applied to the particle at t. In reality F_y is a function of x, y, and t. The particle position at the downstream screen is given the $K_y(t)$ multiplied by the element of the standard transfer matrix element relating transverse angle to downstream transverse position, R_{34} [153].

8.2.1 Theoretical Resolution

The resolution of streaker measurements is given by the smallest longitudinal distance for which the downstream transverse profiles can be differentiated. If each longitudinal slice produces a Gaussian transverse profile centred at $y(t)$, the resolution r is given when $y(t+r) - y(t)$ is greater than the RMS width of the transverse profile, σ_Y. Therefore, the resolution is a function of longitudinal position with

$$r(t) = \frac{\sigma_Y(t)}{R_{34} \left.\frac{dK_y(t')}{cdt'}\right|_t}. \tag{8.2}$$

In the case of a pure drift, R_{34} is the distance from the end of the streaker to a downstream screen.

Without external optics and sufficiently large distance to the screen, the transverse width σ_Y increases linearly with R_{34}. Therefore, the predominant determining resolution is the gradient of the streaking field. Quadrupole or higher-order fields applied by the streaker increase the beam divergence. Increased divergence increases σ_Y for a given R_{34}, increasing (worsening) resolution.

The resolution in a passive streaker is worse (i.e. larger r) at the head of the bunch, where F_y is smaller [154][16][108]. However, the field behind the head of the bunch is excited by the particles at the head. Therefore, the streaked profile does depend on the current at the head of the bunch so the current at the head can still be estimated despite low theoretical resolution. This case shows an important distinction between theoretical and practical resolution. The theoretical, or idealised, resolution at t assumes the longitudinal profile is known for all parts before t since Equation 8.2 assumes $F_y(t)$ is known. In a practical streaker this is not true; an error in the longitudinal profile at the head propagates downstream leading to incorrect measurements of the entire longitudinal profile, since $F_y(t)$ is then incorrect. The obtainable resolution is therefore dependent on the accuracy of the longitudinal profile reconstruction. For an accurate reconstruction the measured streak must match the streak that would be theoretically produced by the same profile. In this case, the resolution in Equation 8.2 holds.

As a figure of merit for the achievable resolution, we will use an average resolution rather than the resolution along the bunch. Similarly to the average force used previously, we define this value as

$$\langle r \rangle = \frac{\sum \rho(t) r(t)}{\sum \rho(t)}, \tag{8.3}$$

where the sum is over a series of longitudinal slices within the bunch and the total bunch charge, Q is given by

$$Q = \sum \rho(t). \tag{8.4}$$

Since the centre of the first slice with finite width is past the head of the bunch, the resolution here is not infinite as is theoretically true at the head.

8.2.2 Longitudinal Profile Reconstruction

An iterative optimisation algorithm is required to measure the longitudinal profile from the downstream streak profile. Neglecting the transverse profile of the beam, or contribution of transverse variation in the streak, the downstream profile is

$$\rho_S(y) = \rho_z(R_{34} K_y(t)), \tag{8.5}$$

where $\rho_z(t)$ is the longitudinal profile. For a given profile, $\rho_z(t)$, the vertical field is given by the convolution

$$F_y(t) = W_y(t) \circledast \rho_z(t). \tag{8.6}$$

Using these two equations the following process can be utilised:

1. For a test profile, calculate $F_y(t)$.
2. Apply $F_y(t)$ to the test profile for a simulated streak profile, $\rho_Y(y)$.
3. The cost factor is given by the difference between simulated and measured streak profiles.
4. Vary the test profile, repeating steps 1-3 to minimise the cost factor.

A similar process has been implemented for other passive streakers, details of which are given in [16]. The choice of cost function and performance of a reconstruction algorithm is described in Section 8.6.

8.3 Streaker Parameter Space

The transverse kicking force increases exponentially with offset from the DLW axis, y_0, for the majority of offsets. The maximal offset possible without beam losses or significant beam evolution within the DLW should be chosen for a dielectric streaker. Beam evolution within the DLW removes the assumption that $F_y(x, y, t)$ within the bunch is constant.

A non-monotonic streak refers to a field profile where the peak F_y value is within the bunch, i.e. when the bunch occupies more than a quarter wavelength of the field. This is a limiting factor for longer bunches. With a non-monotonic streak, at least two longitudinal positions receive the same transverse force and are therefore kicked to the same downstream position. These multiple longitudinal positions would not be resolvable. Two methods mitigate this: decreasing the frequency of modes excited and reducing the contribution of higher order modes. As shown in Figure 8.1(a), for a Gaussian bunch with 200 fs RMS length, a thin dielectric with low permittivity produces a non-monotonic streak for the 200 fs bunch whilst a thick high permittivity dielectric does not. By comparison, in Figure 8.1(b) with short 10 fs bunches, the same two structures produce approximately equal F_y profiles. For shorter bunches, where the bunch length is much smaller than the wavelength of the wakefield, the field generated does not depend on the dielectric thickness or permittivity.

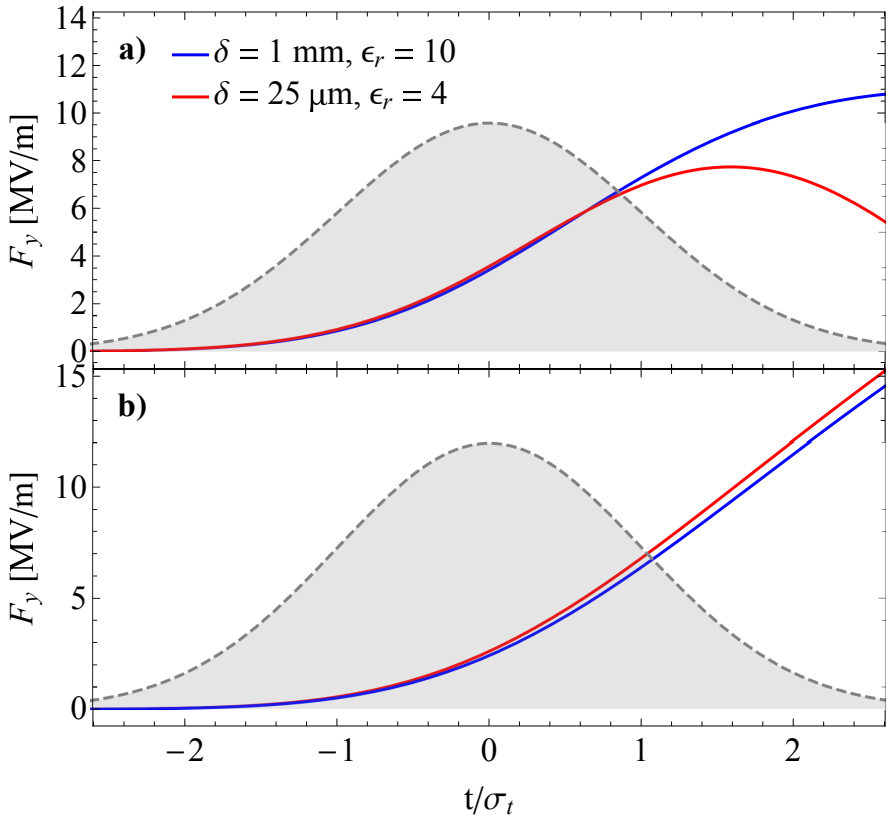

Figure 8.1. F_y profile along Gaussian bunches with (a) 200 fs and (b) 10 fs RMS length for 2 DLWs each with $a = 1$ mm. The offset for each beam, chosen to produce approximately equal F_y values, are (a) 800 μm and (b) 900 μm.

The streak increases with bunch length, as shown in Figure 8.2, up to the bunch length at which the field is non-monotonic. Therefore, the average downstream position (from which $\langle F_y \rangle$ can be calculated) is a function of offset and bunch length. Longer bunch lengths cannot be resolved at large offsets, therefore smaller offsets must be used to avoid a non-monotonic field at the expense of field strength. Measurements of $\langle F_y \rangle$ at multiple offsets could be performed quickly to measure the bunch length.

8.3.1 Mitigation of Higher-Order Terms

The theoretical resolution and reconstruction algorithm assume that F_y is solely dependent on longitudinal position. We have previously discussed the effect of focusing and defocusing forces for a beam on-axis in a planar DLW. These fields are still present off-axis and introduce variation in the vertical field applied across a beam cross-section. This variation implies that particles at different longitudinal positions will receive the same angular kick, and therefore be kicked to the same vertical position. In a similar manner to a non-monotonic streak, these longitudinal positions would not be resolvable. The resolution with transverse variation in F_y is limited by the region of longitudinal positions receiving the same kick.

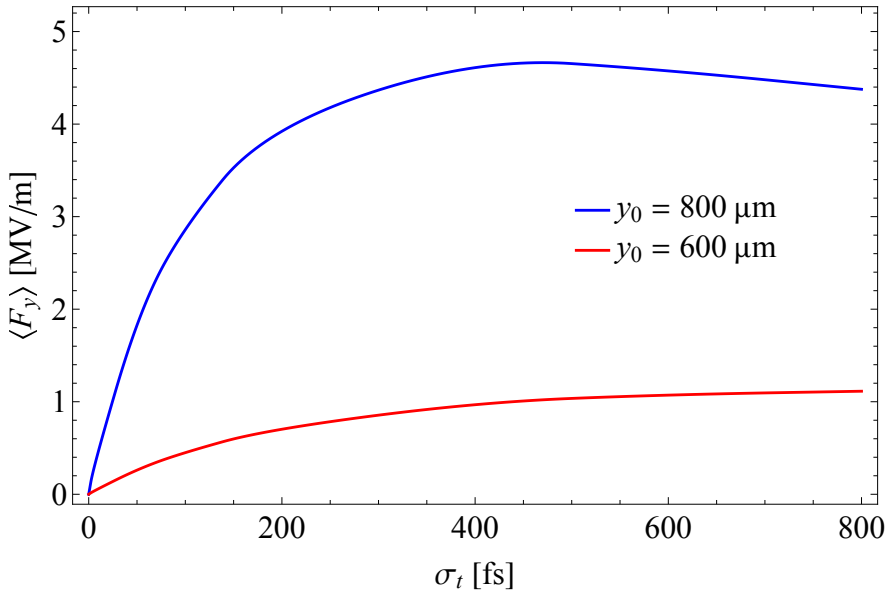

Figure 8.2. Average F_y force for Gaussian bunches of varying bunch length at two offsets from the centre of a DLW with $a = 1$ mm.

Previous studies of dielectric streakers have modelled the transverse variation in streak as solely quadrupole-like [154], however the contribution of higher-order terms increase towards the dielectric plate. As shown in Figure 8.3, non-linear variation in F_y across the transverse bunch profile increases with offset. A second DLW, oriented in a H+V setup as discussed in Chapter 7 can be used to cancel the variation.

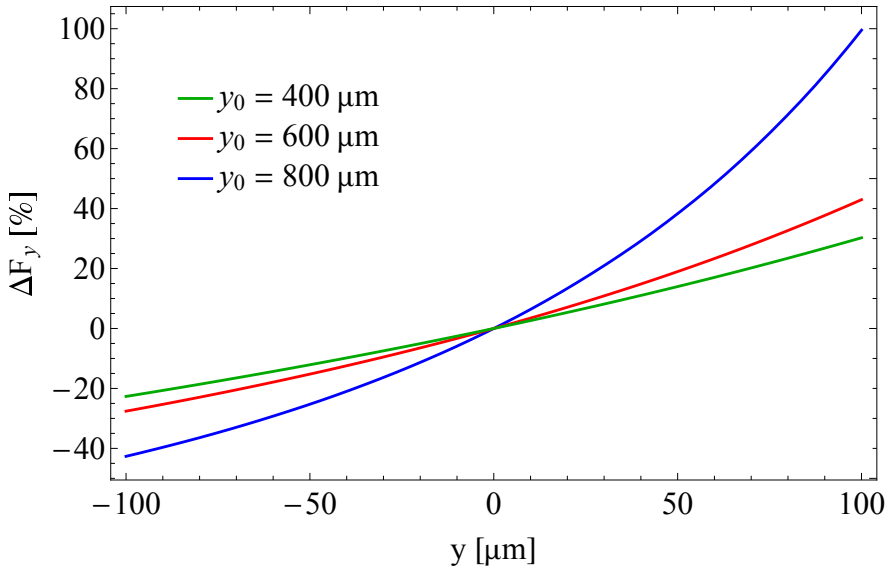

Figure 8.3. Percentage variation in F_y, relative to the beam centre, at three offsets from the centre of a DLW with $a = 1$ mm. The RMS beam width and length are 50 µm and transverse variation in wakefields are independent of longitudinal position.

It is optimal to maximise the beam offset, which in turn maximises the contribution of higher-order modes. These higher order modes would also need to be excited in the second DLW but with the beam in the DLW centre. This can only be achieved by reducing the dielectric gap, with transverse fields proportional to $1/a^3$ [87]. Therefore,

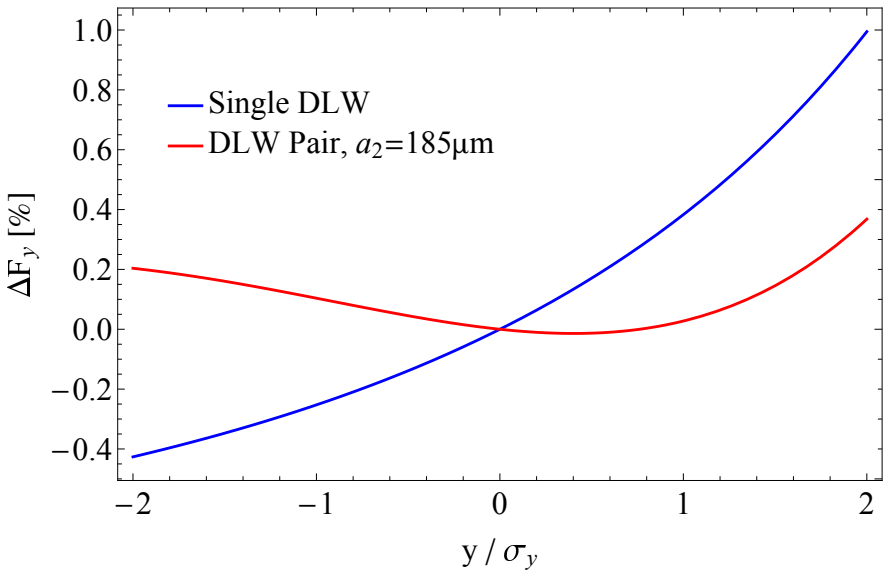

Figure 8.4. Variation in F_y, relative to the beam centre, with and without a second perpendicular DLW.

to ensure the transverse variation is not over-compensated a shorter second DLW is required. To minimise the variation in streaker across the bunch, the second DLW length is set as 0.1 m (first DLW length is 0.2 m). As shown in Figure 8.4, the variation in F_y across the bunch cross-section is reduced from 140% to 35%. The percentage transverse variation in fields is independent of longitudinal position so $\Delta F_y(y)$ is constant along the bunch profile.

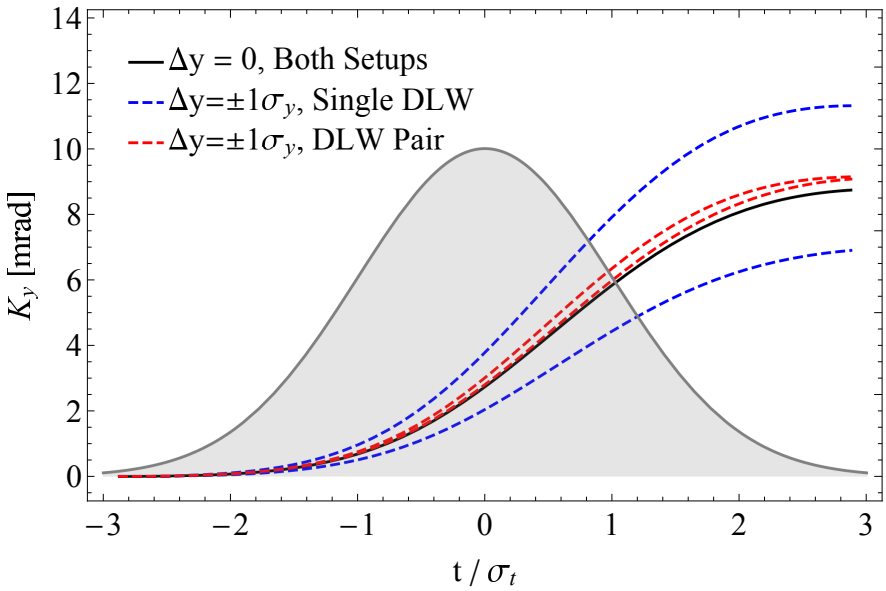

Figure 8.5. Angular kick applied at the beam centre at $\pm\sigma_y$ with and without a second perpendicular DLW. $K_y(t)$ is the same for the single DLW and DLW pair at the beam centre.

The cancellation of non-dipole terms reduces the longitudinal region receiving the same kick. In Figure 8.5 this effect is clear; without the second DLW $K_y = 4$ mrad is applied to particles across a slice of width $1\sigma_t$ whilst with the second DLW this is reduced to $0.1\sigma_t$. There is no cancellation in the streaking term so $K_y(t)$ at $y = 0$ (the bunch centre) is unchanged.

Horizontal focusing forces excited by the first DLW are also cancelled by the second DLW. It is preferable to have a large distance to the downstream screen, to maximise the translation of $K(t)$ to downstream $y(t)$. The horizontal focusing forces, with a single DLW, bring large parts of the beam to a waist before the screen, leading to a very diffuse beam image with regions of low charge density as in Figure 8.6. Cancellation of the focusing forces keeps the beam closer to the pure drift case. Without the second DLW the majority of the beam may not be detectable against a background noise level 5 m from the end of the streaker. The charge density of the streaked beam is very small for $y > 10$ mm for a single DLW. This location is equivalent to the kick received at $t = 0$ (see Figure 8.5), so half the longitudinal profile could be resolved poorly. The second DLW makes the beam image horizontally focused thus increasing the signal to noise ratio at the detector.

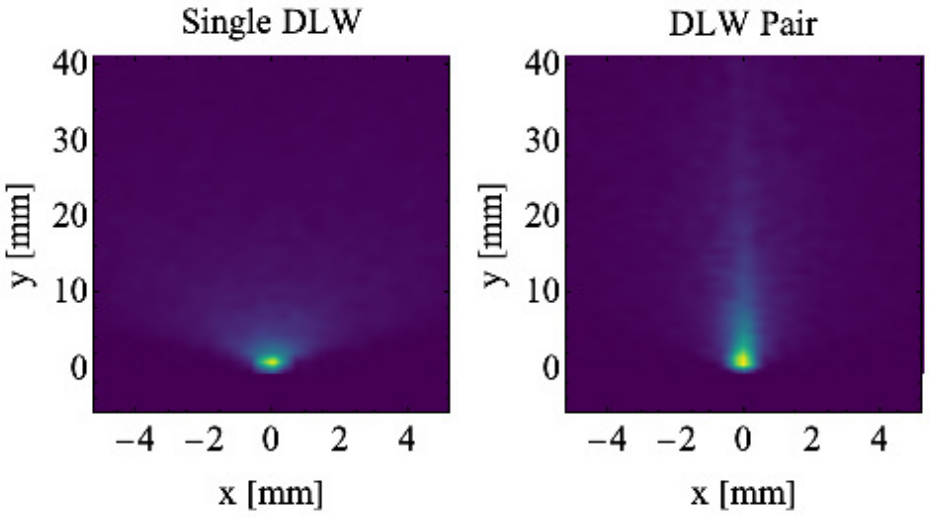

Figure 8.6. Simulated beam images, 5 m downstream from the DLW exit, for a 200 fs Gaussian bunch, with and without a second perpendicular DLW. Simulations are with $y_0 = 800$ µm, $a = 1$ mm, and $a_2 = 185$ µm.

8.4 Dielectric Streaker at Electron Test-Facilities

Accelerator test facilities for future technology are required to operate over a wide range of bunch lengths and charge distribution shapes. Such a facility would be expected to operate over bunch lengths up to ps-scale. Beam parameters, chosen to be comparable to CLARA Phase 2 (250 MeV) operation, used in this section are given in Table 8.1. The important factor for streaker performance is the ratio of bunch charge to beam momentum, as demonstrated by Equation 8.1. Therefore, whilst the simulations here are for a specific facility, the conclusions are relevant to facilities with similar charge to momentum ratios (such as CLEAR [155], FLUTE [156], and SPARC_LAB [157] in Europe). Gaussian and uniform/'flat-top' longitudinal distributions have been chosen as two extreme cases

to compare. The uniform current of the flat-top case provides a constant contribution to the wakefield over the bunch whilst the contribution of a Gaussian profile will increase and decrease over the bunch. The point at which non-monotonic behaviour is seen would therefore be expected to vary. Given the constant wakefield contribution, flat-top bunches would be expected to remain monotonic for longer bunch lengths. For a Gaussian bunch with RMS bunch length σ_t, the corresponding flat-top beam is set with total bunch length $4\sigma_t$.

Parameter	
Bunch Charge [pC]	250
Beam Momentum [MeV/c]	250
RMS Bunch Length, σ_t [fs]	50 - 800
Normalised Emittance [mm mrad]	1
RMS Beam Width, $\sigma_{x,y}$ [μm]	50

Table 8.1. Parameters used to approximate example electron test-facility bunches. Longitudinal bunch distributions are either Gaussian or flat-top in shape.

The streaker chosen must produce a monotonic streak across the full range of bunch lengths. Choosing a thick dielectric with high permittivity reduces the frequency of the wakefield excited. With $\delta = a = 1$ mm and $\epsilon_r = 10$, a positive streak gradient at the tail of both Gaussian and flat-top bunches can be produced. As shown in Figure 8.7, the offset needs to be reduced for longer Gaussian bunches, at the expense of wakefield strength, to achieve a monotonic field. For flat-top bunches a monotonic streak is still achievable across the range of bunch lengths.

The average magnitude of the streak increases with bunch length until the point at which the streak becomes non-monotonic, as shown in Figure 8.2. The average transverse field, $\langle F_y \rangle$, can be measured from the average streak position at the downstream screen and used to evaluate the RMS bunch length. Approximately equal streak lengths (maximal F_y at the tail of the bunch) are produced by Gaussian and flat-top bunches (Figures 8.8 and 8.9), with different profile shapes. Being able to independently measure the bunch length and profile ensures that the likelihood of multiple solutions being found for bunch profile reconstruction is low.

8.4.1 Resolution

Calculations of the resolution from simulations are taken by slicing the beam longitudinally and calculating σ_Y from the second moment of macroparticles in each slice. The theoretical resolution assumes a Gaussian transverse profile since this assumes slices can be resolved if the difference in slice downstream position is greater than the RMS width of each slice. To test this assumption, the profile is compared to a Gaussian distribution with a width of σ_Y. The percentage error in σ_Y is given by the average

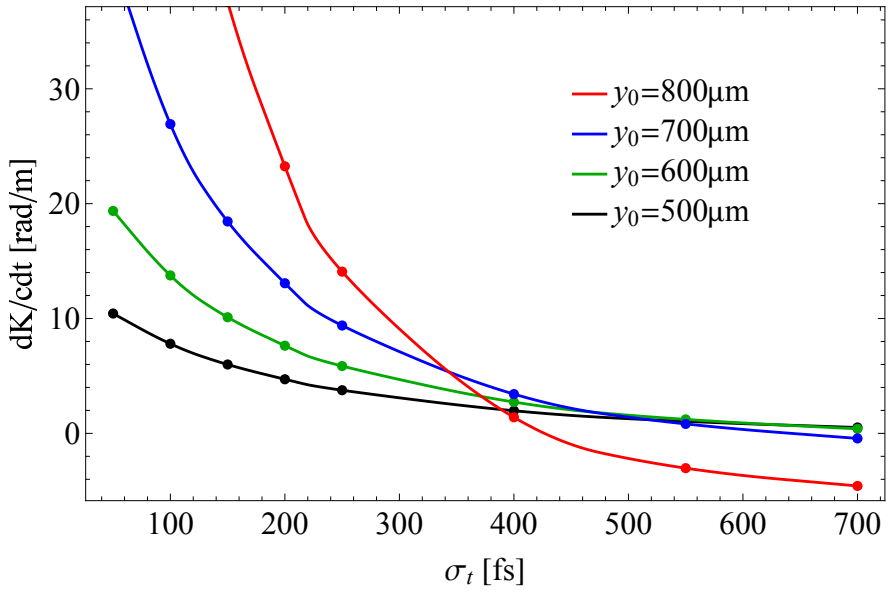

(a) Gaussian

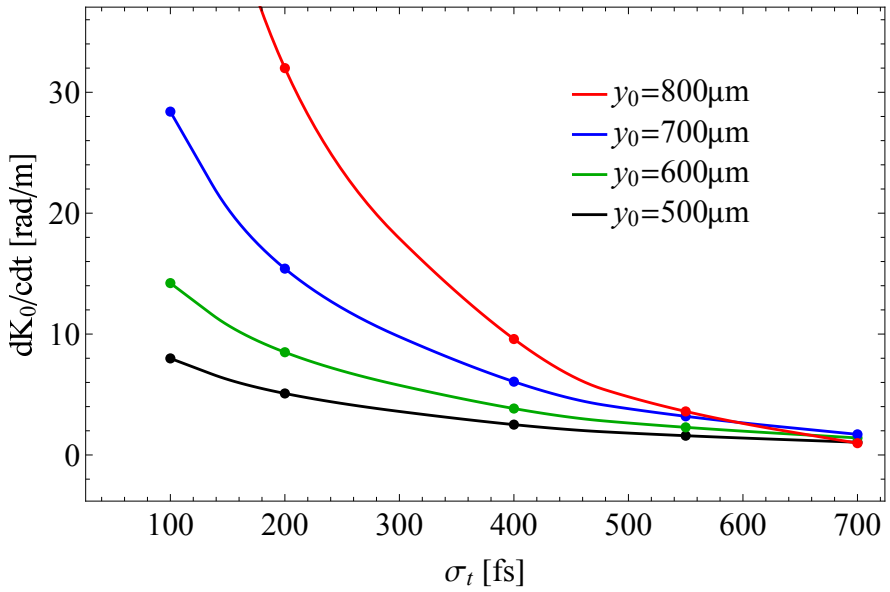

(b) Flat-Top

Figure 8.7. The angular kick gradient at $t = +2\sigma_t$ for Gaussian and flat-top bunches of varying length and initial offset.

percentage variation between the approximated Gaussian profile and actual distribution across the profile. Therefore, the error in σ_Y is an approximation of the validity of assuming a Gaussian transverse profile in Equation 8.2. The gradient of F_y is calculated from the calculated F_y profile so does not contribute to the overall error in $r(t)$.

The resolution along the bunch profile for a 200 fs bunch, with and without the second DLW is shown in Figure 8.10. Transverse variation in F_y defocuses each longitudinal slice, increasing σ_Y and therefore worsening the resolution. The second DLW ensures the resolution is approximately constant, after the bunch head, along the entire bunch and ensures all parts of the bunch can be resolved.

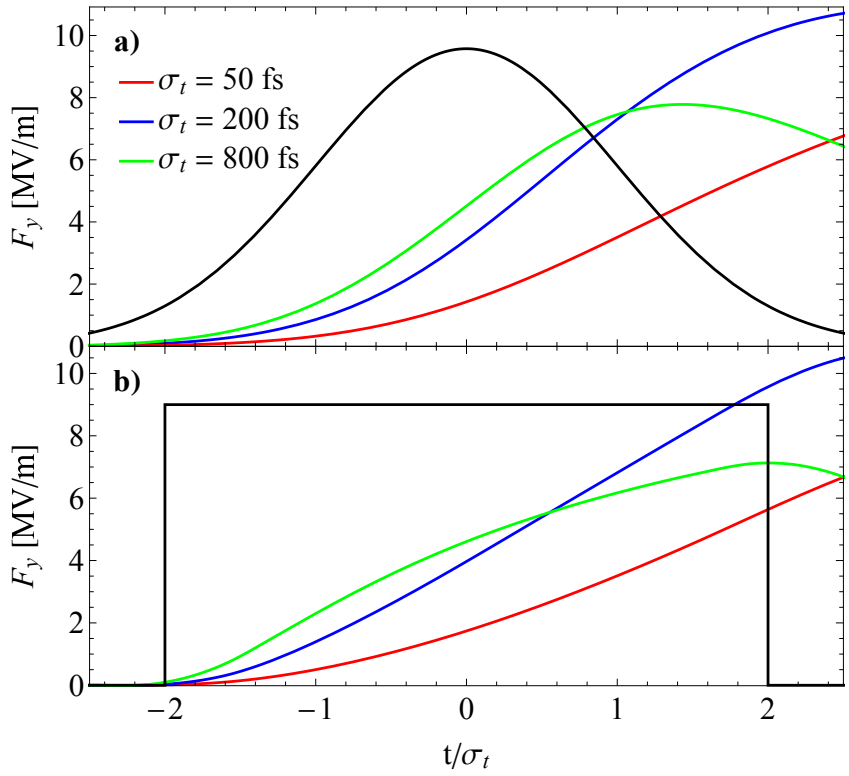

Figure 8.8. F_y as a function of longitudinal position within (a) Gaussian and (b) Flat-Top bunches of varying length with initial offset $y_0 = 800$ µm.

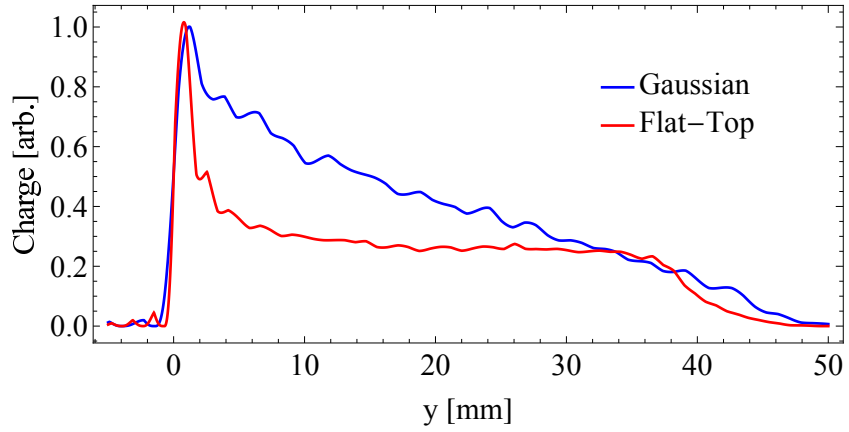

(a) Gaussian and flat-top bunches with $\sigma_t = 200$ fs.

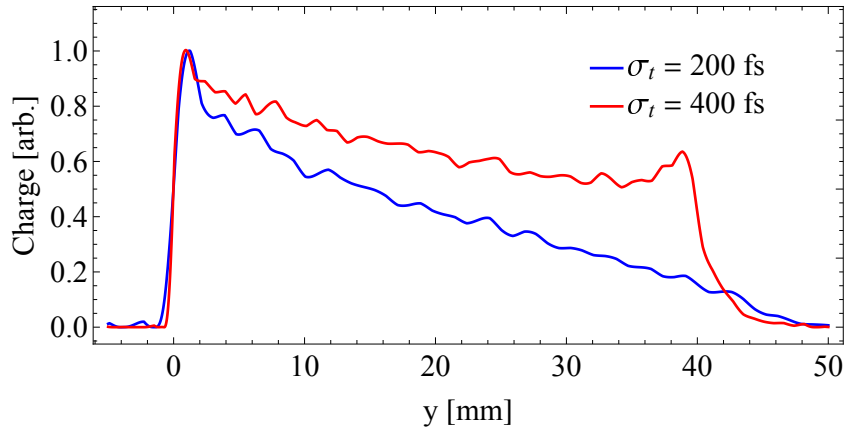

(b) Two Gaussian bunches with $\sigma_t = 200$ and 400 fs.

Figure 8.9. Vertical profiles 5 m downstream from the streaker.

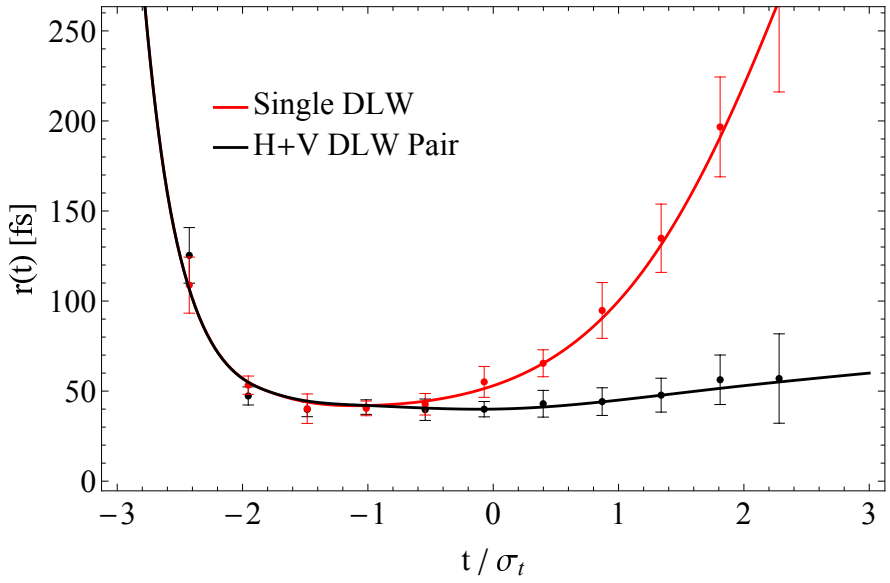

Figure 8.10. Resolution, $r(t)$, as a function of longitudinal position with and without a second perpendicular DLW for a Gaussian bunch with 200 fs RMS bunch length. The initial offset from the DLW centre is 800 µm.

For a given total bunch length, the longitudinal F_y profile is approximately independent of profile distribution, so resolution is approximately constant, as shown in Figure 8.11. The resolution at the head of a Gaussian bunch is poor due to small wakefield contributions where current is low. With a flat-top distribution this is not true so resolution at the head is improved.

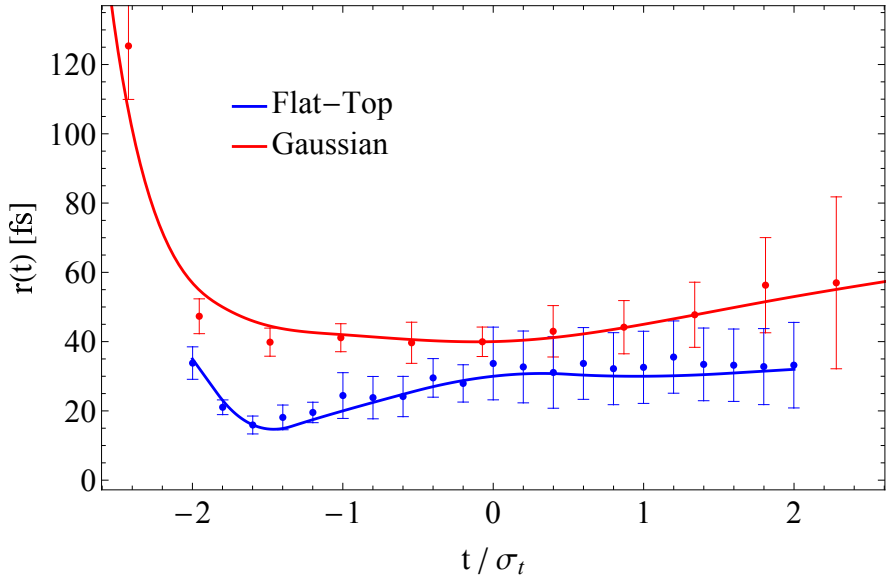

Figure 8.11. Resolution, $r(t)$, as a function of longitudinal position for Gaussian and flat-top bunches with $\sigma_t = 200$ fs. The initial offset from the DLW centre is 800 µm.

In practice, the resolution is only relevant when compared to the bunch length. The resolution, normalised to bunch length, is approximately constant (Figure 8.12), with a small increase in relative resolution for longer bunches. Therefore, the resolution along the bunch is proportional to bunch length. This can be expected given the bunch current, and therefore wakefield strength, is proportional to bunch length. As shown in

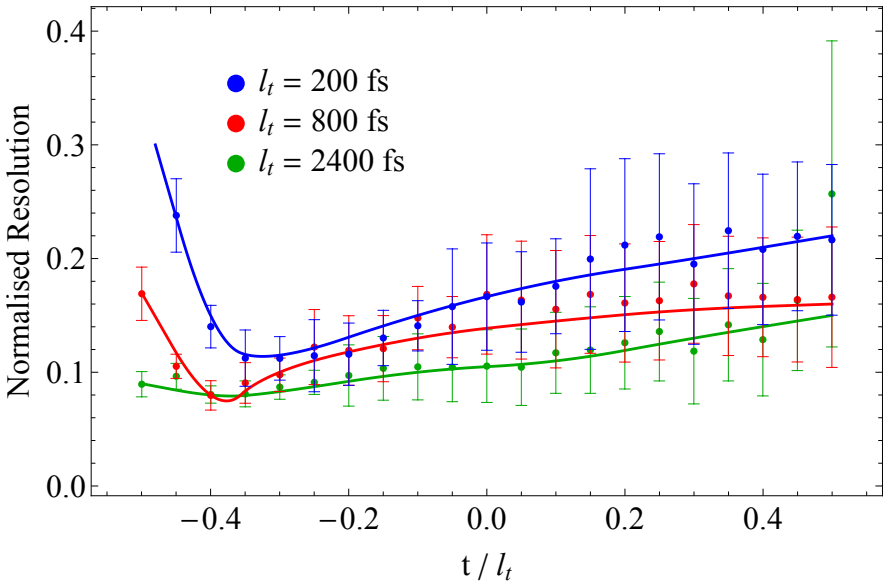

Figure 8.12. Resolution, $r(t)$, normalised to bunch length as a function of longitudinal position for flat-top bunches with varying bunch length. The initial offset from the DLW centre is 800 µm.

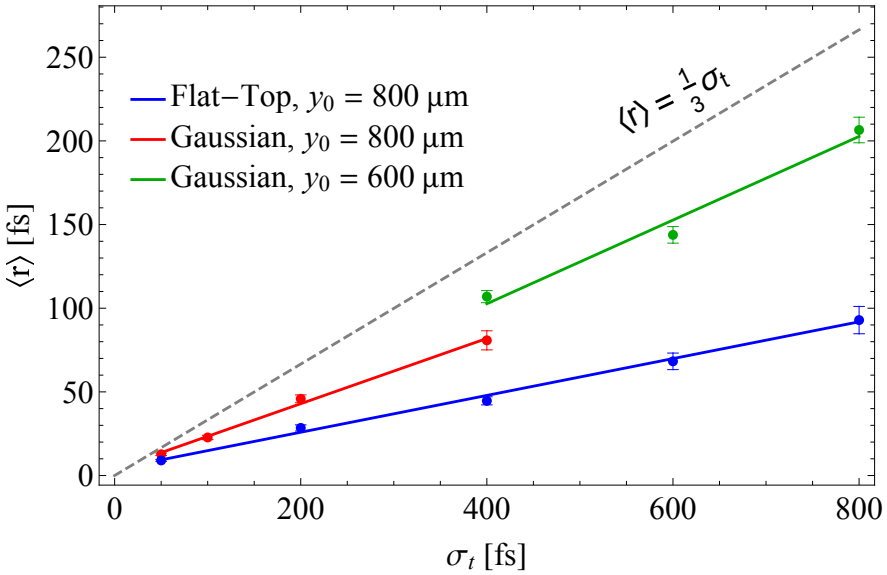

Figure 8.13. Average resolution for Gaussian and flat-top bunches as a function of bunch length. The dashed line shows $r(t) = \sigma_t/3$, the threshold for achievable reconstruction. Each offset is shown upto the point at which the F_y profile is no longer monotonic.

Figure 8.13, the average resolution is also proportional to bunch length. The streak for a Gaussian bunch becomes non-monotonic for $\sigma_t > 400$ fs with $y_0 = 800$ µm so a smaller offset (600 µm) is used for $\sigma_t > 400$ fs to resolve the entire bunch profile. Reducing the beam offset decreases the strength of F_y so $\langle r \rangle(\sigma_t)$ is discontinuous when the offset is changed. For both Gaussian and flat-top bunches, the resolution is below the $\langle r \rangle = \sigma_t/3$ line for the full range of bunch length. We can therefore expect the streaker to accurately reconstruct beams with these parameters for $50 < \sigma_t < 800$ fs. Extrapolating the average resolution would suggest reconstruction possible for $\sigma_t > 800$ fs however the streak becomes non-monotonic for both Gaussian and flat-top profiles beyond this point, for the DLW parameters used here. Using a thicker dielectric or higher permittivity could

further increase the maximum bunch length by increasing the wakefield wavelength.

8.5 Dielectric Streaker for Ultra-Short Bunches

Streaking of shorter bunches is not limited by non-monotonic streaks but instead the reduction of field strength with bunch length. Electron beams with $\sigma_t \sim$ fs and $\sim$ GeV/c momenta have applications in hard x-ray free-electron laser facilities, or are generated by novel acceleration techniques such as laser wakefield acceleration (LWFA). For these beams, increased momentum reduces the kick applied. Beam parameters used in this section to simulate such beams are given in Table 8.2. For applications such as LWFA, energy spread within the bunch is typically large. A correlated energy spread could be accounted for during reconstruction and reduced momentum towards the tail could improve resolution as the kick gradient would increase. Uncorrelated energy spread can be seen as an error factor in the kick received and result in particles at multiple longitudinal positions receiving the same kick. This would blur the overall profile in a similar manner to transverse variation in F_y. One solution to an uncorrelated energy spread could be to measure the streaked profile at an energy spectrometer, measuring the streaked profile of a thin momentum slice.

Parameter	
Bunch Charge [pC]	250
Beam Momentum [GeV/c]	1
RMS Bunch Length, σ_t [fs]	1 - 50
Normalised Emittance [mm mrad]	1
RMS Beam Width, $\sigma_{x,y}$ [μm]	20

Table 8.2. Parameters used for ultra-short type bunches. Both longitudinal and transverse profiles are Gaussian.

The magnitude of streak reduces with bunch length, requiring larger offsets to achieve the same streak strength. As shown in Figure 8.1, an offset of 100 μm from the dielectric is required for a 10 fs bunch to match the magnitude of F_y produced by a 200 fs bunch 200 μm from the dielectric.

The choice of dielectric permittivity or thickness does not affect the magnitude or shape of the streak for shorter bunches (Figure 8.1), since the bunch length is much smaller than the fundamental wavelength of the wakefield. The number of modes required for convergence however is much higher for a thicker dielectric such as used in Section 8.4. To reduce simulation time a DLW with $\delta = 25$ μm and ϵ_r = 4 was chosen. The justification for using a second perpendicularly orientated DLW holds for shorter bunches; the streak variation is minimised for $y_0 = 900$ μm with $a_2 = 95$ μm. Note that to avoid beam losses, the choice of offsets and second DLW gap sets a limit of the

transverse beam size through the streaker.

8.5.1 Resolution

The wakefields excited by Gaussian bunches can be qualitatively described in three stages: increasing $F'_y(t)$ at the head of the bunch (due to $\rho(t)$ and $W_y(t)$ increasing over time), an approximately linear streak, and finally reducing gradient with reducing $\rho(t)$. The time taken for the streak to become linear encompasses a greater portion of shorter bunches (Figure 8.1(b)). Therefore, the region at the head of the bunch with poor resolution is larger as σ_t reduces. For a 10 fs bunch the resolution is approximately constant from $t = -1.5\ \sigma_t$, as shown in Figure 8.14. By comparison, for $\sigma_t = 200$ fs and $y_0 = 800$ µm as in Figure 8.10 this point is $t = -2\ \sigma_t$.

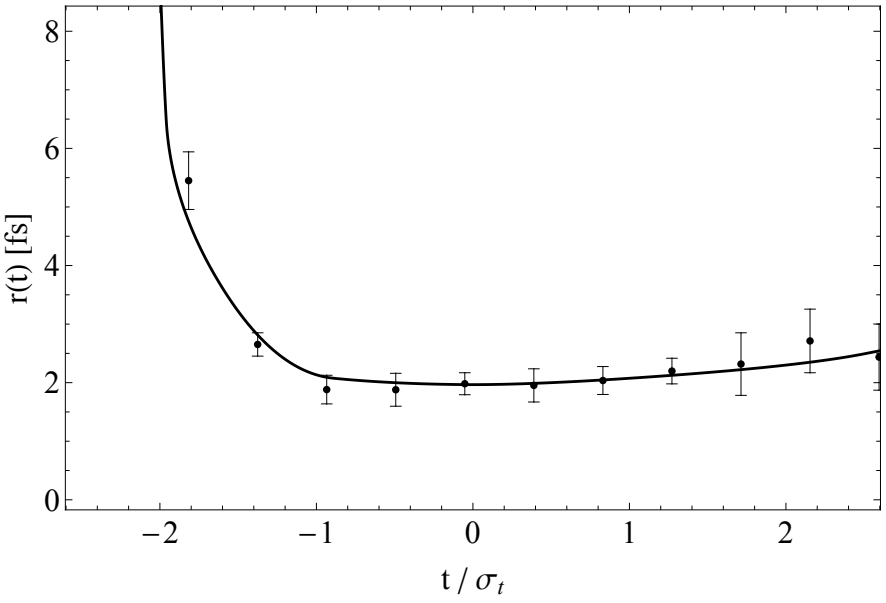

Figure 8.14. Resolution, $r(t)$, as a function of longitudinal position for a Gaussian bunch with 10 fs RMS bunch length, offset 900 µm from the DLW centre.

The average resolution for ultra-short bunches of varying length is shown in Figure 8.15. Using the same criteria as for longer bunches reconstruction can be assumed possible down to $\sigma_t \approx 5$ fs.

8.5.2 RMS Bunch Length Measurement

As the RMS bunch length reduces to fs-scale, it can be assumed that the longitudinal distribution is Gaussian. Using a streaker solely as a bunch length (and not complete profile) diagnostic is still possible in this case. The average F_y force, shown in Figure 8.16, is proportional to bunch length. This relationship is increasingly linear for shorter bunches. The average force directly relates to the average change in downstream position,

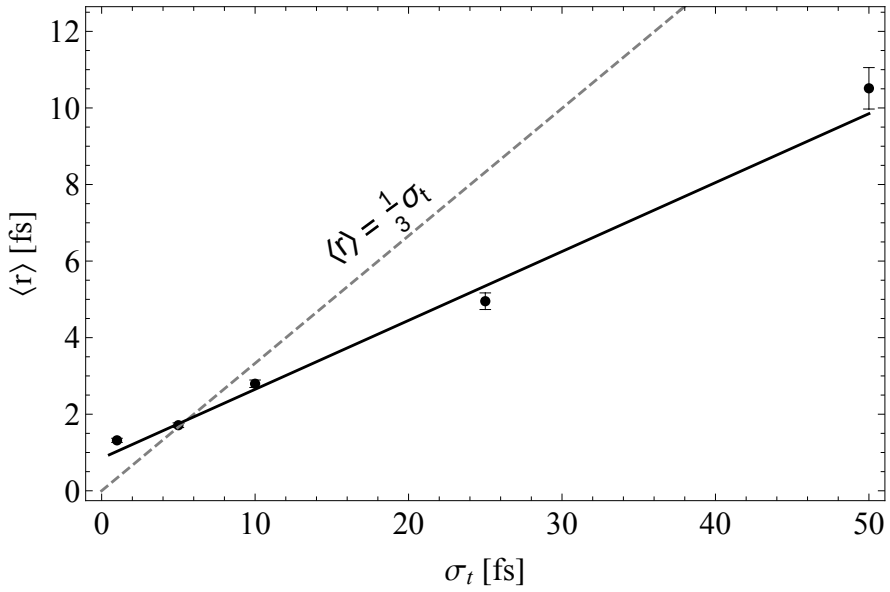

Figure 8.15. Average resolution for Gaussian ultra-short bunches as a function of bunch length. The dashed line shows $r(t) = \sigma_t/3$, the threshold for achievable reconstruction.

Δy, given by

$$\Delta y = \frac{R_{34} l_s \langle F_y \rangle}{E_b}. \tag{8.7}$$

The vertical profile, relative to the average position of the initial bunch, for three ultra-short bunches are shown in Figure 8.17. The streak is small, especially for $\sigma_t = 1$ and 5 fs, however a measurable difference in average streak is observed. The gradient of F_y against σ_t for short bunch lengths is approximately 0.38 MV/m/fs (normalised to charge this is 1.52×10^{-3} MV/m/pC/fs). Therefore, for short bunch lengths the RMS bunch length is

$$\sigma_t[\text{fs}] = \frac{E_b \Delta y}{l_s D Q} \times 6.57 \times 10^{-16}, \tag{8.8}$$

where D (in m) is the distance from the exit of the dielectric streaker to the screen, l_s (in m) is the streaker length, E_b (in eV) is the beam energy, and Q (in C) is the total bunch charge. As an example, for the ultra-short bunch parameters used here with $D = 5$ m, resolving a position change of Δy greater than ≈ 350 μm is required to measure a sub-fs long bunch. This resolution would need to incorporate the imaging resolution, transverse profile jitter, and any beam pointing jitter that would correspond to $\langle F_y \rangle$ jitter from changing offset. Given the performance of current electron beam facilities - in terms of transverse stability and diagnostics [144] - this is not an unreasonable resolution so sub-fs RMS bunch length measurements can be expected.

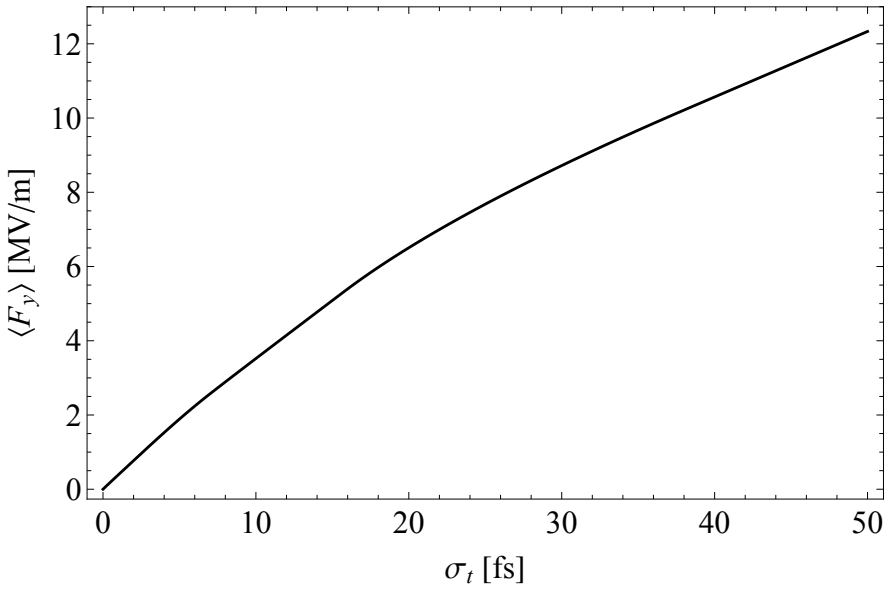

Figure 8.16. Average F_y as a function of bunch length for ultra-short bunches offset 900 µm from the DLW centre.

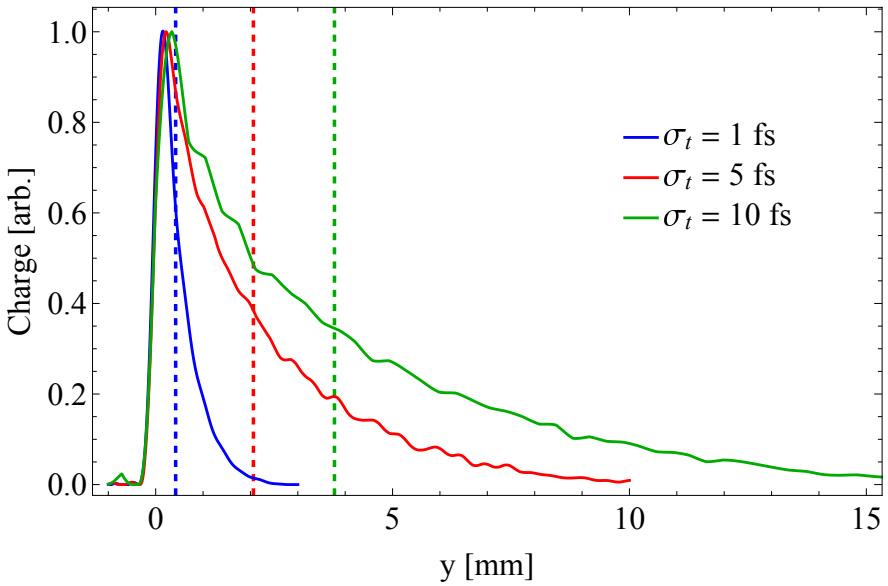

Figure 8.17. Vertical profiles 5 m downstream for ultra-short bunches of varying length. Dashed lines represent the average vertical positions for each bunch at the screen.

8.6 Reconstruction Algorithm

As previously mentioned, the reconstruction algorithm aims to minimise the variation between a measured streak and simulated streak. To ensure the spatial resolution is equal to the measured streak, the simulated streak is given by a histogram of macroparticle positions with bin widths matching the pixel width.

The reconstruction process can utilise a backward or forward propagation method. With forward propagation a test longitudinal profile is used to calculate F_y and propagated to the screen for comparison with a measured profile. The test profile is optimised to

minimise the difference between simulated and measured screen profile (cost function). Alternatively, using a backward propagation method, the test F_y profile is used to backward propagate the measured streak to calculate an improved longitudinal profile. The process is repeated using the new longitudinal profile, converging towards the 'true' solution. This method is outlined in detail in [150]. The results in this section utilise the forward propagation method, whilst the results in Section 6.3.1 used a backward propagation method. A comparison of the two methods is a topic of future study.

The choice of cost function is non-trivial. The vertical profiles can be compared in two ways: each profile normalised to integrated intensity or peak intensity. Bin or pixel intensity are both proportional to bunch charge in that bin or pixel so normalising to integrated intensity is equivalent to normalising to bunch charge. Alternatively, normalising to peak intensity will avoid the optimisation placing too much weight on peak intensity areas close to the head of the bunch. A combination of the two is used for reconstruction here.

Since reconstruction is an optimisation problem, the initial guess directly impacts the accuracy of the measured profile and speed of convergence on a solution. The RMS bunch length can be estimated from the average streak. The bunch length is given by minimising the difference in average streak between the measured streak and a Gaussian of varying lengths. Using this bunch length, an F_y profile is calculated from a Gaussian of this length; the F_y profile is used to map the measured profile to a longitudinal profile which is used as the initial guess.

For each longitudinal profile tested, the F_y profile is calculated. The profile is re-sampled with an increased number of points, to which the appropriate kick to a downstream position is applied. The percentage transverse variation in $F_y(y)$ at each longitudinal position is constant. The fractional variation in streak is converted into a probability density function. The vertical position of each point is randomly applied an additional fractional kick using this PDF. A histogram of downstream positions of each point is then compared to the measured stream and cost function evaluated.

Previous studies of passive streakers which include a reconstruction of the longitudinal profile have used a profile with multiple peak currents [154][108] or returned a profile with an erroneous second peak [16]. It is important to assess whether single-peak functions are a particular weakness of a dielectric streaker.

The reconstruction process has been tested for simulated beams with parameters as in Table 8.4 with $y_0 = 800$ μm. For single-peak distributions, $\sigma_t = 100$ and 600 fs was chosen with Gaussian, flat-top, and skew-Gaussian ($\alpha = \pm 6$) longitudinal distributions. The longer bunches were chosen to test performance for a non-monotonic streak. With

$\sigma_t = 600$ fs, it would be reasonable to reduce the offset to achieve a monotonic streak and with $y_0 = 800$ µm an optimum solution would not be expected. A skew-Gaussian distribution allows for testing performance with high current at the tail and head, depending on the sign of α, where average resolution is improved and worsened respectively. A double-Gaussian was also simulated to match the double-peak solutions of previous studies. Gaussian distributions at the head and tail were chosen with 100 and 200 fs RMS bunch length respectively. The peaks of each were offset by 1.4 ps and the amplitude of the 200 fs Gaussian $1.25\times$ greater than the 100 fs profile.

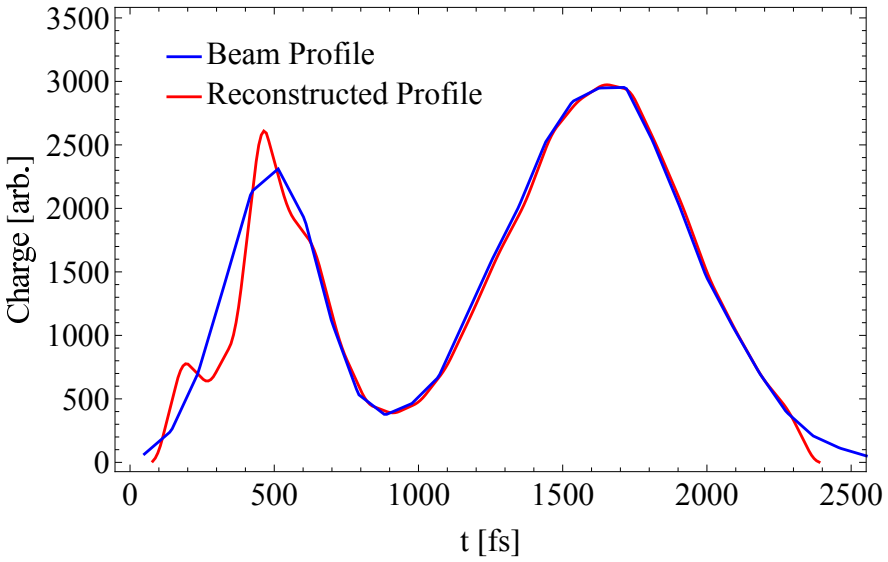

Figure 8.18. Inputted and reconstructed longitudinal profiles for a double-Gaussian beam, with RMS widths 100 and 200 fs at the head and tail respectively.

The reconstructed profile and comparisons of simulated and measured streaks for the double-Gaussian case are shown in Figure 8.18. The reconstruction process correctly reconstructs both Gaussian profiles with the correct length and correctly calculates the offset between the two within 100 fs. The detail of the first Gaussian is significantly worse, as expected given the worse resolution at the bunch head. Multiple distributions can produce the same F_y profile, limiting the ability to indirectly measure the profile at the head of the bunch.

A selection of reconstructed profiles for 100 fs and 600 fs single bunches are shown in Figure 8.19 and 8.20 respectively. The reconstruction performs better for the shorter bunches, as expected given that the transverse field is non-monotonic for 600 fs bunches. The effect of incorrectly reconstructing the head of the bunch is shown in Figure 8.19(d); whilst the overall profile shape is correct there are additional incorrect details present. A smoothed profile could be inferred as either a combination of a Gaussian profile followed by a flat-top profile or (correctly) a singular skewed-Gaussian bunch.

The results for 600 fs bunches do show that a passive streaker can still be used for profile measurements. The non-monotonic fields do result in multiple solutions producing the

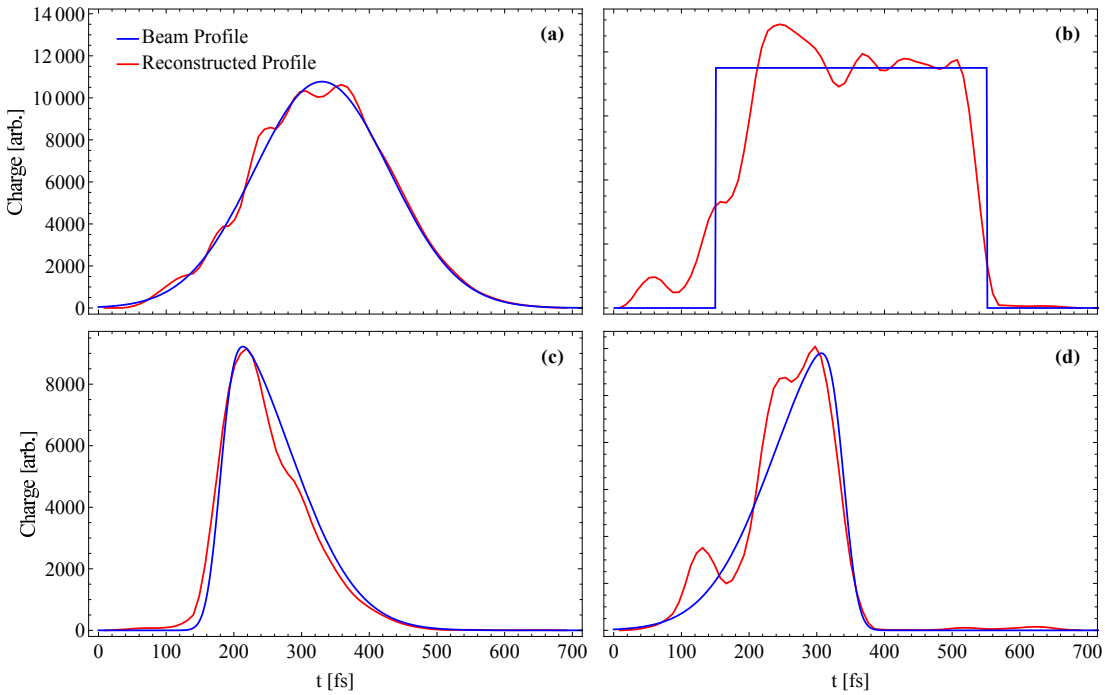

Figure 8.19. Longitudinal profiles for input beams and reconstructed profiles from streaks for a selection of distributions each with $\sigma_t = 100$ fs.

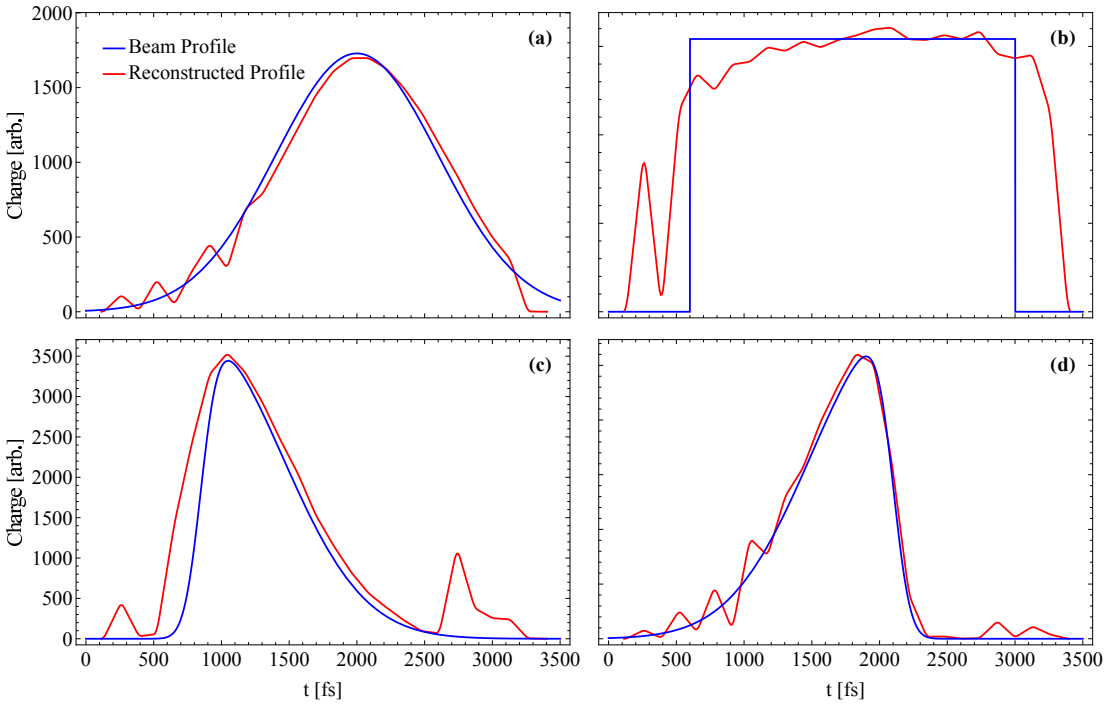

Figure 8.20. Longitudinal profiles for input beams and reconstructed profiles from streaks for a selection of distributions each with $\sigma_t = 600$ fs.

same streak shapes, leading to an increased likelihood of erroneous artifact (such as at the head and tail of Figure 8.20(c)). Positively skewed bunches (with high current at the head) are correctly reconstructed, despite low resolution at the head, supporting the assumption that indirect measurements of areas of low resolution is possible due to those areas exciting the wakefields in higher resolution regions. Overall, the performance for single-peak distributions is worse than the double-Gaussian distribution supporting

the suggestion that a passive streaker is most suited to more complex longitudinal distributions which produce non-smooth streak profiles.

8.7 Summary

In conclusion, we have demonstrated the operating window of a passive dielectric streaker for two types of accelerator: medium energy electron test-facilities and ultra-short higher energy bunches. The importance of quadrupole-like and higher order fields has been demonstrated and influenced the choice of a H+V geometry, unlike other proposed streakers which are either a single cylindrical or planar DLW/corrugated structure. Simulations have shown that a passive device can be used as a longitudinal diagnostic (measuring bunch length and/or profile) in the same manner as a TDC, without the need for external infrastructure or ongoing operating costs. Bunches are successfully reconstructed, with more accurate reconstruction for beams with large current towards the tail of the bunch or non-smooth distributions. This method can be easily implemented at existing facilities given the small physical size of a dielectric streaker (30 cm in the case of simulations in this section). Bunch length measurements are possible down to the fs-scale, and profile reconstruction across an RMS bunch length range of $10 < \sigma_t < 1000$ fs independent of bunch longitudinal profile.

Chapter 9

Conclusions

9.1 Summary

In this thesis, a comprehensive investigation of dielectric wakefield acceleration (DWA) structures, as well as a diagnostic application of dielectric lined waveguides, has been presented through experimental and simulation studies.

A simulation framework called DiWaCAT has been developed, which demonstrates high efficiency and enables the study of DWA with realistic beam parameters. To ensure the reliability of the simulation results, DiWaCAT has been benchmarked against the commercial code CST as well as validated against experimental data. The efficiency of DiWaCAT has facilitated a detailed examination of the key parameters essential for accurately modeling wakefields in planar DLWs. Through optimisation of the mesh layout for field calculations, the framework achieves improved efficiency by reducing unnecessary computations while maintaining accuracy through an appropriate mesh density. Furthermore, the study investigates the mode composition of fields for different DLW structure parameters and examines the implications of the number of modes required for precise simulations.

A series of experiments were conducted at the CLARA/VELA facility, with two types of structures, a variable gap planar DLW and a circular DLW, examined. The transverse and longitudinal fields measured in the planar DLW were in agreement with theoretical expectations. With the same structure gap/aperture, stronger longitudinal fields were measured with the circular DLW than planar structure, as predicted by theory. Transverse field effects, akin to a quadrupole-like force, were observed when propagating through a circular DLW. This observation was likely due to transverse beam size asymmetry and the study of these fields as a cause of beam instability in future DWAs is required.

Experimental measurements of transverse fields using elliptical beams in planar DLWs supported previous findings of beam-breakup (BBU) suppression, as reported in [126]. However, the presence of quadrupole-like fields raised concerns regarding the suitability

of this method for practical DWA applications, especially when scaling up to nC-scale charge.

Efforts to minimise transverse fields in planar DLWs were explored using DiWaCAT, considering beam parameters indicative of potential future DWAs. The study revealed that although elliptical beams helped suppress transverse fields, these fields still led to beam losses within approximately 1 metre of propagation. The presence of quadrupole-like fields exacerbated these losses by focusing the beam towards regions with higher defocusing/kicking fields. Moreover, slice and projected emittance growth resulting from longitudinally varying transverse fields during propagation would hinder the ability to reshape the drive bunch between acceleration stages. However, quadrupole-like fields can be effectively cancelled by using a circular/symmetric beam and a series of orthogonally orientated planar DLWs in an H+V setup. By employing short DLWs to minimise beam size changes within a single DLW, emittance growth can be kept to a minimum. The H+V setup also demonstrated a degree of BBU suppression, where the transverse kick introduced in one DLW is cancelled by the fields in the following DLW orientation. Although the transverse momentum is reduced, complete cancellation of the kick is not achieved, resulting in the development of BBU and subsequent beam losses, albeit after an greater propagation distance.

Furthermore, the work presented in this thesis investigated the use of dielectric wakefield streakers for longitudinal bunch diagnostics across two distinct ranges of beam parameters, relevant to medium-energy electron test-facilities and higher energy ultra-short electron bunches. Through simulation studies, it was demonstrated that dielectric streakers possess a wide operating window of bunch lengths, expanding their applicability to a broad range of accelerator facilities. This finding highlights the potential of dielectric streakers as versatile tools for accurately measuring the longitudinal profile of electron bunches in different beam parameter regimes.

In summary, this thesis has contributed significant insights into the experimental and simulation aspects of dielectric wakefield acceleration structures. The development of the efficient DiWaCAT simulation framework, combined with experimental validation and comprehensive parameter studies, has advanced understanding of wakefield characteristics and potential applications. The findings on minimising transverse fields, cancellation of quadrupole-like fields in an H+V setup, and the versatility of dielectric streakers for bunch diagnostics open new avenues for future research and development in the field of dielectric wakefield acceleration.

9.2 Outlook

Current dielectric wakefield acceleration experiments have been limited to cm-scale propagation distances, whilst studies of longer distances have been limited to simulation studies such

The field of dielectric wakefield acceleration holds great promise, but there are several challenges that need to be addressed before the technology can reach its full potential. Current experiments have been limited in terms of structure length, demonstrating the ability to achieve large accelerating gradients but limited energy gain. To advance practical applications of dielectric wakefield acceleration, it is crucial to conduct experiments with longer accelerating structures that span propagation lengths on the order of metres. Over these propagation lengths it would be possible to extract a large percentage of the drive beam energy, allowing for studies of efficiency and scaleability of DWA.

Such experiments would provide valuable insights into the behavior of dielectric wakefield acceleration over extended distances, enabling a better understanding of the scalability and feasibility of future DWA applications.

While significant progress has been made in understanding the transverse dynamics in planar DLWs, studies on transverse fields in cylindrical DLWs have not been as extensive. Further investigations into these fields are necessary, and it will be essential to develop lightweight simulation software specifically designed for circular DLWs, similar to the capabilities of DiWaCAT for planar DLWs. Proposed methods for beam-breakup (BBU) suppression, such as the use of a quadrupole wiggler, require experimental validation, especially considering the precise tolerances needed for DLW and quadrupole manufacture in these schemes [77][84].

Upgrades to CLARA increasing the beam charge (100 to 250 pC), momentum (35.5 to 250 MeV/c), and transverse beam quality (detailed in [144]) will allow for the continuation of DWA research at this facility. The higher bunch charge should allow for measurement of larger accelerating gradients, with fields $\sim$100 MV/m reasonable with 250 pC charge drive bunches. Detailed study of transverse dynamics is possible at the upgraded facility, given the positioning of interchangeable diagnostics (YAG screens, slits, and dielectric wakefield streaker) within the experimental area (FEBE) and should remain a focus of DWA experiments at the facility [158]. The combination of detailed beam dynamics studies whilst exciting longitudinal fields comparable to those at future DWA applications would provide necessary insights to practical DWA operation. The study of longer DLWs will be possible at CLARA given the 1.8 m long space available within the experimental chambers, as will the study of transverse dynamics

in drive-witness bunch pairs, facilitated by the use of masking or laser pulse shaping techniques.

At Daresbury Laboratory, there is a strong focus on the development of passive beam manipulation and diagnostic devices utilising DLWs. The installation of the dechirper [103] in the CLARA beamline and the planned implementation of a dielectric wakefield streaker in the FEBE hutch [158][109] highlight these efforts. The ongoing development of passive devices should continue, including evaluating the performance of the streaker across the range of bunches expected in CLARA experiments, thereby validating the conclusions drawn in this thesis.

In conclusion, the future of DWA research lies in overcoming the challenges related to structure length, transverse beam dynamics in cylindrical DWA structures, and BBU suppression. The upgrades to the CLARA facility, combined with ongoing developments in passive beam manipulation and diagnostics, provide exciting opportunities to further advance DWA technology. By addressing these challenges and conducting comprehensive experiments, the field of DWA can move closer to practical implementation and open doors to a wide range of applications.

References

[1] A. Sessler, *Engines of Discovery: A Century of Particle Accelerators*. World Scientific, 2014.

[2] J. Brau, Y. Okada, W. N., *et al.*, "ILC reference design report volume 1-executive summary," Tech. Rep., 2007.

[3] A. Cho. (2009). "Chu pegs ILC cost at $25 billion," [Online]. Available: https://web.archive.org/web/20100105091936/http://blogs.sciencemag.org/scienceinsider/2009/05/chu-pegs-ilc-co.html.

[4] S. Belomestnykh, "Rf technologies for future colliders," *Frontiers in Physics*, vol. 10, 2022. DOI: 10.3389/fphy.2022.933479. [Online]. Available: https://www.frontiersin.org/articles/10.3389/fphy.2022.933479.

[5] M. Aicheler, P. Burrows, M. Draper, T. Garvey, P. Lebrun, K. Peach, N. Phinney, H. Schmickler, D. Schulte, and N. Toge, "A Multi-TeV linear collider based on CLIC technology: CLIC Conceptual Design Report," CERN, Tech. Rep., 2012. DOI: 10.5170/CERN-2012-007. [Online]. Available: https://cds.cern.ch/record/1500095.

[6] "2020 Update of the European Strategy for Particle Physics (Brochure)," Geneva, Tech. Rep., 2020. DOI: 10.17181/CERN.JSC6.W89E. [Online]. Available: https://cds.cern.ch/record/2721370.

[7] J. N. Butler, R. S. Chivukula, A. de Gouvêa, *et al.*, "Report of the 2021 U.S. Community Study on the Future of Particle Physics (Snowmass 2021) Summary Chapter," *arXiv preprint arXiv:2301.06581*, 2023.

[8] S. Gourlay, T. Raubenheimer, V. Shiltsev, G. Arduini, R. Assmann, C. Barbier, M. Bai, S. Belomestnykh, S. Bermudez, P. Bhat, *et al.*, "Snowmass' 21 accelerator frontier report," *arXiv preprint arXiv:2209.14136*, 2022.

[9] Science and Technology Facilities Council (STFC), "STFC strategic framework for future accelerator science and technology development," Tech. Rep., Oct. 2022.

[10] ALEGRO Collaboration, *Towards an advanced linear international collider*, Jan. 2019. DOI: 10.48550/ARXIV.1901.10370. [Online]. Available: https://arxiv.org/abs/1901.10370.

[11] C. Geddes, M. Hogan, P. Musumeci, and R. Assmann, "Report of the accelerator frontier topical group 6 on advanced accelerator concepts for Snowmass 2021," *arXiv preprint arXiv:2208.13279*, 2022. [Online]. Available: https://arxiv.org/abs/2208.13279.

[12] R. Assmann, M. Weikum, T. Akhter, D. Alesini, A. Alexandrova, M. Anania, N. Andreev, I. Andriyash, M. Artioli, A. Aschikhin, *et al.*, "EuPRAXIA conceptual design report," *The European Physical Journal Special Topics*, vol. 229, no. 24, pp. 3675–4284, 2020. DOI: 10.1140/epjst/e2021-100018-5. [Online]. Available: https://doi.org/10.1140/epjst/e2021-100018-5.

[13] A. Zholents *et al.*, "A Conceptual Design of a Compact Wakefield Accelerator for a High Repetition Rate Multi User X-ray Free-Electron Laser Facility," in *Proc. 9th International Particle Accelerator Conference (IPAC'18), Vancouver, BC, Canada, April 29-May 4, 2018*, ser. International Particle Accelerator Conference, Geneva, Switzerland: JACoW Publishing, Jun. 2018, pp. 1266–1268, ISBN: 978-3-95450-184-7. DOI: doi:10.18429/JACoW-IPAC2018-TUPMF010. [Online]. Available: http://jacow.org/ipac2018/papers/tupmf010.pdf.

[14] S. Antipov, S. Baturin, C. Jing, M. Fedurin, A. Kanareykin, C. Swinson, P. Schoessow, W. Gai, and A. Zholents, "Experimental demonstration of energy-chirp compensation by a tunable dielectric-based structure," *Phys. Rev. Lett.*, vol. 112, p. 114 801, 11 Mar. 2014. DOI: 10.1103/PhysRevLett.112.114801. [Online]. Available: https://link.aps.org/doi/10.1103/PhysRevLett.112.114801.

[15] T. Pacey, Y. Saveliev, G. Xia, and J. Smith, "Simulation studies for dielectric wakefield programme at CLARA facility," *Nuclear Instruments and Methods in Physics Research Section A: Accelerators, Spectrometers, Detectors and Associated Equipment*, vol. 909, pp. 261–265, 2018, 3rd European Advanced

Accelerator Concepts workshop (EAAC2017), ISSN: 0168-9002. DOI: https://doi.org/10.1016/j.nima.2017.12.038. [Online]. Available: https://www.sciencedirect.com/science/article/pii/S0168900217314286.

[16] S. Bettoni, P. Craievich, A. A. Lutman, and M. Pedrozzi, "Temporal profile measurements of relativistic electron bunch based on wakefield generation," *Phys. Rev. Accel. Beams*, vol. 19, p. 021 304, 2 Feb. 2016. DOI: 10.1103/PhysRevAccelBeams.19.021304. [Online]. Available: https://link.aps.org/doi/10.1103/PhysRevAccelBeams.19.021304.

[17] P. Gibbon, "Introduction to plasma physics," in *Proceedings of the CERN-Accelerator-School course: High Gradient Wakefield Accelerators*, 2019, pp. 77–95. [Online]. Available: https://arxiv.org/abs/2007.04783.

[18] J. Vieira, R. Fonseca, and L. Silva, "Multidimensional plasma wake excitation in the non-linear blowout regime," in *Proceedings of the CERN-Accelerator-School course: Plasma Wake Acceleration*, 2014, pp. 79–108.

[19] J. M. Dawson, "Nonlinear electron oscillations in a cold plasma," *Phys. Rev.*, vol. 113, pp. 383–387, 2 Jan. 1959. DOI: 10.1103/PhysRev.113.383. [Online]. Available: https://link.aps.org/doi/10.1103/PhysRev.113.383.

[20] R. M. G. M. Trines and P. A. Norreys, "Wave-breaking limits for relativistic electrostatic waves in a one-dimensional warm plasma," *Physics of Plasmas*, vol. 13, no. 12, p. 123 102, 2006. DOI: 10.1063/1.2398927. [Online]. Available: https://doi.org/10.1063/1.2398927.

[21] W. Lu, C. Huang, M. M. Zhou, W. B. Mori, and T. Katsouleas, "Limits of linear plasma wakefield theory for electron or positron beams," *Physics of Plasmas*, vol. 12, no. 6, p. 063 101, 2005. DOI: 10.1063/1.1905587. [Online]. Available: https://doi.org/10.1063/1.1905587.

[22] J. Wenz and S. Karsch, "Physics of Laser-Wakefield Accelerators (LWFA)," in *Proceedings of the CERN-Accelerator-School course: High Gradient Wakefield Accelerators*, 2019, pp. 108–95. [Online]. Available: https://arxiv.org/abs/2007.04622.

[23] M. Tzoufras, W. Lu, F. S. Tsung, *et al.*, "Beam loading by electrons in nonlinear plasma wakes," *Physics of Plasmas*, vol. 16, no. 5, p. 056 705, May 2009, ISSN:

1070-664X. DOI: 10.1063/1.3118628. [Online]. Available: https://doi.org/10.1063/1.3118628.

[24] R. Pompili, D. Alesini, M. P. Anania, *et al.*, "Energy spread minimization in a beam-driven plasma wakefield accelerator," *Nature Physics*, vol. 17, no. 4, pp. 499–503, Apr. 2021. DOI: 10.1038/s41567-020-01116-9. [Online]. Available: https://doi.org/10.1038/s41567-020-01116-9.

[25] C. A. Lindstrøm, J. M. Garland, S. Schröder, L. Boulton, G. Boyle, J. Chappell, R. D'Arcy, P. Gonzalez, A. Knetsch, V. Libov, G. Loisch, A. Martinez de la Ossa, P. Niknejadi, K. Põder, L. Schaper, B. Schmidt, B. Sheeran, S. Wesch, J. Wood, and J. Osterhoff, "Energy-spread preservation and high efficiency in a plasma-wakefield accelerator," *Phys. Rev. Lett.*, vol. 126, p. 014 801, 1 Jan. 2021. DOI: 10.1103/PhysRevLett.126.014801. [Online]. Available: https://link.aps.org/doi/10.1103/PhysRevLett.126.014801.

[26] T. Tajima and J. M. Dawson, "Laser electron accelerator," *Phys. Rev. Lett.*, vol. 43, pp. 267–270, 4 Jul. 1979. DOI: 10.1103/PhysRevLett.43.267. [Online]. Available: https://link.aps.org/doi/10.1103/PhysRevLett.43.267.

[27] C. E. Clayton, K. A. Marsh, A. Dyson, M. Everett, A. Lal, W. P. Leemans, R. Williams, and C. Joshi, "Ultrahigh-gradient acceleration of injected electrons by laser-excited relativistic electron plasma waves," *Phys. Rev. Lett.*, vol. 70, pp. 37–40, 1 Jan. 1993. DOI: 10.1103/PhysRevLett.70.37. [Online]. Available: https://link.aps.org/doi/10.1103/PhysRevLett.70.37.

[28] D. Strickland and G. Mourou, "Compression of amplified chirped optical pulses," *Optics Communications*, vol. 56, no. 3, pp. 219–221, 1985, ISSN: 0030-4018. DOI: https://doi.org/10.1016/0030-4018(85)90120-8. [Online]. Available: https://www.sciencedirect.com/science/article/pii/0030401885901208.

[29] W. P. Leemans, A. J. Gonsalves, H.-S. Mao, K. Nakamura, C. Benedetti, C. B. Schroeder, C. Tóth, J. Daniels, D. E. Mittelberger, S. S. Bulanov, J.-L. Vay, C. G. R. Geddes, and E. Esarey, "Multi-GeV electron beams from capillary-discharge-guided subpetawatt laser pulses in the self-trapping regime," *Phys. Rev. Lett.*, vol. 113, p. 245 002, 24 Dec. 2014. DOI: 10.1103/PhysRevLett.

113.245002. [Online]. Available: https://link.aps.org/doi/10.1103/PhysRevLett.113.245002.

[30] S. Steinke, J. van Tilborg, C. Benedetti, C. G. R. Geddes, C. B. Schroeder, J. Daniels, K. K. Swanson, A. J. Gonsalves, K. Nakamura, N. H. Matlis, B. H. Shaw, E. Esarey, and W. P. Leemans, "Multistage coupling of independent laser-plasma accelerators," *Nature*, vol. 530, no. 7589, pp. 190–193, 2016. DOI: 10.1038/nature16525. [Online]. Available: https://doi.org/10.1038/nature16525.

[31] A. J. Gonsalves, K. Nakamura, J. Daniels, C. Benedetti, C. Pieronek, T. C. H. de Raadt, S. Steinke, J. H. Bin, S. S. Bulanov, J. van Tilborg, C. G. R. Geddes, C. B. Schroeder, C. Tóth, E. Esarey, K. Swanson, L. Fan-Chiang, G. Bagdasarov, N. Bobrova, V. Gasilov, G. Korn, P. Sasorov, and W. P. Leemans, "Petawatt laser guiding and electron beam acceleration to 8 GeV in a laser-heated capillary discharge waveguide," *Phys. Rev. Lett.*, vol. 122, p. 084 801, 8 Feb. 2019. DOI: 10.1103/PhysRevLett.122.084801. [Online]. Available: https://link.aps.org/doi/10.1103/PhysRevLett.122.084801.

[32] P. Chen, J. M. Dawson, R. W. Huff, and T. Katsouleas, "Acceleration of electrons by the interaction of a bunched electron beam with a plasma," *Phys. Rev. Lett.*, vol. 54, pp. 693–696, 7 Feb. 1985. DOI: 10.1103/PhysRevLett.54.693. [Online]. Available: https://link.aps.org/doi/10.1103/PhysRevLett.54.693.

[33] A. Caldwell, K. Lotov, A. Pukhov, and F. Simon, "Proton-driven plasma-wakefield acceleration," *Nature Physics*, vol. 5, no. 5, pp. 363–367, 2009. DOI: 10.1038/nphys1248. [Online]. Available: https://doi.org/10.1038/nphys1248.

[34] P. Chen, J. M. Dawson, R. W. Huff, and T. Katsouleas, "Acceleration of electrons by the interaction of a bunched electron beam with a plasma," *Phys. Rev. Lett.*, vol. 54, pp. 693–696, 7 Feb. 1985. DOI: 10.1103/PhysRevLett.54.693. [Online]. Available: https://link.aps.org/doi/10.1103/PhysRevLett.54.693.

[35] B. Hidding, G. Manahan, O. Karger, A. Knetsch, G. Wittig, D. Jaroszynski, Z. Sheng, Y. Xi, A. Deng, J. Rosenzweig, *et al.*, "Ultrahigh brightness bunches from hybrid plasma accelerators as drivers of 5th generation light sources," *Journal of*

Physics B: Atomic, Molecular and Optical Physics, vol. 47, no. 23, p. 234 010, 2014.

[36] J. B. Rosenzweig, B. Breizman, T. Katsouleas, and J. J. Su, "Acceleration and focusing of electrons in two-dimensional nonlinear plasma wake fields," *Phys. Rev. A*, vol. 44, R6189–R6192, 10 Nov. 1991. DOI: 10.1103/PhysRevA.44.R6189. [Online]. Available: https://link.aps.org/doi/10.1103/PhysRevA.44.R6189.

[37] J. B. Rosenzweig, D. B. Cline, B. Cole, H. Figueroa, W. Gai, R. Konecny, J. Norem, P. Schoessow, and J. Simpson, "Experimental observation of plasma wake-field acceleration," *Phys. Rev. Lett.*, vol. 61, pp. 98–101, 1 Jul. 1988. DOI: 10.1103/PhysRevLett.61.98. [Online]. Available: https://link.aps.org/doi/10.1103/PhysRevLett.61.98.

[38] I. Blumenfeld, C. E. Clayton, F.-J. Decker, M. J. Hogan, C. Huang, R. Ischebeck, R. Iverson, C. Joshi, T. Katsouleas, N. Kirby, W. Lu, K. A. Marsh, W. B. Mori, P. Muggli, E. Oz, R. H. Siemann, D. Walz, and M. Zhou, "Energy doubling of 42 GeV electrons in a metre-scale plasma wakefield accelerator," *Nature*, vol. 445, no. 7129, pp. 741–744, 2007. DOI: 10.1038/nature05538. [Online]. Available: https://doi.org/10.1038/nature05538.

[39] G. Xia, A. Caldwell, C. Huang, and W. Mori, "Simulation study of proton-driven PWFA based on CERN SPS beam," in *Proceedings of 2011 Particle Accelerator Conference*, (New York, NY, USA), vol. 110328, 2011, pp. 301–303. [Online]. Available: https://accelconf.web.cern.ch/pac2011/papers/mop108.pdf.

[40] "AWAKE, the advanced proton driven plasma wakefield acceleration experiment at CERN," *Nuclear Instruments and Methods in Physics Research Section A: Accelerators, Spectrometers, Detectors and Associated Equipment*, vol. 829, pp. 76–82, 2016, 2nd European Advanced Accelerator Concepts Workshop - EAAC 2015, ISSN: 0168-9002. DOI: https://doi.org/10.1016/j.nima.2016.02.026. [Online]. Available: https://www.sciencedirect.com/science/article/pii/S0168900216001881.

[41] The AWAKE Collaboration, "Experimental observation of proton bunch modulation in a plasma at varying plasma densities," *Phys. Rev. Lett.*, vol. 122, p. 054 802,

5 Feb. 2019. DOI: 10.1103/PhysRevLett.122.054802. [Online]. Available: https://link.aps.org/doi/10.1103/PhysRevLett.122.054802.

[42] The AWAKE Collaboration, "Experimental observation of plasma wakefield growth driven by the seeded self-modulation of a proton bunch," *Phys. Rev. Lett.*, vol. 122, 5 Feb. 2019. DOI: 10.1103/PhysRevLett.122.054801. [Online]. Available: https://link.aps.org/doi/10.1103/PhysRevLett.122.054801.

[43] E. Gschwendtner, "AWAKE Run 2 at CERN," in *Proc. IPAC'21*, (Campinas, SP, Brazil), ser. International Particle Accelerator Conference, JACoW Publishing, Geneva, Switzerland, Aug. 2021, pp. 1757–1760, ISBN: 978-3-95450-214-1. DOI: 10.18429/JACoW-IPAC2021-TUPAB159. [Online]. Available: https://jacow.org/ipac2021/papers/tupab159.pdf.

[44] The AWAKE Collaboration, "Acceleration of electrons in the plasma wakefield of a proton bunch," *Nature*, vol. 561, no. 7723, pp. 363–367, 2018. DOI: 10.1038/s41586-018-0485-4. [Online]. Available: https://doi.org/10.1038/s41586-018-0485-4.

[45] B. E. Blue, C. E. Clayton, C. L. O'Connell, F.-J. Decker, M. J. Hogan, C. Huang, R. Iverson, C. Joshi, T. C. Katsouleas, W. Lu, K. A. Marsh, W. B. Mori, P. Muggli, R. Siemann, and D. Walz, "Plasma-wakefield acceleration of an intense positron beam," *Phys. Rev. Lett.*, vol. 90, p. 214 801, 21 May 2003. DOI: 10.1103/PhysRevLett.90.214801. [Online]. Available: https://link.aps.org/doi/10.1103/PhysRevLett.90.214801.

[46] S. Corde, E. Adli, J. M. Allen, W. An, C. I. Clarke, C. E. Clayton, J. P. Delahaye, J. Frederico, S. Gessner, S. Z. Green, M. J. Hogan, C. Joshi, N. Lipkowitz, M. Litos, W. Lu, K. A. Marsh, W. B. Mori, M. Schmeltz, N. Vafaei-Najafabadi, D. Walz, V. Yakimenko, and G. Yocky, "Multi-gigaelectronvolt acceleration of positrons in a self-loaded plasma wakefield," *Nature*, vol. 524, no. 7566, pp. 442–445, 2015. DOI: 10.1038/nature14890. [Online]. Available: https://doi.org/10.1038/nature14890.

[47] Y. Li, G. Xia, K. V. Lotov, A. P. Sosedkin, and Y. Zhao, "High-quality positrons from a multi-proton bunch driven hollow plasma wakefield accelerator," *Plasma Physics and Controlled Fusion*, vol. 61, no. 2, p. 025 012, Jan. 2019. DOI: 10.

1088/1361-6587/aaf121. [Online]. Available: https://dx.doi.org/10.1088/1361-6587/aaf121.

[48] B. W. Zotter and S. A. Kheifets, *Impedances and wakes in high-energy particle accelerators*. World Scientific, 1998.

[49] J. D. Jackson, *Classical electrodynamics*. John Wiley & Sons, 2021.

[50] B. Bolotovskii, "Theory of Cerenkov Radiation (III)," *Soviet Physics Uspekhi*, vol. 4, no. 5, p. 781, May 1962. DOI: 10.1070/PU1962v004n05ABEH003380. [Online]. Available: https://dx.doi.org/10.1070/PU1962v004n05ABEH003380.

[51] K. L. Bane, P. Chen, and P. B. Wilson, "On collinear wake field acceleration," in *Proceedings of the 1985 Particle Accelerator Conference (PAC1985)*, A. Strathdee, Ed., vol. 32, 1985, pp. 3524–3526. DOI: 10.1109/TNS.1985.4334416.

[52] M. C. Thompson, H. Badakov, A. M. Cook, J. B. Rosenzweig, R. Tikhoplav, G. Travish, I. Blumenfeld, M. J. Hogan, R. Ischebeck, N. Kirby, R. Siemann, D. Walz, P. Muggli, A. Scott, and R. B. Yoder, "Breakdown limits on gigavolt-per-meter electron-beam-driven wakefields in dielectric structures," *Phys. Rev. Lett.*, vol. 100, p. 214 801, 21 May 2008. DOI: 10.1103/PhysRevLett.100.214801. [Online]. Available: https://link.aps.org/doi/10.1103/PhysRevLett.100.214801.

[53] B. D. O'Shea, G. Andonian, S. K. Barber, C. I. Clarke, P. D. Hoang, M. J. Hogan, B. Naranjo, O. B. Williams, V. Yakimenko, and J. B. Rosenzweig, "Conductivity induced by high-field terahertz waves in dielectric material," *Phys. Rev. Lett.*, vol. 123, p. 134 801, 13 Sep. 2019. DOI: 10.1103/PhysRevLett.123.134801. [Online]. Available: https://link.aps.org/doi/10.1103/PhysRevLett.123.134801.

[54] W. Gai, P. Schoessow, B. Cole, R. Konecny, J. Norem, J. Rosenzweig, and J. Simpson, "Experimental demonstration of wake-field effects in dielectric structures," *Phys. Rev. Lett.*, vol. 61, pp. 2756–2758, 24 Dec. 1988. DOI: 10.1103/PhysRevLett.61.2756. [Online]. Available: https://link.aps.org/doi/10.1103/PhysRevLett.61.2756.

[55] B. D. O'Shea, G. Andonian, S. K. Barber, K. L. Fitzmorris, S. Hakimi, J. Harrison, P. D. Hoang, M. J. Hogan, B. Naranjo, O. B. Williams, V. Yakimenko, and J. B. Rosenzweig, "Observation of acceleration and deceleration in gigaelectron-volt-per-metre gradient dielectric wakefield accelerators," *Nature Communications*, vol. 7, no. 1, p. 12 763, 2016. [Online]. Available: https://doi.org/10.1038/ncomms12763.

[56] N. Majernik, G. Andonian, O. B. Williams, B. D. O'Shea, P. D. Hoang, C. Clarke, M. J. Hogan, V. Yakimenko, and J. B. Rosenzweig, "Positron driven high-field terahertz waves via dielectric wakefield interaction," *Phys. Rev. Res.*, vol. 4, p. 023 065, 2 Apr. 2022. DOI: 10.1103/PhysRevResearch.4.023065. [Online]. Available: https://link.aps.org/doi/10.1103/PhysRevResearch.4.023065.

[57] N. Schönenberger and P. Hommelhoff, "Dielectric laser acceleration," in *Proceedings of the CERN-Accelerator-School course: High Gradient Wakefield Accelerators*, 2019, pp. 265–283. [Online]. Available: https://arxiv.org/abs/2008.03958.

[58] D. Cesar, S. Custodio, J. Maxson, P. Musumeci, X. Shen, E. Threlkeld, R. J. England, A. Hanuka, I. V. Makasyuk, E. A. Peralta, K. P. Wootton, and Z. Wu, "High-field nonlinear optical response and phase control in a dielectric laser accelerator," *Communications Physics*, vol. 1, no. 1, p. 46, 2018. DOI: 10.1038/s42005-018-0047-y. [Online]. Available: https://doi.org/10.1038/s42005-018-0047-y.

[59] K. Soong, R. Byer, E. Colby, R. England, and E. Peralta, "Laser damage threshold measurements of optical materials for direct laser accelerators," in *AIP Conference Proceedings*, American Institute of Physics, vol. 1507, 2012, pp. 511–515. DOI: 10.1063/1.4773749. [Online]. Available: https://doi.org/10.1063/1.4773749.

[60] U. Niedermayer, K. Leedle, P. Musumeci, and S. A. Schmid, "Beam dynamics in dielectric laser acceleration," *Journal of Instrumentation*, vol. 17, no. 05, P05014, 2022. DOI: 10.1088/1748-0221/17/05/P05014. [Online]. Available: https://doi.org/10.1088/1748-0221/17/05/P05014.

[61] K. Leedle, A. Ceballos, H. Deng, O. Solgaard, R. Fabian Pease, R. Byer, and J. Harris, "Dielectric laser acceleration of sub-100 keV electrons with silicon dual-pillar grating structures," *Opt. Lett.*, vol. 40, no. 18, pp. 4344–4347, Sep. 2015. DOI: 10.1364/OL.40.004344. [Online]. Available: https://opg.optica.org/ol/abstract.cfm?URI=ol-40-18-4344.

[62] J. Breuer, R. Graf, A. Apolonski, and P. Hommelhoff, "Dielectric laser acceleration of nonrelativistic electrons at a single fused silica grating structure: Experimental part," *Phys. Rev. ST Accel. Beams*, vol. 17, p. 021 301, 2 Feb. 2014. DOI: 10.1103/PhysRevSTAB.17.021301. [Online]. Available: https://link.aps.org/doi/10.1103/PhysRevSTAB.17.021301.

[63] A. Grudiev, S. Calatroni, and W. Wuensch, "New local field quantity describing the high gradient limit of accelerating structures," *Phys. Rev. ST Accel. Beams*, vol. 12, p. 102 001, 10 Oct. 2009. DOI: 10.1103/PhysRevSTAB.12.102001. [Online]. Available: https://link.aps.org/doi/10.1103/PhysRevSTAB.12.102001.

[64] H. Kong, M. Chung, D. S. Doran, G. Ha, S. .-H. Kim, J. .-H. Kim, W. Liu, X. Lu, J. Power, J. .-M. Seok, S. Shin, J. Shao, C. Whiteford, and E. Wisniewski, "Fabrication of THz corrugated wakefield structure and its high power test," *Scientific Reports*, vol. 13, no. 1, p. 3207, 2023. DOI: 10.1038/s41598-023-29997-9. [Online]. Available: https://doi.org/10.1038/s41598-023-29997-9.

[65] M. Dal Forno, V. Dolgashev, G. Bowden, C. Clarke, M. Hogan, D. McCormick, A. Novokhatski, B. Spataro, S. Weathersby, and S. G. Tantawi, "Rf breakdown tests of mm-wave metallic accelerating structures," *Phys. Rev. Accel. Beams*, vol. 19, p. 011 301, 1 Jan. 2016. DOI: 10.1103/PhysRevAccelBeams.19.011301. [Online]. Available: https://link.aps.org/doi/10.1103/PhysRevAccelBeams.19.011301.

[66] D. Wang, S. Antipov, C. Jing, J. G. Power, M. Conde, E. Wisniewski, W. Liu, J. Qiu, G. Ha, V. Dolgashev, C. Tang, and W. Gai, "Interaction of an ultrarelativistic electron bunch train with a W-Band accelerating structure: High power and high gradient," *Phys. Rev. Lett.*, vol. 116, p. 054 801, 5 Feb. 2016. DOI: 10.1103/

PhysRevLett.116.054801. [Online]. Available: https://link.aps.org/doi/10.1103/PhysRevLett.116.054801.

[67] M. Peng, J. Shao, C. Jing, *et al.*, "Generation of High Power Short Rf Pulses using an X-Band Metallic Power Extractor Driven by High Charge Multi-Bunch Train," in *Proc. 10th International Particle Accelerator Conference (IPAC'19)*, ser. International Particle Accelerator Conference, Geneva, Switzerland: JACoW Publishing, Jun. 2019, pp. 734–737. DOI: doi:10.18429/JACoW-IPAC2019-MOPRB069. [Online]. Available: http://jacow.org/ipac2019/papers/moprb069.pdf.

[68] C. Jing, "Short-pulse wakefield structure r&d for high gradient and high efficiency acceleration," International Workshop on Future Linear Colliders, LCWS2021, 2021, [Online]. Available: https://indico.cern.ch/event/995633/contributions/4274781/attachments/2211573/3742946/short_pulse_LCWS21_2.pdf.

[69] W. Gai, M. Conde, R. Konecny, J. Power, P. Schoessow, J. Simpson, X. Sun, and P. Zou, "Experimental demonstration of two beam acceleration using dielectric step-up transformer," in *PACS2001. Proceedings of the 2001 Particle Accelerator Conference*, vol. 3, 2001, 1880–1882 vol.3. DOI: 10.1109/PAC.2001.987214.

[70] J. Shao, C. Jing, E. Wisniewski, G. Ha, M. Conde, W. Liu, J. Power, and L. Zheng, "Development and high-power testing of an X-Band dielectric-loaded power extractor," *Phys. Rev. Accel. Beams*, vol. 23, p. 011 301, 1 Jan. 2020. DOI: 10.1103/PhysRevAccelBeams.23.011301. [Online]. Available: https://link.aps.org/doi/10.1103/PhysRevAccelBeams.23.011301.

[71] C. Jing, J. Power, J. Shao, G. Ha, P. Piot, X. Lu, A. Zholents, A. Kanareykin, S. Kuzikov, J. B. Rosenzweig, *et al.*, "Continuous and coordinated efforts of structure wakefield acceleration (SWFA) development for an energy frontier machine," *arXiv preprint arXiv:2203.08275*, 2022.

[72] X. Lu, J. Shao, J. Power, C. Jing, G. Ha, P. Piot, M. Shapiro, E. Nanni, J. Rosenzweig, G. Andonian, *et al.*, "Advanced RF structures for wakefield acceleration and high-gradient research," *arXiv preprint arXiv:2203.08374*, 2022.

[73] J. Rosenzweig, H. Ancelin, G. Andonian, S. Baryshev, S. Baturin, A. Fukasawa, C. Hansel, M. Hogan, G. Lawler, W. Lynn, N. Majernik, J. Mann, P. Manwani, B.

O'Shea, Y. Sakai, D. Storey, O. Williams, M. Yadav, and V. Yakimenko, "Physics Goals of DWA Experiments at FACET-II," in *Proc. IPAC'21*, (Campinas, SP, Brazil), ser. International Particle Accelerator Conference, JACoW Publishing, Geneva, Switzerland, Aug. 2021, pp. 3922–3925, ISBN: 978-3-95450-214-1. DOI: 10.18429/JACoW-IPAC2021-THPAB071. [Online]. Available: https://jacow.org/ipac2021/papers/thpab071.pdf.

[74] Q. Gao, G. Ha, C. Jing, S. P. Antipov, J. G. Power, M. Conde, W. Gai, H. Chen, J. Shi, E. E. Wisniewski, D. S. Doran, W. Liu, C. E. Whiteford, A. Zholents, P. Piot, and S. S. Baturin, "Observation of high transformer ratio of shaped bunch generated by an emittance-exchange beam line," *Phys. Rev. Lett.*, vol. 120, p. 114 801, 11 Mar. 2018. DOI: 10.1103/PhysRevLett.120.114801. [Online]. Available: https://link.aps.org/doi/10.1103/PhysRevLett.120.114801.

[75] S. S. Baturin and A. Zholents, "Upper limit for the accelerating gradient in the collinear wakefield accelerator as a function of the transformer ratio," *Phys. Rev. Accel. Beams*, vol. 20, p. 061 302, 6 Jun. 2017. DOI: 10.1103/PhysRevAccelBeams.20.061302. [Online]. Available: https://link.aps.org/doi/10.1103/PhysRevAccelBeams.20.061302.

[76] C. Jing, J. G. Power, M. Conde, W. Liu, Z. Yusof, A. Kanareykin, and W. Gai, "Increasing the transformer ratio at the Argonne wakefield Accelerator," *Phys. Rev. ST Accel. Beams*, vol. 14, p. 021 302, 2 Feb. 2011. DOI: 10.1103/PhysRevSTAB.14.021302. [Online]. Available: https://link.aps.org/doi/10.1103/PhysRevSTAB.14.021302.

[77] D. Y. Shchegolkov, E. I. Simakov, and A. A. Zholents, "Towards a practical multi-meter long dielectric wakefield accelerator: Problems and solutions," *IEEE Transactions on Nuclear Science*, vol. 63, no. 2, pp. 804–811, 2016. DOI: 10.1109/TNS.2015.2482820.

[78] G. Loisch, G. Asova, P. Boonpornprasert, *et al.*, "Observation of high transformer ratio plasma wakefield acceleration," *Phys. Rev. Lett.*, vol. 121, p. 064 801, 6 Aug. 2018. DOI: 10.1103/PhysRevLett.121.064801. [Online]. Available: https://link.aps.org/doi/10.1103/PhysRevLett.121.064801.

[79] P. Muggli, V. Yakimenko, M. Babzien, E. Kallos, and K. P. Kusche, "Generation of trains of electron microbunches with adjustable subpicosecond spacing," *Phys. Rev. Lett.*, vol. 101, p. 054 801, 5 Jul. 2008. DOI: 10.1103/PhysRevLett.101.054801. [Online]. Available: https://link.aps.org/doi/10.1103/PhysRevLett.101.054801.

[80] S. Schröder, K. Ludwig, A. Aschikhin, R. D'Arcy, M. Dinter, P. Gonzalez, S. Karstensen, A. Knetsch, V. Libov, C. A. Lindstrøm, F. Marutzky, P. Niknejadi, A. Rahali, L. Schaper, A. Schleiermacher, B. Schmidt, S. Thiele, A. de Zubiaurre Wagner, S. Wesch, and J. Osterhoff, "Tunable and precise two-bunch generation at FLASHForward," *Journal of Physics: Confererence Series*, vol. 1596, no. 1, p. 012 002, Jul. 2020. DOI: 10.1088/1742-6596/1596/1/012002. [Online]. Available: https://dx.doi.org/10.1088/1742-6596/1596/1/012002.

[81] W. H. Tan, P. Piot, and A. Zholents, "Formation of temporally shaped electron bunches for beam-driven collinear wakefield accelerators," *Phys. Rev. Accel. Beams*, vol. 24, p. 051 303, 5 May 2021. DOI: 10.1103/PhysRevAccelBeams.24.051303. [Online]. Available: https://link.aps.org/doi/10.1103/PhysRevAccelBeams.24.051303.

[82] W. Tan, "Compact wakefield accelerator with advanced beam manipulations," Ph.D. dissertation, Northern Illinois University, 2022.

[83] V. Balakin, A. Novokhatski, and V. Smirnov, "VLEPP: Transverse beam dynamics, 12th int," in *Conf. On High Energy Accel., FNAL*, vol. 119, 1983.

[84] W. Tan, A. Huebl, R. Jambunathan, R. Lehé, A. Myers, P. Piot, T. Rheaume, J.-L. Vay, and W. Zhang, "Simulation Studies of Drive Beam Instability in a Dielectric Wakefield Accelerator," in *Proc. IPAC'22*, (Bangkok, Thailand), ser. International Particle Accelerator Conference, JACoW Publishing, Geneva, Switzerland, Jul. 2022, pp. 645–648, ISBN: 978-3-95450-227-1. DOI: 10.18429/JACoW-IPAC2022-MOPOMS012. [Online]. Available: https://jacow.org/ipac2022/papers/mopoms012.pdf.

[85] D. Shchegolkov, E. Simakov, and A. Zholents, "Simulation Studies of BBU Suppression Methods and Acceptable Tolerances in Dielectric Wakefield Accelerators," in *Proc. 6th International Particle Accelerator Conference (IPAC'15)*, (Richmond, VA, USA), ser. International Particle Accelerator Conference, Geneva,

Switzerland: JACoW, Jun. 2015, pp. 2685–2688, ISBN: 978-3-95450-168-7. DOI: https://doi.org/10.18429/JACoW-IPAC2015-WEPJE007. [Online]. Available: http://jacow.org/ipac2015/papers/wepje007.pdf.

[86] A. Zholents, W. Gai, S. Doran, R. Lindberg, J. Power, N. Strelnikov, Y. Sun, E. Trakhtenberg, I. Vasserman, C. Jing, A. Kanareykin, Y. Li, Q. Gao, D. Shchegolkov, and E. Simakov, "A preliminary design of the collinear dielectric wakefield accelerator," *Nuclear Instruments and Methods in Physics Research Section A: Accelerators, Spectrometers, Detectors and Associated Equipment*, vol. 829, pp. 190–193, 2016, 2nd European Advanced Accelerator Concepts Workshop - EAAC 2015, ISSN: 0168-9002. DOI: https://doi.org/10.1016/j.nima.2016.02.003. [Online]. Available: https://www.sciencedirect.com/science/article/pii/S0168900216001479.

[87] S. S. Baturin and A. Zholents, "Stability condition for the drive bunch in a collinear wakefield accelerator," *Phys. Rev. Accel. Beams*, vol. 21, p. 031 301, 3 Mar. 2018. DOI: 10.1103/PhysRevAccelBeams.21.031301. [Online]. Available: https://link.aps.org/doi/10.1103/PhysRevAccelBeams.21.031301.

[88] L. Xiao, W. Gai, and X. Sun, "Field analysis of a dielectric-loaded rectangular waveguide accelerating structure," *Phys. Rev. E*, vol. 65, p. 016 505, 1 Dec. 2001. DOI: 10.1103/PhysRevE.65.016505. [Online]. Available: https://link.aps.org/doi/10.1103/PhysRevE.65.016505.

[89] Ö. Apsimon, G. Burt, R. B. Appleby, R. J. Apsimon, D. M. Graham, and S. P. Jamison, "Six-dimensional phase space preservation in a terahertz-driven multistage dielectric-lined rectangular waveguide accelerator," *Phys. Rev. Accel. Beams*, vol. 24, p. 121 303, 12 Dec. 2021. DOI: 10.1103/PhysRevAccelBeams.24.121303. [Online]. Available: https://link.aps.org/doi/10.1103/PhysRevAccelBeams.24.121303.

[90] W. J. Lynn, G. Andonian, N. Majernik, and J. B. Rosenzweig, "Strong Quadrupole Wakefield Based Focusing in Dielectric Wakefield Accelerators," in *Proc. IPAC'21*, (Campinas, Brazil, May 2021), JACoW Publishing, Geneva, Switzerland, 2021, pp. 4059–4061. DOI: 10.18429/JACoW-IPAC2021-THPAB155. [Online]. Available: https://jacow.org/ipac2021/papers/THPAB155.pdf.

[91] T. Overton, T. Pacey, Y. Saveliev, and G. Xia, "Beam Dynamics and Drive Beam Losses Within a Planar Dielectric Wakefield Accelerator," in *Proc. IPAC'22*, (Bangkok, Thailand), ser. International Particle Accelerator Conference, JACoW Publishing, Geneva, Switzerland, Jul. 2022, pp. 641–644, ISBN: 978-3-95450-227-1. DOI: 10.18429/JACoW-IPAC2022-MOPOMS010. [Online]. Available: https://jacow.org/ipac2022/papers/mopoms010.pdf.

[92] W. Lynn, G. Andonian, N. Majernik, *et al.*, "Demonstration of transverse stability in an alternating symmetry planar dielectric structure," in *Proc. IPAC'23*, (Venezia), ser. IPAC'23 - 14th International Particle Accelerator Conference, JACoW Publishing, Geneva, Switzerland, May 2023, pp. 972–976. [Online]. Available: https://indico.jacow.org/event/41/contributions/1645.

[93] A. Novokhatski, "Wakefield potentials of corrugated structures," *Phys. Rev. ST Accel. Beams*, vol. 18, p. 104 402, 10 Oct. 2015. DOI: 10.1103/PhysRevSTAB.18.104402. [Online]. Available: https://link.aps.org/doi/10.1103/PhysRevSTAB.18.104402.

[94] P. Craievich, "Passive longitudinal phase space linearizer," *Phys. Rev. ST Accel. Beams*, vol. 13, p. 034 401, 3 Mar. 2010. DOI: 10.1103/PhysRevSTAB.13.034401. [Online]. Available: https://link.aps.org/doi/10.1103/PhysRevSTAB.13.034401.

[95] H. Deng, M. Zhang, C. Feng, T. Zhang, X. Wang, T. Lan, L. Feng, W. Zhang, X. Liu, H. Yao, L. Shen, B. Li, J. Zhang, X. Li, W. Fang, D. Wang, M.-e. Couprie, G. Lin, B. Liu, Q. Gu, D. Wang, and Z. Zhao, "Experimental demonstration of longitudinal beam phase-space linearizer in a free-electron laser facility by corrugated structures," *Phys. Rev. Lett.*, vol. 113, p. 254 802, 25 Dec. 2014. DOI: 10.1103/PhysRevLett.113.254802. [Online]. Available: https://link.aps.org/doi/10.1103/PhysRevLett.113.254802.

[96] F. Fu, R. Wang, P. Zhu, L. Zhao, T. Jiang, C. Lu, S. Liu, L. Shi, L. Yan, H. Deng, C. Feng, Q. Gu, D. Huang, B. Liu, D. Wang, X. Wang, M. Zhang, Z. Zhao, G. Stupakov, D. Xiang, and J. Zhang, "Demonstration of nonlinear-energy-spread compensation in relativistic electron bunches with corrugated structures," *Phys. Rev. Lett.*, vol. 114, p. 114 801, 11 Mar. 2015. DOI: 10.1103/PhysRevLett.

114.114801. [Online]. Available: https://link.aps.org/doi/10.1103/PhysRevLett.114.114801.

[97] P. Emma, M. Venturini, K. L. F. Bane, G. Stupakov, H.-S. Kang, M. S. Chae, J. Hong, C.-K. Min, H. Yang, T. Ha, W. W. Lee, C. D. Park, S. J. Park, and I. S. Ko, "Experimental demonstration of energy-chirp control in relativistic electron bunches using a corrugated pipe," *Phys. Rev. Lett.*, vol. 112, p. 034 801, 3 Jan. 2014. DOI: 10.1103/PhysRevLett.112.034801. [Online]. Available: https://link.aps.org/doi/10.1103/PhysRevLett.112.034801.

[98] Z. Zhang, K. Bane, Y. Ding, Z. Huang, R. Iverson, T. Maxwell, G. Stupakov, and L. Wang, "Electron beam energy chirp control with a rectangular corrugated structure at the linac coherent light source," *Phys. Rev. ST Accel. Beams*, vol. 18, p. 010 702, 1 Jan. 2015. DOI: 10.1103/PhysRevSTAB.18.010702. [Online]. Available: https://link.aps.org/doi/10.1103/PhysRevSTAB.18.010702.

[99] M. Guetg *et al.*, "Commissioning of the RadiaBeam / SLAC Dechirper," in *Proc. of International Particle Accelerator Conference (IPAC'16)*, ser. International Particle Accelerator Conference, Geneva, Switzerland: JACoW, Jun. 2016, pp. 809–812. DOI: doi:10.18429/JACoW-IPAC2016-MOPOW044. [Online]. Available: http://jacow.org/ipac2016/papers/mopow044.pdf.

[100] S. Bettoni *et al.*, "Beam Manipulation Using Self-Induced Fields in the SwissFEL Injector," in *Proc. 9th International Particle Accelerator Conference (IPAC'18)*, (Vancouver, BC, Canada), ser. International Particle Accelerator Conference, Geneva, Switzerland: JACoW Publishing, Jun. 2018, pp. 3401–3404. DOI: doi:10.18429/JACoW-IPAC2018-THPAK074. [Online]. Available: http://jacow.org/ipac2018/papers/thpak074.pdf.

[101] Y.-W. Gong, M. Zhang, W.-J. Fan, D. Gu, and M.-H. Zhao, "Beam performance of the SHINE dechirper," *Nuclear Science and Techniques*, vol. 32, no. 3, p. 29, 2021. DOI: 10.1007/s41365-021-00860-8. [Online]. Available: https://doi.org/10.1007/s41365-021-00860-8.

[102] T. Pacey, "Development of novel applications of dielectric wakefield structures for electron accelerators," Ph.D. dissertation, The University of Manchester, 2019.

[103] M. Colling, D. Dunning, B. Fell, T. Pacey, and Y. Saveliev, "Mechanical Design of a Dielectric Wakefield Dechirper System for CLARA," in *Proc. 10th International Particle Accelerator Conference (IPAC'19), Melbourne, Australia, 19-24 May 2019*, (Melbourne, Australia), ser. International Particle Accelerator Conference, Geneva, Switzerland: JACoW Publishing, Jun. 2019, pp. 1912–1915, ISBN: 978-3-95450-208-0. DOI: doi:10.18429/JACoW-IPAC2019-TUPRB108. [Online]. Available: http://jacow.org/ipac2019/papers/tuprb108.pdf.

[104] A. Gillespie, "Bunch length diagnostics: Current status and future directions," in *Proceedings of the CERN-Accelerator-School course: Beam Instrumentation*, 2018, pp. 305–317. [Online]. Available: https://arxiv.org/abs/2005.05715.

[105] A. Novokhatski *et al.*, "RadiaBeam/SLAC Dechirper as a Passive Deflector," in *Proc. of International Particle Accelerator Conference (IPAC'16)*, ser. International Particle Accelerator Conference, Geneva, Switzerland: JACoW, Jun. 2016, pp. 817–819. DOI: doi:10.18429/JACoW-IPAC2016-MOPOW046. [Online]. Available: http://jacow.org/ipac2016/papers/mopow046.pdf.

[106] J. Zemella, K. Bane, A. Fisher, M. Guetg, Z. Huang, R. Iverson, P. Krejcik, A. Lutman, T. Maxwell, A. Novokhatski, G. Stupakov, Z. Zhang, M. Harrison, and M. Ruelas, "Measurements of wake-induced electron beam deflection in a dechirper at the linac coherent light source," *Phys. Rev. Accel. Beams*, vol. 20, p. 104 403, 10 Oct. 2017. DOI: 10.1103/PhysRevAccelBeams.20.104403. [Online]. Available: https://link.aps.org/doi/10.1103/PhysRevAccelBeams.20.104403.

[107] J. Seok, M. Chung, H.-S. Kang, C.-K. Min, and D. Na, "Use of a corrugated beam pipe as a passive deflector for bunch length measurements," *Phys. Rev. Accel. Beams*, vol. 21, p. 022 801, 2 Feb. 2018. DOI: 10.1103/PhysRevAccelBeams.21.022801. [Online]. Available: https://link.aps.org/doi/10.1103/PhysRevAccelBeams.21.022801.

[108] P. Dijkstal, A. Malyzhenkov, P. Craievich, E. Ferrari, R. Ganter, S. Reiche, T. Schietinger, P. Jurani ć, and E. Prat, "Self-synchronized and cost-effective time-resolved measurements at x-ray free-electron lasers with femtosecond resolution," *Phys. Rev. Research*, vol. 4, p. 013 017, 1 Jan. 2022. DOI: 10.1103/

PhysRevResearch.4.013017. [Online]. Available: https://link.aps.org/doi/10.1103/PhysRevResearch.4.013017.

[109] T. Pacey, D. Angal-Kalinin, A. Bainbridge, J. Henderson, J. Jones, N. Joshi, S. Mathisen, T. Overton, A. Pollard, Y. Saveliev, E. Snedden, C. Swain, C. Tollervey, D. Walsh, and J. Wolfenden, "Development of a 6D Electron Beam Diagnostics Suite for Novel Acceleration Experiments at FEBE on CLARA," in *Proc. 11th Int. Beam Instrum. Conf. (IBIC'22)*, ser. International Beam Instrumentation Conference, JACoW Publishing, Geneva, Switzerland, Dec. 2022, pp. 1–5, ISBN: 978-3-95450-241-7. DOI: 10.18429/JACoW-IBIC2022-MO1C3. [Online]. Available: https://jacow.org/ibic2022/papers/mo1c3.pdf.

[110] D. Mihalcea, P. Piot, and P. Stoltz, "Three-dimensional analysis of wakefields generated by flat electron beams in planar dielectric-loaded structures," *Phys. Rev. ST Accel. Beams*, vol. 15, p. 081 304, 8 Aug. 2012. DOI: 10.1103/PhysRevSTAB.15.081304. [Online]. Available: https://link.aps.org/doi/10.1103/PhysRevSTAB.15.081304.

[111] S. Y. Park and J. L. Hirshfield, "Theory of wakefields in a dielectric-lined waveguide," *Phys. Rev. E*, vol. 62, pp. 1266–1283, 1 Jul. 2000. DOI: 10.1103/PhysRevE.62.1266. [Online]. Available: https://link.aps.org/doi/10.1103/PhysRevE.62.1266.

[112] C. Wang and J. L. Hirshfield, "Theory for wakefields in a multizone dielectric lined waveguide," *Phys. Rev. ST Accel. Beams*, vol. 9, p. 031 301, 3 Mar. 2006. DOI: 10.1103/PhysRevSTAB.9.031301. [Online]. Available: https://link.aps.org/doi/10.1103/PhysRevSTAB.9.031301.

[113] K.-Y. Ng, "Wake fields in a dielectric-lined waveguide," *Phys. Rev. D*, vol. 42, pp. 1819–1828, 5 Sep. 1990. DOI: 10.1103/PhysRevD.42.1819. [Online]. Available: https://link.aps.org/doi/10.1103/PhysRevD.42.1819.

[114] M. R. Spiegel, *Complex Variables: With an Introduction to Conformal Mapping and Its Applications*. McGraw-Hill, 2009.

[115] S. S. Baturin and A. D. Kanareykin, "Cherenkov radiation from short relativistic bunches: General approach," *Phys. Rev. Lett.*, vol. 113, p. 214 801, 21 Nov. 2014. DOI: 10.1103/PhysRevLett.113.214801. [Online]. Available: https://link.aps.org/doi/10.1103/PhysRevLett.113.214801.

[116] S. S. Baturin and A. D. Kanareykin, "New method of calculating the wakefields of a point charge in a waveguide of arbitrary cross section," *Phys. Rev. Accel. Beams*, vol. 19, p. 051 001, 5 May 2016. DOI: 10.1103/PhysRevAccelBeams.19.051001. [Online]. Available: https://link.aps.org/doi/10.1103/PhysRevAccelBeams.19.051001.

[117] I. Wolfram Research, *Mathematica, Version 13.2*, Champaign, IL, 2022. [Online]. Available: https://www.wolfram.com/mathematica.

[118] H. Wiedemann, *Particle Accelerator Physics*. Springer Nature, 2015.

[119] S. S. Baturin, I. L. Sheinman, A. M. Altmark, and A. D. Kanareykin, "Transverse operator method for wakefields in a rectangular dielectric loaded accelerating structure," *Phys. Rev. ST Accel. Beams*, vol. 16, p. 051 302, 5 May 2013. DOI: 10.1103/PhysRevSTAB.16.051302. [Online]. Available: https://link.aps.org/doi/10.1103/PhysRevSTAB.16.051302.

[120] N. Onishchenko, D. Y. Sidorenko, and G. Sotnikov, "Acceleration of electrons by wake fields of a regular train of bunches in a dielectric waveguide of finite length," *Ukrainian Journal of Physics*, vol. 48, no. 1, pp. 17–26, 2003.

[121] G. Sotnikov, I. Onishchenko, and T. Marshall, "3D analysis of wake field excitation in a dielectric loaded rectangular resonator," *AIP Conference Proceedings*, vol. 877, no. 1, pp. 888–894, Nov. 2006, ISSN: 0094-243X. DOI: 10.1063/1.2409230. [Online]. Available: https://doi.org/10.1063/1.2409230.

[122] B. Jiang, C. Jing, P. Schoessow, J. Power, and W. Gai, "Formation of a novel shaped bunch to enhance transformer ratio in collinear wakefield accelerators," *Phys. Rev. ST Accel. Beams*, vol. 15, p. 011 301, 1 Jan. 2012. DOI: 10.1103/PhysRevSTAB.15.011301. [Online]. Available: https://link.aps.org/doi/10.1103/PhysRevSTAB.15.011301.

[123] A. O'Hagan and T. Leonard, "Bayes estimation subject to uncertainty about parameter constraints," *Biometrika*, vol. 63, no. 1, pp. 201–203, 1976.

[124] A. Tremaine, J. Rosenzweig, and P. Schoessow, "Electromagnetic wake fields and beam stability in slab-symmetric dielectric structures," *Phys. Rev. E*, vol. 56, pp. 7204–7216, 6 Dec. 1997. DOI: 10.1103/PhysRevE.56.7204. [Online]. Available: https://link.aps.org/doi/10.1103/PhysRevE.56.7204.

[125] S. S. Baturin, G. Andonian, and J. B. Rosenzweig, "Analytical treatment of the wakefields driven by transversely shaped beams in a planar slow-wave structure," *Phys. Rev. Accel. Beams*, vol. 21, p. 121 302, 12 Dec. 2018. DOI: 10.1103/PhysRevAccelBeams.21.121302. [Online]. Available: https://link.aps.org/doi/10.1103/PhysRevAccelBeams.21.121302.

[126] B. D. O'Shea, G. Andonian, S. S. Baturin, C. I. Clarke, P. D. Hoang, M. J. Hogan, B. Naranjo, O. B. Williams, V. Yakimenko, and J. B. Rosenzweig, "Suppression of deflecting forces in planar-symmetric dielectric wakefield accelerating structures with elliptical bunches," *Phys. Rev. Lett.*, vol. 124, p. 104 801, 10 Mar. 2020. DOI: 10.1103/PhysRevLett.124.104801. [Online]. Available: https://link.aps.org/doi/10.1103/PhysRevLett.124.104801.

[127] T. Overton, *tobyoverton/DiWaCAT: DiWaCAT v0*, version v0.1, Sep. 2023. DOI: 10.5281/zenodo.8321426. [Online]. Available: https://doi.org/10.5281/zenodo.8321426.

[128] J. Teunissen and U. Ebert, "Controlling the weights of simulation particles: Adaptive particle management using k-d trees," *Journal of Computational Physics*, vol. 259, pp. 318–330, 2014, ISSN: 0021-9991. DOI: https://doi.org/10.1016/j.jcp.2013.12.005. [Online]. Available: https://www.sciencedirect.com/science/article/pii/S0021999113008048.

[129] S. Jalas, I. Dornmair, R. Lehe, H. Vincenti, J. Vay, M. Kirchen, and A. Maier, "Accurate Modelling of Plasma Acceleration with Arbitrary Order Pseudo-Spectral Particle-in-Cell Methods," *Physics of Plasmas*, vol. 24, no. 3, Mar. 2017, ISSN: 1070-664X. DOI: 10.1063/1.4978569. [Online]. Available: https://doi.org/10.1063/1.4978569.

[130] J. P. Boris *et al.*, "Relativistic plasma simulation-optimization of a hybrid code," in *Proc. Fourth Conf. Num. Sim. Plasmas*, 1970, pp. 3–67.

[131] J.-L. Vay, "Simulation of beams or plasmas crossing at relativistic velocity," *Physics of Plasmas*, vol. 15, no. 5, p. 056 701, 2008. [Online]. Available: https://doi.org/10.1063/1.2837054.

[132] H. Qin, S. Zhang, J. Xiao, J. Liu, Y. Sun, and W. M. Tang, "Why is Boris algorithm so good?" *Physics of Plasmas*, vol. 20, no. 8, p. 084 503, 2013. [Online]. Available: https://doi.org/10.1063/1.4818428.

[133] S. Zenitani and T. Umeda, "On the Boris solver in particle-in-cell simulation," *Physics of Plasmas*, vol. 25, no. 11, p. 112 110, 2018. [Online]. Available: https://doi.org/10.1063/1.5051077.

[134] D. Dunning, H. C. Cortés, J. Jones, and N. Thompson, "Multi-Objective FEL Design Optimisation Using Genetic Algorithms," in *Proc. FEL'19*, (Hamburg, Germany), ser. Free Electron Laser Conference, JACoW Publishing, Geneva, Switzerland, Nov. 2019, pp. 711–714, ISBN: 978-3-95450-210-3. DOI: 10.18429/JACoW-FEL2019-THP065. [Online]. Available: http://jacow.org/fel2019/papers/thp065.pdf.

[135] K. Floettmann, *ASTRA - a space charge tracking algorithm*, 2000. [Online]. Available: http://www.desy.de/~mpyflo.

[136] M. Borland, "User's manual for ELEGANT," *APS LS-231, May*, vol. 6, 1993.

[137] M. De Loos and S. Van der Geer, "General Particle Tracer: A new 3D code for accelerator and beamline design," in *5th European Particle Accelerator Conference*, vol. 1241, 1996. [Online]. Available: https://accelconf.web.cern.ch/e96/PAPERS/THPG/THP001G.PDF.

[138] M. Dohlus and T. Limberg, *CSRTrack user's manual v1.2*, 2007. [Online]. Available: http://www.desy.de/fel-beam/csrtrack/.

[139] S. Hill, "Tri-linear interpolation," *Graphics Gems IV*, pp. 521–525, 1994.

[140] L. K. Arata, "Tricubic interpolation," *Graphics Gems V*, pp. 107–110, 1995.

[141] Dassault Systemes, *CST Studio Suite, "CST Microwave Studio"*, 2008. [Online]. Available: https://cst.com.

[142] T. H. Pacey, Y. Saveliev, A. Healy, P. G. Huggard, B. Alderman, P. Karataev, K. Fedorov, and G. Xia, "Continuously tunable narrow-band terahertz generation with a dielectric lined waveguide driven by short electron bunches," *Phys. Rev. Accel. Beams*, vol. 22, p. 091 302, 9 Sep. 2019. DOI: 10.1103/PhysRevAccelBeams.22.091302. [Online]. Available: https://link.aps.org/doi/10.1103/PhysRevAccelBeams.22.091302.

[143] Tech-X Corporation, *Https://www.txcorp.com/vsim*.

[144] D. Angal-Kalinin, A. Bainbridge, A. D. Brynes, *et al.*, "Design, specifications, and first beam measurements of the compact linear accelerator for research and applications front end," *Phys. Rev. Accel. Beams*, vol. 23, p. 044 801, 4 Apr. 2020. DOI: 10.1103/PhysRevAccelBeams.23.044801. [Online]. Available: https://link.aps.org/doi/10.1103/PhysRevAccelBeams.23.044801.

[145] H. Bartosik, Y. Papaphilippou, and A. Wolski, "A first taste of nonlinear beam dynamics," in *Proceedings of the CERN-Accelerator-School course: Introduction to Particle Accelerators*, pp. 295–331. [Online]. Available: https://arxiv.org/abs/2201.01532.

[146] Y. Saveliev, T. Pacey, J. Jones, and G. Xia, "First dielectric wakefield experiments at Daresbury Laboratory," *Journal of Physics: Conference Series*, vol. 1596, no. 1, p. 012 015, Jul. 2020. DOI: 10.1088/1742-6596/1596/1/012015. [Online]. Available: https://dx.doi.org/10.1088/1742-6596/1596/1/012015.

[147] P. Lu, H. Vennekate, A. Arnold, P. Michel, P. Murcek, J. Teichert, and R. Xiang, "Transverse emittance measurement by slit-scan method for an SRF photo injector," in *Proceedings FEL'13*, 2013. [Online]. Available: https://accelconf.web.cern.ch/FEL2013/papers/tupso44.pdf.

[148] M. Zhang, "Emittance formula for slits and pepper-pot measurement," Fermi National Accelerator Lab.(FNAL), Batavia, IL (United States), Tech. Rep., 1996.

[149] K. Bane and G. Stupakov, "Using surface impedance for calculating wakefields in flat geometry," *Phys. Rev. ST Accel. Beams*, vol. 18, p. 034 401, 3 Mar. 2015. DOI: 10.1103/PhysRevSTAB.18.034401. [Online]. Available: https://link.aps.org/doi/10.1103/PhysRevSTAB.18.034401.

[150] P. Dijkstal, "Temporal FEL pulse shaping and diagnostics at SwissFEL with tileted electron beams," Ph.D. dissertation, ETH Zurich, 2022.

[151] V. Yakimenko, L. Alsberg, E. Bong, G. Bouchard, C. Clarke, C. Emma, S. Green, C. Hast, M. J. Hogan, J. Seabury, N. Lipkowitz, B. O'Shea, D. Storey, G. White, and G. Yocky, "FACET-II facility for advanced accelerator experimental tests," *Phys. Rev. Accel. Beams*, vol. 22, p. 101 301, 10 Oct. 2019. DOI: 10.1103/PhysRevAccelBeams.22.101301. [Online]. Available: https://link.aps.org/doi/10.1103/PhysRevAccelBeams.22.101301.

[152] T. Pacey, D. Dunning, Y. Saveliev, and G. Xia, "Phase Space Manipulation of Sub-Picosecond Electron Bunches Using Dielectric Wakefield Structures," in *Proc. of International Particle Accelerator Conference (IPAC'17), Copenhagen, Denmark, 14â 19 May, 2017*, (Copenhagen, Denmark), ser. International Particle Accelerator Conference, Geneva, Switzerland: JACoW, May 2017, pp. 3302–3304, ISBN: 978-3-95450-182-3. DOI: https://doi.org/10.18429/JACoW-IPAC2017-WEPVA021. [Online]. Available: http://jacow.org/ipac2017/papers/wepva021.pdf.

[153] K. Wille, *The physics of particle accelerators: an introduction*. Clarendon Press, 2000.

[154] P. Craievich and A. A. Lutman, "Effects of the quadrupole wakefields in a passive streaker," *Nuclear Instruments and Methods in Physics Research Section A: Accelerators, Spectrometers, Detectors and Associated Equipment*, vol. 865, pp. 55–59, 2017. DOI: 10.1016/j.nima.2016.10.010. [Online]. Available: https://doi.org/10.1016/j.nima.2016.10.010.

[155] R. Corsini, W. Farabolini, P. Korysko, A. Malyzhenkov, V. Rieker, and K. Sjobak, "Status of the CLEAR User Facility at CERN and its Experiments," in *Proc. LINAC'22*, (Liverpool, UK), ser. International Linear Accelerator Conference, JACoW Publishing, Geneva, Switzerland, Sep. 2022, pp. 753–757. DOI: 10.18429/JACoW-LINAC2022-THPOPA05. [Online]. Available: https://jacow.org/linac2022/papers/thpopa05.pdf.

[156] M. J. Nasse, M. Schuh, S. Naknaimueang, *et al.*, "FLUTE: A versatile linac-based THz source," *Review of Scientific Instruments*, vol. 84, no. 2, Feb. 2013, ISSN: 0034-6748. DOI: 10.1063/1.4790431. eprint: https://pubs.aip.org/aip/rsi/article-pdf/doi/10.1063/1.4790431/16149882/022705_1_online.pdf. [Online]. Available: https://doi.org/10.1063/1.4790431.

[157] M. Ferrario, D. Alesini, M. Anania, *et al.*, "SPARC_LAB present and future," *Nuclear Instruments and Methods in Physics Research Section B: Beam Interactions with Materials and Atoms*, vol. 309, pp. 183–188, 2013, The 5th International Conference "Channeling 2012", "Charged & Neutral Particles Channeling Phenomena" September 23-28,2012, Alghero (Sardinia), Italy, ISSN: 0168-583X. DOI: https://doi.org/10.1016/j.nimb.2013.03.049. [On-

line]. Available: https://www.sciencedirect.com/science/article/pii/S0168583X13003844.

[158] D. Angal-Kalinin, A. Bainbridge, J. Jones, T. Pacey, Y. Saveliev, and E. Snedden, "The Design of the Full Energy Beam Exploitation (FEBE) Beamline on CLARA," in *Proc. LINAC'22*, (Liverpool, UK), ser. International Linear Accelerator Conference, JACoW Publishing, Geneva, Switzerland, Sep. 2022, pp. 585–588, ISBN: 978-3-95450-215-8. DOI: 10.18429/JACoW-LINAC2022-TUPORI18. [Online]. Available: https://jacow.org/linac2022/papers/tupori18.pdf.